Compositional Influences on the Microstructures, Phase Stability, and Mechanical Properties of $TiCr_2$ Laves Phase Alloys

by

Katherine C. Chen

SUBMITTED TO THE DEPARTMENT OF MATERIALS SCIENCE AND
ENGINEERING IN PARTIAL FULFILLMENT OF THE REQUIREMENTS
FOR THE DEGREE OF

DOCTOR OF PHILOSOPHY

at the

MASSACHUSETTS INSTITUTE OF TECHNOLOGY

June 1996

Author___________________________________
Department of Materials Science and Engineering
May 3, 1996

Certified by______________
Professor Samuel M. Allen
Thesis Supervisor

Certified by______________________

Thesis Supervisor

Accepted by_______________________________
F. Rubner
TDK Professor of Materials Science and Engineering
Chair, Departmental Committee on Graduate Students

Compositional Influences on the Microstructures, Phase Stability, and Mechanical Properties of $TiCr_2$ Laves Phase Alloys

by
Katherine C. Chen

Submitted to the Department of Materials Science and Engineering on May 3, 1996
in partial fulfillment of the requirements for the degree of Doctor of Philosophy

Abstract

The compositional influences on the microstructures, phase stability, and mechanical properties of $TiCr_2$-base alloys have been addressed in efforts to improve the toughness of Laves phase intermetallics. Single-phase stoichiometric and nonstoichiometric $TiCr_2$, two-phase binary alloys containing $TiCr_2$, and ternary $TiCr_2$-base Laves phases have been characterized, and various effects on the mechanical properties of $TiCr_2$ have been assessed by a microindentation technique.

In binary Ti-Cr alloys, a combination of metallography, x-ray diffraction, lattice constant measurements, density measurements, and electron microprobe analysis have been used to establish a narrow single-phase $TiCr_2$ Laves phase field extending towards Ti-rich compositions. Anti-site substitutions and Cr-site vacancies were identified as the defect mechanisms accompanying off-stoichiometry. The Laves phase crystal structures (*C*14, *C*36, and *C*15) were also studied as a function of composition and annealing temperature. The effects of alloy composition, crystal structure, and presence of a second phase on the mechanical properties were investigated. Indentation revealed that the maximum hardness and minimum fracture toughness values occur at the stoichiometric $TiCr_2$ composition. Vacancies found in the off-stoichiometric compositions may aid the complex atomic motions involved in the synchroshear deformation mechanism.

Microstructures and the orientation relationship of the beta-(Ti,Cr) bcc phase and $TiCr_2$ Laves phase are discussed in the analysis of two-phase Ti-Cr alloys. Lath-shaped, equiaxed, and lamellar $TiCr_2$ precipitates were encountered. Indentation results are correlated with the microstructures, and deformation-induced defects in $TiCr_2$ from room-temperature compression tests are examined by TEM. Large improvements in the toughness exhibited by two-phase alloys are attributed to crack deflection, crack bridging, and beta phase/$TiCr_2$ interface debonding. These results suggest that Laves phase intermetallics will have to be developed as two-phase systems in order to possess adequate toughness for practical purposes.

Reports of improved ductility in Laves phases resulting from alloying elements that occupy both sublattice sites and/or that lower the stacking fault energies were explored with ternary $TiCr_2$-base alloys. Effects of alloying element site occupancy and crystal structure stabilization were studied systematically with Fe, Nb, V, and Mo additions. Alloying $TiCr_2$ did not result in greatly improved toughness, and the sublattice-site occupancy proved to have little effect. However, alloying elements that stabilized the cubic *C*15 structure or affected the single-phase solubility limits (and precipitated a second phase) were found to be the most effective factors improving the toughness of $TiCr_2$-base alloys, and indicate new toughening strategies.

Thesis Supervisor: Samuel M. Allen	Title: Professor of Physical Metallurgy
Thesis Supervisor: James D. Livingston	Title: Senior Lecturer

Acknowledgments

I would first like to acknowledge Dr. Gunter Gottstein, my undergraduate academic honors advisor at Michigan State University, who was absolutely instrumental in introducing me to the wonderful world of materials science and who encouraged me to go to graduate school at MIT. I am also indebted to the US Department of Defense for funding the first few years of my graduate studies, and to Professors Sam Allen and Jim Livingston for letting me join the Laves phase intermetallics group. I have been fortunate to have two thesis advisors with different experiences and approaches to field my many questions and concerns.

Professors Ali Argon and John Vander Sande are appreciated for serving on my thesis committee and for their useful comments. Special thanks goes to Yin Lin Xie for always being helpful in the labs and acting like a surrogate group member when there were no other group members to talk to about my research. My experience at MIT has been truly enlightened due to my fellow classmates and officemates: Yaping, Ariel, Honglin, Beth, Heather, Ann, Arun, Patrick, Jerry, Christophe, Mark, Bruce, Erik and many others.

Norm Sun is acknowledged for his constant friendship, for keeping me company during the all-night vacuum-furnace sessions, and for making sure I didn't work all the time. My housemates, Martin Burkhardt, Melanie Sherony, and later Charrissa Lin, have made living in Cambridge a pleasant and memorable experience. My buddies, Linda Yuen, Vince Wong, and Nancy Chen, have always been there for me throughout the years and I thank them for their friendship. Eternal thanks go out to my friends in Michigan, Chicago, and California for their support, encouragement, and feigned interest in my research work.

Lastly, I would like to thank Carson, my siblings, and my parents for believing in me and for enduring my complaints and sometimes less-than-positive attitude about graduate school. This thesis is dedicated to my family, and hereafter, they will be required to address me as Dr. Chen.

Table of Contents

List of Figures

List of Tables

Chapter 1

Introduction and Background

1.1 INTRODUCTION

As the demand for high-performance materials continually pushes the limits of today's superalloys in high-temperature structural applications, alternatives such as intermetallic compounds are actively being sought. By virtue of their ordered structure and strong atomic bonds, intermetallics generally have high yield stresses, large elastic moduli, and high melting temperatures. Self-diffusion rates tend to be slower than in disordered alloys and pure metals, resulting in microstructural stability and good creep resistance. Depending on the elemental constituents, some intermetallic compounds may possess excellent oxidation resistance (for instance, those containing Cr or Al). Other intermetallics, such as TiAl, exhibit low densities, resulting in very attractive high "specific" properties (i.e., property/density). Unfortunately, the strong bonding that gives intermetallics their desirable properties also leads to brittleness at low temperatures. Before many practical applications can be realized, intermetallics with more ductility and toughness must be developed.

Considerable research has been devoted to the nickel aluminides and titanium aluminides, partly due to their relatively simple crystal structures. Yet, the Laves phases comprise the single largest class of intermetallics. The Laves phases number over 1000 binary and ternary compounds, and just the sheer number of potential intermetallics for applications warrants the investigation of this class of materials. Laves phases are topologically close-packed AB_2 compounds that have complex crystal structures ($C14$, $C36$, or $C15$) involving two dissimilar-sized atoms with 12 or 24 atoms per unit cell.

Although Laves phase intermetallics have been studied for their magnetic, superconducting, and hydrogen-storing properties, little is known about their mechanical properties. Due to their complicated crystal structures and well-deserved reputation for brittleness at low temperatures, Laves phases have generally been avoided, rather than exploited, as structural materials. However, the *C*14 and *C*15 crystal structures are actually analogous to the hcp and fcc structures (by virtue of the stacking sequences of close-packed atomic layer units), and their respective slip systems have also been identified to be analogous [1]. The Laves phases are thus not so intimidating, and furthermore, evidence for some room-temperature ductility has been documented in the HfV_2 Laves phase in a two-phase alloy [2]. This demystification of the complicated and brittle Laves phase has spawned attempts to study their mechanical properties and to improve the room-temperature toughness in order to develop these materials as high-temperature structural materials. Laves phase intermetallics now stand as candidates for future turbine components and other high-temperature, high-strength applications [1]. A better understanding of the factors influencing the mechanical behavior of Laves phases is thus greatly needed in order to find ways of gaining greater deformability and toughness.

This thesis presents the research findings of the compositional influences on the microstructures, phase stability, and mechanical properties of $TiCr_2$-base Laves phase alloys. Prior studies have identified alloys containing $TiCr_2$ Laves phases to have promising mechanical properties and oxidation resistance at elevated temperatures [3,4]. The Ti-Cr system is a model candidate for studying the compositional dependencies of Laves phases since chemically-homogeneous, single-phase $TiCr_2$ is stable over a range of compositions near stoichiometry. $TiCr_2$ precipitates from a bcc solid solution, as opposed to almost all other Laves phases which are generally formed by an eutectic reaction. Microstructural control is also possible through annealing treatments. A series of experiments are performed on $TiCr_2$-base alloys of different compositions. The characterization and mechanical properties of the alloys are broken down into three different sections in this thesis: (i) single-phase stoichiometric and nonstoichiometric $TiCr_2$, (ii) two-phase binary alloys containing $TiCr_2$, and (iii) single-phase, $TiCr_2$-base ternary Laves compounds. Each of these sections permits a separate investigation of different effects on the toughness of $TiCr_2$.

The single-phase field of $TiCr_2$ is first defined and characterized in Chapter 2. Uncertainties in the most recent phase diagram [5] required the determination of the solubility ranges and crystal structures of $TiCr_2$ as a function of temperature by metallography, electron microprobe analysis (EMPA), and x-ray diffraction (XRD). The defect mechanism accompanying nonstoichiometric $TiCr_2$ is also identified by x-ray diffraction and density measurements. These defects, in turn, account for any changes or trends in the mechanical properties among the alloys in the single-phase $TiCr_2$ field. Vacancies have been proposed by Hazzledine [6] to aid the movement of synchro-Shockley dislocations, and thus could increase deformability. The disruption of the close-packed structure of the Laves phase is believed to facilitate the complex atomic motions involved in the deformation process of synchroshear [2,7].

The brittleness of Laves phases severely limits the possible room temperature mechanical tests. Quantitative measurements of the flow and fracture of materials are needed for comparisons among all the different alloy compositions. Chapter 3 describes an indentation technique used to assess the microhardness and fracture toughness of the $TiCr_2$-base alloys. The indentation crack character and behavior are also studied. The single-phase alloys characterized in Chapter 2 are then evaluated by indentation. The effects of alloy composition (e.g., nonstoichiometry), crystal structure, and presence of a second phase on the mechanical properties of $TiCr_2$ are discussed. These results also serve as the baseline for comparisons with both the two-phase alloys and the ternary alloys.

Two-phase alloys are the logical progression in the development towards practical materials, and two-phase Ti-Cr binary alloys (Ti-rich beta+$TiCr_2$ and Cr-rich beta+$TiCr_2$) are studied next in Chapter 4. Since the properties of a two-phase system are dependent upon the properties of the individual phases, the beta bcc phase is characterized as well as the $TiCr_2$ precipitates. A range of interesting microstructures is revealed with the different Ti-Cr alloy compositions. Control of the microstructure (by alloy composition selection and annealing treatment) is essential to the tailoring of materials for specific properties, and therefore the microstructures and the orientation relationship of the two phases are analyzed. Results from indentation of the two-phase alloys are discussed and compared against the single-phase $TiCr_2$ alloys in Chapter 5. Room-temperature compression tests were also performed on the two-phase alloys. Deformation-induced defect structures in $TiCr_2$ are examined by qualitative comparisons of transmission electron microscopy (TEM) images. The mechanical properties of the two-phase, $TiCr_2$-base alloys are compared with other two-phase Laves systems.

Chapter 6 addresses the effects of alloying additions to single-phase $TiCr_2$. Ternary $TiCr_2$-base Laves phases are tested by indentation and compared to the binary $TiCr_2$ Laves phases. Particular attention is paid to the atomic site on which the alloying element substitutes. Enhanced deformability has been reported in HfV_2 with additions of Nb, and has been proposed to be due to the alloying element residing on both the Hf and V sublattices, thereby "opening up" the close-packed structure for easier atomic movements in the synchroshear mechanism [2,7]. Ternary alloy compositions were selected for the alloying element to occupy the Ti-sublattice, Cr-sublattice, or both sublattices. Alloying has also been proposed to lower the stacking fault energies of Laves phases which might induce twinning and/or phase transformations upon deformation [2]. Stress-induced *C*36 to *C*15 transformations have been reported in the $ZrFe_2$ Laves phase [8], and offer another means of improving the deformation of Laves phases. Whether these toughening mechanisms can be applied to another Laves phase is explored with the $TiCr_2$-base alloys, thus testing the generality of these theories. Changes in the stacking fault energies, phase (crystal structure) stabilities, lattice constants, and solubility limits due to alloying are investigated.

The final chapter summarizes the main conclusions of this thesis. The comprehensive survey of single-phase stoichiometric and nonstoichiometric $TiCr_2$, $TiCr_2$ in two-phase alloys, and $TiCr_2$-base ternary Laves phases culminates in a grand picture of how the alloy composition affects the microstructure, crystal structure, and mechanical properties of $TiCr_2$-base alloys. The most influential factors on the mechanical properties of $TiCr_2$-base alloys are determined and discussed. Understanding these effects is essential to the design and development of Laves phases as useful structural materials.

1.2 BACKGROUND

1.2.1 Crystal Structures

The Laves phases are comprised of three different, but closely-related crystal structures, namely *C*15 (cubic), *C*14 (hexagonal), and *C*36 (dihexagonal) in the Strukturbericht designation. The smaller and more abundant B atoms make up tetrahedra linked corner-to-corner. Different arrangements of the tetrahedral networks give the different crystal structures, as seen in Figure 1.1 [9]. The larger A atoms then fit into the interstices enclosed by the B-atom tetrahedra, and are arranged in the wurtzite structure for *C*14 or the diamond structure for *C*15. The *C*36 structure can be considered as a mixture of the *C*14 and *C*15 structures.

Alternatively, the Laves phase structures may be pictured by the stacking of close-packed layer units. These elementary stacking units consist of four interpenetrating atomic layers, as seen in Figure 1.2 [10]. These layer units of four planes can be of two types, primed (X', Y', Z') or unprimed (X, Y, Z), which distinguishes between different

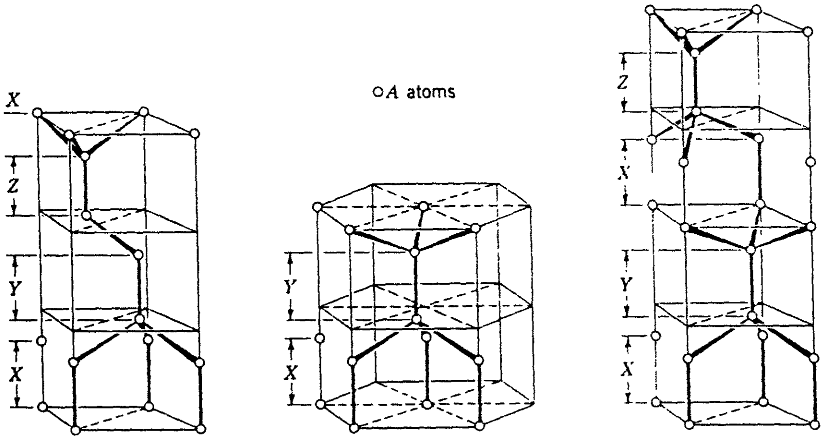

C15 C14 C36

Figure 1.1 (a) Distribution of the A atoms and stacking of layers in Laves phases [9].

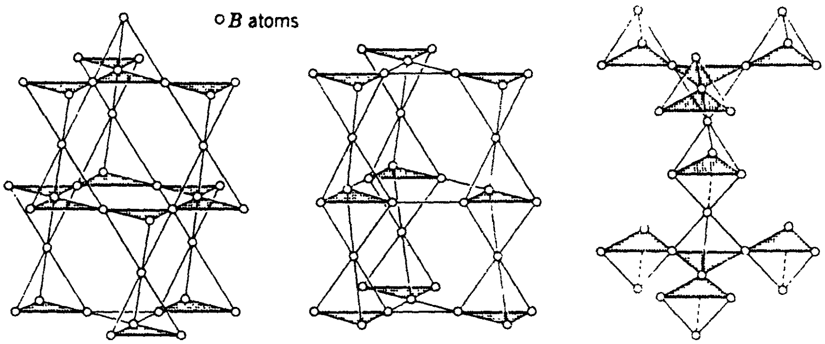

C15 C14 C36

(b) Distribution of the B atoms and stacking of tetrahedra in Laves phases [9].

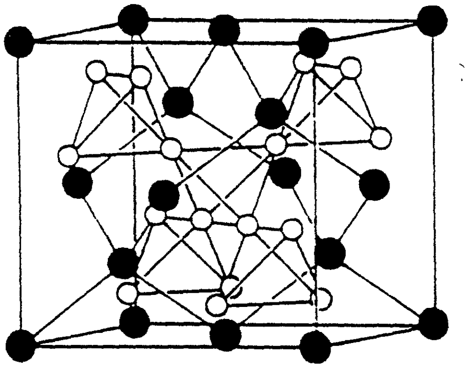

(c) The cubic unit cell for the C15 Laves phases [10].

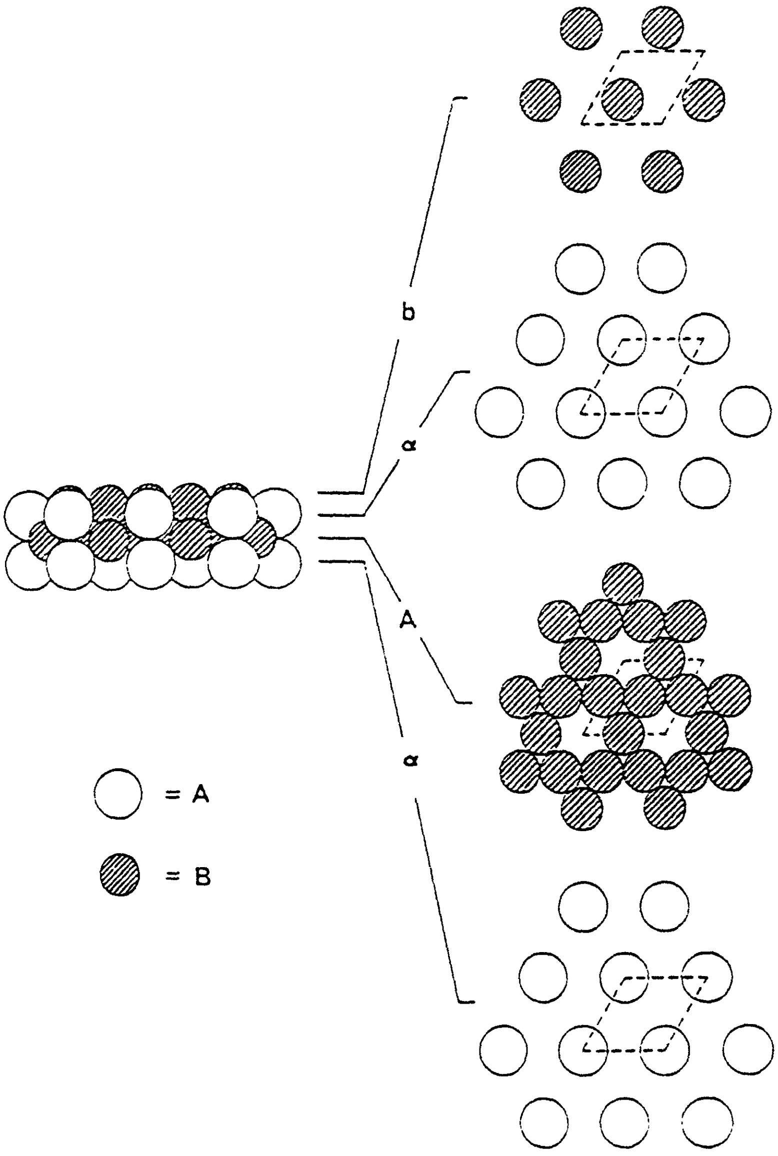

*C*15: αAαcβBβaγCγb... or XYZXYZ...

*C*14: αAαcβBβc... or XY'XY'...

*C*36: αAαcβBβcαAαbγCγb... or XY'X'ZXY'X'Z...

Figure 1.2 The basic four-layer stacking unit and the stacking sequences of the different Laves phase crystal structures [10].

stackings within the layer units. Using this nomenclature, the cubic *C*15 structure is represented by XYZ stacking, *C*14 by XY'XY', and *C*36 by XY'X'Z. The similarities in stacking to simple fcc (*A*1) and hcp (*A*3) structures are readily apparent, differing in that the stacking units are close-packed planes rather than the four atomic layers in the Laves phases. There are also similarities in the mechanical behavior. The slip systems in the *C*15 and *C*14 structures have been found to mimic those of fcc and hcp structures, respectively [11,12]. The slip model for the Laves phases, however, is not so simple and will be discussed later.

1.2.2 Phase Stability

1.2.2.a *size factors*

The Laves phases are also known as "size-factor" compounds that have a complicated close-packed structure with an ideal radius ratio, $r_A/r_B = \sqrt{3/2} = 1.225$. The larger A atoms have a coordination number of 16 (4A+12B atoms) and the B atoms have a 12-fold coordination (6A+6B atoms). The formation and stability of the Laves phases have been attributed to these geometrical factors [13,14]. But in actuality, Laves phases exist with radius ratios ranging from 1.05 to 1.68, and favorable ratios do not necessarily guarantee the formation of a Laves phase. The ability of the atoms to expand or contract to achieve the ideal radius ratio has been cited to be a better criterion for the formation of Laves phases [15].

Edwards [16] offered a combined geometrical-chemical model to give qualitative explanations for Laves phase stability. Lattice dimensions based solely on a geometrical model were then corrected for A-B chemical interactions due to electronegativity differences. An empirical equation for a calculated lattice parameter as a function of individual atomic radii and electronegativities appeared to provide an excellent fit with observed lattice parameters for many Laves phases. Many other investigators have discussed the competing influences of chemical factors and geometrical principles [17,18].

1.2.2.b *electronic factors*

Electronic influences are also used to explain Laves phase formation, and are invoked to explain the phase stability among the Laves crystal structures. The electron to atom ratio, *e/a*, has been used to explain which crystal structure will be stable [19-21]. The different crystal structures are associated with specific ranges of *e/a* values. Particular *e/a* ratios are related to filled Brillouin zones and represent the transition to a new structure which becomes more energetically favorable. Experimental observations of magnetic susceptibility [22], specific heat coefficients [14,23], and elastic constants [24] confirm these concepts. These studies were performed across a binary join of two different Laves phases, such as $MgCu_2$–$MgZn_2$.

Homogeneity ranges of structures in ternary Laves phases also show a dependence on the *e/a* ratio, as seen in Table 1.1 [14]. Komura and Kitano [25] have found an electron concentration dependence on stacking variants, and have discovered new stacking variants of 6, 8, 9, 10, etc. (*C*15 has the stacking variant of 3, *C*14 has 2, and *C*36 has 4.) Liu [26] has also found various stacking sequences in $Mg(Cu,Ni)_2$ compounds, suggesting a compositional dependence of stacking fault energies.

The relative electronegativities of the constituent atoms and amount of electron transfer are also thought to play a role in phase stability [27,28]. The electron transfer gives an ionic contribution to the bond, and increases as the electronegativity difference between the A and B atoms increases. The additional stability of the bond is reflected in the increased relative heats of formation.

Many theoretical models have been applied by solid-state theorists to explore the electronic structure and bonding of Laves phases [29,30]. Density of states functions and contour maps of valence electron distributions reveal local maximum electron densities concentrated in the center of the B-atom tetrahedra and between the large minority A atoms. This statement holds even when the electron transfers between the A and B atoms are in different directions [31,32]. The effects of directional bonds on deformation mechanisms in Laves phases are unknown.

Table 1.1 Values of e/a ratios in the homogeneity ranges of phases with the $MgCu_2$ (*C*15), $MgNi_2$ (*C*36), and $MgZn_2$ (*C*14) structures in ternary magnesium alloys [14].

System	$MgCu_2$-type (*C*15)	$MgNi_2$-type (*C*36)	$MgZn_2$-type (*C*14)
$MgCu_2 - MgZn_2$	1.33–1.75	1.83–1.90	1.98–2.00
$MgCu_2 - MgAl_2$	1.33–1.73	1.84–1.95	2.03–2.05
$MgCu_2 - MgSi_2$	1.33–1.71	1.81–1.89	1.81–2.01
$MgAg_2 - MgZn_2$	1.72–1.75	1.78–1.90	1.98–2.00

Concentration ranges are expressed in terms of valence electrons/atom: Cu,Ag=1; Mg,Zn=2; Al=3; Si=4.

1.2.3 Mechanical Properties

1.2.3.a *slip systems*

Studies of the mechanical behavior of Laves phases are quite limited, especially examinations of room-temperature deformation. A ductile-brittle transition is generally found around $0.6T_m$, and substantial plasticity is usually only found at high temperatures [1,33-36]. Paufler et al. [12] studied single-crystal $MgZn_2$, the prototype hexagonal *C*14 structure, and found the dominant slip system to be {0001}<1120>. Prismatic slip could be induced with the appropriate orientations, and other studies [26] have been able to activate other slip systems in the hexagonal Laves phase. Moran [11] demonstrated that $MgCu_2$, the prototype cubic *C*15 structure, deformed by the {111}<110> slip system and {111}<112> twin system. Subsequent studies concerning polycrystalline Laves phases and other Laves phase systems confirmed that the *C*14 and *C*15 slip systems are analogous to hcp and fcc [2,37].

1.2.3.b *synchroshear*

The actual deformation of the Laves phases is quite complicated due to their complex crystal structures, and involves the coordinated shifting of atoms in a process called "synchroshear" [38]. In order to understand this process, it is necessary to study the stacking sequence of close-packed planes in more detail. For example (see Figure 1.2), the sequencing of the *C*15 structure is: αAαcβBβaγCγb..., where the Greek letters are the larger A atoms, the capital Roman letters are the dense "Kagome net" of B atoms, and the small Roman letters are the less-dense plane of B atoms. Figure 1.3 shows the geometries of the two different types of "sandwiches" that occur in the sequence [39]. From the relative packing differences and interlayer spacings, it is apparent that the αAα type sandwich is more rigid and will stay intact, while shear will occur within the more deformable αcβ type sandwich. In synchroshear, the smaller atoms shear by $1/6[\bar{2}11]$ while synchronously, the larger atoms shear by $1/6[\bar{1}\bar{1}2]$, as in Figure 1.4. In other words, the smaller atoms move from the "c-site" to the "b-site" while the larger atoms move from the "β-site" to the "γ-site" Slip, twinning, and phase transformations can be explained by dislocation models and synchroshear [40]. Allen et al. [41,42] have confirmed these concepts by observing stacking faults and phase transformations by TEM. Chu [39] has also explained twinning in *C*15 structures by synchroshear.

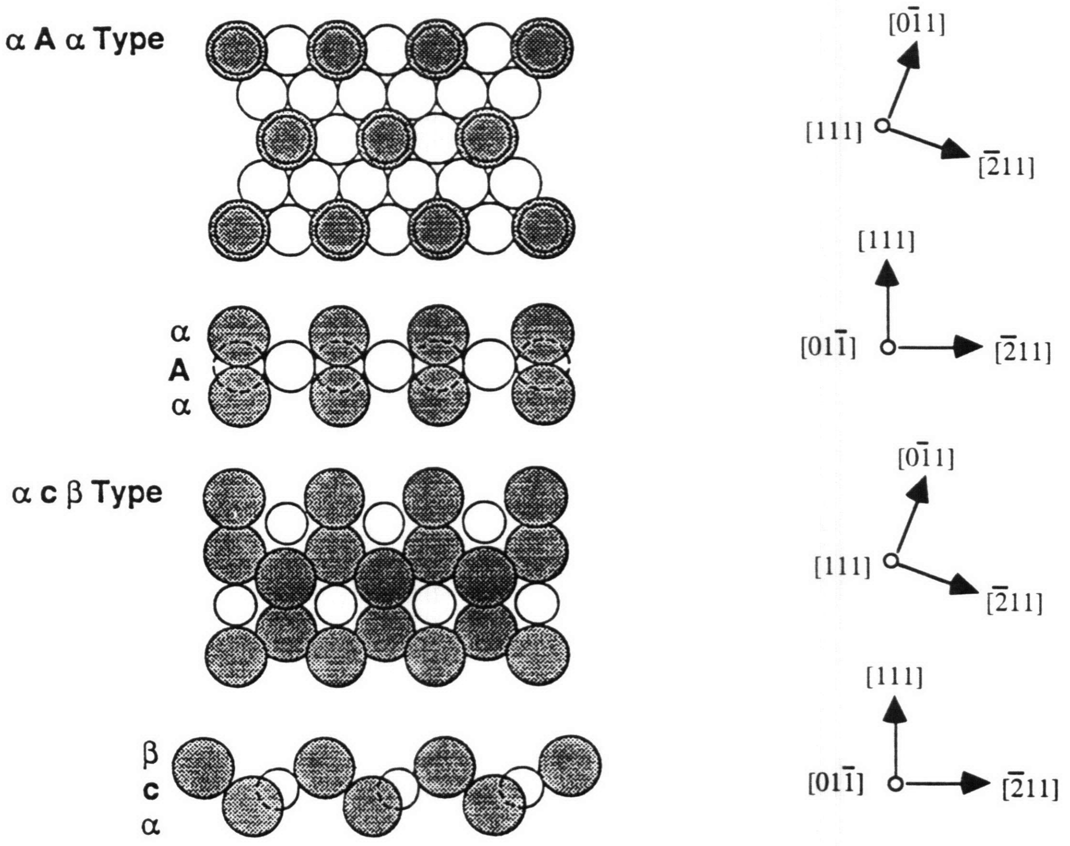

Figure 1.3 The two types of "sandwiches" in the *C*15 structure: the rigid αAα type and the more deformable αcβ type [39].

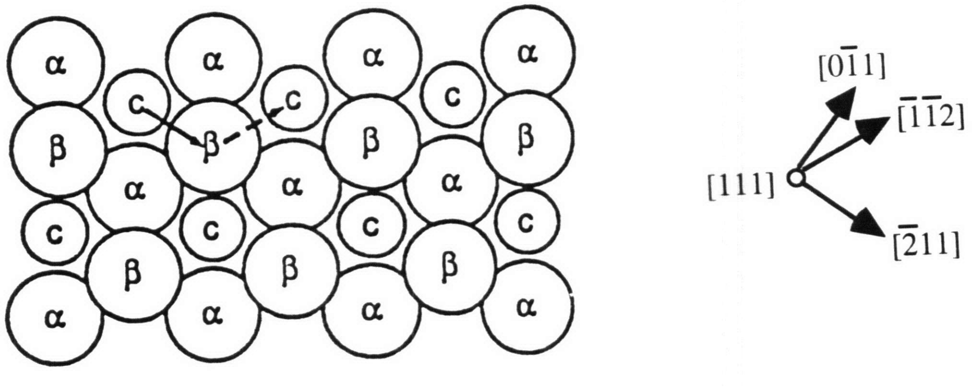

Figure 1.4 Synchroshear within the αcβ type sandwich. The smaller atoms move from the "c-site" to the "b-site" (solid arrow), while the larger atoms move from the "β-site" to the "γ-site" (dashed arrow) [39].

While synchroshear is the accepted deformation mechanism of Laves phases, the actual factors influencing the process are currently unknown. Suggestions that defects (such as vacancies and other atoms) can affect synchroshear have been largely left unexplored. Translating the knowledge of the effects on the micromechanics of synchroshear to the macroscopic and measurable mechanical properties is essential to the development of Laves phases and provides the motivation for this research.

1.3 REFERENCES

1. J. D. Livingston, phys. stat. sol. (a), **131**, 415 (1992).
2. J. D. Livingston and E. L. Hall, J. Mater. Res., **5**, 5 (1990).
3. R. L. Fleischer and R. J. Zabala, Metal. Trans., **21A**, 2149 (1990).
4. G. Sauthoff, Z. Metallkd., **80**, 337 (1989).
5. J. L. Murray, Binary Alloy Phase Diagrams, **10**(3), 219 (1989).
6. P.M. Hazzledine, submitted to TMS.
7. F. Chu and D.P. Pope, *Mat. Res. Soc. Symp. Proc. Vol. 288*, (1992); Mat. Sci. Eng., **A170**, 39 (1993).
8. Y. Liu, S.M. Allen, and J.D. Livingston, Metall. Trans., **23A**, 3303 (1992).
9. C. Barrett and T. B. Massalski, *The Structure of Metals and Alloys*, 3rd ed., Pergamon Press, p.256-259 (1980).
10. C. W. Allen, K. C. Liao, and A. E. Miller, J. Less-Common Metals, **52**, 109 (1977).
11. J. B. Moran, Trans. MS AIME, **233**, 1473 (1965).
12. P. Paufler, J. Marschner and G. E. R. Schulze, phys. stat. sol., **40**, 573 (1970).
13. A. K. Sinha, Progr. Mater. Sci., **15**, 79 (1972).
14. J. H. Wernick, *Intermetallic Compounds*, ed. J. H. Westbrook, J. Wiley & Sons, p.197 (1977).
15. A. E. Dwight, Trans. ASM, **53**, 479 (1961).
16. A. R. Edwards, Metall. Trans., **3**, 1365 (1972).

17. F. Laves, "Crystal Structure and Atomic Size," *Theory of Alloy Phases*, (ASM), p124 (1956).

18. M. V. Nevitt, "Alloy Chemistry of Transition Elements," *Electron Structure and Alloy Chemistry of the Transition Elements*, ed. P.A. Beck, J. Wiley & Sons, p.101 (1963).

19. R. P. Elliott and W. Rostoker, Trans. ASM, **50**, 617 (1958).

20. K. P. Gupta, S. K. Si, and R. C. Mittel, Trans. Indian Inst. Metals, **33**, 314 (1980).

21. F. Laves and H. Witte, Metallwertschaft, **15**, 840 (1936).

22. H. Klee and H. Witte, Z. Physik. Chem., **202**, 352 (1954).

23. W. E. Wallace and R. S. Craig, "Electron Concentration and Phase Stability in Laves Phases and Ni-Al Alloys," *Phase Stability in Metals and Alloys*, eds. Rudman, Stringer and Jaffee, p.225 (1967).

24. G. W. Shannette and J. F. Smith, J. Appl. Physics, **42**, 2799 (1971).

25. Y. Komura and Y. Kitano, Acta Cryst., **B33**, 2496 (1977).

26. Y. Liu, J.D. Livingston, and S.M. Allen, Metall. Trans., **26A**, 1441 (1995).

27. W. M. Rumball, J. Less-Common Metals, **20**, 191 (1970).

28. P. Rennert and A. M. Radwan, phys. stat. sol. (b), **79**, 167 (1977).

29. R. Haydock and R. L. Johannes, J. Phys. F: Metal Phys., **5**, 2055 (1975).

30. J. Hafner, J. Phys F: Metal Phys., **15**, 1879 (1985); Phys. Rev. B, **15**, 617 (1977).

31. O. Johnson, J. Phys. Chem. Solids, **45**, 811 (1984).

32. T. Ohba, Y. Kitano, and Y. Komura, Acta Cryst., **C40**, 1 (1984).

33. P. Paufler and G. E. R. Schulze, phys. stat. sol., **36**, 609 (1969).

34. D. Hinz, P. Paufler, and G. E. R. Schulze, phys. stat. sol., **24**, 77 (1967).

35. Y. Ohba and N. Sakuma, Acta metall., **37**, 2377 (1989).

36. T. Muller and P. Paufler, phys. stat. sol. (a), **40**, 471 (1977).

37. J. D. Livingston, E. L. Hall, and E. F. Koch, *Mater. Res. Soc. Symp. Proc. Vol. 133*, 243 (1989).

38. M. L. Kronberg, Acta metall. **5**, 507 (1957); **9**, 970 (1961); J. nucl. Mater. **1**, 85 (1959).

39. F. Chu, Ph.D. Thesis, U. of Pennsylvania, (1993).

40. P. M. Hazzledine, K. S. Kumar, D. B. Miracle, and A. G. Jackson, *Mater. Res. Soc. Symp. Proc. Vol. 288*, 591 (1992).

41. C.W. Allen, P. Delavignette, and S. Amelinckx, phys. stat. sol. (a), **9**, 237 (1972).

42. C.W. Allen, *Mater. Res. Soc. Symp. Proc. Vol. 39*, 141 (1985); and K.C. Liao, phys. stat. sol. (a), **74**, 673 (1982).

Chapter 2

Characterization of single-phase $TiCr_2$

2.1 INTRODUCTION

The Laves phases are generally considered to be line compounds at strict AB_2 compositions. However, solubility ranges exist for about 25% of the known binary Laves phases [1]. Solubility ranges tend to exist for those Laves phases that have a radius ratio (r_A/r_B) close to the ideal 1.225 value. Intermetallics incorporate constitutional defects for the nonstoichiometric compositions.

Off-stoichiometry in the $NbCr_2$ and YAl_2 Laves phases are accompanied by different defect mechanisms, depending on which side of the stoichiometric compound the composition occurs [2,3]. A-rich compositions of the AB_2 Laves phases are accommodated by vacancies, while the B-rich compositions result from anti-site substitutions. The types of constitutional defects are important because they may affect mechanical properties. Vacancies have been proposed to assist the synchroshear deformation mechanism, and could possibly increase the ductility of Laves phases [4]. The mechanical properties of intermetallics can be very sensitive to the composition and crystal structure, and thus a detailed knowledge of the single-phase field of $TiCr_2$ is needed.

Uncertainties in the most recently published Ti-Cr phase diagram (Figure 2.1) [5] have prompted the need for a careful examination around the $TiCr_2$ composition. Solubility limits of the $TiCr_2$ Laves phase and the temperatures and compositions related to transitions of the Laves crystal structure (*C*14, *C*36, and *C*15) are in question. In this regard, Figure 2.1 is quite different from an earlier version of the Ti-Cr phase diagram [6].

The goals of this chapter are to establish the compositions and crystal structures of the single-phase $TiCr_2$ field. The lattice constants, crystal structure transformation rates, and densities are used to identify the defect mechanism of nonstoichiometric $TiCr_2$.

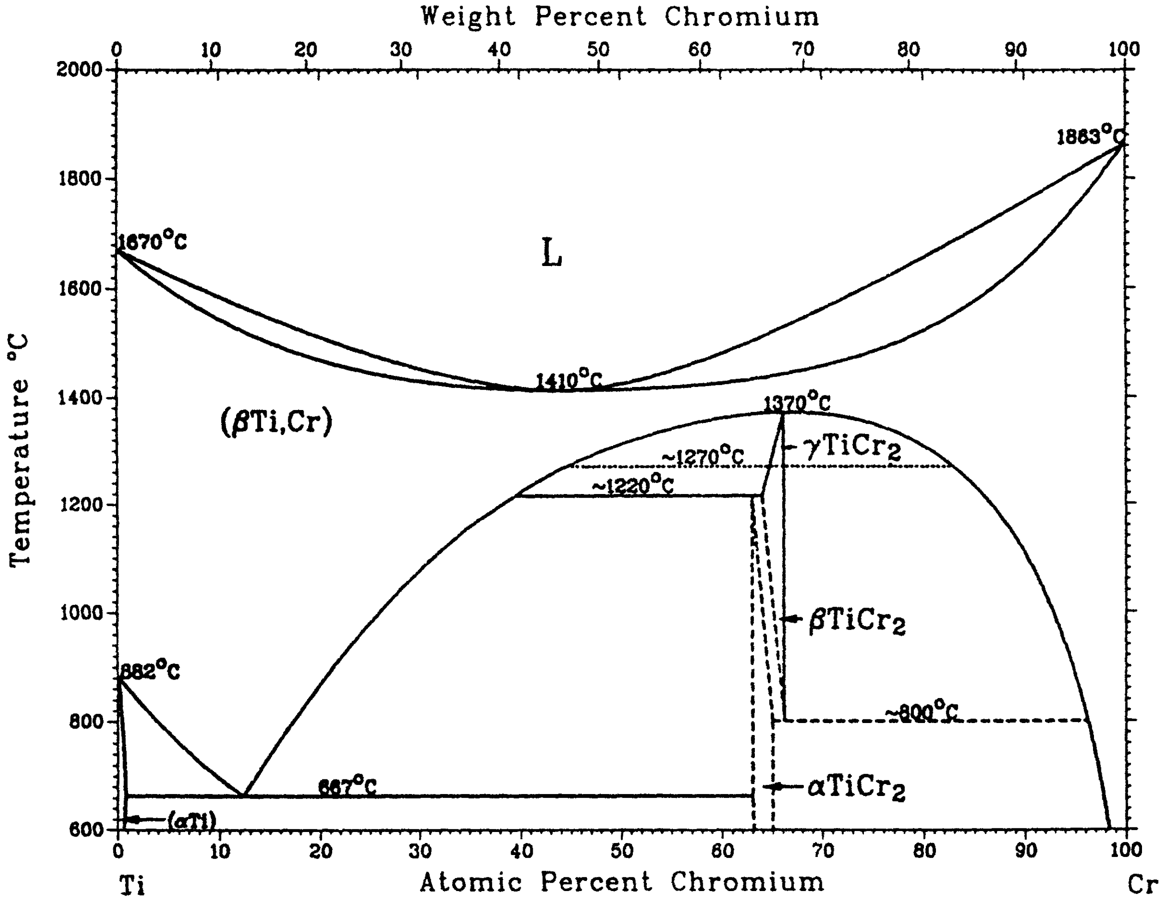

Figure 2.1 The equilibrium Ti-Cr phase diagram [5].

2.2 EXPERIMENTAL PROCEDURES

Several Ti-Cr alloys were arc-cast into 50 gram buttons by the Materials Preparation Center of Ames Laboratory at Iowa State University. High-purity titanium (EL60) and chromium (electrothermic reduced) were used. To minimize contamination, the arc-melting chamber was evacuated and then back-filled with ultra-high purity argon. Zirconium was melted as a getter for impurities. The constituent elements were then arc-melted on a water-cooled copper hearth plate in a partial pressure atmosphere of argon. Titanium was melted, and then the chromium was added last to minimize any vapor loss due to its high volatility. The alloys were flipped and remelted several times to ensure homogeneity (as areas of unmelted and unmixed Cr were found in earlier castings). Most of the alloy buttons fractured into about 3 pieces during cooling, due to thermal shock. Porosity was found in the top center portion of each ingot, which was the last part of the ingot to solidify. The porosity was most likely caused by gas evolution and/or shrinkage during solidification. This portion of the ingot was largely avoided in later characterization and mechanical properties studies.

Chemical analyses were performed on small amounts (about 0.5 g) of the as-cast alloys at Ames Laboratory. Compositions of the alloys were determined by an ICP-AES (atomic emission) instrument. The minor elements, oxygen and nitrogen, were detected by inert gas fusion. Oxygen content in the alloys was in the range of 82-178 ppm, while nitrogen was found to be 20-46 ppm. Impurities picked up during subsequent heat treatments were possible, but were not determined.

For each annealing treatment, the alloys were wrapped in tantalum foil to prevent oxidation. Heat treatments at temperatures of 1200°C and higher were performed in a vacuum furnace with pressures in the 10^{-6} Torr range. Homogenization treatments at 1380°C and 1395°C were performed. The alloys were placed in a Mo wire-mesh basket that sat at the bottom of the vacuum furnace. The power was shut-off at the end of the treatment and resulted in a quick drop in temperature (a few hundred degrees within minutes). A faster quench was not used in order to avoid cracks due to thermal shock. The annealing treatments at 1200°C and 1300°C were designed to isolate a particular crystal structure, and were thus oil-quenched. The samples were suspended in the vacuum furnace by Mo wire during the anneal, and then dropped through a gate valve into a small vat of diffusion-pump oil at the bottom of the furnace. For the lower temperature heat treatments, the alloys were encapsulated in a quartz tube that was back-filled with argon, annealed in a box furnace, and water quenched.

The samples were extremely brittle and generally had to be mounted in an epoxy in order to be gripped for cutting without the whole alloy breaking apart. This way, the epoxy absorbed most of the forces of the vice-like holding apparatus rather than the alloy samples themselves. The alloys were sectioned by a high-speed, thin diamond blade. The cold mount epoxy was later removed by heating in a N,N-Dimethyl Formamide solution.

The same regimen of grinding, polishing, and etching was followed for all the alloys. SiC paper, progressing from 240 to 1200 grit, was used for grinding. Up to this stage, numerous small, crater-like holes or "pull-outs" dominated the surface, which is a common problem found in hard, brittle material. Diamond paste was found to be too aggressive to alleviate the "pull-out" problem, but alumina lapping paper (12 and 3 μm) was successful. The resin-bonded alumina particles had a coating which polished down the material to achieve a smooth surface. Fine polishing was then accomplished using an alumina powder solution (0.3 and 0.05 μm) on a soft polishing cloth. The samples were ultrasonically cleaned in distilled water after each polishing step.

The alloys were etched in a solution of 50% glycerin, 25% HNO_3, and 25% HF. Micrographs of each sample were taken on an Olympus optical microscope and catalogued according to composition and annealing temperature. Back-scattered electron images of unetched samples were taken in an environmental scanning electron microscope (SEM), which did not require the samples to be coated. The beta phase showed ample contrast to distinguish it from the Laves phase in the two-phase alloys by SEM.

Carbon-coated samples were used for electron microprobe analysis (EMPA). A JEOL 733 Superprobe was employed to determine the compositions of the annealed samples by comparing energy dispersion spectra with elemental standards. The beam focused to a spot size of 0.1 μm, and the detection limit was about 0.1 wt%. A data reduction and correction program was used to treat deviations caused by the effects of atomic number, absorption, and fluorescence [7].

X-ray diffraction (XRD) was used to determine the crystal structures and lattice constants of the $TiCr_2$ Laves phases. A Rigaku 300 Diffractometer with Cu-K_α radiation (λ = 1.54180 Å) was used. Powder samples were prepared with small amounts of a Si standard (NIST 640b) for correcting 2θ readings [8]. Crystal structures were also determined by transmission electron microscopy (TEM) with a JEOL 200CX microscope operating at 200 kV.

Density measurements employed Archimedes' method [9], using a density kit and a Mettler analytical balance. The sample was first weighed in air, and then in distilled water at a room temperature of 22°C. The difference in weight is the buoyancy force, and when divided by the liquid density ($\rho = 0.9979$ g/ml), gives the sample volume. The sample density is then simply the sample weight in air divided by the sample volume.

2.3 THE SINGLE-PHASE $TiCr_2$ LAVES FIELD

2.3.1 Microstructures

Six different alloy compositions ranging from Ti-62 at% Cr to Ti-69 at% Cr were selected to study the single-phase Laves field. The as-cast microstructures of these Ti-Cr alloys were dendritic and compositionally inhomogeneous on a fine scale, as seen in Figure 2.2. Homogenization in the single-phase beta bcc field was attempted at 1380°C for 24 hours. When some of the alloys showed a coarsened two-phase microstructure, although no longer dendritic, the alloys were subjected to a second homogenization step at 1395°C for 12 hours. This treatment successfully homogenized all the alloys (Figure 2.3). Since the alloys were placed in the vacuum furnace at a point below the thermocouple, the alloys could have been at a lower temperature than the thermocouple

Table 2.1 Laves phase compositions at selected temperatures and crystal structures, determined by electron microprobe.

Nominal alloy composition	microstructure	$TiCr_2$ Laves phase composition (at% Cr): *C*14 (1300°C)	*C*36 (1200°C)	*C*15 (1000°C)
Ti-62 Cr	β-Ti(Cr) + $TiCr_2$	63.75 ± 0.34	63.57 ± 0.08	64.13 ± 0.14
Ti-64 Cr	$TiCr_2$	64.06 ± 0.09	63.60 ± 0.12	63.94 ± 0.16
Ti-66 Cr	$TiCr_2$	65.11 ± 0.10	65.22 ± 0.07	65.00 ± 0.18
Ti-67 Cr	$TiCr_2$	65.84 ± 0.06	66.06 ± 0.06	65.66 ± 0.13
Ti-68 Cr	β-Cr(Ti) + $TiCr_2$	66.38 ± 0.12	66.30 ± 0.03	66.06 ± 0.31
Ti-69 Cr	β-Cr(Ti) + $TiCr_2$	66.20 ± 0.18	66.31 ± 0.04	65.94 ± 0.20

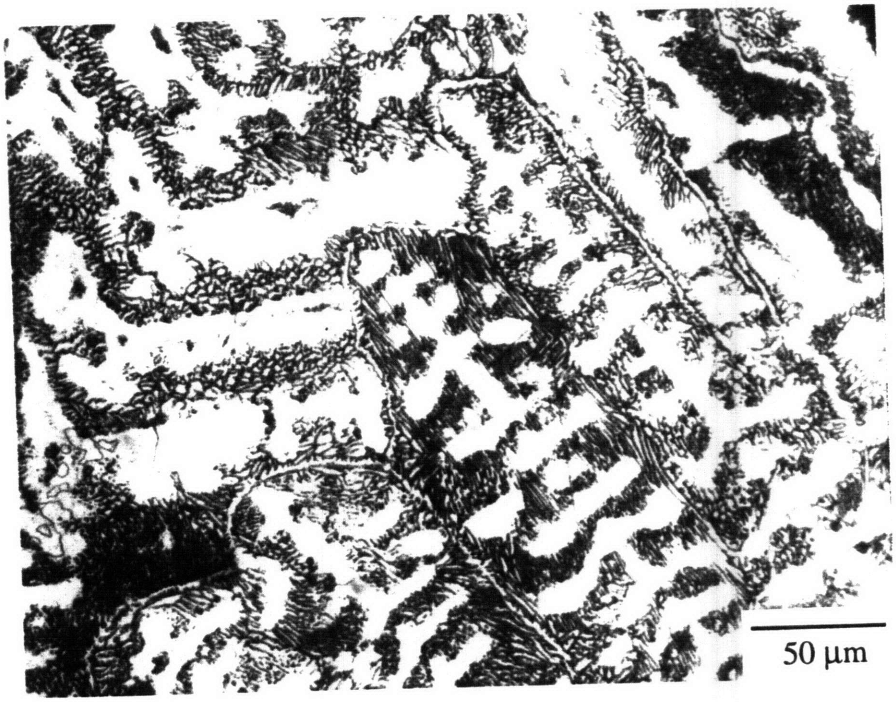

Figure 2.2 The as-cast dendritic microstructure of the Ti-62 Cr alloy.

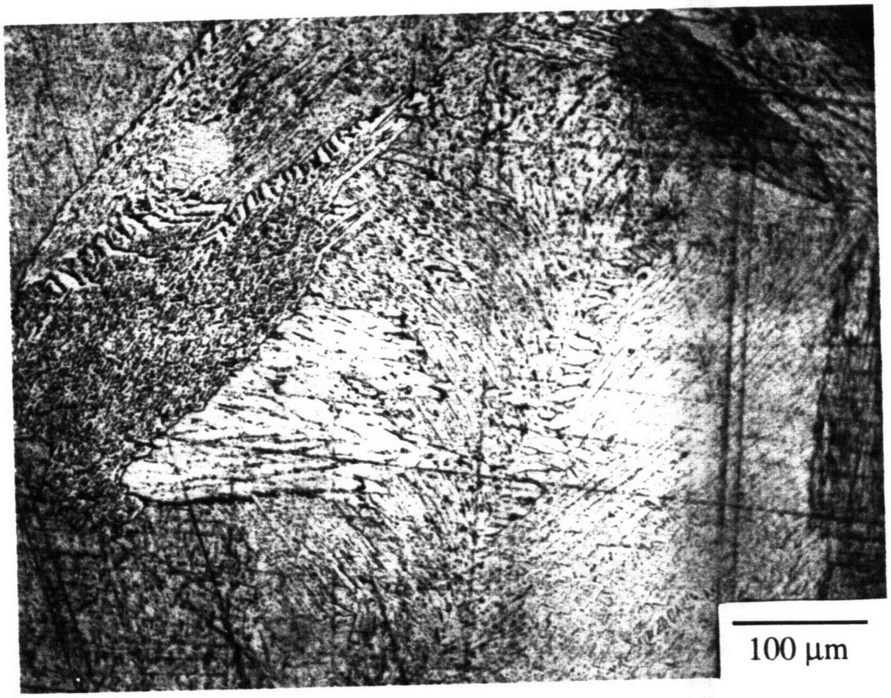

Figure 2.3 The Ti-64 Cr alloy after the homogenization treatment at 1395°C.

reading. The exact decomposition temperature (identified as 1370°C by the phase diagram) of the bcc to Laves phase was not the aim of this study, and was not investigated further.

Annealing treatments at 1300°C, 1200°C, and 1000°C were performed on all six of the alloys. Metallography revealed that the solubility limits of $TiCr_2$ had been reached as some of alloys fell into the two-phase regions of β-Ti(Cr)+$TiCr_2$ and β-Cr(Ti)+$TiCr_2$ (Table 2.1). Figure 2.4 shows optical and SEM micrographs of the Ti-62 Cr alloy at 1300°C. The elongated dark phase is the Ti-rich beta phase. The same alloy annealed at 1000°C showed a different microstructure, as seen in Figure 2.5. The beta phase here is more spherical and dispersed within the $TiCr_2$ matrix. The etched sample in the optical micrograph also shows some subgrain structure, most likely twinning in the *C*15 structure. The alloys of nominal compositions, Ti-64 Cr, 66 Cr, and 67 Cr were mostly all single-phase, and relatively featureless. Figure 2.6 demonstrates how the grain boundaries were often jagged in the single-phase alloys. The Ti-69 Cr alloy contained many small Cr-rich beta particles, shown in Figure 2.7. Because it is now Cr-rich, the beta phase is now lighter in contrast than the $TiCr_2$ matrix in the SEM micrographs.

2.3.2 Laves phase compositions

Electron microprobe analysis pinpointed the single-phase Laves composition ranges, which are listed in Table 2.1 along with the metallographic findings. The standard deviations come from the averaging of microprobe compositions from several random locations on each sample. The *C*14 $TiCr_2$ composition range at 1300°C was Ti-63.8 Cr to Ti-66.3 Cr, and is larger and more Ti-rich than the current phase diagram indicates. The *C*36 range at 1200°C was roughly the same with Ti-63.6 Cr to Ti-66.3 Cr. The single-phase field at 1000°C was more narrow and determined to be Ti-64.0 Cr to Ti- 66.0 Cr. In a diffusion couple experiment, Thoma and Perepezko [10] report the $TiCr_2$ range to be from Ti-64.5 Cr to Ti-66.5 Cr at 1000°C.

For the single-phase Ti-66 Cr and Ti-67 Cr alloys (Table 2.1), the microprobe-determined compositions reveal that the target compositions were not quite met, and the nonuniform compositions found across the later annealing treatments probably reflect some Cr-vapor loss during processing. The larger standard deviations of the Laves phase composition in the two-phase alloys might come from inadvertently including some of the beta phase in the probe scan.

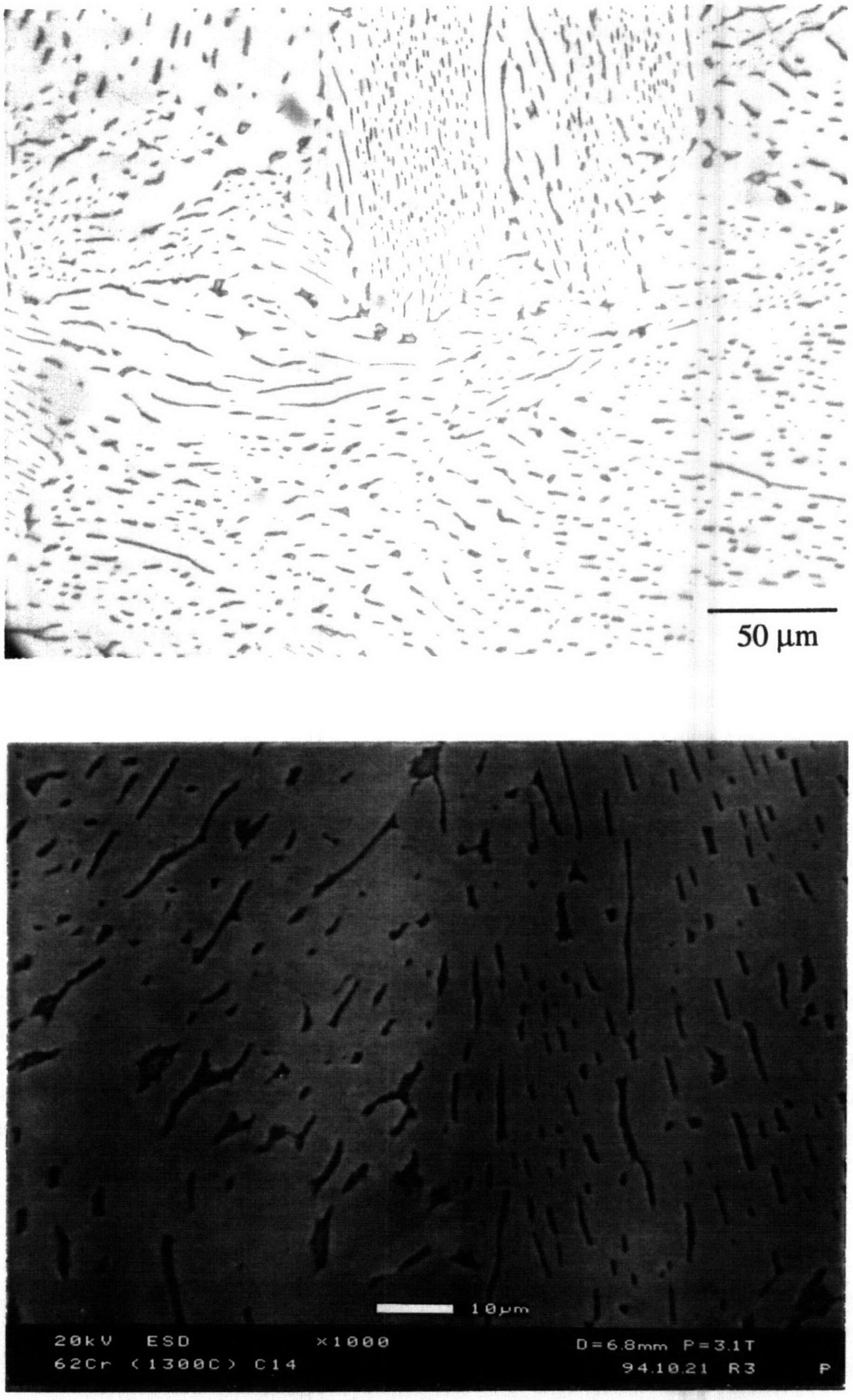

Figure 2.4 (**a**) Optical and (**b**) SEM micrograph of β-Ti(Cr)+$TiCr_2$ in the Ti-62 Cr alloy at 1300°C.

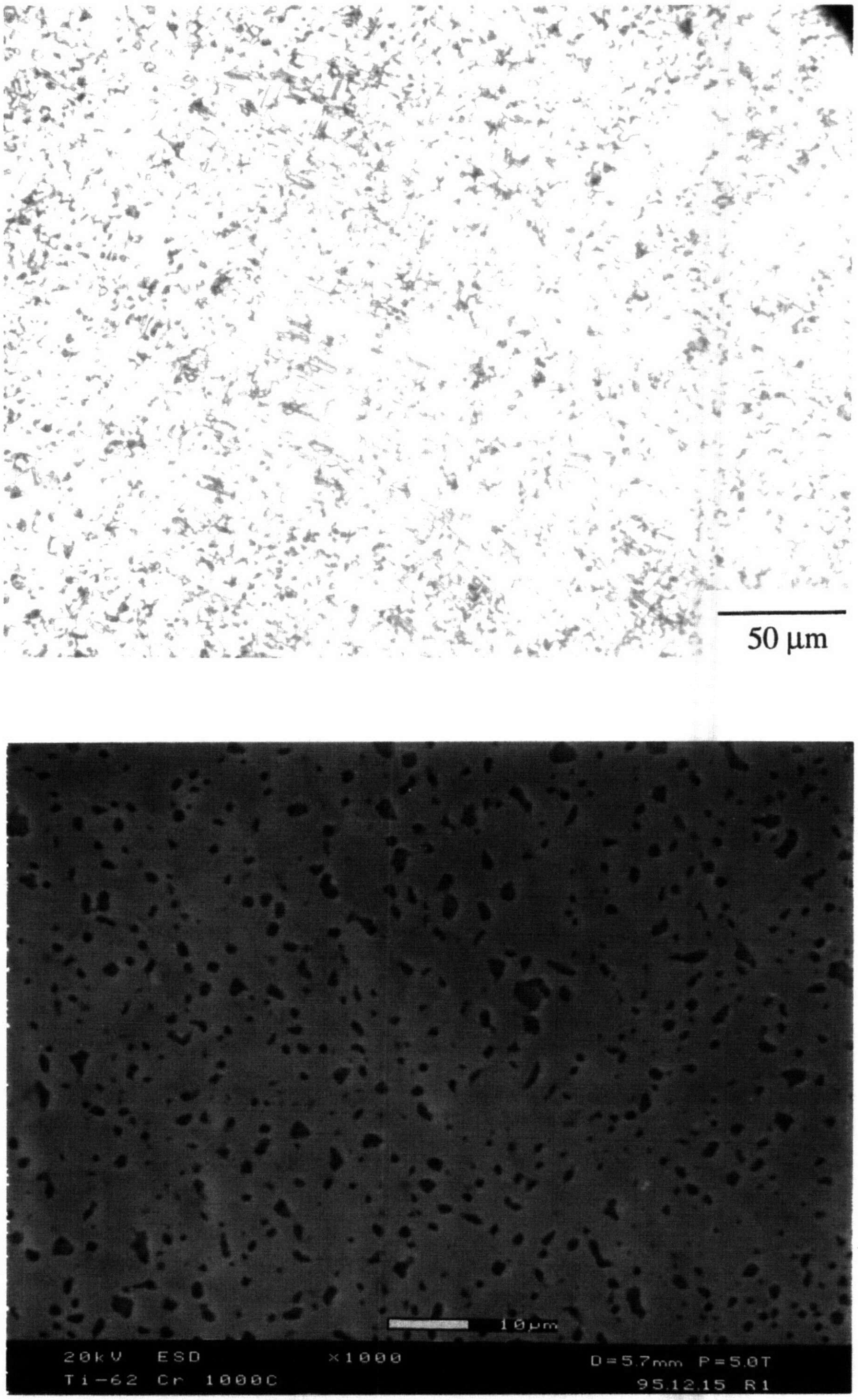

Figure 2.5 **(a)** Optical and **(b)** SEM micrograph of β-Ti(Cr)+$TiCr_2$ in the Ti-62 Cr alloy at 1000°C.

Figure 2.6 Optical micrograph of single-phase $TiCr_2$ at 1000°C.

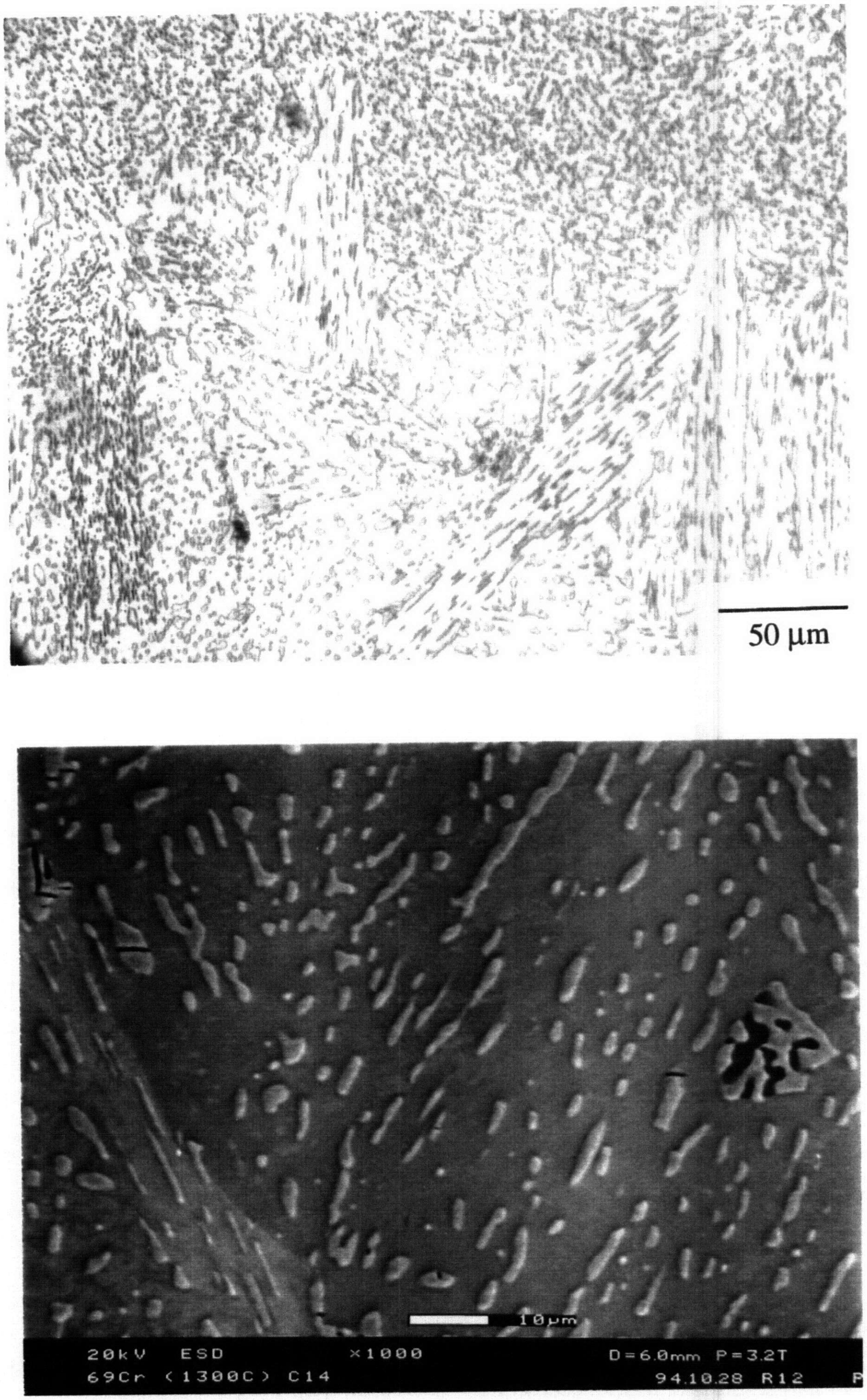

Figure 2.7 **(a)** Optical and **(b)** SEM micrograph of β-Cr(Ti)+$TiCr_2$ in the Ti-69 Cr alloy at 1300°C.

Interestingly, the perfect stoichiometric composition of Ti-66.7 Cr (representing full occupation of sites) was never achieved. In fact, the $TiCr_2$ Laves phase was originally incorrectly identified as a Ti_2Cr_3 intermetallic [11]. Also, off-stoichiometry was found on only one side, towards Ti-rich compositions. The equilibrium Laves structure is thus nonstoichiometric and must contain some defects.

2.4 CRYSTAL STRUCTURES AND POLYTYPISM

$TiCr_2$ exhibits polytypism, as do all the other XCr_2 Laves phases, where X = Zr, Hf, Nb, and Ta (Table 2.2) [3]. The differences among the *C*14, *C*36, and *C*15 crystal structures lie in the stacking sequences of the four-layer units, and the transformation from one crystal structure to another can be achieved by the movement of a Shockley partial dislocation through the crystal at appropriate planes [12].

Levinger [13] first identified the *C*14 hexagonal $TiCr_2$ phase at 1300°C. Minayeva et al. [14] reported that the *C*14→*C*15 transition was composition dependent, occurring at 1225°C for Ti-rich compositions, and 800°C for Cr-rich compositions. However, Gross and Lamborn [15] claimed that the dependence of the $TiCr_2$ structure on compositions was due to a cooling rate effect.

Determining the transition temperatures or compositions is difficult since the hexagonal phase is persistent and the structural transformation can be very slow. In this work, the crystal structures of $TiCr_2$ were studied by TEM and x-ray diffraction.

Table 2.2 Polytypism of XCr_2 Laves phases (X = Ti, Zr, Hf, Nb and Ta).

Laves phase, XCr_2	Laves crystal structure	X-crystal structure
$TiCr_2$	*C*14/*C*36/*C*15	Ti-bcc, hcp
$ZrCr_2$	*C*14/*C*36/*C*15	Zr-bcc, hcp
$HfCr_2$	*C*14/*C*15	Hf-hcp
$NbCr_2$	*C*14/*C*15	Nb-bcc
$TaCr_2$	*C*14/*C*15	Ta-bcc

2.4.1 TEM

Figures A.1-A.3 in Appendix A show an electron diffraction pattern and TEM image for each Laves crystal structure. A Ti-60 Cr alloy (on hand from earlier studies by J.D. Livingston at General Electric Company) was used for this portion of the study. The *C*14 structure was detected at 1300°C, *C*36 at 1230°C, and *C*15 at 1000°C, which were consistent with the phase diagram of Figure 2.1. The sample annealed at 1230°C (*C*36) was later annealed at 1300°C for 4 hours, and the crystal structure changed to *C*14. Also, a sample annealed at 1300°C (*C*14) was later annealed at 1150°C, and displayed the *C*36 structure. The results of these secondary annealing treatments confirm that the equilibrium crystal structure of $TiCr_2$ is temperature dependent. The as-cast alloy did not experience as fast a quench as the annealed samples, and was found to be *C*36.

The hexagonal Laves crystal structures could easily be identified as *C*14 or *C*36 by the electron diffraction pattern with a $[1\bar{2}10]$ zone axis. The periodicity of the stacking sequences is reflected along the direction of (0001) planes. Since the *C*36 structure has a c-axis twice as long as the *C*14 structure (from the XYXZ vs. XYXY stacking sequence), the distance to the $(0001)_{C36}$ spot is half the length on the diffraction pattern (and in reciprocal space) of the $(0001)_{C14}$ spot.

The TEM images of the different crystal structures also had distinct characteristics. The *C*36 sample contained numerous faults, as opposed to the *C*14 structure which was relatively featureless. The *C*36 structure, often described as half hexagonal and half cubic, has been thought to be an intermediate step between the *C*14 and *C*15 structures, and not a true equilibrium crystal structure. The *C*15 diffraction pattern and image usually exhibited twinning on the {111}<112> system.

2.4.2 X-Ray Diffraction

Because JCPDS data for the hexagonal $TiCr_2$ phases were not available, values for the 2θ positions and relative intensities (using Cu-K_α radiation) were calculated by a Cerius crystal-modeling software program. Table B.1 in Appendix B lists the calculated values for the *C*14 (**a**=4.922 Å and **c**=7.962 Å), *C*36 (**a**=4.922 Å and **c**=15.924 Å) and *C*15 (**a**=6.940 Å) structures. The *hkl* indices are positioned within the table to correspond to 2θ values close to one another. Peak overlap could obscure the presence of a certain structure. For example, the *C*36 structure contains all the same peak positions as the *C*14 and several more, and thus if a mixture of the two phases existed, the *C*14 structure may go undetected. The lack of certain peaks and the relative intensities were used to help identify the crystal structures of the alloy samples. The experimental scans were compared against the generated standards, and were found to match very well.

Representative XRD scans of each of the Laves crystal structures can be found in Appendix C. Scans of the Ti-67 Cr alloy at 1300°C and 1200°C clearly show the *C*14 and *C*36 crystal structures, respectively in Figures C.1 and C.2. The scan of the Ti-62 Cr alloy at 1000°C shows the *C*15 and beta phase (Figure C.3). The alloys with small amounts of the beta phase showed small peaks corresponding to the bcc phase. The XRD results of all the annealed alloys are listed in Table 2.3.

At 1000°C and 48 hours, the crystal structure appeared to depend on the composition, as the phase diagram suggests. The Ti-62 Cr and Ti-64 Cr alloys (Ti-rich) showed a mixture of *C*36 and *C*15 structures, while the other alloys remained at *C*36. Figure 2.8 is an optical micrograph of the Ti-64 Cr alloy with areas of *C*15 and *C*36. (The *C*36 areas resemble the microstructure in Figure 2.4, and the *C*15 areas resemble Figure 2.5.) However, a longer anneal for 500 hours at the same temperature produced larger amounts of the *C*15 structure in the Ti-62 Cr and Ti-64 Cr alloys, and also led to *C*15 formation in the Ti-66 Cr alloy (Figure 2.9). Although the *C*36 diffraction peaks overlap the *C*15 peaks, the relative intensities and the absence of the *C*36 peaks can be used to qualitatively ascertain the amounts of the *C*15 structure. Also the peak at $2\theta = 52.7°$ is unique to the *C*15 structure.

Table 2.3 $TiCr_2$ Laves phase crystal structures as a function of annealing temperature and time.

Nominal alloy composition	$TiCr_2$ Laves phase crystal structures: 1300°C/4 hrs.	1200°C/6 hrs.	1000°C/48 hrs.	1000°C/500 hrs.
Ti-62 Cr	*C*14	*C*36	*C*15	*C*15
Ti-64 Cr	*C*14	*C*36	*C*15/(*C*36)	*C*15
Ti-66 Cr	*C*14	*C*36	*C*36	*C*15/(*C*36)
Ti-68 Cr	*C*14	*C*36	*C*36	*C*36
Ti-69 Cr	*C*14	*C*36	*C*36	*C*36

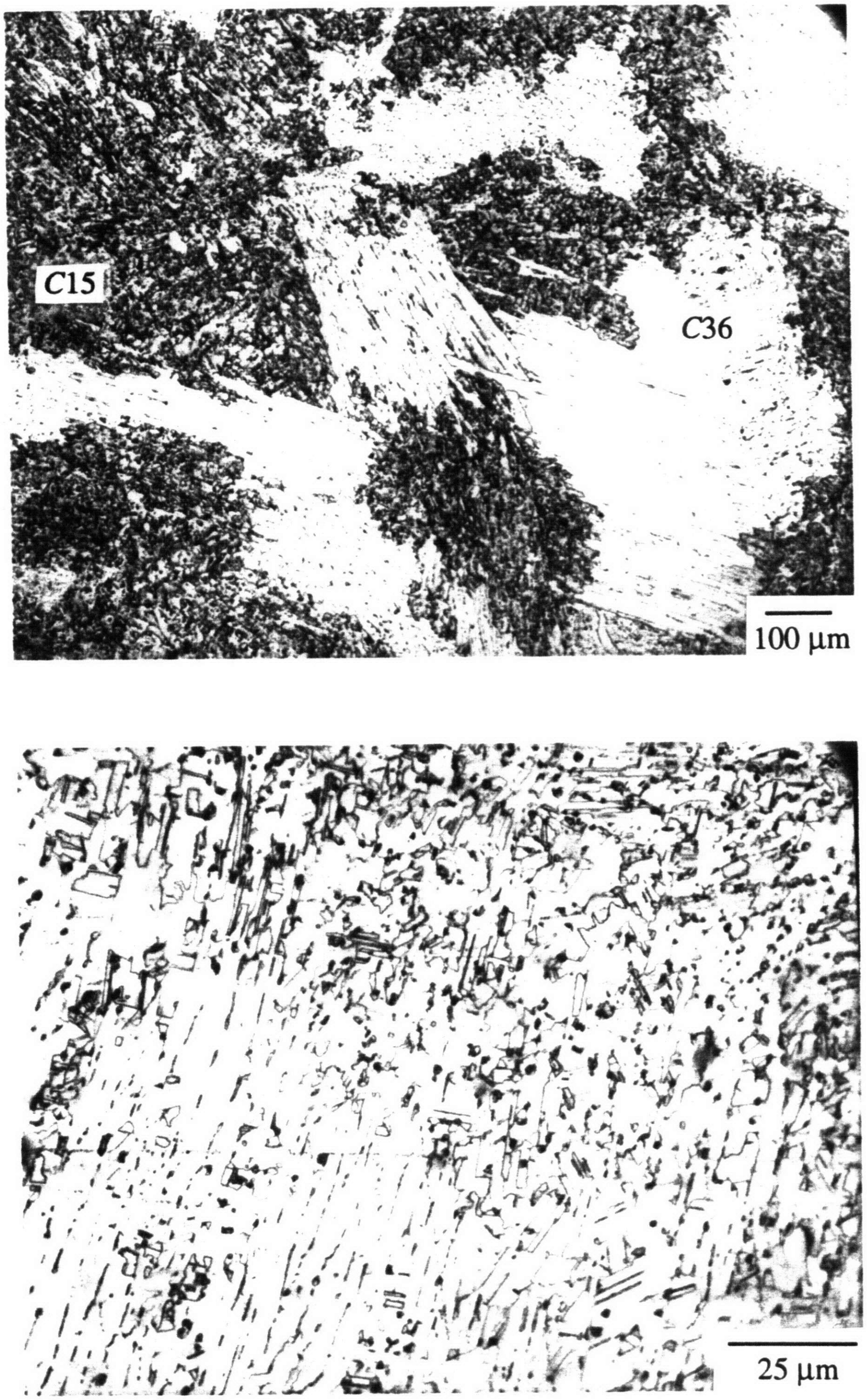

Figure 2.8 Optical micrographs of the Ti-64 Cr alloy annealed at 1000°C at **(a)** 82.5X and **(b)** 660X. Areas of *C*15 and *C*36 coexist.

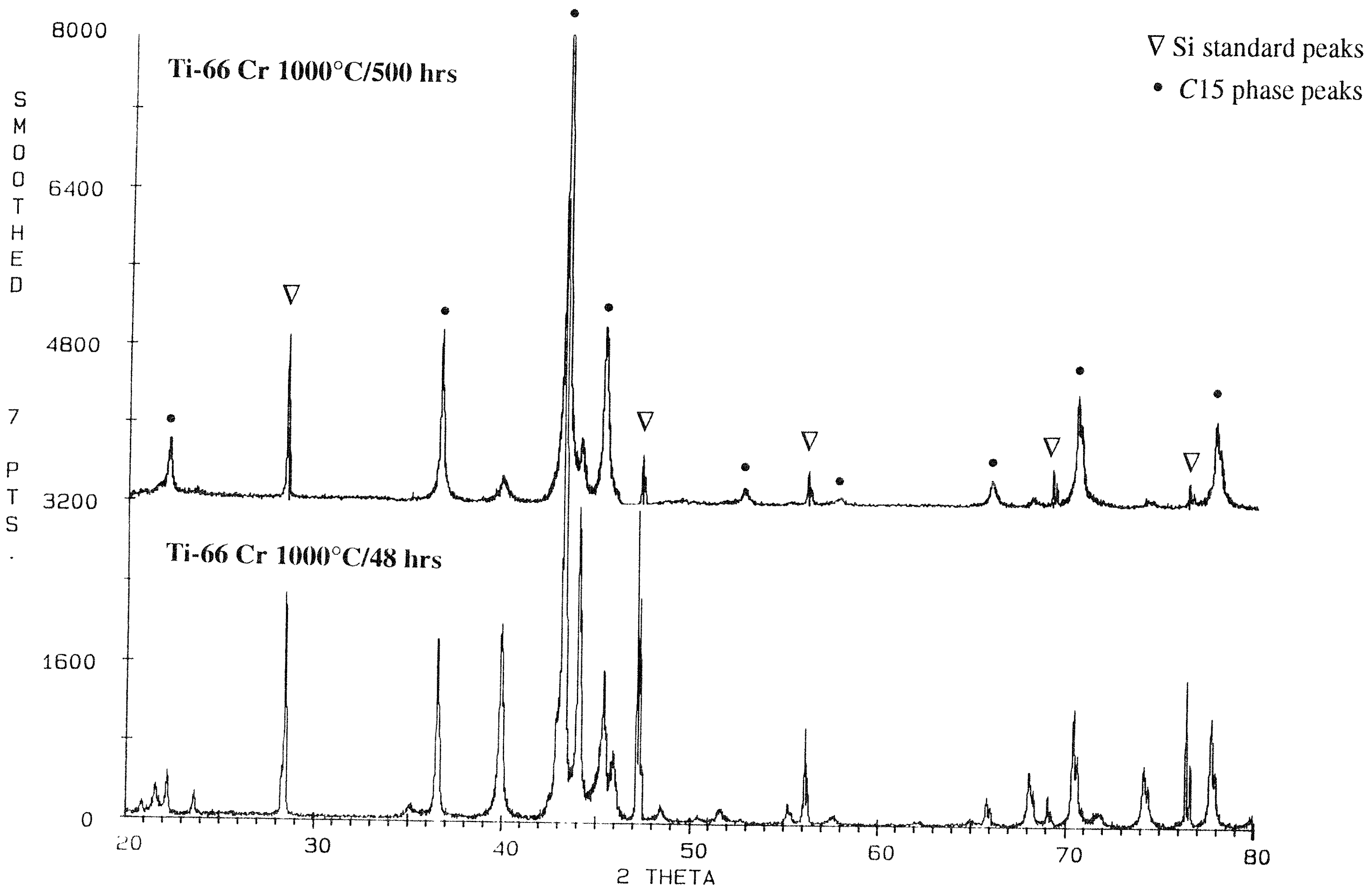

Figure 2.9 X-ray diffraction scans showing the emergence of the *C*15 crystal structure from the *C*36 structure with increased annealing time at 1000°C in the Ti-66 Cr alloy.

Although the current phase diagram indicates an equilbrium two-phase region containing two different Laves crystal structures, α-$TiCr_2$ ($C15$) + β-$TiCr_2$ ($C36$) , such a mixture is not possible if the change in polytypes is a first-order reaction. The increase in volume fraction of the $C15$ structure with time indicates that $C15$ is the equilibrium crystal structure at 1000°C, and the $C36 \rightarrow C15$ transformation is sluggish. Exact transformation temperatures were not studied, and could possibly be composition dependent. Several other Laves systems have been reported to have a slow $C36 \rightarrow C15$ transformation [5,16], and this has been the cause of misidentification of equilibrium Laves crystal structures.

In efforts to test whether the $C36$ crystal structure was truly an equilibrium structure, a Ti-64 Cr alloy annealed at 1000°C with areas of $C15$ and $C36$ was given a second heat treatment at 1200°C for 6 hours. If the $C36$ structure is an intermediate step towards the $C15$ structure, then the $C14 \rightarrow C15$ transition temperature must occur between 1300°C and 1200°C, and the $C15$ structure should remain stable at 1200°C (unless a large thermal hysteresis exists). The crystal structure reverted back to $C36$, signifying that $C36$ is indeed the equilibrium structure at 1200°C. In addition, the intensities of the experimental scans of $C36$ closely matched those of the calculated standards.

2.5 LATTICE CONSTANTS

The lattice constants of the $TiCr_2$ Laves phases were determined by collecting x-ray diffraction information at very small steps and slow scans in order to carefully select the 2θ peak positions. The positions were then corrected by a small off-set determined by the Si standard. Several well-defined peaks in the 2θ range of 30—150° were used. The 2θ positions and corresponding *hkl* indices were then entered into a program that computed the lattice parameter by a least-squares method. The results are found in Table 2.4. Data came from the Ti-Cr alloys annealed at 1300°C for $C14$, 1200°C for $C36$, and 1000°C for the $C15$ structure. The reported standard deviations come from the fitting of data to a straight line, rather than experimental errors. For comparisons, an adjusted lattice constant, **a'**, is calculated for the hexagonal phases, by taking the cube root of the unit cell volume of 12 atoms. The larger **a'** values for the higher-temperature annealed samples are consistent with thermal expansion effects. The change in lattice constant with composition was **da'**/dc = -0.87 Å for $C14$, **da'**/dc = -0.68 Å for $C36$, and **da**/dc = -0.49 Å

Table 2.4 Lattice constants of the *C*14, *C*36 and *C*15 $TiCr_2$ Laves phases.

Alloy	*C*14 **a** (Å)	*C*14 **c** (Å)	**c/a**	vol (Å^3)	**a'** (Å)
Ti-62 Cr	4.9336 ± 0.0005	7.9636 ± 0.0007	1.614	167.9	6.9502
Ti-64 Cr	4.9341 ± 0.0002	7.9622 ± 0.0003	1.614	167.9	6.9503
Ti-66 Cr	4.9235 ± 0.0002	7.9596 ± 0.0003	1.617	167.1	6.9396
Ti-67 Cr	4.9184 ± 0.0002	7.9596 ± 0.0003	1.618	166.8	6.9348
Ti-68 Cr	4.9155 ± 0.0002	7.9599 ± 0.0004	1.619	166.6	6.9321
Ti-69 Cr	4.9148 ± 0.0006	7.9596 ± 0.0009	1.620	166.5	6.9314

Alloy	*C*36 **a** (Å)	*C*36 **c** (Å)	**c/2a**	1/2 vol (Å^3)	**a'** (Å)
Ti-62 Cr	4.9224 ± 0.0004	15.9951± 0.0013	1.625	167.82	6.9496
Ti-64 Cr	4.9223 ± 0.0005	15.9892 ± 0.0013	1.624	167.75	6.9486
Ti-66 Cr	4.9129 ± 0.0002	15.9730 ± 0.0007	1.626	166.94	6.9374
Ti-67 Cr	4.9087 ± 0.0004	15.9623 ± 0.0014	1.626	166.54	6.9319
Ti-68 Cr	4.9054 ± 0.0003	15.9560 ± 0.0011	1.626	166.25	6.9279
Ti-69 Cr	4.9050 ± 0.0003	15.9591 ± 0.0011	1.627	166.26	6.9280

Alloy	*C*15 **a** (Å)	1/2 vol (Å^3)
Ti-62 Cr	6.9440 ± 0.0001	167.42
Ti-64 Cr	6.9439 ± 0.0002	167.41
Ti-66 Cr	6.9387 ± 0.0004	167.03

Table 2.5 Comparisons with lattice constants of $TiCr_2$ found in the literature.

*C*14 **a**	*C*14 **c**	**c/a**	reference
4.922	7.945	1.614	Levinger, 1953 [13]
4.932	7.961	1.617	Farrar et al., 1963 [17]
4.918	7.960	1.618	this study

*C*15 **a**	reference
6.943	Duwez et al., 1952 [18]
6.91	Cuff et al., 1952 [19]
6.9647	Thoma, 1992 [20]
6.9387	this study

for *C*15. The lattice constants are similar to those found in the literature, as seen in Table 2.5 [13,17-20]. Discrepancies may be due to different heat treatments and exact compositions used.

The lattice constants are plotted against the nominal alloy compositions in Figures 2.10-2.12. The single-phase Laves fields are discerned and match the findings of the microprobe and metallographic analyses mentioned earlier. The change in the *C*14 **c** lattice constant in Figure 2.10 however, shows a smaller composition range and is not fully understood. Within the single-phase region, the lattice constants increase with increasing deviation from stoichiometry for all three Laves crystal structures. The **c/a** ratio of the hexagonal phases decreases slightly with off-stoichiometry.

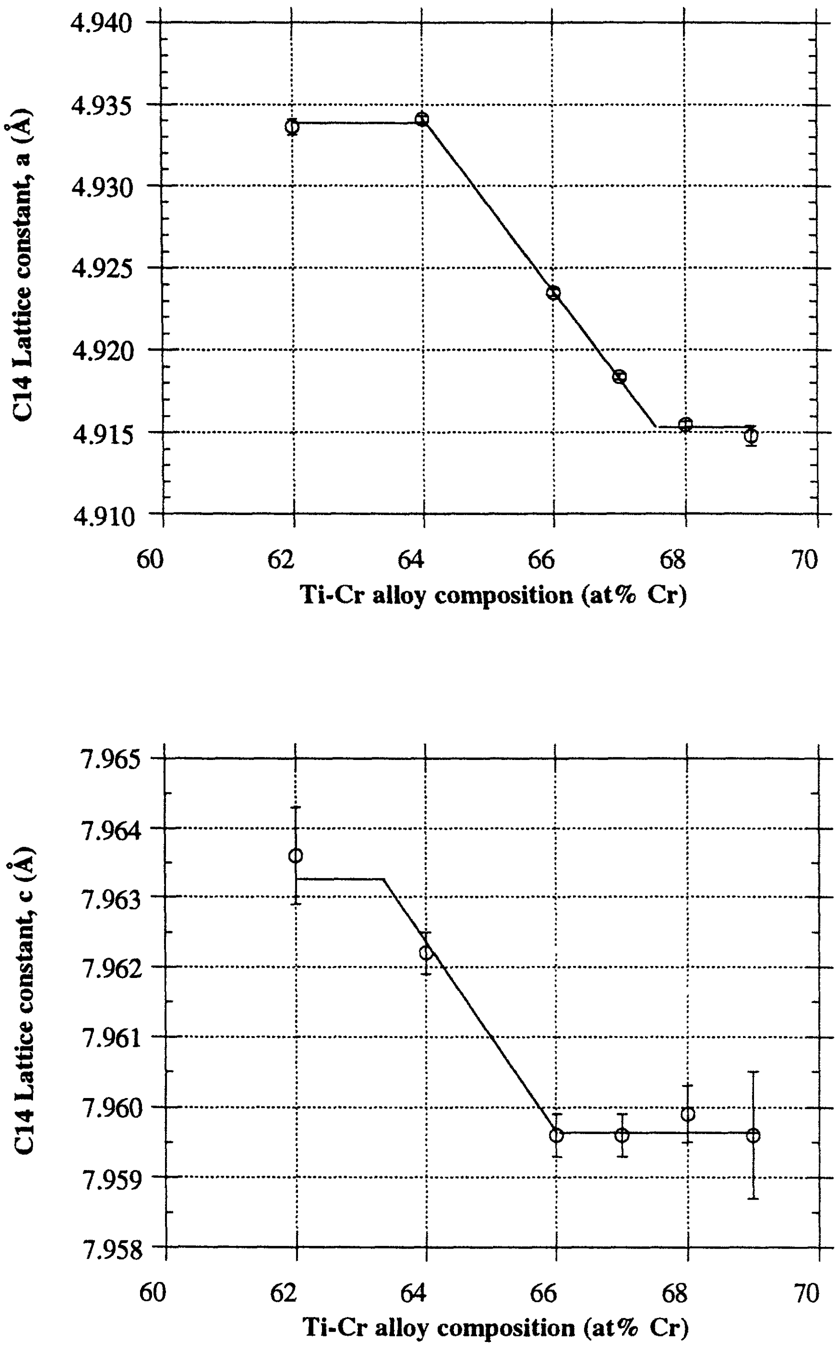

Figure 2.10 Room temperature lattice constants vs. alloy composition for the *C*14 Laves phase. Within the single-phase Laves field, lattice constants increase with increasing off-stoichiometry.

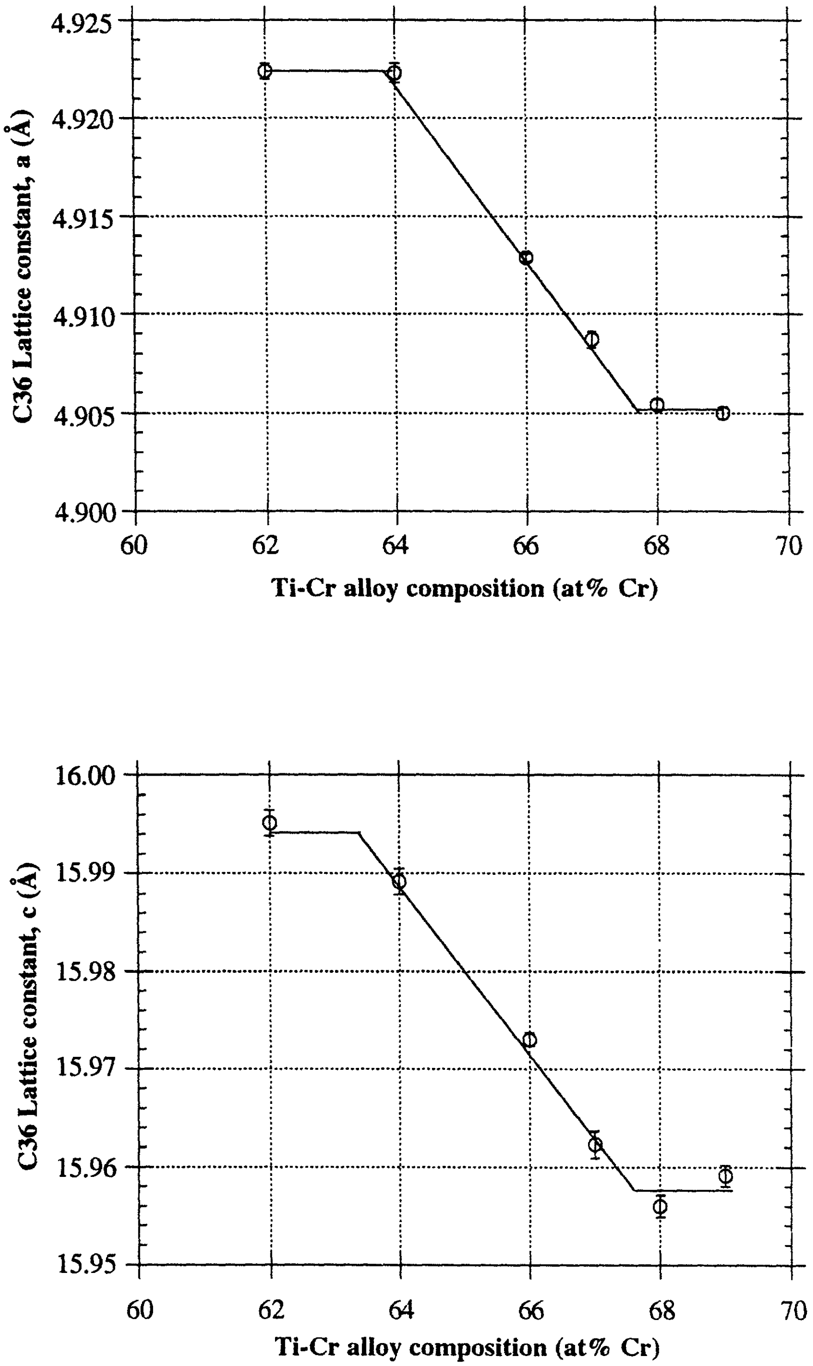

Figure 2.11 Lattice constants vs. alloy composition for the *C*36 Laves phase.

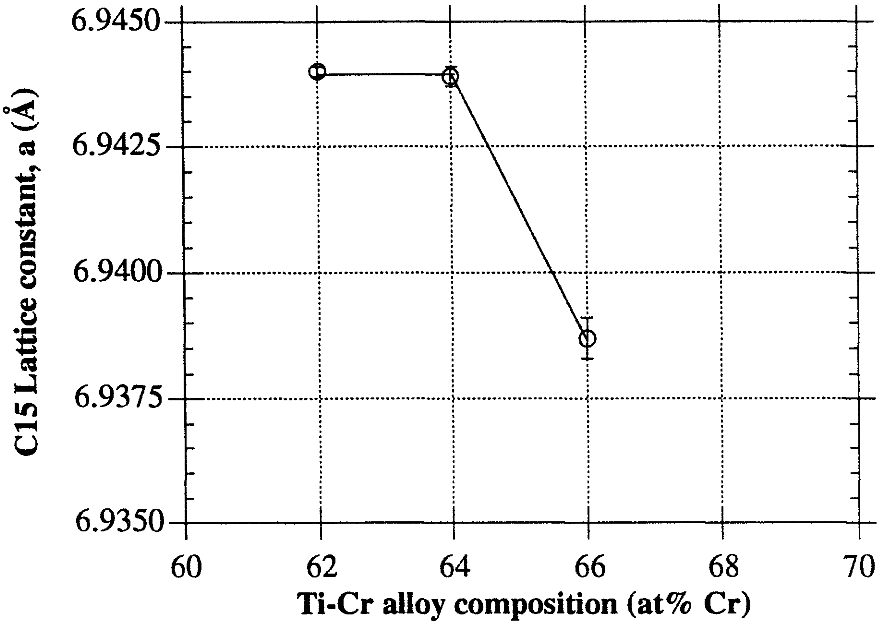

Figure 2.12 *C*15 Laves phase lattice constant vs. alloy composition.

2.6 DENSITY

The densities of the single-phase *C*14 alloys were measured and are plotted as a function of the composition (determined from electron microprobe) in Figure 2.13. The error in the density measurement is estimated to be 0.001 g/cm^3, and less than the size of the density marker size in the plot. The density decreases with decreasing Cr-content of the Laves phase. Calculated densities of nonstoichiometric $TiCr_2$ Laves phases by the anti-site substitution and vacancy defect mechanisms are also plotted and listed in Table 2.6. For a given alloy composition (determined from EMPA), the mass was calculated for the appropriate atoms with anti-site substitution and with the Cr-vacancy defect mechanism. The density was then computed with the appropriate volume (found experimentally from lattice constants determined from XRD). The experimental values fall in between the two calculated densities.

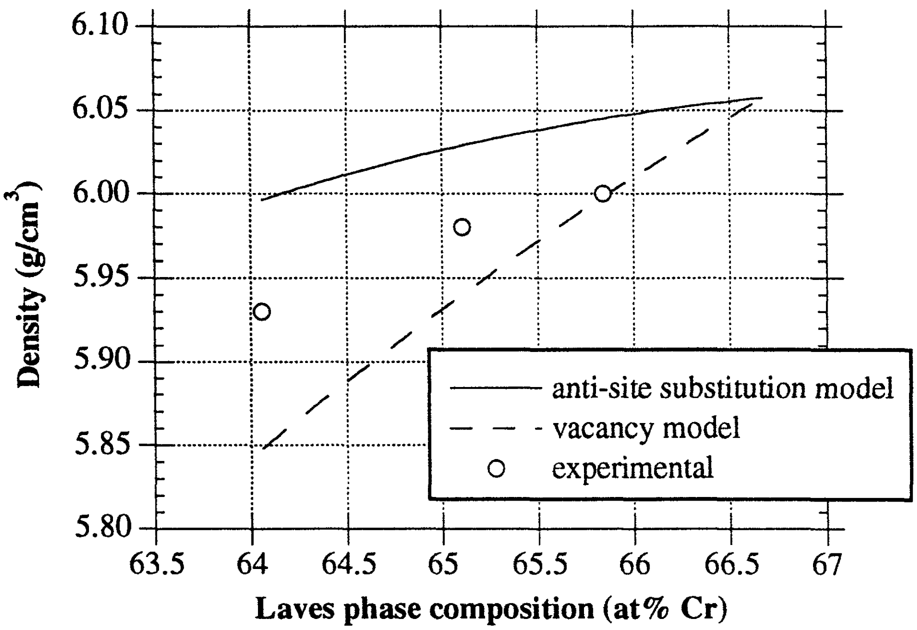

Figure 2.13 Densities of the single-phase *C*36 Laves samples vs. composition (at T=22°C). The off-stoichiometric Laves densities are compared against calculated densities with anti-site substitution and vacancy defect mechanisms.

Table 2.6 Density of *C*14 $TiCr_2$ as a function of composition and calculated densities by anti-site substitution and vacancy defect mechanisms.

$TiCr_2$ composition (at%)	experimental density (g/cm^3)	anti-site substitution density (g/cm^3)	vacancy density (g/cm^3)
Ti-66.7 Cr		6.050	6.050
Ti-65.84 Cr	6.0082	6.047	5.989
Ti-65.11 Cr	5.9784	6.029	5.915
Ti-64.06 Cr	5.9273	5.996	5.826

2.7 DISCUSSION OF NONSTOICHIOMETRY

The nonstoichiometry of the Ti-rich $TiCr_2$ must be accommodated by either the formation of vacancies on the Cr-sites, or by excess Ti atoms replacing Cr atoms by an anti-site substitution. Ti interstitials were ruled out on account of the close-packed structure of the Laves phases. Also, "tetrader" substitutions consisting of one Ti atom on four Cr sites were unlikely, as Bruckner et al. [21] determined for $ZrFe_2$ and $TiFe_2$ Laves phases. Farrar et al. [17] and Duwez et al. [18] attributed the nonstoichiometric $TiCr_2$ to excess Ti atoms, but without any experimental evidence.

The $TiCr_2$ lattice constant behavior, where the lattice constant increases with Ti-rich compositions, seems to suggest the anti-site mechanism of the larger-sized Ti atom on the Cr-sublattice. However, the similar trend of the lattice constant increasing with increasing off-stoichiometry in Nb-rich $NbCr_2$ has been attributed to Cr-site vacancies although vacancies are generally thought to decrease the lattice constant (and based on other reasons not applicable to the $TiCr_2$ system) [5]. In addition, recall that the *C*36→*C*15 transformation occurred faster for the Ti-rich alloys at 1000°C. Vacancies play a major role in diffusion and could aid in the movement of Shockley partials in the transformation process [2]. Diffusion rates increase as off-stoichiometry of NiAl increases, due to the increase of defects [22]. Thus, vacancies on the Cr-sublattice are plausible.

The density measurements helped elucidate the defect mechanism producing the Ti-rich $TiCr_2$. The experimental densities of the Laves samples occur between the calculated densities of the two different defect mechanisms, indicating that both mechanisms are operative. The lattice constant behavior and structural transformation rate observations can now both be explained.

Close to Ti-66 Cr, the experimental density lies close to the expected vacancy model value and then with increasing deviation from stoichiometry, the experimental densities seem to follow the same slope and curvature trends as the anti-site substitution values. Possibly, vacancies are created first and then Ti atoms start substituting for Cr atoms for continuing off-stoichiometry. The radius ratio, r_{Ti}/r_{Cr} is 1.141, and falls below the ideal value of 1.225. Considering a hard-sphere model of the $TiCr_2$ Laves phase, the Cr atoms are "too big" for the most efficient packing of the two dissimilar-sized atoms. Vacancies on the Cr-sublattice are needed, and thus perfect stoichiometry does not occur in $TiCr_2$. With the existence of some vacancies on the Cr-sites, the larger-sized Ti may be able to substitute on the Cr-sublattice, and Ti-rich $TiCr_2$ results.

The effects on the mechanical properties of $TiCr_2$ due to these defect structures and the different crystal structures are investigated in the next chapter.

2.8 REFERENCES

1. D.J. Thoma and J.H. Perepezko, submitted to Journal of Alloys and Compounds.
2. D.J. Thoma and J.H. Perepezko, Mater. Sci. and Eng., **A156**, 97 (1992).
3. J.C. Foley, D.J. Thoma, and J.H. Perepezko, Metall. Trans., **25A**, 230 (1994).
4. P.M. Hazzledine, *Twinning in Advanced Materials*, ed. M.H. Yoo and M. Wutting, TMS, (1994).
5. J.L. Murray, Binary Alloy Phase Diagrams, **10**, 219 (1989).
6. J.L. Murray, Bull Alloy Phase Diagr., **2**, 174 (1981).
7. K.F.J. Heinrich, *Electron Probe Quantitation*, ed. K.F.J. Heinrich and D.E. Newbury, Plenum Press, 9 (1991).
8. W. Parrish and A.J.C. Wilson, *International Tables for X-Ray Crystallography Vol. 2*, 216 (1959).
9. ASTM D 3800-79, ASTM E 12-70.
10. D.J. Thoma and J.H. Perepezko, *Experimental Methods of Phase Diagram Determination*, ed. J.E. Morral, R.S. Schiffman, and S.M. Merchant, TMS, 45 (1994).
11. M.K. McQuillan, J. Inst. Met., **80**, 379 (1951).
12. C.W. Allen and K.C. Liao, phys. stat. sol. (a), **74**, 673 (1982).
13. B.W. Levinger, Trans. AIME J. Metals, **197**, 196 (19553).
14. S.A. Minayeva, P.B. Budberg, and A.L. Gavze, Russ. Metallo., **4**, 144 (1971).
15. K.A. Gross and I.R. Lamborn, J. Inst. Met., **88**, 416 (1960).
16. K.S. Kumar and P.M. Hazzledine, *Mat. Res. Soc. Symp. Proc. Vol 364*, 1383 (1994).
17. P.A. Farrar and H. Margolin, Trans. AIME, **227**, 1342 (1963).
18. P. Duwez and J.L. Taylor, Trans. ASM, **44**, 495 (1952).
19. F.B. Cuff, N.J. Grant, and C.F. Floe, Trans. AIME, **194**, 848 (1952).

20. D.J. Thoma, Ph.D. Thesis, U. of Wisconsin, (1992).

21. W. Bruckner, K. Kleinstuck, and G.E.R. Schulze, phys. stat. sol., **23**, 475 (1967).

22. G.F. Hancock and B.R. McDonnell, phys. stat. sol. (a), **4,** 143 (1971).

Chapter 3

Mechanical properties of single-phase $TiCr_2$

3.1 INTRODUCTION

A careful study of the mechanical responses of single-phase $TiCr_2$ based on composition, crystal structure, and microstructure is the aim of this chapter, and will serve as a baseline for single-phase $TiCr_2$ properties (to be later used for comparisons with two-phase binary alloys and ternary Laves phases). The mechanical behavior of intermetallic compounds can be sensitive to composition, especially near the stoichiometric composition. The deformation properties of the Laves phase $MgZn_2$ has been reported to be strongly dependent on the compositions within the range of homogeneity [1]. Deviations from stoichiometry in the intermetallic NiAl result in increases in hardness and strength. Ni vacancies were found to be more potent strengtheners per unit addition than Ni anti-site defects [2]. The effects of nonstoichiometry in $TiCr_2$ are studied in this chapter.

Possible mechanical testing methods for single-phase $TiCr_2$ are quite limited due to the inherent brittleness of Laves phases. Also, segregation, porosity, and/or microcracks from processing can influence the bulk property results. Microindentation offers a means to locally impart large deformation to a small, flaw-free test sample, thereby avoiding such problems. Several indentations may be made on a single specimen, and no machining of special sizes or shapes is required. High hydrostatic pressures develop beneath the indenter, and since the small sample volume that undergoes plastic flow is surrounded by elastic material, side-flow is restricted or constrained. In turn, greater mean stresses are required to cause plastic flow than in uniaxial compression, which offers no resistance to bulk side flow [3]. In general, roughly two-thirds of the pressure under the indenter is hydrostatic and one-third is shear stress.

Indentation has become a very popular method to test brittle material due to its simplicity and ability to provide information on both the flow and fracture of materials. The indentation impression size measures the material's hardness or resistance to deformation, and is an indicator of strength. Cracks that emanate from the impression corners relate to the resistance to fracture and are used to determine the fracture toughness.

Hardness values and fracture toughness values of the $TiCr_2$ alloys are obtained by Vickers microindentation. The crack type in $TiCr_2$ is identified, and the fracture toughness equation is discussed. Comparisons are made among the different Laves crystal structures and with different alloy compositions near the $TiCr_2$ stoichiometry. The presence of vacancies is suggested to aid the movement of dislocations necessary for synchroshear. At the end of this chapter, hardness, toughness, and brittleness values of the $TiCr_2$ alloys are compared with other material types.

3.2 EXPERIMENTAL PROCEDURES

A Leco microhardness tester was used at room-temperature for the indentation studies. A load of 500 g was generally used, and applied for about 12 seconds. Vickers and Knoop diamond pyramid indenters were used, following ASTM guidelines [4]. Impression diagonals and crack lengths were measured with an environmental scanning electron microscope (SEM) at high magnifications for improved accuracy. The "size effect" associated with small indentations being inaccurately measured by optical microscopy can be diminished by measuring lengths by SEM [5].

Samples were fine polished with a colloidal 0.05 μm alumina suspension solution. Exner [6] has recommended fine grade polishing to remove the compressive surface stresses that may form during sample preparation and which can reduce crack lengths, resulting in faulty and nonreproducible toughness measurements.

The Vickers hardness number (*HV*) is based on the contact area of the indenter with the test material:

$$HV = 1854.4\ P/(d_1)^2 \tag{3.1}$$

where P is the load in kilograms-force and d_1 is the mean diagonal of the indentation impression in microns. The Knoop hardness number (HK) is determined by the projected area:

$$HK = 14229\ P/(d_2)^2 \tag{3.2}$$

where d_2 is now the length of the long diagonal (in microns) of the Knoop indentation. The above ASTM [4] equations give hardness values in the units of kg/mm^2 although a more up-to-date and suitable unit for force/area is the Pascal. More recent literature tends to report hardness values in GPa, and can easily be converted by the relation, 1 kg/mm^2 = 10^{-2} GPa. The hardness values presented here are the traditional kg/mm^2 units.

At least five indentations were made on each sample. Average crack lengths were determined by dividing the total lengths of all the radial cracks by four to represent an "average" crack at each impression corner. The fracture toughness, K, was calculated by an equation developed by Anstis et al., which was based on elastic/plastic indentation fracture mechanics [7]:

$$K = 0.016\ (\mathrm{E}/H)^{1/2}\ (P/c^{3/2}) \tag{3.3}$$

H is the hardness value, and c is the average crack length. A Young's modulus value (E) of 235 GPa was taken from Thoma's work [8]. Justification for using this equation is discussed in the following section.

Testing and measuring conditions were made as identical as possible for fair comparisons among the different alloy samples. Large scatter between readings and among other reported values for hardness and fracture toughness usually accompanies the indentation method. Factors such as the modulus of the indenter and sample, friction between the indenter and material, anisotropy of the material, and sample preparation can influence the results. The relative values among the $TiCr_2$ alloys are significant when obtained under the same conditions. Measurements of indentation diagonals and crack lengths were made at the same magnifications. Indentations with lateral cracks, or spallation, were generally avoided in the measurements, unless they were truly representative of the alloy behavior.

3.3 INDENTATION

3.3.1 Load dependence

The hardness of a material is assumed to be load-independent, but in reality, hardness values tend to be larger at very small loads. Errors in measuring indentations become greater as the loads and impression diagonals get smaller. Small indentation measurements made by optical microscopy (with the microhardness tester itself) tend to be inaccurate and result in higher hardness values [5]. However, indentations at different loads were magnified to similar sizes when measured with the SEM, and a load dependence of microhardness still resulted, as seen in Figure 3.1.

Experimental evidence for the dependence of microhardness values on the test load for hard metallic and ceramic materials has been documented [9]. Deiter [10] claims that at lighter loads, the small amount of elastic recovery, which is usually negligible at higher loads, becomes appreciable. McClintock and Argon [11] have explained that the increase

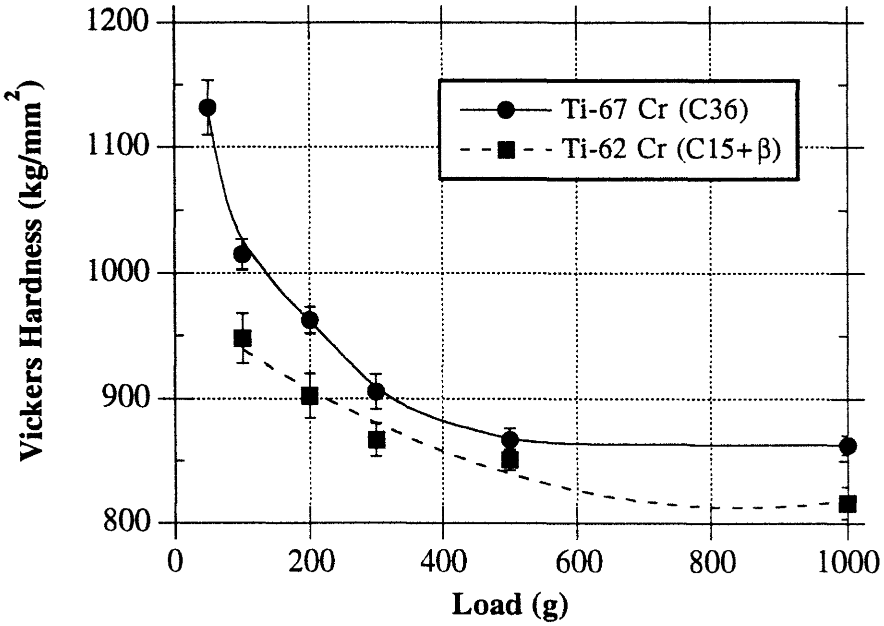

Figure 3.1 Load dependence of microhardness in $TiCr_2$ alloys. A plateau occurs around a load of 500 g.

in hardness with smaller loads occurs when the impression size approaches the slip-band length at the equivalent strain. Also, strain gradients around the impression require larger dislocation densities than those normally encountered in cold-worked metals at comparable strain levels.

As Virk et al. [9] suggest, the microhardness plateau region should be identified in order to have meaningful hardness values for comparisons. A plateau is established around a load of 500 g in Figure 3.1, and hardness values at this load will later be used for comparisons. The 500 g load also ensured that for the alloys that fell outside of the single-phase Laves field, the representative two-phase microstructures were sampled since the impression diagonal was at least several times the length scale of the two-phase microstructure.

3.3.2 Crack character and fracture toughness

Much literature has been focused on crack formation by indentation. Figure 3.2 displays schematics of the different crack types that may form by sharp indenters. Radial cracks are parallel to the load axis, and are close to the surface, usually emanating from the indentation corner. Median cracks are generated beneath the plastic deformation zone at the elastic-plastic contact in circular segments, also in the direction of loading. The final crack morphology is often the half-penny configuration, although it is unclear whether the half-penny was formed by growth of the median crack towards the surface, growth of the radial crack propagation downward, or the coalescence of the two sets of cracks [12]. Radial cracks have also been claimed to be distinct entities and not necessarily precursors to the half-penny morphology [12]. Lateral cracks are usually circular in form and run nearly parallel to the surface. Variations of these basic crack types also exist. Secondary radial cracks emanate from the edge of the indentation impression, adjacent to rather than at the corner, and propagate into the surrounding material at an angle to the load axis, remaining close to the surface. Shallow lateral cracks are generally bounded by radial or secondary radial cracks, and are found at the edge of the impression and run parallel to the surface.

Fracture toughness equations have been developed based on the crack character. Palmqvist [13] noted cracks radiating from the indentation corners and suggested that cracking could be used as a quantitative measure of toughness. Shallow radial cracks have also been termed Palmqvist cracks, labeled as l in Figure 3.3. An empirical relationship for the surface crack resistance, W, is determined by the total length of the cracks, L_T, and load, P:

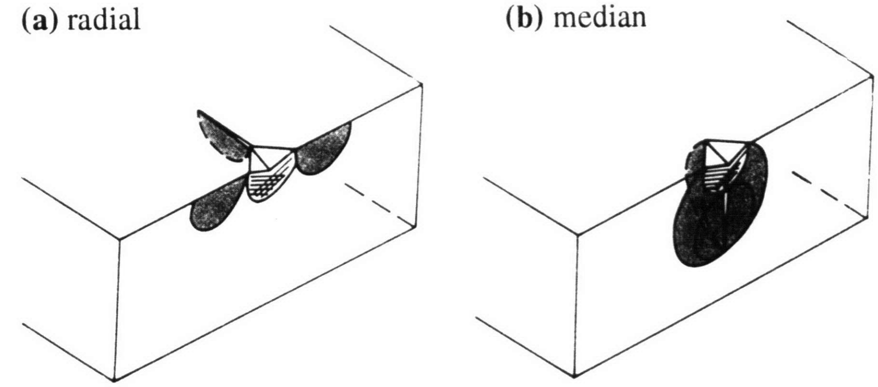
(a) radial

(b) median

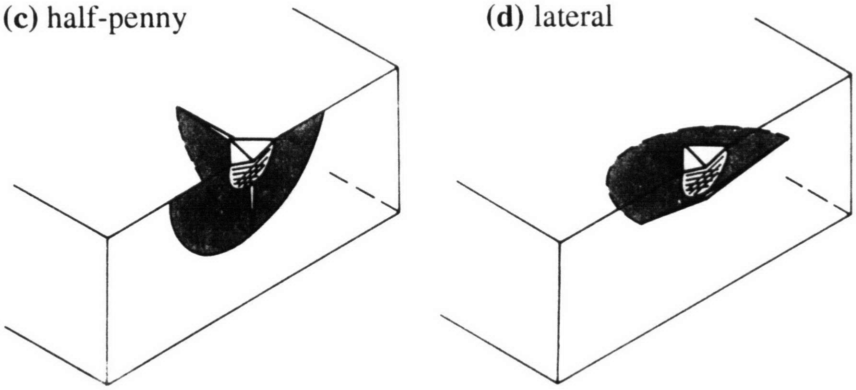
(c) half-penny

(d) lateral

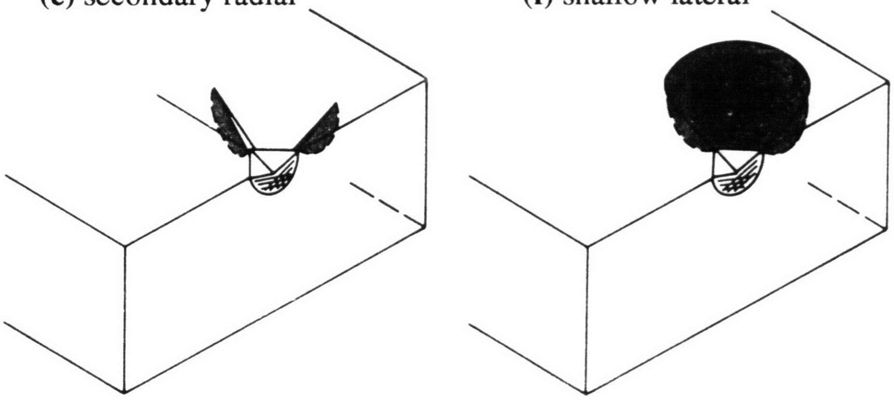
(e) secondary radial

(f) shallow lateral

Figure 3.2 Isometric sections of idealized crack morphologies with associated plastic deformation zones at Vickers indentation contacts: **(a)** radial cracks, **(b)** median cracks (the full circle indicates the extent just after initiation, and the truncated circle the possible extent on continued loading), **(c)** half-penny cracks, **(d)** lateral cracks, **(e)** secondary radial cracks, and **(f)** shallow lateral cracks [12].

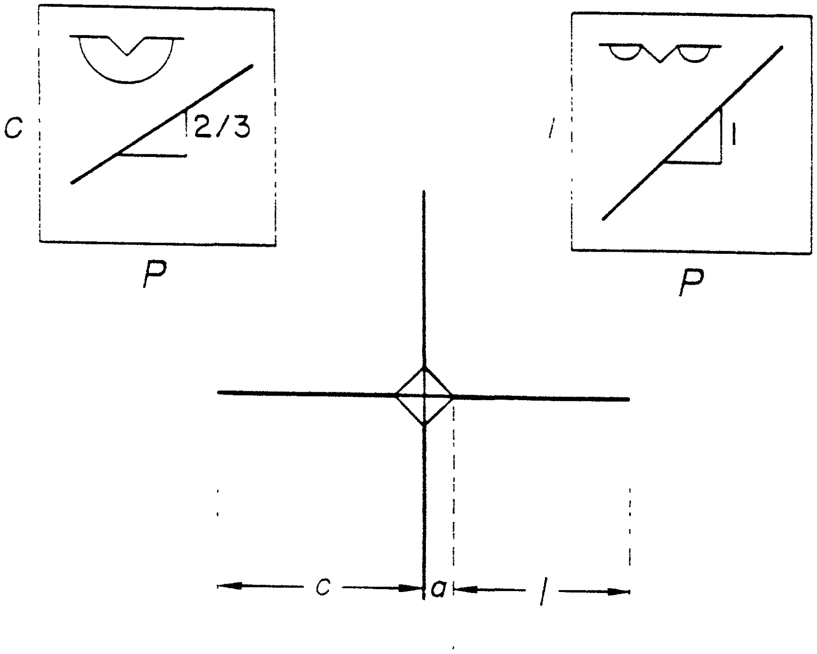

Figure 3.3 Surface trace dimensions used to estimate toughness from Vickers indentation cracks. The insets show the predicted behavior for the two extremes of assumed subsurface geometry (half-penny and Palmqvist crack types) in logarithmic coordinates [12].

$$W = P/L_T \tag{3.4}$$

However, there is no simple connection between W and the critical strain energy release rate [14]. Shetty et al. [15] and Niihara [16] have suggested the relationship:

$$K = \beta(HW)^{1/2} \tag{3.5}$$

where K is the critical stress intensity factor, H is the hardness and β is a nondimensional constant determined by the indenter geometry. Nonetheless, this relationship has been met with only moderate success, and often a different relationship based on the half-penny model works better.

Well-developed indentation cracks with the half-penny shape, c (Figure 3.3), have the relationship to the load, P:

$$k = P/c^{3/2} \tag{3.6}$$

where k is an empirically derived constant. Evans and Charles [17] were the first to introduce an analytical fracture toughness equation based on fracture mechanics and dimensional analysis. Crack growth is purported to by driven by the residual stress field from the strain mismatch of the plastically deformed zone embedded in the surrounding elastic restraining matrix. This residual driving force expands the crack system into the final half-penny configuration. The fracture toughness, K, is given by the expression:

$$K\Phi/H\sqrt{a} = 0.15\mathrm{m}\,(c/a)^{-3/2} \tag{3.7}$$

where Φ is the constraint factor (≈ 3), H is the hardness, m is a correction term, and a is the impression radius. Several investigators [18] have modified the original Evans and Charles equation, but most keep the same two features: K is proportional to $P/c^{3/2}$, (which models the cracks in a center loaded position from the deformed-zone/elastic-zone interface) and the ratio E/H (modulus/hardness) appears (representing the residual stress from the deformation mismatch).

Anstis et al. [7] have further developed the equation for fracture toughness by calibrating the indentation parameters with fracture toughness values measured by conventional fracture mechanics techniques and have concluded that:

$$K = 0.016\,(\mathrm{E}/H)^{1/2}\,(P/c^{3/2}) \tag{3.3}$$

This equation has been widely used for estimating the fracture toughness from crack length data.

Crack length versus indentation load data were plotted for two different $TiCr_2$ alloys in two different manners. Figure 3.4 gives the Palmqvist crack relationship of P vs. L_T, while Figure 3.5 plots P vs. $c^{3/2}$ in accordance to the half-penny model. The data fits to the half-penny model better, but Shetty et al. [19] caution that it is impossible to discriminate between the two crack models based on the load-dependence of crack lengths alone.

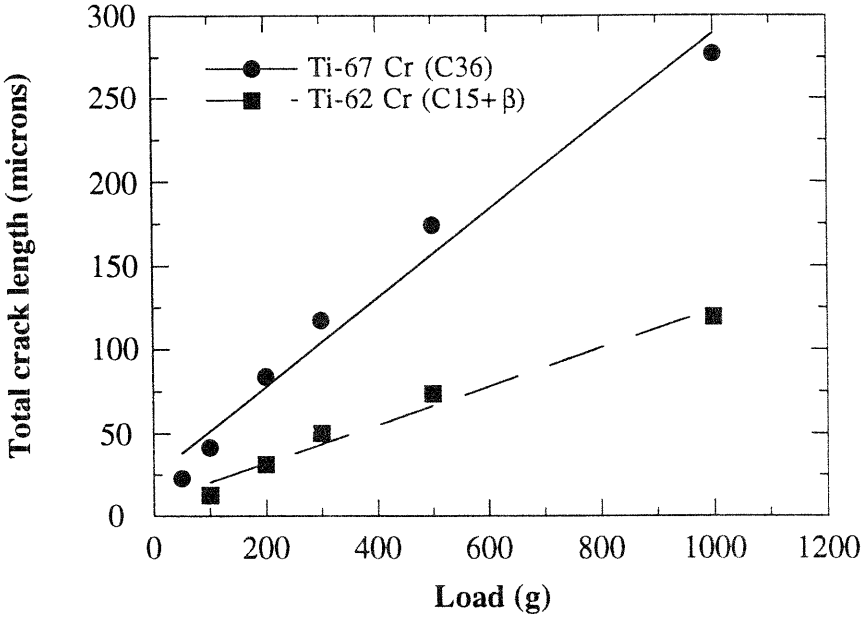

Figure 3.4 Indentation load versus total crack length in the Palmqvist crack relationship.

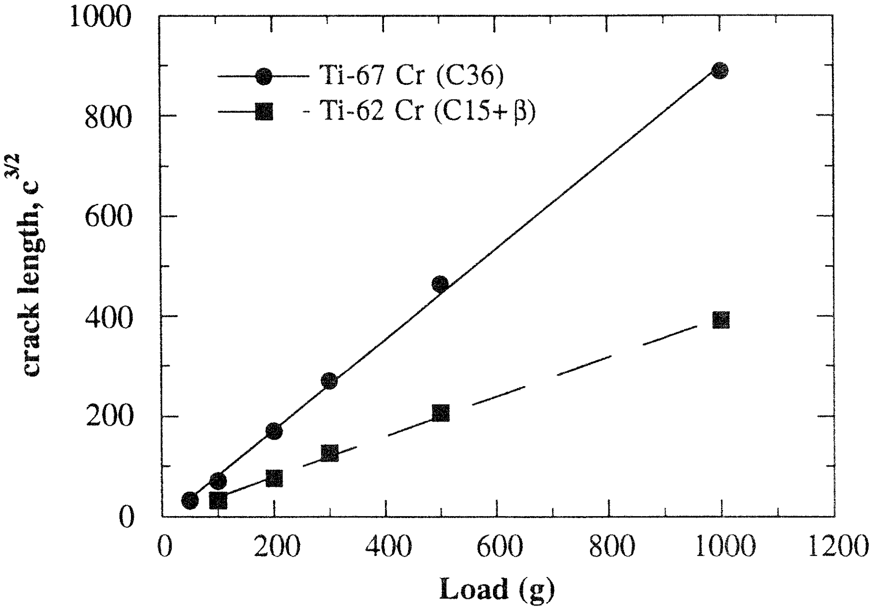

Figure 3.5 Indentation load versus the average radial crack length to the 3/2 power in the half-penny model, showing the $k=P/c^{3/2}$ relationship.

In a review of indentation cracking, Cook and Pharr [12] concluded that crack lengths alone were no guarantee of crack morphology. Serial sectioning of indentations on $TiCr_2$ was therefore performed. Successive layers were polished off and are displayed in Figure 3.6. The amount sectioned off or the depth, *d*, of the cracks in relation to the surface was determined by measuring secondary indentations off to the side and using the geometry of the Vickers indentation impression:

$$d = (a_1 - a_2)\,\frac{\sqrt{2}}{2}\cot\alpha = 0.286\,(a_1 - a_2) \tag{3.8}$$

where $\alpha = 68°$ is the semi-angle between the Vickers pyramid faces, and a_1 and a_2 represent the half-diagonals of the indentation impression before and after the sectioning, respectively. Figure 3.6 reveals that the cracks are shallow radial cracks or Palmqvist cracks, and do not conform to the half-penny configuration. The cracks are unconnected underneath the deformation zone. Secondary radial cracks (to the right of the top corner) are also seen to run at an angle to the axial load direction.

Thus, although the indentation cracks in $TiCr_2$ are Palmqvist in nature, they obey the $k=P/c^{3/2}$ relationship used for the half-penny cracks. Using equation (3.3), the fracture toughness is seen to be fairly load-independent past a load of 200 g in Figure 3.7, and thus the Anstis et al. [7] equation has been used to compute the fracture toughness of the $TiCr_2$ alloys. Laugier [20] has demonstrated that Palmqvist cracks are successfully described by analyses based on the half-penny geometry. Modeling the cracks as rectangular entities rather than semi-circles, the stress intensity factor differed from the center-loaded half-penny case by only a factor that was less than the variation to be expected experimentally. This surprising result indicates the relative insensitivity of the surface stress intensity factor (that controls crack extension) to marked changes in the crack geometry, and that the local conditions near the intersection of the crack front and the surface remain relatively unchanged [21].

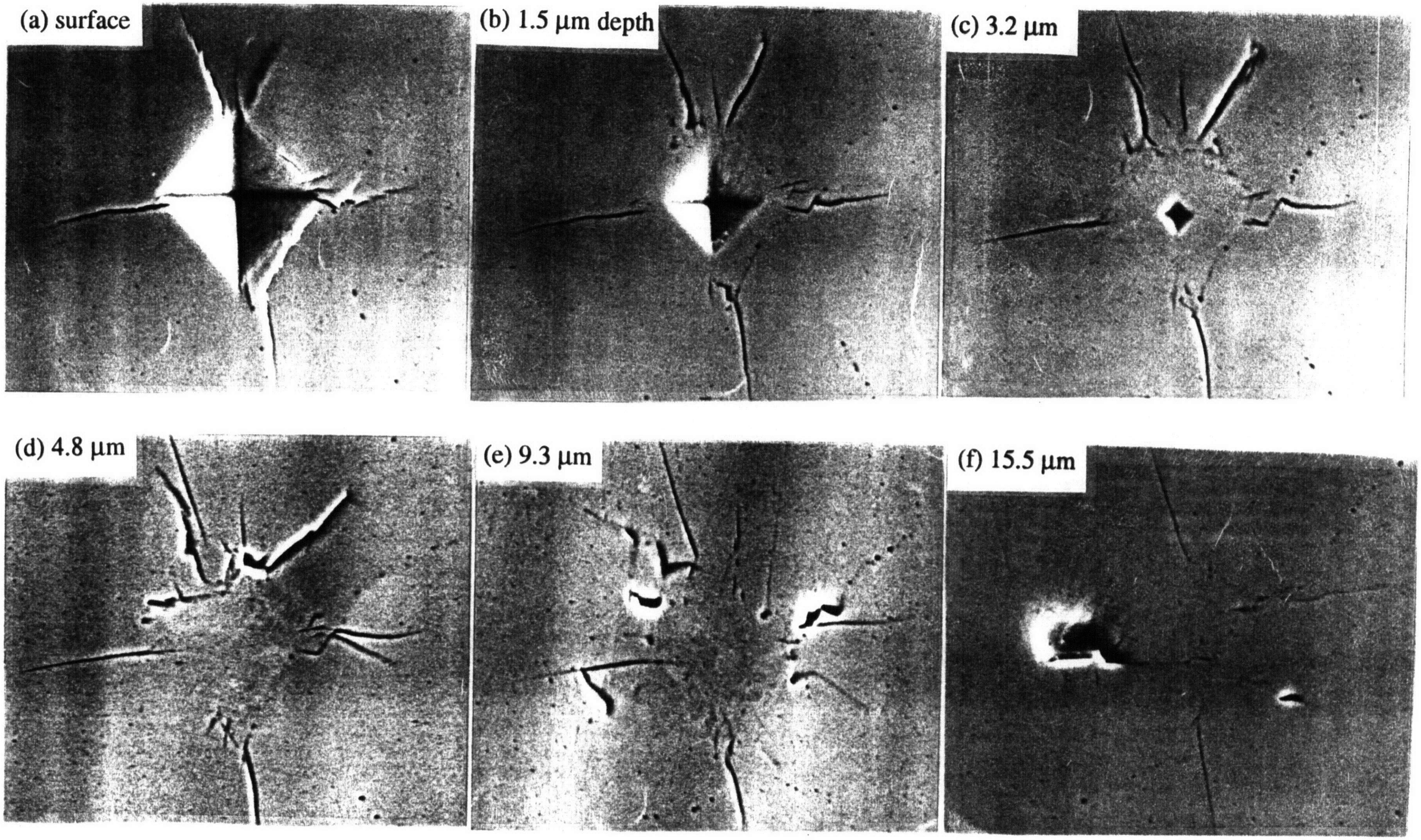

Figure 3.6 Serial sectioning of a Vickers indentation on Ti-66 Cr alloy annealed at 1000°C. Shallow radial cracks or Palmqvist cracks are revealed.

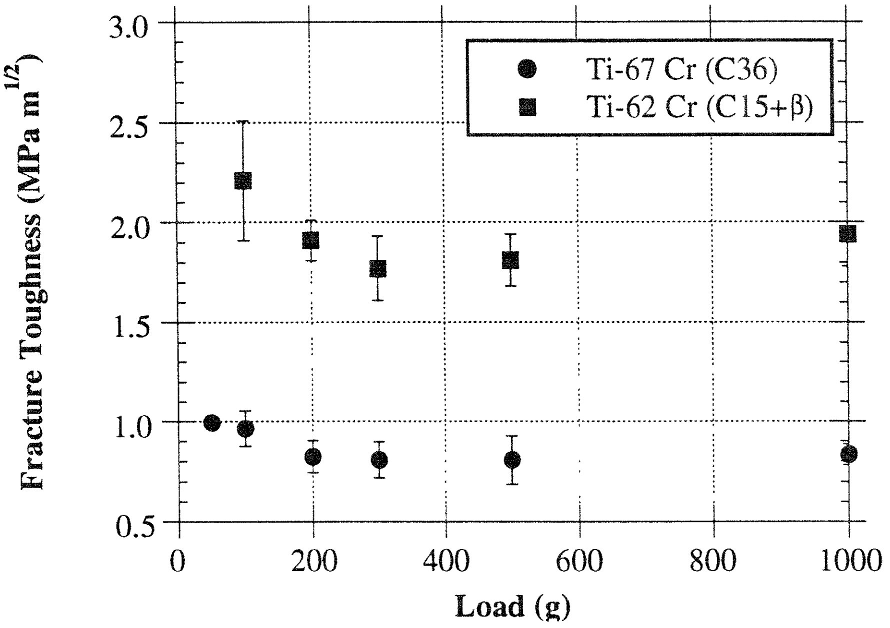

Figure 3.7 Load-independence of $TiCr_2$ fracture toughness based on Anstis [7] equation.

3.4 RESULTS

3.4.1 Microhardness

Indentations were performed on the six different binary alloys (described in Chapter 2) after several different heat treatments that produced different Laves crystal structures and microstructures. SEM micrographs of the indentations can be seen in Figure 3.8. Table 3.1 lists the microhardness values of the $TiCr_2$ alloys by composition and crystal structure. Table 3.2 compares other values of $TiCr_2$ found in the literature [8,22-24]. The scatter in reported values of microhardness comes from different indenters, loads,

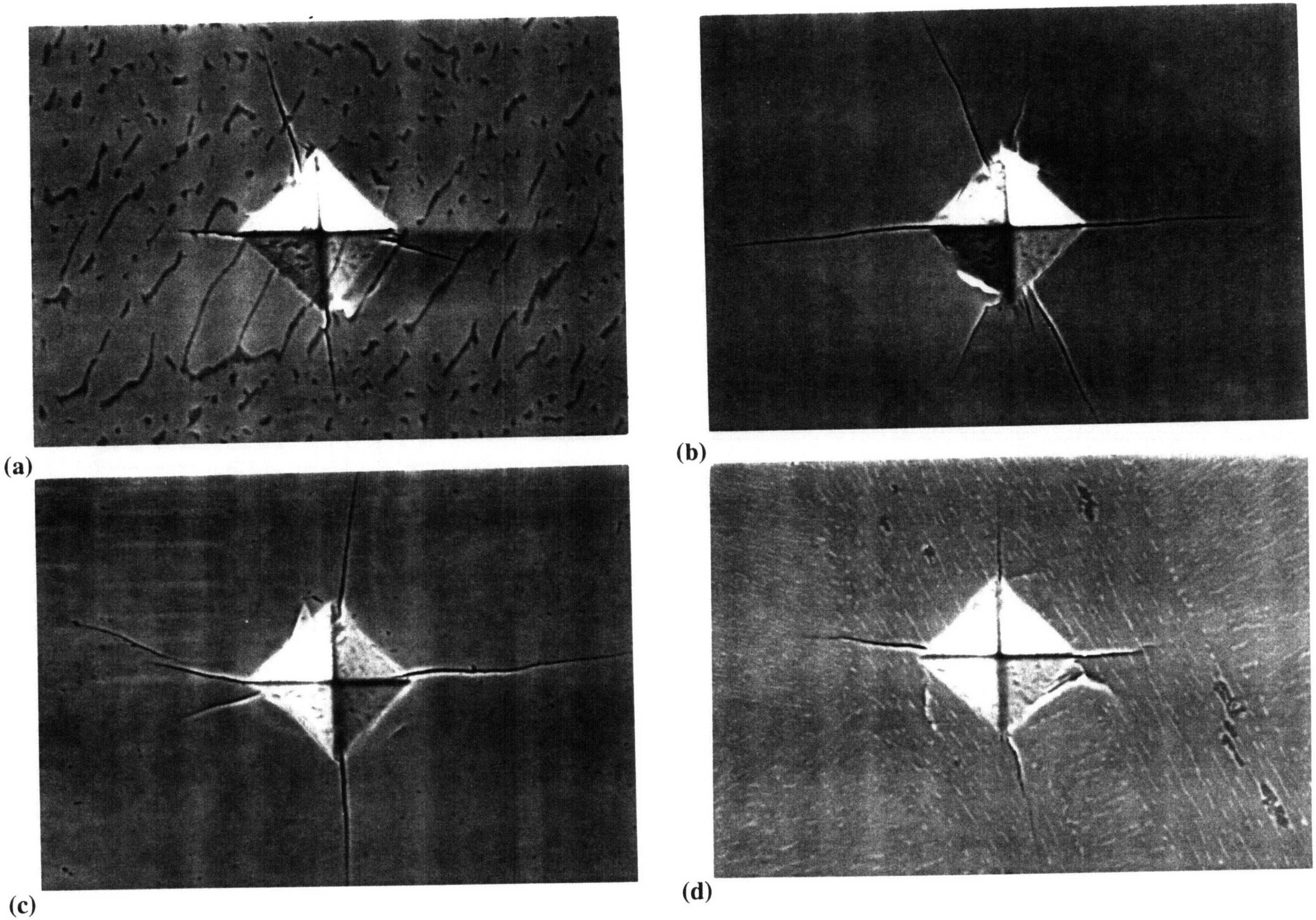

Figure 3.8 SEM micrographs of indentation of *C*36 $TiCr_2$ alloys. **(a)** Ti-62 Cr, **(b)** Ti-66 Cr, **(c)** Ti-67 Cr, and **(d)** Ti-69 Cr alloy. Note the reduction in crack lengths in the two-phase microstructures which lead to greater fracture toughness than the single-phase alloys.

Table 3.1 Vickers microhardness of $TiCr_2$ alloys at room-temperature and 500 g load.

alloy composition	*C*14 microhardness, kg/mm^2 (1300°C)	*C*36 microhardness, kg/mm^2 (1200°C)	*C*15 microhardness, kg/mm^2 (1000°C)
Ti-62 Cr (two-phase)	839.3 ± 10.9	838.2 ± 20.4	853.1 ± 14.0
Ti-64 Cr	852.8 ± 22.8	864.1 ± 14.8	890.5 ± 9.9
Ti-66 Cr	841.4 ± 14.5	879.7 ± 18.8	853.4 ± 17.2 (*C*36/*C*15)
Ti-67 Cr	845.4 ± 13.1	894.4 ± 11.7	
Ti-68 Cr (two-phase)	847.5 ± 14.8	867.8 ± 16.6	
Ti-69 Cr (two-phase)	849.5 ± 15.3	874.6 ± 5.5	

and testing conditions, which can give very different results. Overall, the hardness of $TiCr_2$ is quite high.

Figure 3.9 plots all the microhardness data points. The single-phase Laves region is marked by the arrows along the x-axis. The *C*14 alloys showed no distinct microhardness variation with alloy composition. Since the grain sizes are much larger than the indentation size, the indentations were effectively on single crystals of unknown orientations, and thus anisotropies of this hexagonal phase may have masked any compositional influences. However, the *C*36 alloys did exhibit a compositional dependence on hardness. Figure 3.10 reveals this dependence in measurements made at two different loads. A maximum hardness is found for the single-phase alloy closest to the stoichiometric composition. The decrease in hardness in the two-phase alloys (outside the Ti - 64–67 at% Cr range) can be attributed to the softer bcc beta phase.

Some concern exists over the authenticity of hardness measurements when cracks are formed. Measurements of the impression diagonals may be less reliable when cracks are present, and the Vickers hardness numbers should be regarded as the "lower limit" in hardness values. Therefore, Knoop indentation, which generally does not produce cracking, was also used on the *C*36 $TiCr_2$ alloys at a load of 500 g. However, the same compositional trend with microhardness was found, as seen in Figure 3.11.

Table 3.2 Hardness measurements of $TiCr_2$ in the literature.

Reference	Hardness (kg/mm^2)	Testing conditions
Samsonova and Budberg, 1966 [22]	800-850	N/A
Stone, 1977 [23]	980	50 g load
Fleischer and Zabala, 1990 [24]	780-980	diamond pyramid indenter, 500-1000 g
Thoma, 1992 [8]	1050	Berkovitch indenter, 500 nm depth
this study	894	Vickers indenter, 500 g load

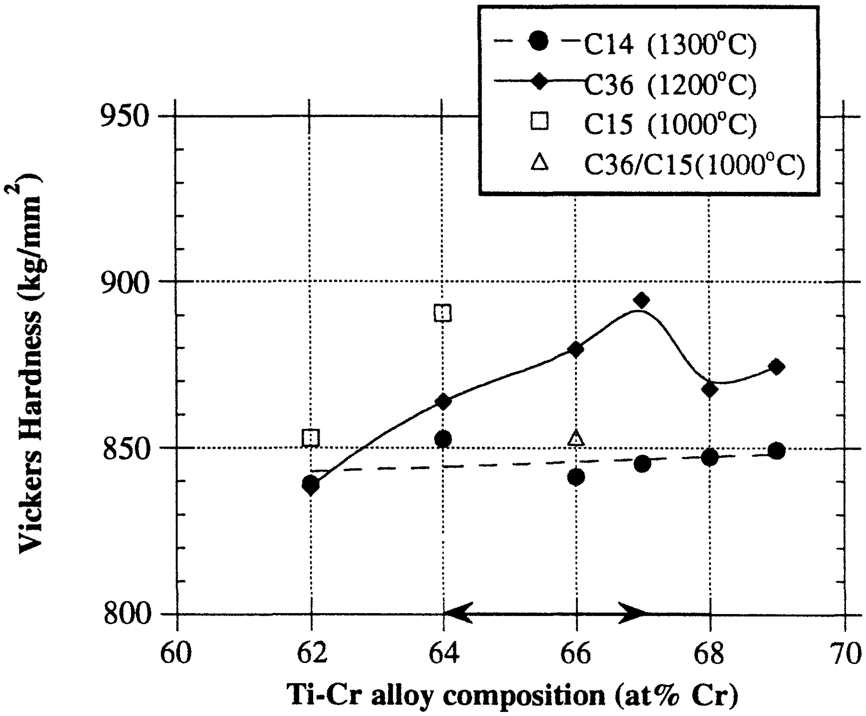

Figure 3.9 Microhardness values of $TiCr_2$ alloys based on alloy composition and crystal structure.

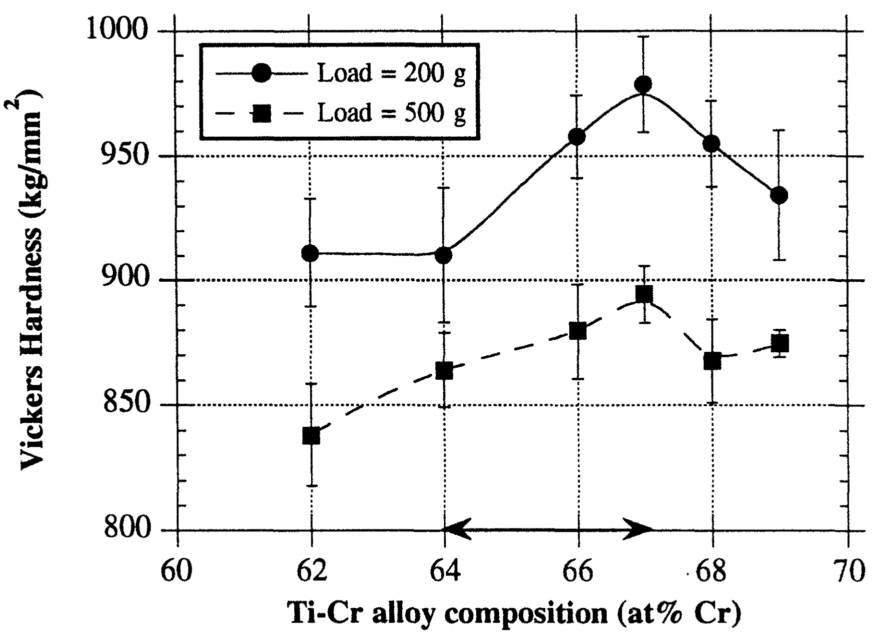

Figure 3.10 Compositional dependence of microhardness for *C*36 $TiCr_2$ alloys. A maximum in hardness occurs at the stoichiometric $TiCr_2$ composition.

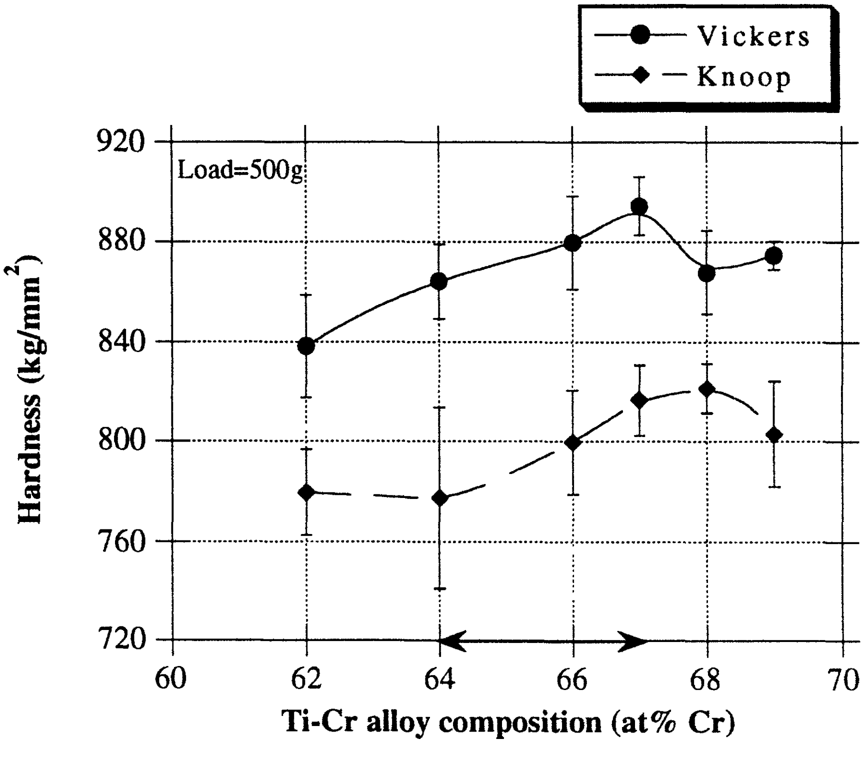

Figure 3.11 Vickers and Knoop indentation on the *C*36 $TiCr_2$ alloys.

Because the *C*15 structure was not uniformly achieved in all the alloy compositions, the composition dependence of hardness in *C*15 $TiCr_2$ could not be determined directly. However, the Ti-rich, two-phase alloys with the *C*15 structure have higher hardness values than the corresponding hexagonal structures at the same alloy compositions, suggesting that the *C*15 structure has the highest hardness. The Ti-66 Cr alloy at 1000°C had a mix of *C*36 and *C*15 structures, and appears to have much lower hardness. Thus, the $TiCr_2$ Laves phase hardness is not only dependent upon the composition, but also the crystal structure.

The observed hardness behavior in the *C*36 single-phase Laves region contradicts the usual trend found in intermetallics. Westbrook [25] had documented that in several systems, the stoichiometric composition has the lowest hardness, and increasing off-stoichiometric compositions show increased hardness at low homologous temperatures. The defects in the nonstoichiometric compounds are thought to interfere with dislocations, and thus produce hardening. At higher homologous temperatures, the defects have a softening effect. At the higher temperatures, the diffusion rates are enhanced, and dislocation climb becomes easier.

On the other hand, Paufler et al. [26,27] documented a similar maximum hardness at the stoichiometric compositions of $MgZn_2$ and $NbFe_2$ Laves phases. The defects associated with off-stoichiometry were shown to decrease the mobility of the dislocations, but the dislocation density also increased to produce the overall decrease in hardness, as seen in Figure 3.12.

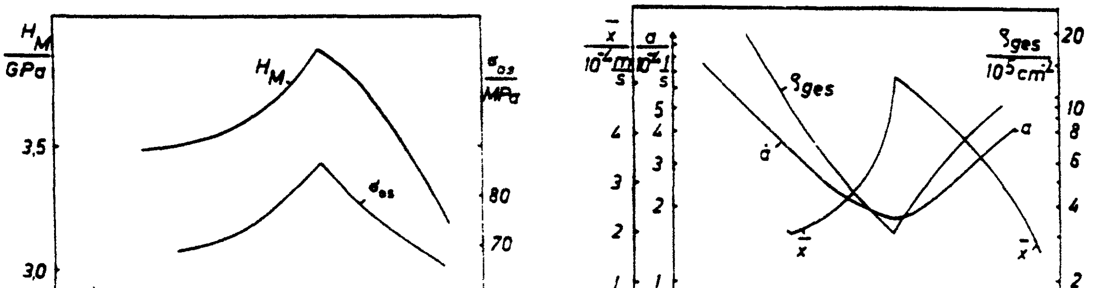

Figure 3.12 The effect of composition on the mechanical properties of $MgZn_2$ [27]. Maximum hardness (H_M) and stress (σ_{os}) are found at the stoichiometric $MgZn_2$ composition. The dislocation velocity ($\bar{x}$) decreases with off-stoichiometric compositions, but the dislocation density (ρ) also increases, producing the decrease in hardness values.

3.4.2 Fracture Toughness

The fracture toughness values of the $TiCr_2$ alloys are listed in Table 3.3, and plotted in Figure 3.13. Different crystal structures and alloys with varying amounts of a second phase are plotted all together. Within the single-phase region (denoted by the arrows along the composition axis), the values for fracture toughness are quite low. The *C*15 structure at Ti-64 Cr shows notable improvement over the hexagonal structures (*C*36 and *C*14) at the same alloy composition. The cubic structure may offer more deformability due to the additional crystal symmetry and available slip systems. Many investigators employ this finding for other intermetallic systems. $TiAl_3$ has been alloyed in attempts to change the tetragonal $D0_{22}$ crystal structure to the cubic $L1_2$ structure to improve the ductility [28].

The Ti-66 Cr alloy annealed at 1000°C contains a mixture of the *C*15 and *C*36 structures, and provides a test sample for a potential stress-induced phase transformation as a means of "transformation toughening". In $ZrFe_2$, embryos of *C*15 in the *C*36 Laves alloy were discovered to grow upon applied stress from room-temperature compression [29]. Alloys exhibiting polytypism are thought to have low stacking fault energies, and may enhance twinning to improve toughness [30]. However, the low fracture toughness value in this particular *C*15/*C*36 sample indicates that such a mechanism does not occur in $TiCr_2$.

Table 3.3 Fracture Toughness of $TiCr_2$ alloys measured by indentation (500 g load).

alloy composition	*C*14 fracture toughness MPa $m^{1/2}$	*C*36 fracture toughness MPa $m^{1/2}$	*C*15 fracture toughness MPa $m^{1/2}$
Ti-62 Cr (two-phase)	2.24 ± 0.22	1.54 ± 0.22	1.85 ± 0.31
Ti-64 Cr	0.93 ± 0.10	1.10 ± 0.25	1.47 ± 0.17
Ti-66 Cr	0.76 ± 0.10	0.93 ± 0.12	0.76 ± 0.11 (*C*36/*C*15)
Ti-67 Cr	0.75 ± 0.17	0.91 ± 0.14	
Ti-68 Cr (two-phase)	2.61 ± 0.47	1.18 ± 0.11	
Ti-69 Cr (two-phase)	2.69 ± 0.57	1.76 ± 0.21	

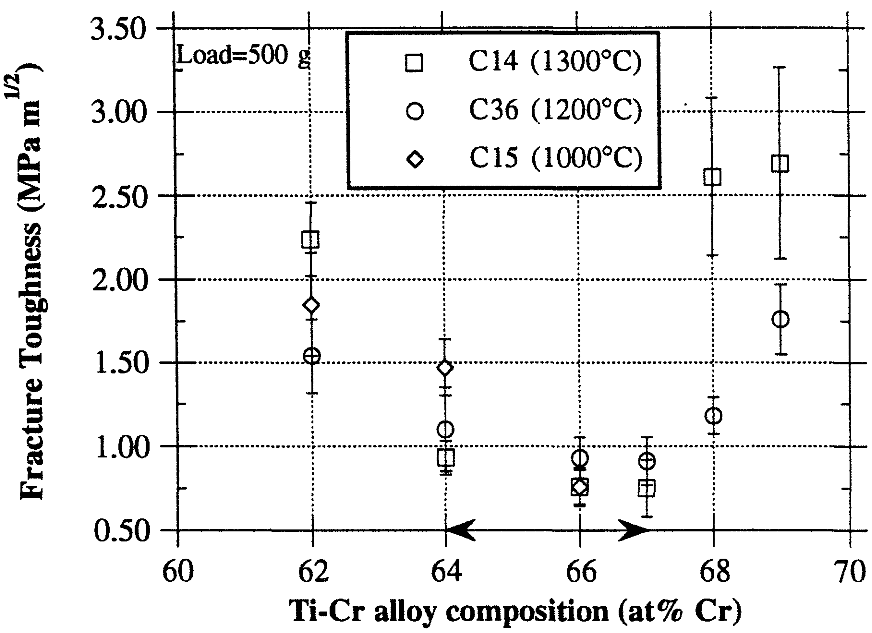

Figure 3.13 Fracture toughness values of $TiCr_2$ alloys based on alloy composition and crystal structure.

Figure 3.14 shows the compositional dependence of the fracture toughness in the *C*36 $TiCr_2$ alloys. The minimum fracture toughness value occurs at the stoichiometric $TiCr_2$ composition. The opposite trend was observed with the microhardness values. Within the single-phase Laves field, slight increases in the fracture toughness were found with increased deviation from stoichiometry. Disorder in the off-stoichiometric compositions (excess Ti and/or Cr vacancies) results in greater toughness. More faults and dislocations may exist, which translate into greater deformation. The lower hardness values of the off-stoichiometric compositions are consistent with this idea.

Hazzledine [31] has reasoned that vacancies can assist the movement of synchro-Shockley dislocations. Plasticity in the Laves phases relies on the motion of these dislocations to produce slip, twinning, and stress-induced phase transformations. A Shockley dislocation can have a core that is split over two closely-spaced planes, which performs the necessary atomic shifting required in synchroshear [32]. At the core, atoms must swap positions, and vacancies are believed to facilitate this process. A vacancy moving along with a kink in a dislocation enables the atomic interchange to take place without much dilatation of the crystal. Currently, there is no direct evidence that vacancies are involved with the motion of synchro-dislocations, but on the whole, experimental work on the Laves phases show that phase transformations tend to be sluggish and plasticity normally occurs only at temperatures about two-thirds the melting temperature. At the higher temperatures, the dislocations have greater mobility (and is attributed to vacancies). Furthermore, the trends displayed in this indentation study of the single-phase $TiCr_2$ alloys are entirely consistent with Hazzledine's postulate. The off-stoichiometric alloys, which were found to possess vacancies (in Chapter 2), exhibit decreased hardness and increased fracture toughness compared to the stoichiometric $TiCr_2$ sample. Thus, the improved deformability in the off-stoichiometric compositions can be explained by the presence of vacancies assisting the synchroshear deformation process.

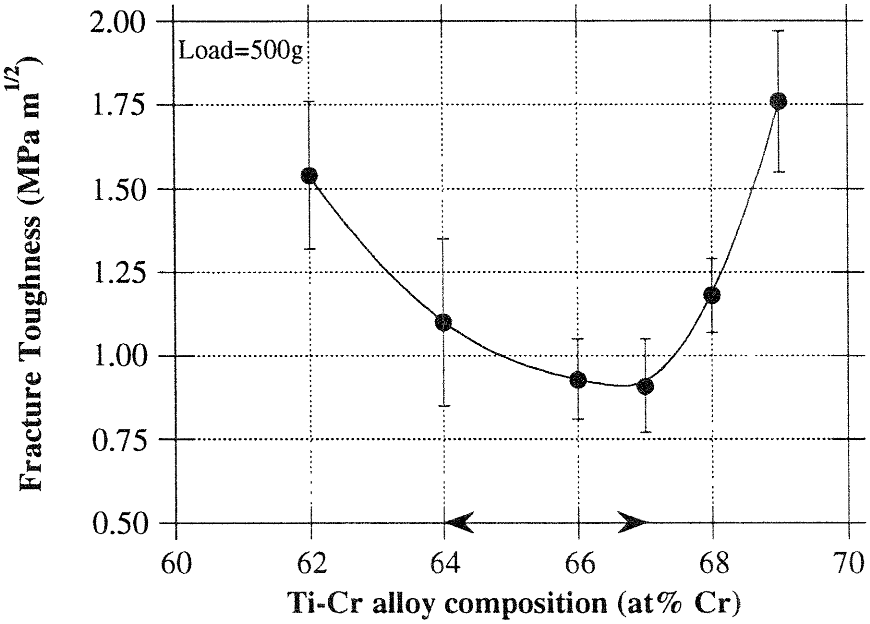

Figure 3.14 Compositional dependence of fracture toughness found in the *C*36 $TiCr_2$ alloys. A minimum in toughness occurs at the stoichiometric $TiCr_2$ composition.

Marked improvements in the fracture toughness are displayed by the two-phase alloys, and are due to the dispersed ductile beta phase. The substantial increase in toughness in the Cr-rich *C*14 alloys at 1300°C stems from the numerous dispersed beta particles present due to the higher equilibrium volume fraction of the beta phase than the same alloy composition at 1200°C. The radial cracks were often disrupted by or terminated at the beta phase particles, as seen in Figure 3.15. High magnification of a crack in the two-phase Ti-62 Cr alloy (Figure 3.16) shows the crack circumventing the beta particle. Debonding of the bcc/Laves phase interface is an important mechanism to relieve some of the deformation energy [33].

The increase in toughness with small amounts of a second, more ductile phase is much greater than that arising from nonstoichiometry in the single-phase $TiCr_2$ Laves phase compositions, or from variations in the crystal structure. The slight reduction in hardness by the introduction of a second phase may be well worth the improvements in toughness.

Lawn and Marshall [34] have proposed an index of brittleness as the ratio of hardness to fracture toughness, H/K. Table 3.4 lists the hardness, fracture toughness, and brittleness of several different materials for comparisons with $TiCr_2$. The single-phase, stoichiometric *C*36 $TiCr_2$ is relatively very brittle, with only single-crystal sapphire and silicon being more brittle. However, $TiCr_2$ with small amounts of the beta phase (5-13 vol%) drastically improves the brittleness factor. Such findings lead to the resolution that the Laves phases will most likely be part of a two-phase system in practical applications. The next two chapters will investigate the microstructures and resulting mechanical properties of two-phase Ti-Cr alloys, where the major or matrix phase is the bcc beta phase.

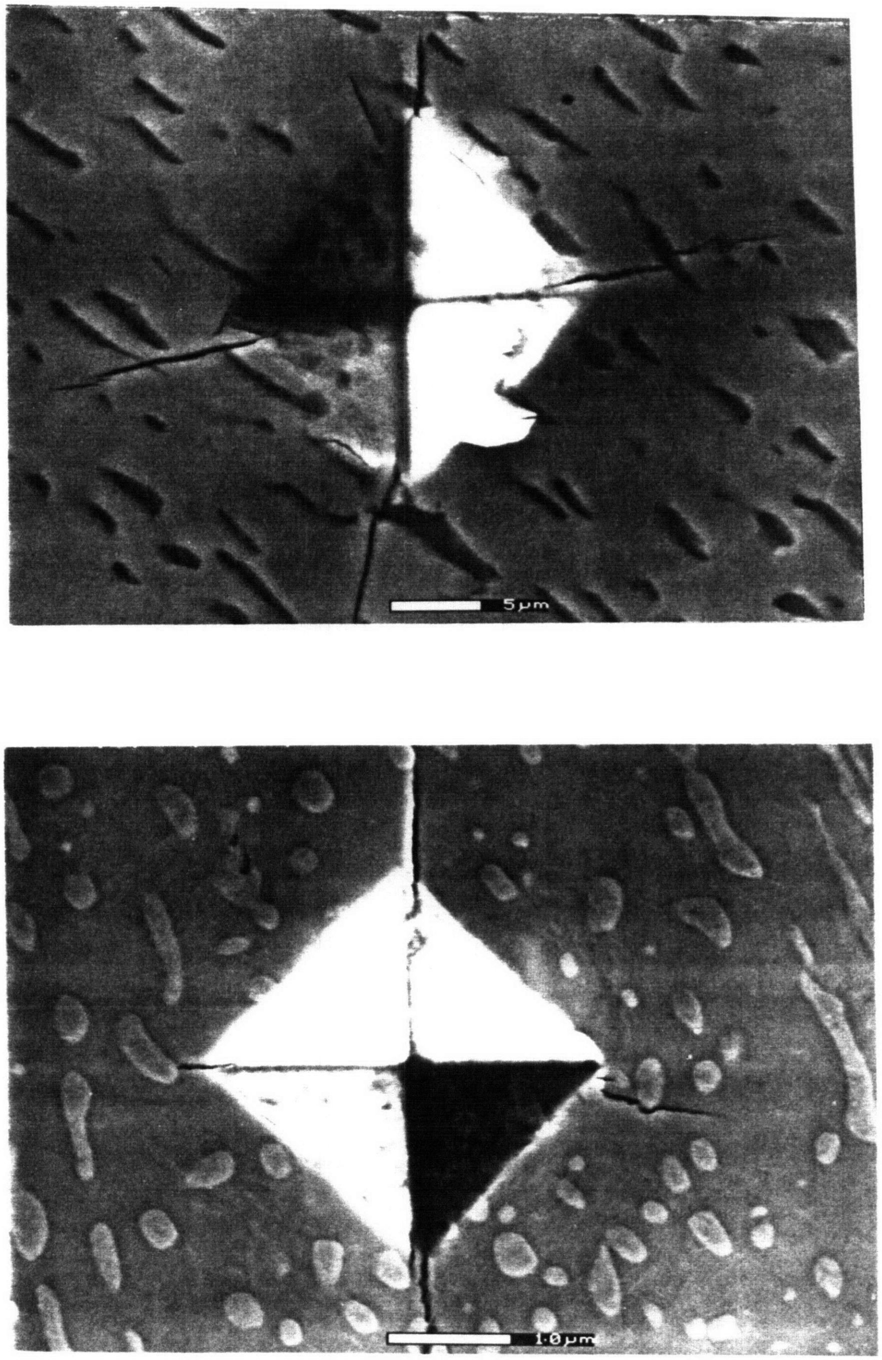

Figure 3.15 SEM images of radial cracks disrupted by or terminated at beta phase particles in the two-phase $TiCr_2$ alloys: **(a)** Ti-62 Cr and **(b)** Ti-69 Cr.

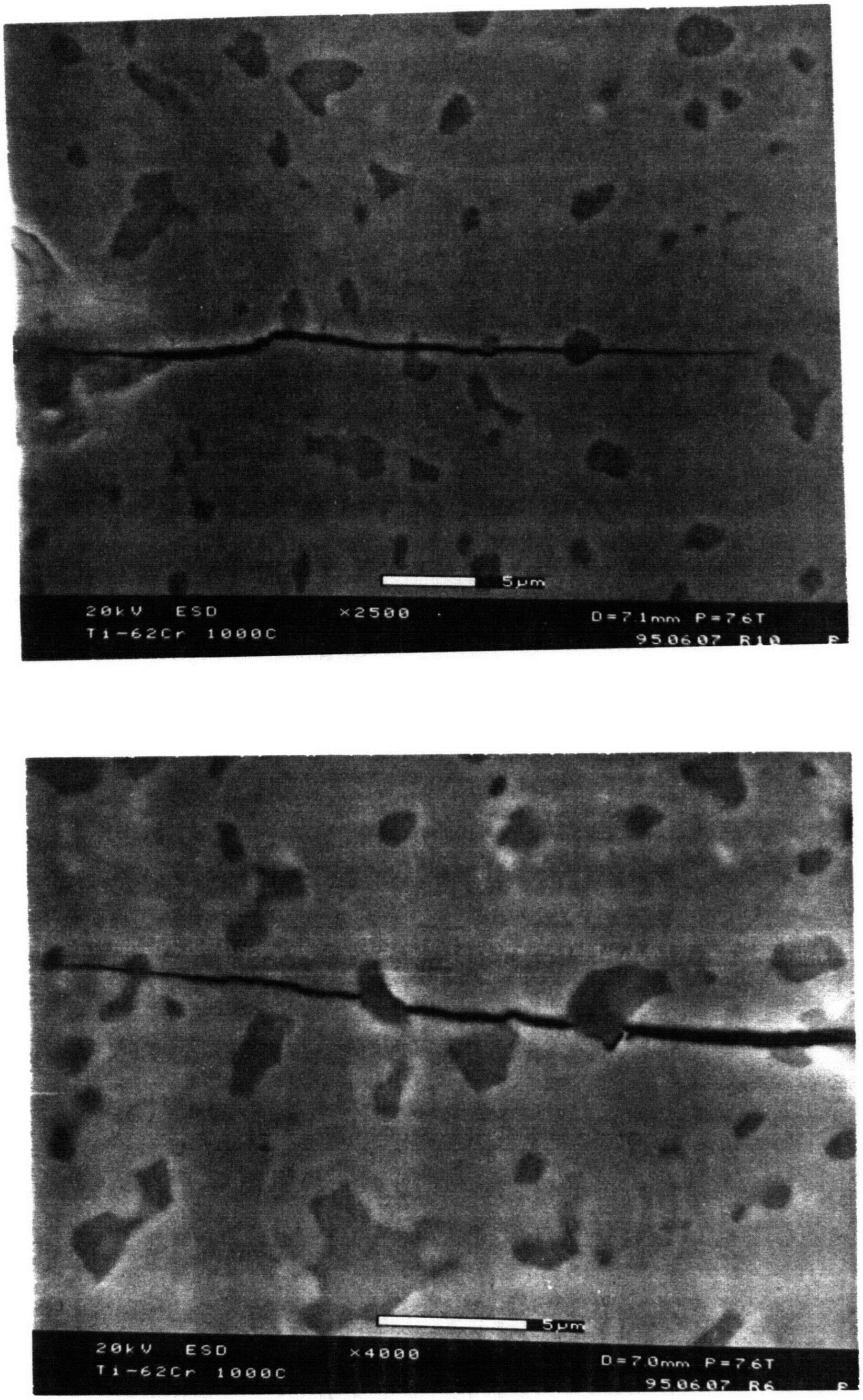

Figure 3.16 SEM micrographs of radial cracks circumventing the beta phase particles in the Ti-62 Cr alloy.

Table 3.4 Hardness, fracture toughness, and brittleness parameters of various materials.

Material	Hardness, H (kg/mm^2)	Toughness, K ($MPa\ m^{1/2}$)	Brittleness, H/K ($\mu m^{-1/2}$)	Reference
Fe (med-strength steel)	500	50	0.1	[32]
NaCl (single xtal)	24	0.4	0.6	[32]
WC/Co (12%)	1320	16	0.8	[17]
ZnS	190	1.0	1.9	[17]
Al_2O_3 (MgO doped)	1200	4	3.0	[32]
Ti-69 Cr (*C*14+β)	850	2.7	3.2	
Ti-62 Cr (*C*15+β)	853	1.9	4.6	
SiC	1930	4.0	4.8	[17]
MgF_2	580	0.9	6.4	[32]
soda-lime glass (amorph)	550	0.75	7.3	[7]
MgO	920	1.2	7.7	[32]
SiO_2 (glass)	620	0.7	8.9	[32]
$TiCr_2$ (*C*36)	894	0.91	9.8	
Sapphire (single xtal)	2300	2.1	11.0	[17]
Si (single xtal)	900	0.7	12.9	[7]

3.5 REFERENCES

1. T. Muller and P. Paufler, phys. stat. sol. (a) **40**. 471 (1977).
2. D.B. Miracle, Acta metall. mater., **41**, 649 (1993).
3. D.B. Marshall and B.R. Lawn, "Indentation of Brittle Materials", *Microindentation Techniques in Materials Science and Engineering*, ASTM 889, eds. P.J. Blau and B.R. Lawn, Am Soc for Testing and Materials, (1986).
4. ASTM E384-89, E92-82.
5. R.M. Westrich, "Use of the Scanning Electron Microscope in Microhardness Testing of High-Hardness Materials", *Microindentation Techniques in Materials Science and Engineering*, ASTM 889, eds. P.J. Blau and B.R. Lawn, Am Soc for Testing and Materials, (1986).
6. H.E. Exner, Trans. Met. Soc. AIME, **245**, 677 (1969).
7. G.R. Anstis, P. Chantikul, B.R. Lawn, and D.B. Marshall, J. Am Ceram. Soc., **64,** 533 (1981).
8. D.J. Thoma, Ph.D. Thesis, U. of Wisconsin, (1992).
9. I.S. Virk, M.B. Winnicka, and R.A. Varin, Scripta Metall. et Mater., **24,** 2181 (1990).
10. G.E. Dieter, *Mechanical Metallurgy* , McGraw-Hill, (1986).
11. F.A. McClintock and A.S. Argon, *Mechanical Behavior of Materials* , Addison-Wesley Publ. Co. (1966).
12. R.F. Cook and G.M. Pharr, J. Am. Ceram. Soc., **73**, 787 (1990).
13. S. Palmqvist, Jernkontorets Ann., **141,** 302 (1957); Arch. Eisenhuttenwes, **33**, 629 (1962).
14. E.L. Exner, J.R. Pickens, and J. Gurland, Metall. Trans., **9A**, 736 (1978).
15. D.K. Shetty, I.G. Wright, P.N. Mincer, and A.H. Clauer, J. Mater. Sci., **20**, 1873 (1985).
16. K. Niihara, J. Mater. Sci. Lett., **2**, 221 (1983).
17. A.G. Evans and E.A. Charles, J. Am. Ceram. Soc., **59**, 371 (1976).

18. I.J. McColm, *Ceramic Hardness*, Plenum Press, (1990).
19. D.K. Shetty, A.R. Rosenfield, and W.H. Duckworth, J. Am Ceram. Soc., **68**, C282 (1985).
20. M.T. Laugier, *Inst. Phys. Conf. Ser. No. 75: Chapter 5*, 449 (1986).
21. M.T. Laugier, J. Am. Ceram. Soc., **68**, C51 (1985).
22. N.N. Samsonova and P.B. Budberg, Poroshokovaya Metallurgiya, **8**(44), 49 (1966).
23. H.E.N. Stone, J. Mat. Sci., **12**, 1416 (1977).
24. R.L. Fleischer and R.J. Zabala, Metall. Trans., **21A**, 1951 (1990).
25. J.H. Westbrook, *Mechanical Properties of Intermetallic Compounds*, ed. J.H. Westbrook, John Wiley & Sons, Inc., (1960).
26. P. Paufler, K. Eichler and G.E.R. Schulze, Monatsberichte, **12**, 949 (1970).
27. P. Paufler, Chemische Gesellschaft, **9**, 175 (1984).
28. S. Zhang, J.P. Nic, and D.E. Mikkola, Scripta Metall. et Mater., **24**, 57 (1990).
29. Y. Liu, S.M. Allen, and J.D. Livingston, Metall. Trans., **23A**, 3303 (1992).
30. J.D. Livingston and E.L. Hall, J. Mater. Res., **5**, 5 (1990).
31. P.M. Hazzledine, submitted to TMS.
32. P.M. Hazzledine, K.S. Kumar, D.B. Miracle, and A.G. Jackson, *Mater. Res. Soc. Symp. Proc. Vol. 288*, 591 (1992); P.M. Hazzledine and P. Pirouz, Scripta Met, (1993).
33. M.F. Ashby, F.J. Blunt, and M. Bannister, Acta Metall., **37**, 1847 (1989).
34. B.R. Lawn and D.B. Marshall, J. Am, Ceram. Soc., **62**, 347 (1979).

Chapter 4

Characterization of two-phase binary alloys

4.1 INTRODUCTION

As seen from the previous chapter, the Laves phases are extremely brittle, and the greatest hopes in finding practical applications for these intermetallics lie in two-phase systems. Studies on two-phase alloys indicate that room-temperature toughness can be improved while still maintaining high-temperature strength, and these will be discussed in more detail in the next chapter. Many Laves compounds can be found in a two-phase equilibrium with a terminal solid solution. Table 4.1 lists such possibilities with transition metals, excluding the Lanthanide elements [1]. Since the phases are thermodynamically stable, problems found in composites, such as interfacial reactions, are avoided. Also, simultaneous fabrication of the "matrix" and "reinforcement" can be accomplished in a single step by controlled solidification [2].

Microstructural design now becomes an integral part in developing the Laves phases as useful structures. The mechanical properties of a two-phase alloy depend on the size, shape, volume fraction, distribution, and orientation relationship of the second phase. Understanding and controlling the microstructures are essential to tailoring materials for desired properties.

The Ti-Cr system is unique from almost all other binary alloy Laves phase systems in that the $TiCr_2$ intermetallic precipitates from a solid solution decomposition rather than from forming by a eutectic reaction (see Figure 2.1 for the Ti-Cr phase diagram). This feature allows some control over the microstructure. A continuous bcc solid solution spans the entire Ti-Cr composition range. Two-phase alloys on both the Ti-rich and Cr-rich sides of the $TiCr_2$ composition are possible with this solid solution phase. Very

Table 4.1 Two-phase Laves systems and crystal structures of transition metals.

AB_2 Laves phase		A-rich	B-rich
$CdCo_2$	*C*36		Cu-fcc
$CoHf_2$	*C*15		Hf-hcp
$HfCo_2$	*C*15	Hf-hcp	
$HfCr_2$	*C*14/*C*15	Hf-hcp	Cr-bcc
$HfFe_2$	*C*14/*C*36/*C*15	Hf-hcp	
$HfMo_2$	*C*36/*C*15	Hf-bcc	Mo-bcc
$HfMn_2$	C14/C36		Mn-bcc, hcp
HfV_2	*C*15	Hf-bcc, hcp	V-bcc
HfW_2	*C*15	Hf-bcc	W-bcc
$MgCo_2$	*C*14	Mg-hcp	Co-fcc, hcp
$MgCu_2$	*C*15		Cu-fcc
$MgNi_2$	*C*36		Ni-fcc
$MgZn$	*C*14		Zn-hcp
$MoFe_2$	*C*14		Fe-bcc
$NbCr_2$	*C*14/*C*15	Nb-bcc	Cr-bcc
$NbFe_2$	*C*14		Fe-bcc
$NbMn_2$	*C*14		Mn-bcc
$ScCo_2$	*C*15		Co-fcc, hcp
$ScFe_2$	*C*14/*C*36/*C*15	Sc-bcc	Fe-fcc, bcc
$TaCo_2$	*C*14/*C*36/*C*15		Co-fcc
$TaCr_2$	*C*14/*C*15	Ta-bcc	Cr-bcc
$TaFe_2$	*C*14		Fe-fcc, bcc
$TaMn_2$	*C*14		Mn-bcc, fcc
TaV_2	*C*15	Ta-bcc	V-bcc
$TiCr_2$	*C*14/*C*36/*C*15	Ti-bcc, hcp	Cr-bcc
$TiFe_2$	*C*14		Fe-bcc
WBe_2	*C*14	W-bcc	
WFe_2	*C*14		Fe-bcc
$ZrCr_2$	*C*14/*C*36/*C*15	Zr-bcc,hcp	Cr-bcc
$ZrFe_2$	*C*15		Fe-bcc
$ZrMn_2$	*C*14	Zr-bcc, hcp	
$ZrMo_2$	*C*15	Zr-bcc, hcp	Mo-bcc
ZrV_2	*C*15	Zr-bcc, hcp	V-bcc
ZrW_2	*C*15	Zr-bcc	W-bcc

different microstructures can be produced by different alloy compositions and annealing treatments.

4.2 EXPERIMENTAL PROCEDURES

Titanium-rich Ti-Cr binary alloys were obtained from General Electric (Corporate Research and Development, Schenectady, NY). Compositions of Ti-30 at% Cr and Ti-40 at% Cr were arc-cast into 60 g buttons. The tops and bottoms of the arc-cast buttons were sliced off to discard regions of possible chemical segregation and porosity associated with solidification. Chromium-rich Ti-Cr binary alloys of Ti-80 at% Cr and Ti-87.5 at% Cr were arc-cast at the Materials Preparation Center of Ames Laboratory, Iowa.

A range of temperatures and times were used for various annealing treatments within the two-phase field of β-Ti(Cr)+$TiCr_2$ and β-Cr(Ti)+$TiCr_2$. Samples were encapsulated in a quartz tube with a tantalum getter, under a vacuum of about 10^{-5} Torr, and then back-filled with argon gas. A box furnace was used for annealing treatments up to 1190°C, and a vacuum furnace was used for anneals at 1200°C and above. Most heat treatments were followed by air-cooling since water-quenching proved to have no beneficial effect. The Cr-rich alloys also went through a homogenization treatment, as described for the single phase $TiCr_2$ alloys in Chapter 2.

Standard metallographic procedures were followed for polishing and etching. Samples in a bakelite or cold epoxy mount were polished by a series of SiC grinding paper, diamond pastes, and finishing with an alumina powder solution of 0.05 μm for a fine polish. A solution of 25% HF, 25% HNO_3, and 50% glycerin was used for etching. The Cr-rich alloys, however, could not be etched unless electrolytic etching was employed [3]. Photographs were taken on an Olympus optical microscope and an environmental scanning electron microscope (ESEM). The ESEM allowed examination of unetched microstructures and fine microstructural details at high magnifications.

Compositions were determined by electron microprobe analysis (EMPA). Image analysis software was used to determine volume percentages of second phases and the mean intercept spacing of the Cr-rich alloys from scanned ESEM images of representative microstructures. A straight line of known length was drawn randomly across the microstructure, intersecting the phases at various angles. The mean intercept spacing is defined by the number of intersections with $TiCr_2$ within the length of the test line [4].

Transmission electron microscopy (TEM) samples were prepared by first slicing a thin piece of the bulk material and then mechanically grinding the slice down to a thickness of approximately 200-300 microns. The Ti-rich alloys could be punched into 3 mm discs without cracking, while discs of the more brittle Cr-rich alloys were cut by an ultrasonic disc cutter. A combination of dimpling, jet polishing, and ion milling was used. An electrolyte of perchloric acid in methanol [5] was found to give the best results for jet-polishing.

X-ray diffraction was performed on a Rigaku 300 diffractometer. Since the Ti-rich beta phase was difficult to crush into fine powder, polished slabs of the Ti-rich alloys were used. The small grain size gave an adequate range of random orientations for polycrystalline diffraction. The Cr-rich alloys were studied using powder samples.

4.3 MICROSTRUCTURES

4.3.1 As-cast conditions

The as-cast Ti-rich alloys were almost completely single-phase β-Ti(Cr), with no evidence of any $TiCr_2$ from x-ray or electron diffraction. Optical microscopy revealed etch pits outlining significant subgrain structure. These etch pits may represent dislocations that later serve as potent nucleation sites or diffusion paths for precipitation, as the subgrain structure is later seen running through the precipitates in the annealed samples. In the Ti-40 Cr alloy, some precipitation is seen along the grain boundary, and some random clusters of precipitates are found by TEM, as seen in Figure 4.1. The heavily-faulted structure of the precipitates complicated the identification by electron diffraction, but the faulted structure is characteristic of the Laves phases or related-layered structures that may be precursors to the Laves phase [6]. These occasional precipitates in the as-cast condition may later play a part in the bimodal size distribution of Laves phase precipitates in the annealed Ti-40 Cr alloy.

The as-cast Cr-rich alloys were dendritic and required a solutionizing treatment to remove the chemical inhomogenities. In the as-cast condition, x-ray diffraction displayed only the bcc structure. After the homogenization step, the Ti-87.5 Cr alloy was uniformly all beta phase, but the Ti-80 Cr alloy had areas of single-phase beta while other areas were of a fine two-phase microstructure. Figure 4.2 depicts the boundary region between

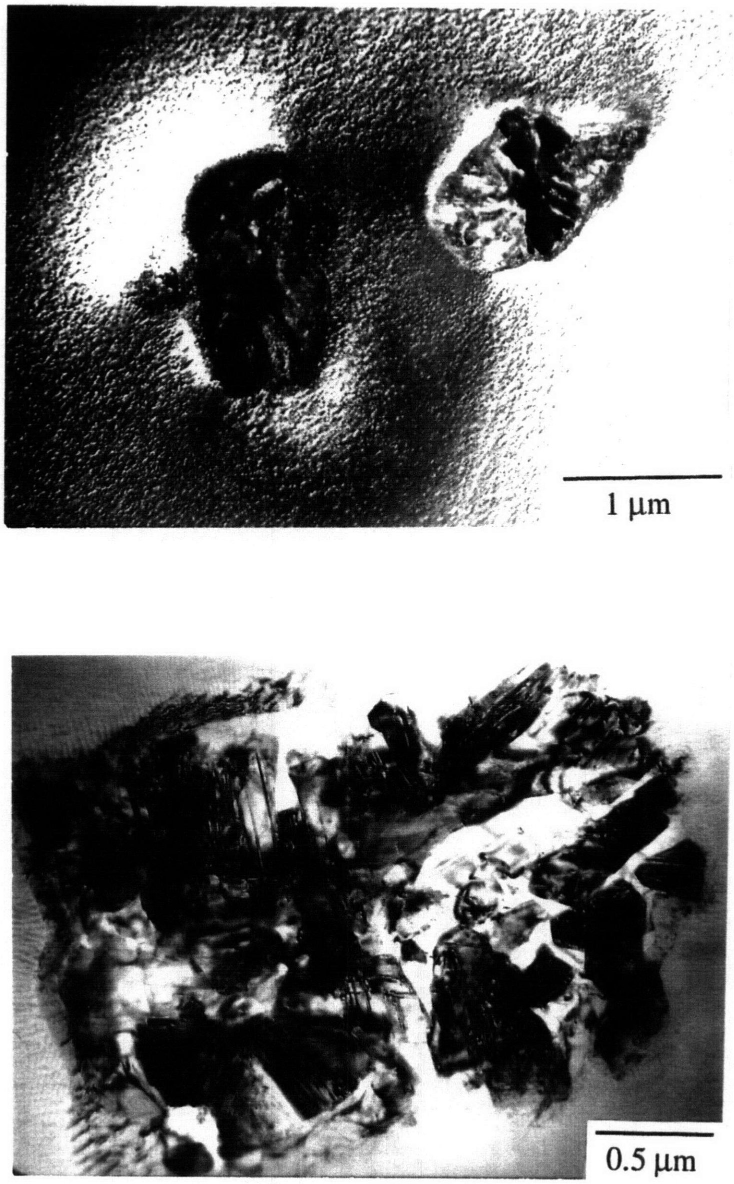

Figure 4.1 TEM of clusters of precipitates in the β-bcc phase of the as-cast Ti-40 Cr alloy at **(a)** 20kX and **(b)** 37kX.

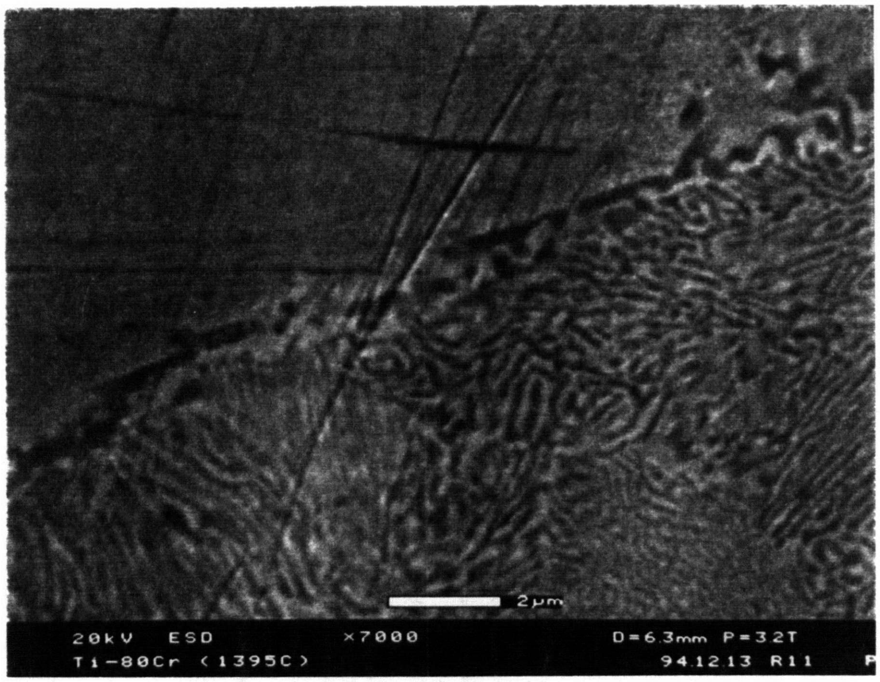

Figure 4.2 Cellular precipitation in the Ti-80 Cr alloy after homogenization at 1380°C for 24 hours.

the two different areas. In discontinuous precipitation, colonies often nucleate only on one side of the grain boundary. The two-phase lamellar structure is reminiscent of cellular precipitation, which usually occurs at lower temperatures where solute partitioning is easier via grain boundary diffusion rather than by lattice diffusion. The discontinuous precipitation reaction occurs at the moving interface of the grain boundary. The two-phase structure could be seen only at high magnifications in the SEM.

Random microhardness measurements concur with the microstructural observations. Figure 4.3 plots the frequency of hardness values, and two distinct peaks result. The high hardness value peak is attributed to the fine two-phase areas, while the lower value corresponds to the single-phase beta.

4.3.2 Omega phase

The beta phase itself is metastable and forms an hcp omega phase (ω) by an athermal transformation during the quench from anneals [7,8]. The omega phase was found in the beta phase of all the Ti-Cr alloy compositions studied. The omega phase transformation in Ti alloys has been studied by others for its relationship to spontaneous vitrification of the β-Ti bcc phase [9,10] and as a precursor to the precipitation of the α-Ti hcp phase [8].

Figure 4.4 (a) shows a TEM image of the Ti-40 Cr as-cast alloy, with a high density of the ω-phase aligned along the <111> directions. The ω particles are quite small (10-15 Å) and have a high density (10^{18}-10^{19} particles/cm^3). The beta [110] diffraction pattern in Figure 4.4 (b) has the characteristic diffuse "quasi-circular" streaking. The diffuse intensity arcs correspond to the octahedral sites of the reciprocal lattice (Figure 4.5) [11]. This can be explained by a 2/3<111> longitudinal displacement wave through the lattice, or by collapsing a pair of neighboring (111) planes to the intermediate position and leaving the next plane unaltered, and so on (Figure 4.6) [7,12]. The omega phase hardens and embrittles the beta phase by straining the matrix [13], and it cannot be avoided by rapid quenching.

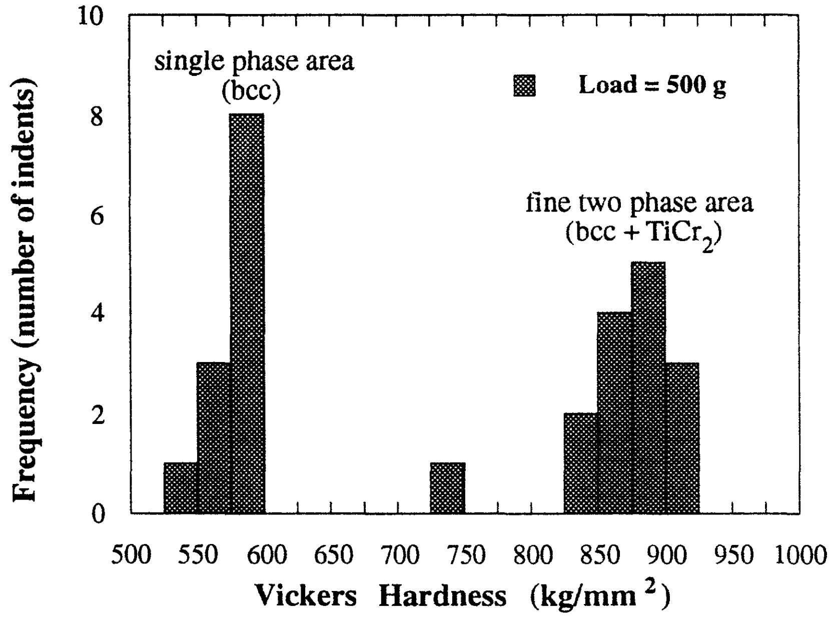

Figure 4.3 Plot of random microhardness indentations on the Ti-80 Cr alloy annealed at 1380°C.

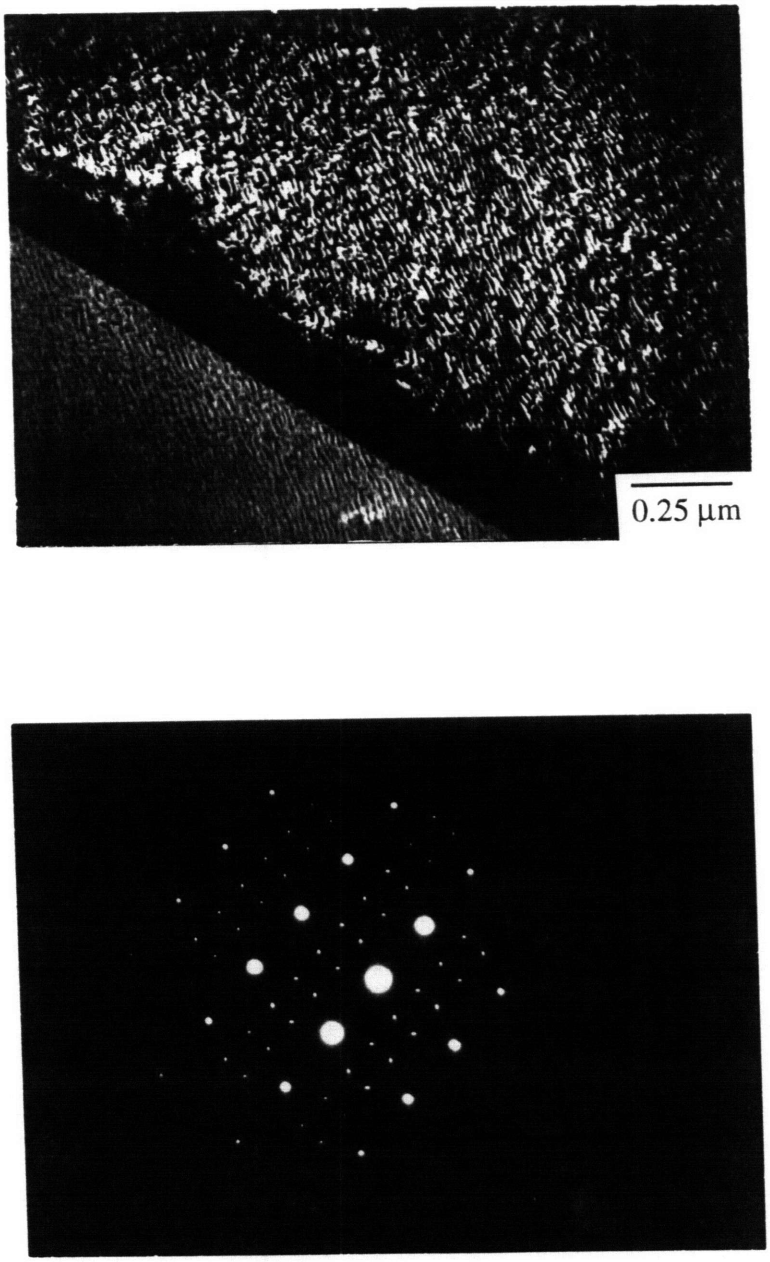

Figure 4.4 **(a)** TEM image of β-Ti(Cr) containing the omega (ω) phase. **(b)** The $[110]_\beta$ electron diffraction pattern with diffuse streaking.

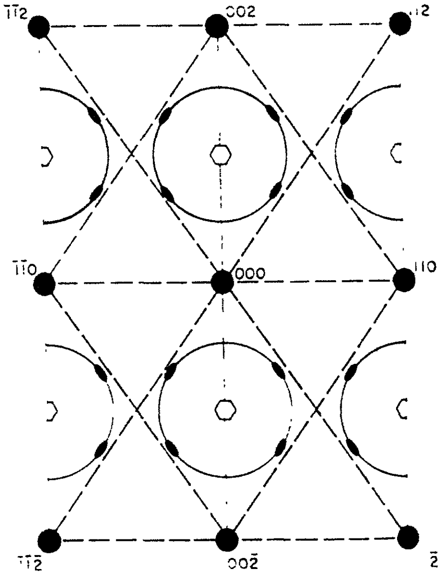

Figure 4.5 Reciprocal lattice section, $[110]_\beta$ zone normal, showing the ω reflections (filled ellipses) moved toward the octahedral sites and away from the dotted rectilinear streaks [11].

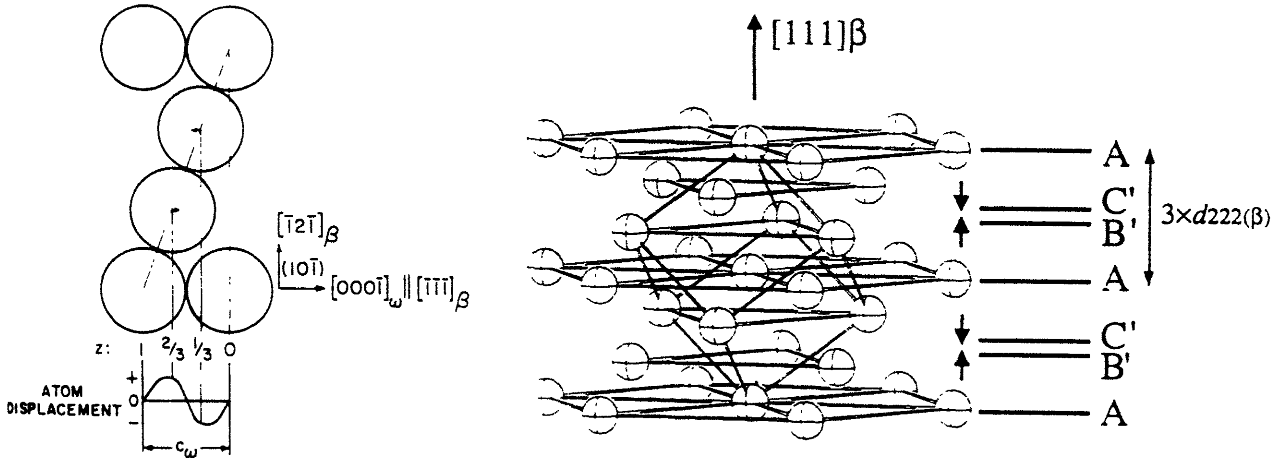

Figure 4.6 Formation of the omega phase. **(a)** A $(10\bar{1})$ section through the parent bcc unit cell. A 2/3<111> longitudinal displacement wave causes atomic motions (as indicated by the arrows) needed to form the ω phase. **(b)** Planes B' and C' move up and down respectively to coincide midway between the A planes to form the omega phase [7,12].

4.3.3 ANNEALED ALLOYS

4.3.3.a *Ti-rich alloys*

The Ti-30 Cr alloys have distinct lath-shaped $TiCr_2$ precipitates with an aspect ratio of about 10 to 1. Figures 4.7 and 4.8 show optical and SEM photographs of specimens annealed at 850°C and 950°C, respectively. A high density of precipitates is found along the grain boundaries, and the lath particles clearly show preferred orientations within each grain. The orientation relationship between the $TiCr_2$ precipitate and the bcc matrix is discussed in Section 4.4. The microstructure remained fairly constant among the different annealing treatments for this alloy. The volume fractions of the Laves phase decreased with increasing annealing temperatures, and matched the calculated values from the phase diagram, as seen in Table 4.2. The high temperature anneals also produced larger laths with sharper boundaries. TEM images of microstructures from a low and high temperature anneal are shown in Figure 4.9.

TEM also revealed dense dislocations in the matrix surrounding the Laves precipitates (Figure 4.10). These dislocations are thought to form during the quench after the heat treatment since most dislocations should be annealed out during the high-temperature anneals. Dislocations may be generated upon cooling due to the mismatch of thermal expansion coefficients of the matrix and the precipitate. The precipitates also consistently show contrast along the length of the lath, which results from a twin relationship of the two sides. Figure 4.11 shows parallel laths and the accompanying twinned $[110]_{C15}$ electron diffraction pattern. Within a set of parallel lath precipitates, the same orientation always occurred on the same side of the twin boundary.

Table 4.2 Annealing treatments of Ti-rich, two-phase alloys.

	Ti-30 Cr Laves volume%		Ti-40 Cr Laves volume%	
Temperature	(phase diagram)	(image analyzer)	(phase diagram)	(image analyzer)
800°C	28%		49%	47%
850°C	24%	24%	47%	
900°C	21%	20%	44%	
950°C	16%	16%	41%	36%
1000°C	10%		37%	47%?
1200°C	0%		9%	8%

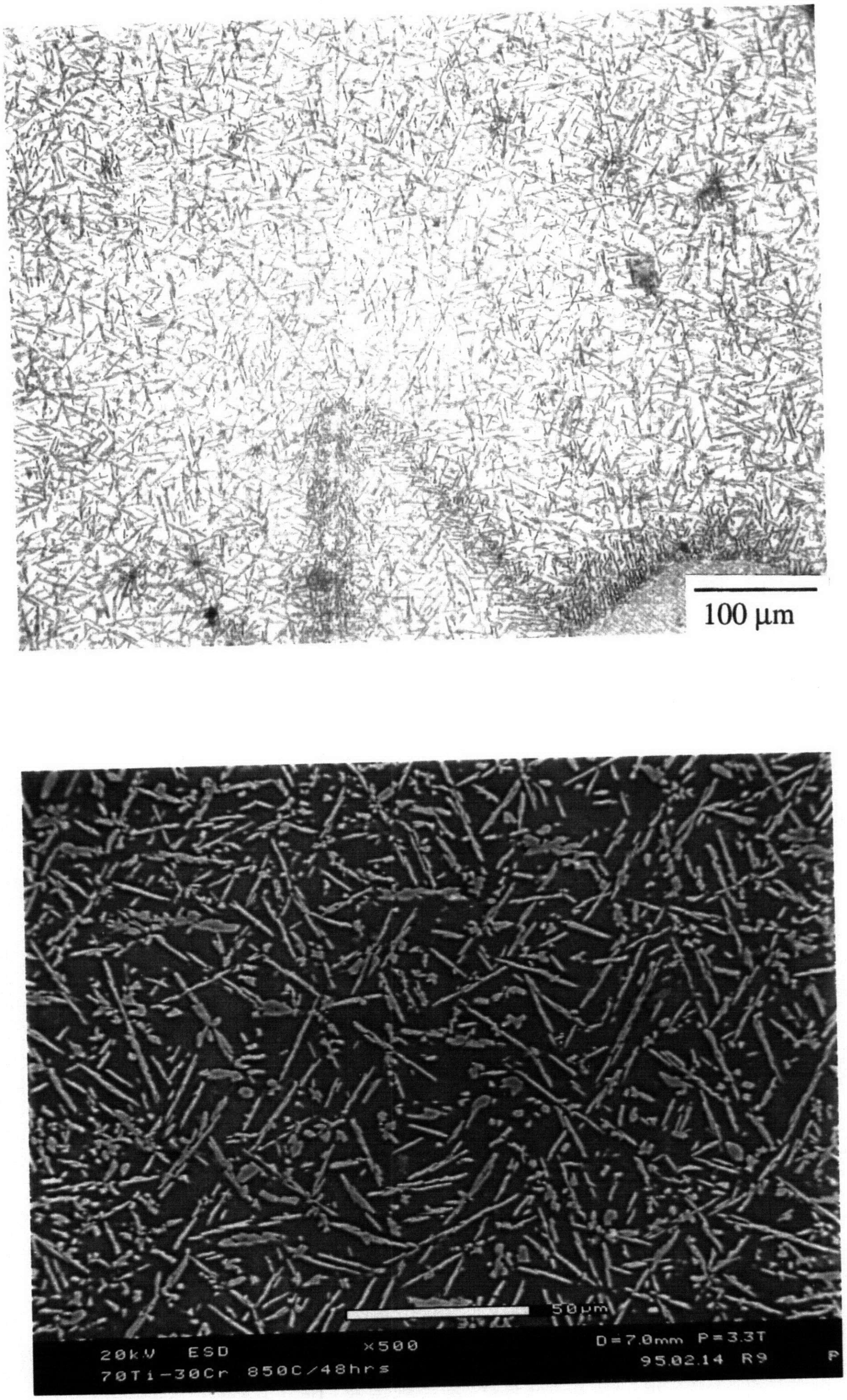

Figure 4.7 (**a**) Optical and (**b**) SEM micrographs of the Ti-30 Cr alloy annealed at 850°C and 48 hours.

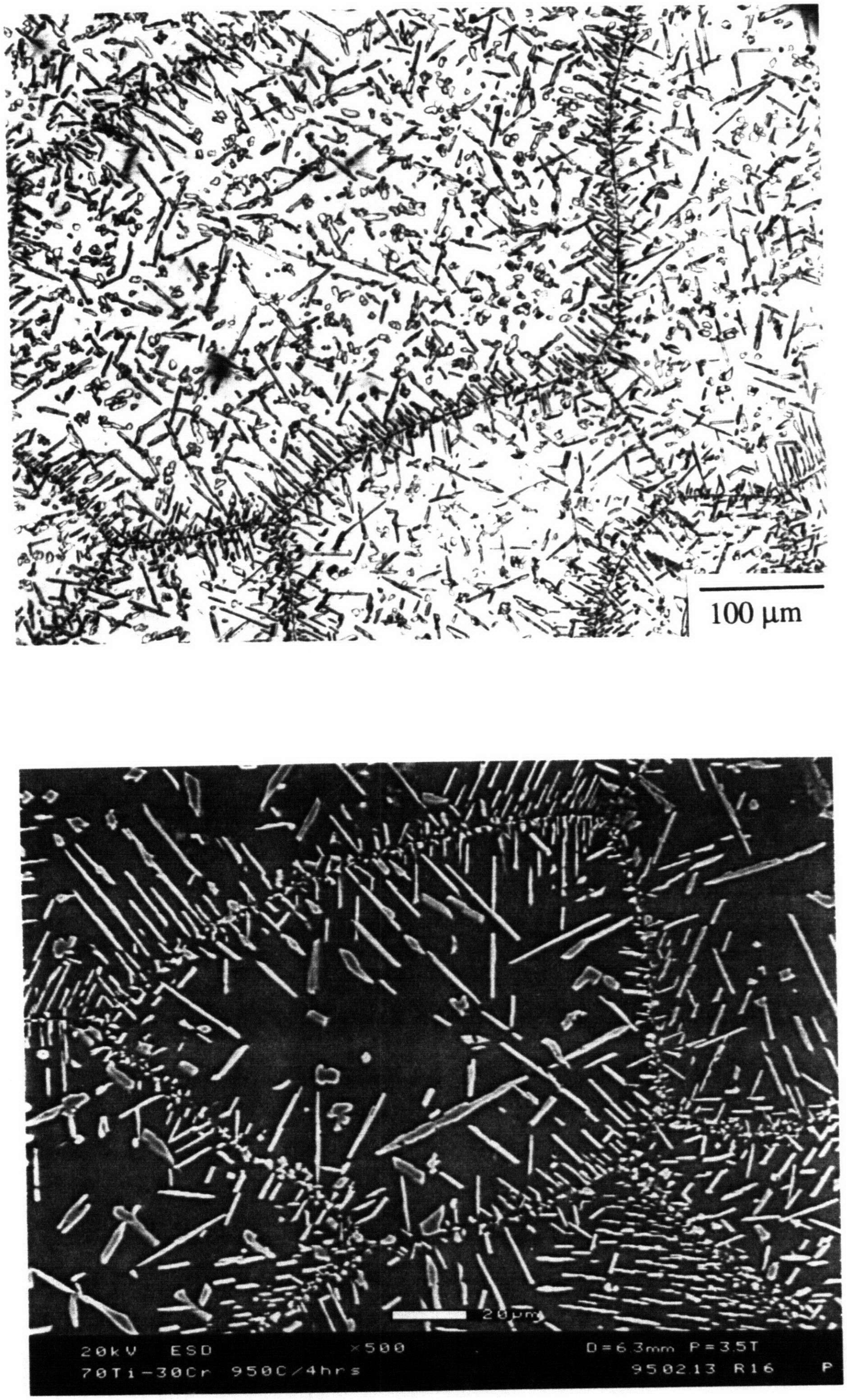

Figure 4.8 (**a**) Optical and (**b**) SEM micrographs of the Ti-30 Cr alloy annealed at 950°C and 24 hours.

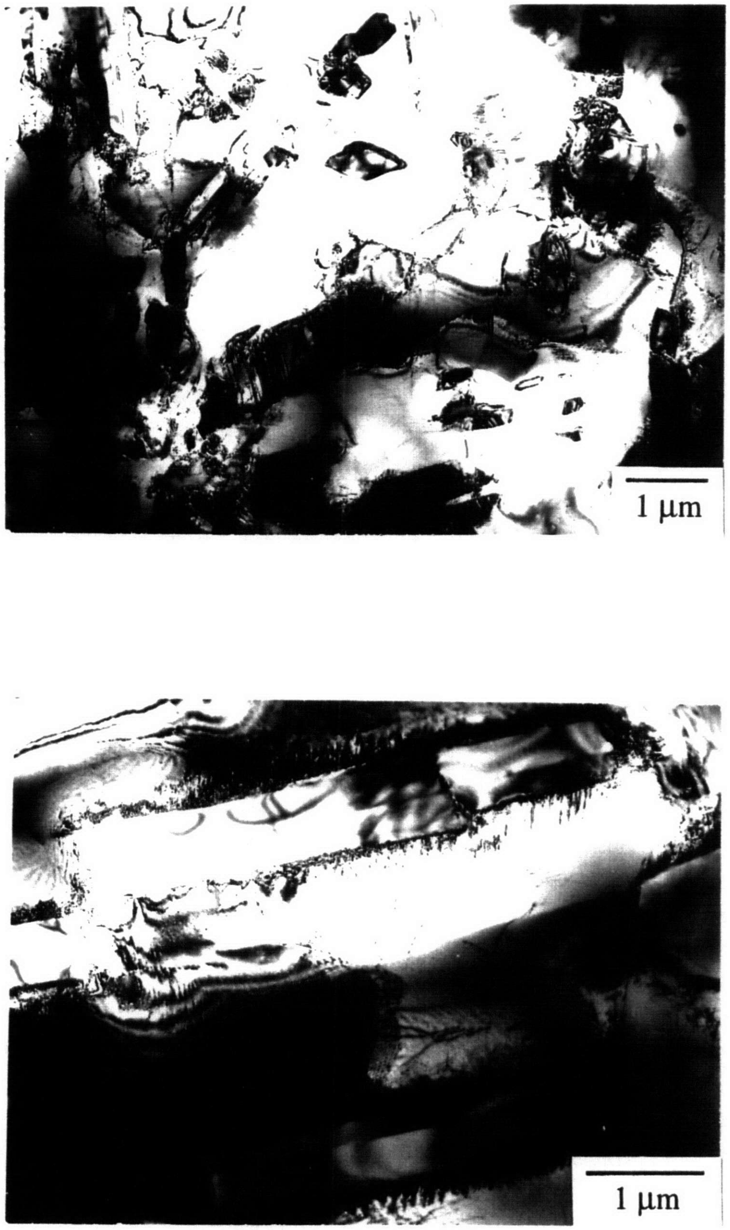

Figure 4.9 TEM images of the Ti-30 Cr alloy annealed at **(a)** low temperatures and **(b)** high temperatures.

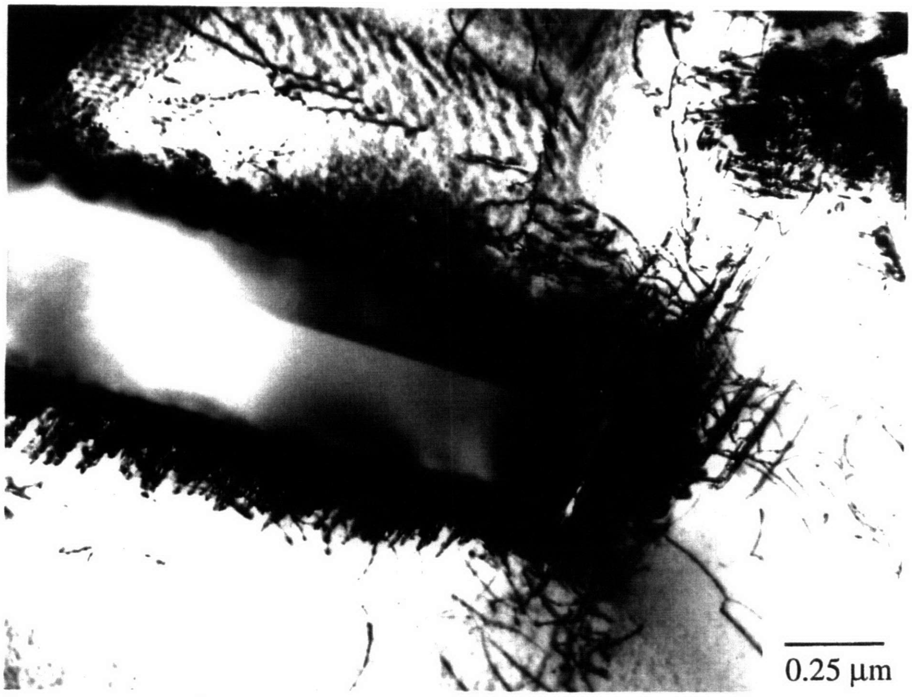

Figure 4.10 Dislocations surrounding the lath-shaped $TiCr_2$ precipitate.

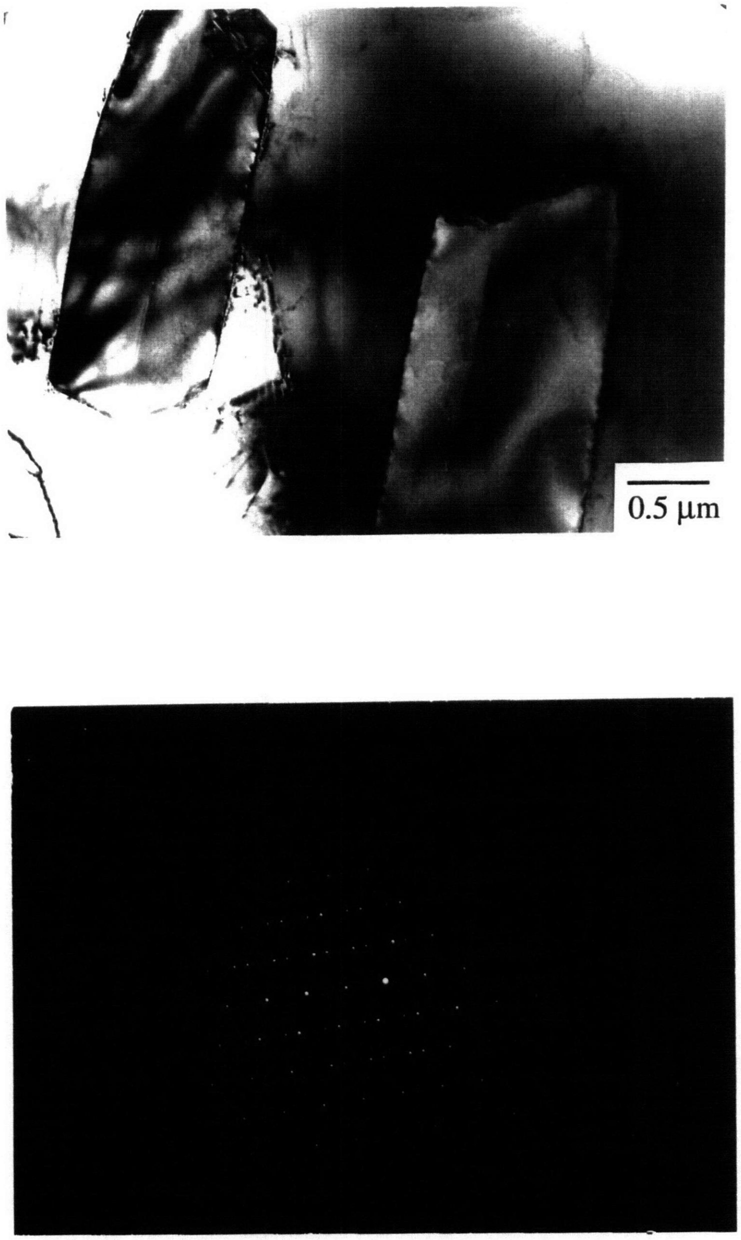

Figure 4.11 (**a**) Parallel twinned $TiCr_2$ precipitates and (**b**) the *C*15 [110] twinned diffraction pattern.

The Ti-40 Cr alloy had a markedly different microstructure. A bimodal distribution of equiaxed precipitates can be seen in Figure 4.12. Annealing at 1000°C for 24 hours, followed by air-cooling, produced large $TiCr_2$ precipitates about 10-15 μm in diameter and also submicron-sized precipitates. Again, precipitation was more extensive along the grain boundaries. Twin bands were also revealed by optical microscopy of etched samples.

Figure 4.13(a) illustrates how annealing treatments of the Ti-40 Cr alloy at lower temperatures also produced similar bimodal distributions of $TiCr_2$ precipitates. TEM showed that the smaller precipitates were heavily faulted, as seen in Figure 4.13(b). The source of the precipitate size differences may come from the initial clusters found in the as-cast material, rather than from additional precipitation from a supersaturated solid solution during the quench, (as used to form duplex structures in superalloys). The bimodal distribution persisted despite water quenching after the anneal. Annealing at 950°C for 168 hours produced a coarsened microstructure with very few of the small

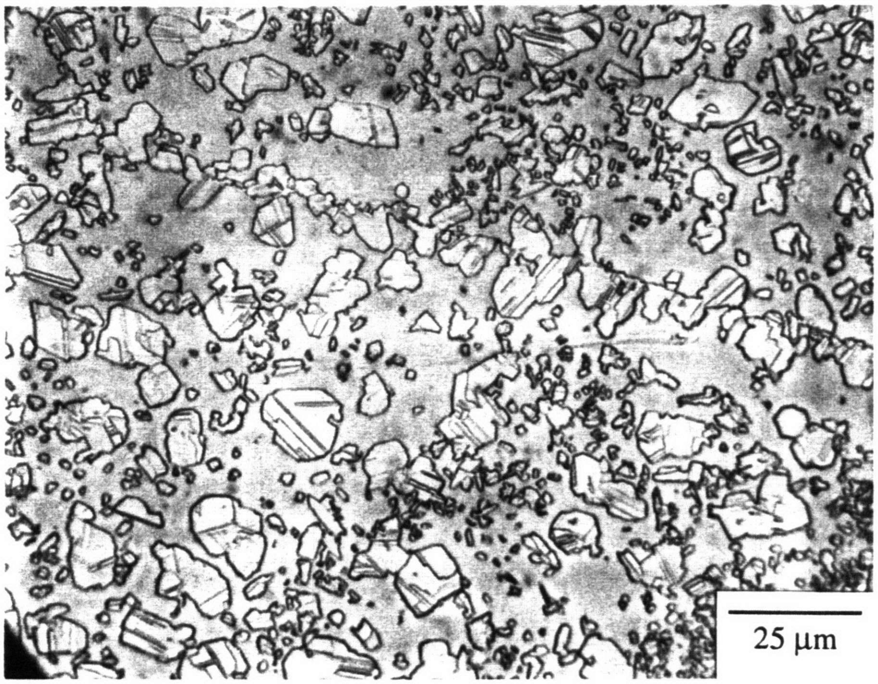

Figure 4.12 Bimodal distribution of equiaxed $TiCr_2$ precipitates in the Ti-40 Cr alloy annealed at 1000°C for 24 hours.

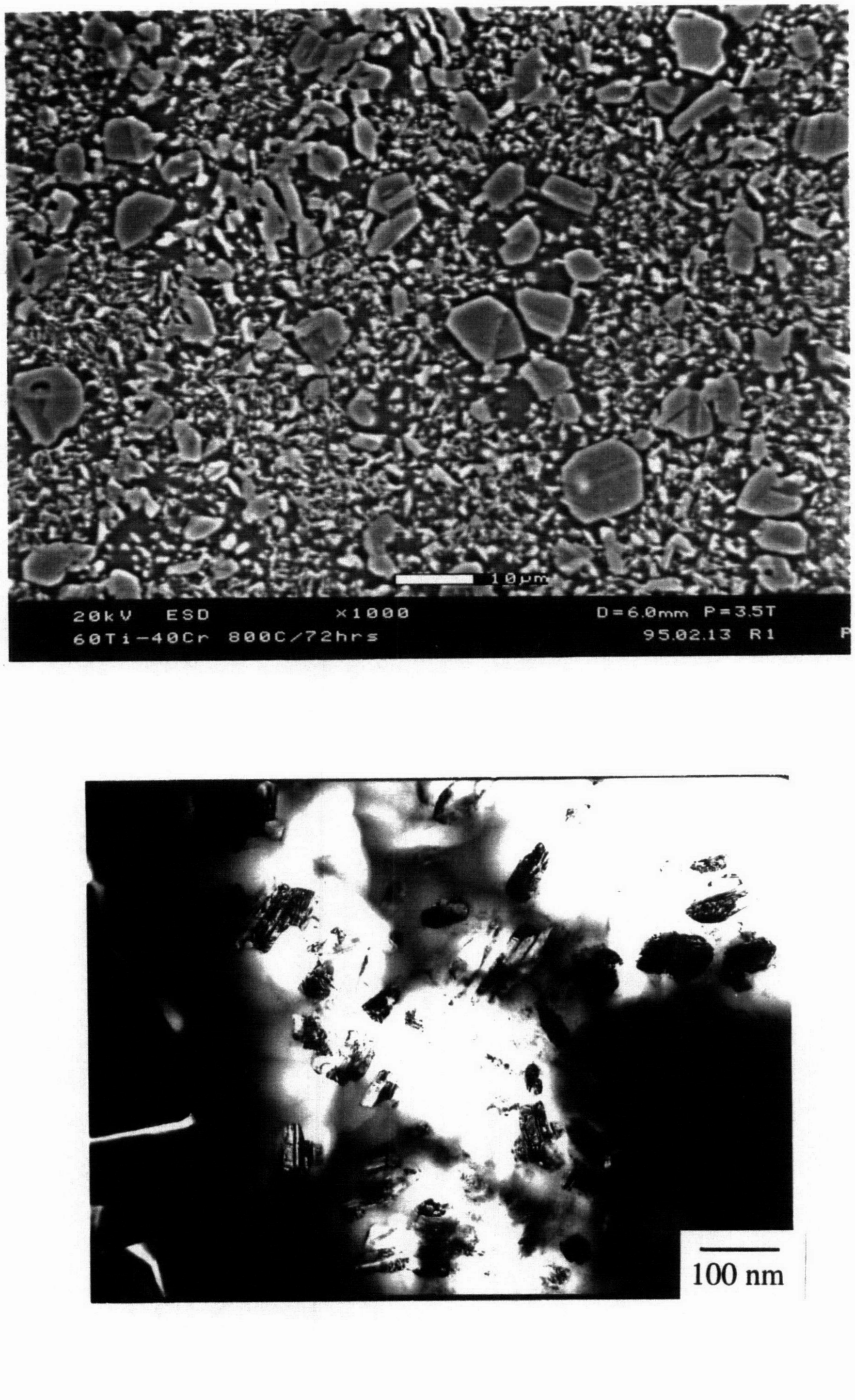

Figure 4.13 (**a**) SEM micrograph of the Ti-40 Cr alloy annealed at 800°C and (**b**) TEM of the small faulted precipitates.

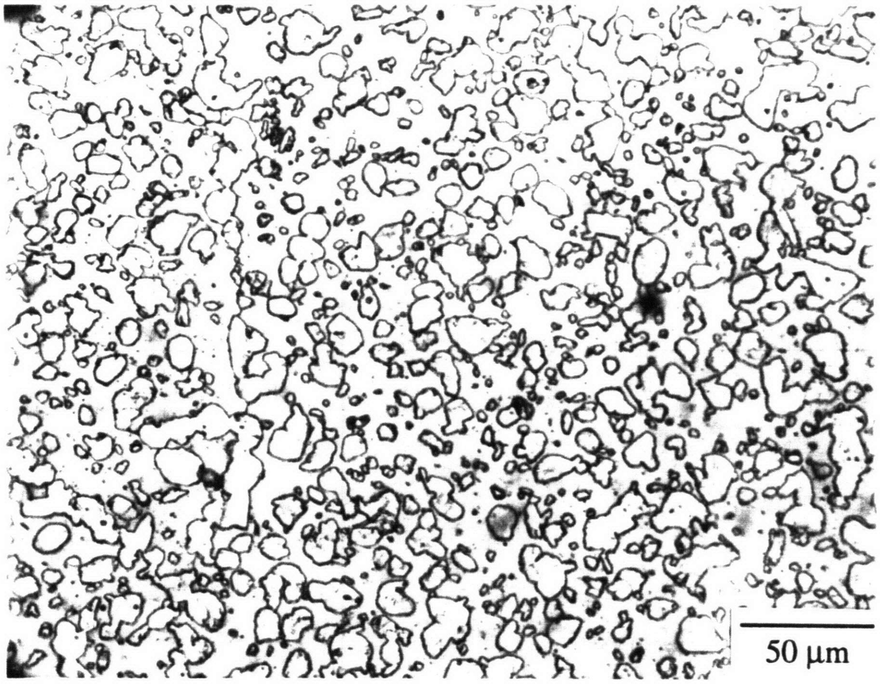

Figure 4.14 Coarsened microstructure of Ti-40 Cr at 950°C and 168 hours.

precipitates (Figure 4.14), suggesting that the smaller precipitates are indeed part of the equilibrium $TiCr_2$ forming at the annealing temperature. At longer annealing times, these smaller precipitates will dissolve according to coarsening laws. Coarsening effects are clearly demonstrated in Figure 4.15, where the number of small precipitates decreases as the annealing time increases, and the larger precipitates become larger. The combined volume fraction of the small and large precipitates also came close to those determined by the phase diagram.

Cuff et al. [14] show similar microstructures of large equiaxed $TiCr_2$ precipitates with twins, but no small precipitates are seen. The microstructure with lath-shaped precipitates in the Ti-30 Cr alloy has not been reported in the literature, although some lath-like morphologies have been reported. Elongated $TiCr_2$ in the growth direction of a bainite structure has been described by Lee and Aaronson in hypoeutectic Ti-Cr compositions [15], and proeutectic $TiCr_2$ has been reported as Widmanstatten plates by Aaronson et al. [16].

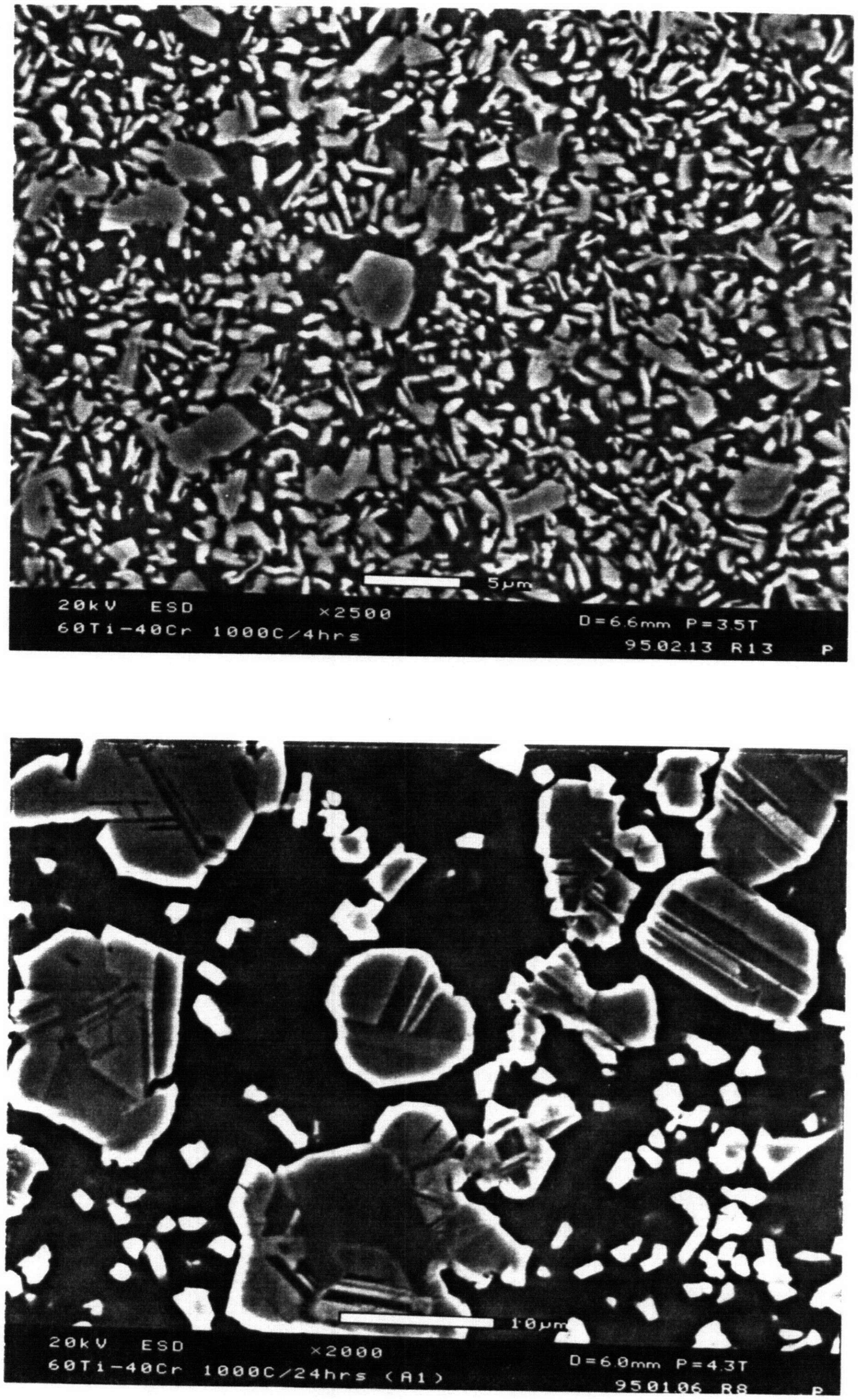

Figure 4.15 Coarsening effects over time in Ti-40 Cr at 1000°C for **(a)** 4 hours and **(b)** 24 hours.

The precipitate morphology difference between the two Ti-rich alloys is not entirely understood. Since both alloys at the same annealing temperature would have the same beta phase and $TiCr_2$ compositions, both alloys should have similar interfacial and misfit strain energies. The main difference between the two alloys at the same annealing temperature is the volume fraction of $TiCr_2$, and accordingly the Ti-40 Cr alloy has a larger driving force for precipitation. The volume fraction of the second phase can have some effect on the morphology of coherent precipitates [17]. The Ti-40 Cr alloy annealed at a high temperature (and thus having a lower volume fraction and driving force), produced more lath-like shaped precipitates, as seen in Figure 4.16. However, the crystal structure of these precipitates at 1200°C may be different than at lower temperatures, so caution must be exercised in making a comparison with Figure 4.8.

4.3.3.b *Twinning in Ti-rich alloys*

Twin bands in the large equiaxed $TiCr_2$ precipitates can be seen in Figure 4.17. The twinning conformed to the {111}<112> twinning system typically found in fcc crystals. Different variants of this twinning system could also be found within a single precipitate, as seen in Figure 4.18(a). The electron diffraction pattern in Figure 4.18(b) represents double twinning. Faulting and/or twinning on different {111} planes is indicative of the cubic *C*15 crystal structure, and can be used as a tool to help identify the crystal structure of the Laves phase using TEM images.

Twinning in $TiCr_2$ has been reported by many others as well [11,18]. Twinning has also been found in the $NbCr_2$ Laves phase. Chu [19] describes annealing twins forming by the accumulation of faceted $NbCr_2$ grain boundaries, while others suggest that the twinning occurs due to a *C*14 to *C*15 phase transformation [20]. The $TiCr_2$ in the Ti-rich alloys, however, are thought to have the *C*15 structure at the annealing temperatures and thus would not experience such a transformation. Also, the *C*14 to *C*15 transformation cannot explain the existence of more than one twin plane. An alternative explanation is that the twin might provide a mechanism for growth.

Twinned lath-like dendrites have been observed in germanium crystals [21,22]. Two {111} closely spaced twins propagate in the <112> direction as a flat strip with {111} flat surfaces rather than <100> rods. As seen in Figure 4.19 [23], the twinned {111} planes form a 141° re-entrant corner where nucleation can rapidly occur at the center of the groove, and atom layers can then spread over the entire face of the groove quickly. Figure 4.20 shows a TEM "edge-on" view of a twinned $TiCr_2$ precipitate with a 141° groove. The re-entrant corner formed by the twin allows for fast growth along the <112>

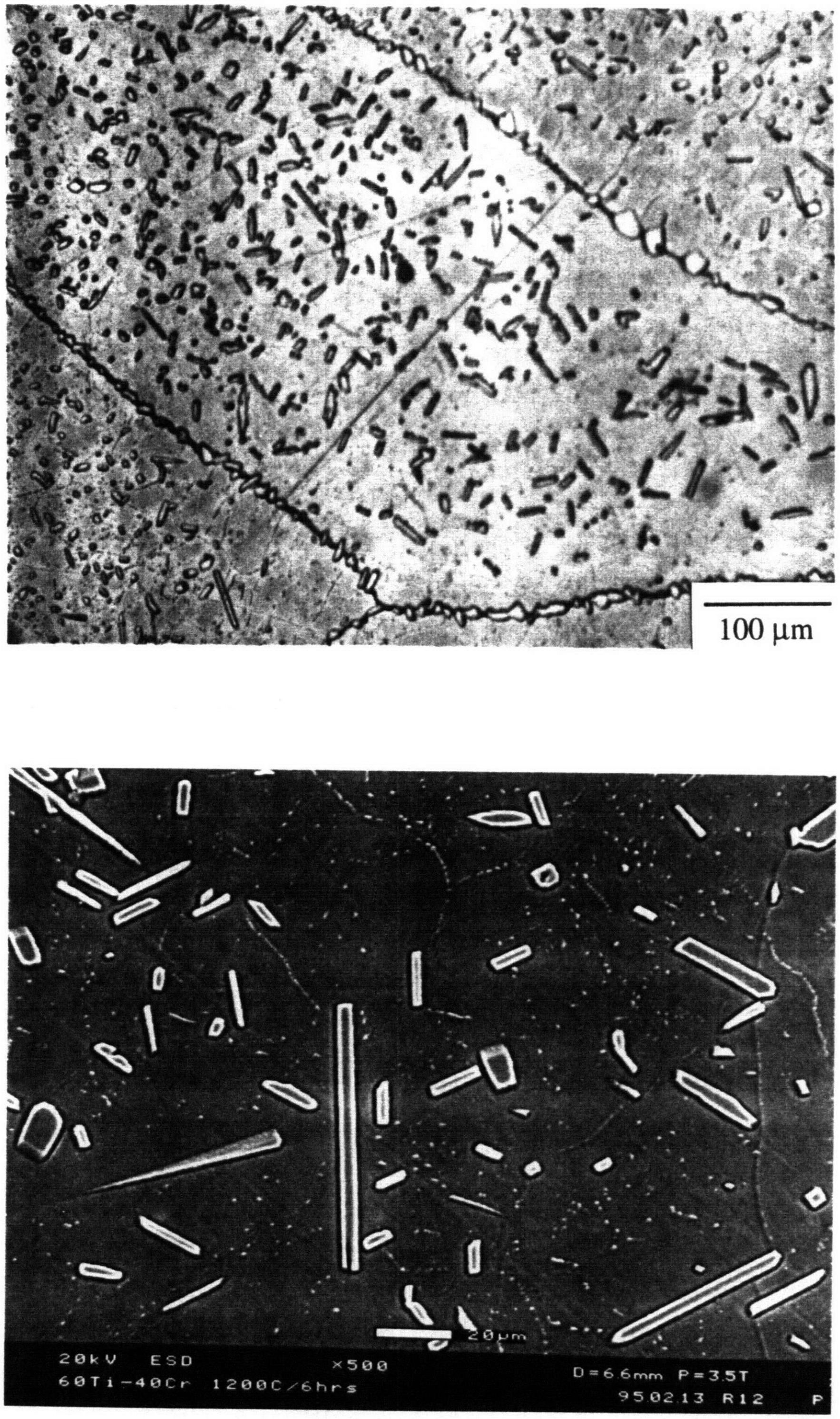

Figure 4.16 (**a**) Optical and (**b**) SEM micrograph of lath-like $TiCr_2$ precipitates in the Ti-40 Cr alloy at 1200°C and 6 hours.

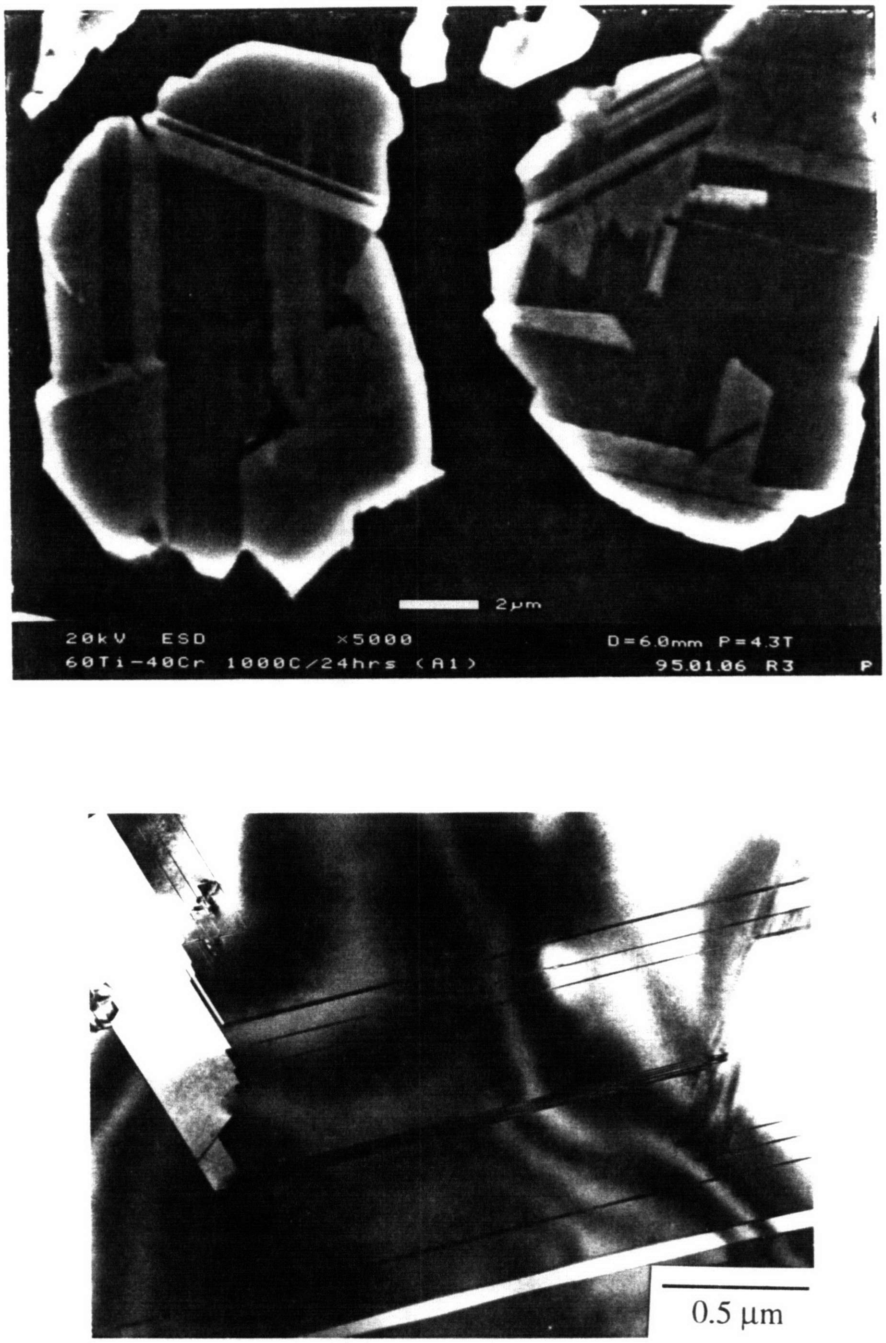

Figure 4.17 Large twin bands by **(a)** SEM and **(b)** TEM in the Ti-40 Cr alloy.

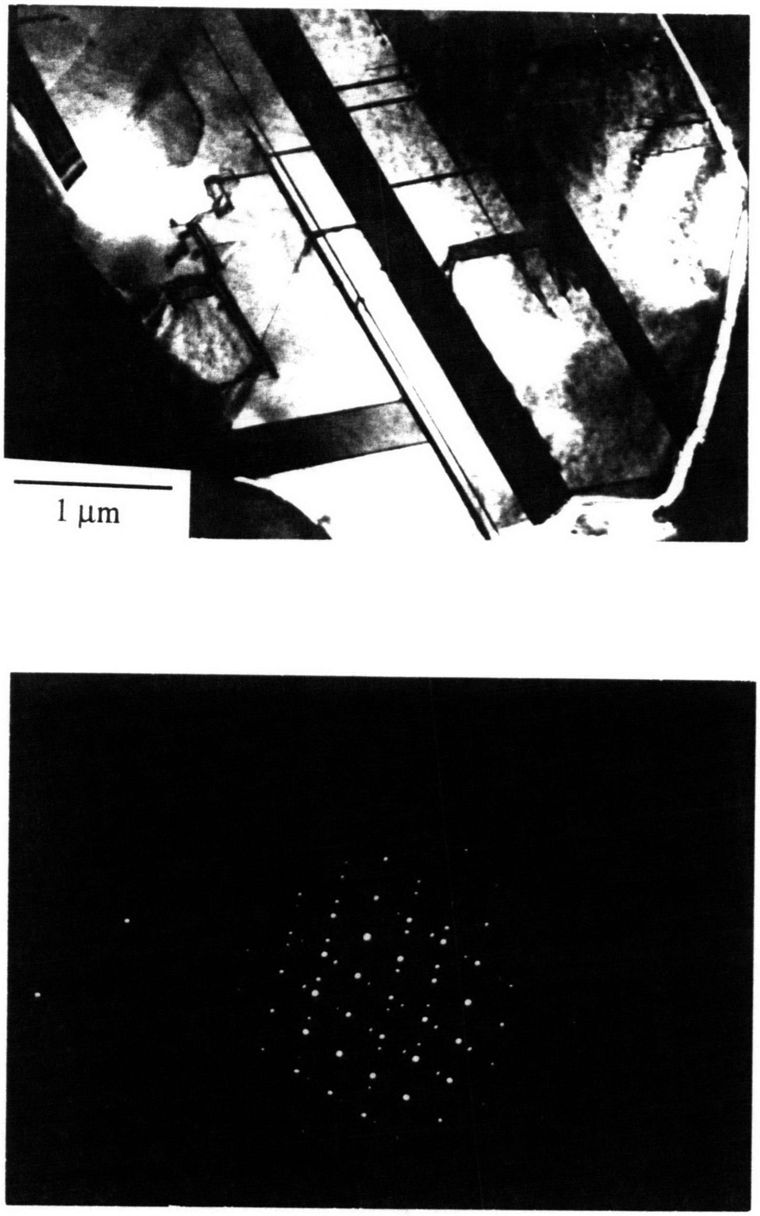

Figure 4.18 (**a**) TEM image of different variants of twinning and (**b**) double twinning diffraction pattern in $C15$ $TiCr_2$.

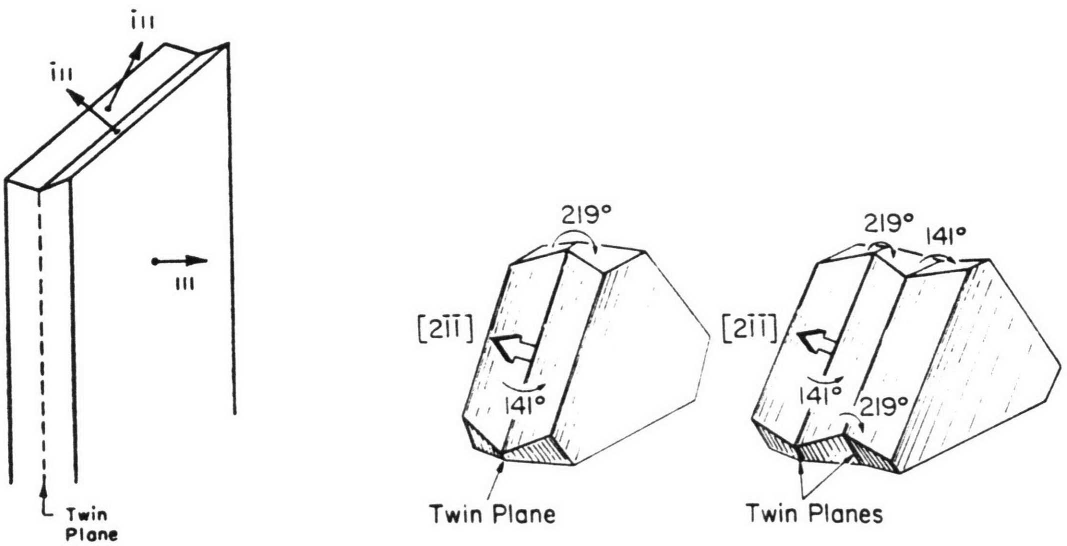

Figure 4.19 Schematic of dendrite tip-morphology and angles between crystal faces for lath-like dendrites of Ge and Si containing twin planes [21,23].

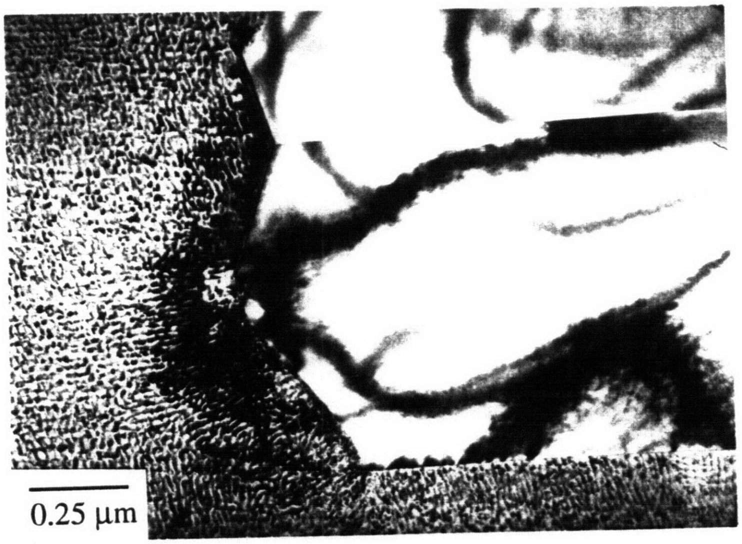

Figure 4.20 TEM image of twinned $TiCr_2$ precipitate with a 141° re-entrant corner groove.

direction, and results from a balance between the minimum radius of curvature at the dendrite tip and the minimum undercooling [23]. Twinned embryos have also been proposed for the precipitation of twinned rods in Cu-Zn alloy [24]. The twinned lath precipitates of the Ti-30 Cr alloy may also form by similar mechanisms.

4.3.3.c *Cr-rich alloys*

Table 4.3 lists the heat treatments of the Ti-80 Cr and Ti-87.5 Cr alloys and the corresponding mean intercept spacing. The microstructures of the Cr-rich alloys are on a much finer scale than the Ti-rich alloys and resemble eutectic and discontinuous precipitation structures, as can be seen in Figures 4.21-4.23. The fine eutectoid-like microstructures may result from the slow diffusion found in the Cr-rich alloys. The cellular precipitation found in the as-cast Ti-80 Cr alloy indicates that even at high annealing temperatures, the precipitation mechanism adopted is one that is usually found at low temperatures with low driving forces and more sluggish kinetics. Although the Cr-rich alloys could not be etched by the same solution used for the Ti-rich alloys, contrast between the two phases could be distinguished by SEM, with the darker phase being the $TiCr_2$ Laves phase. Microstructures of the eutectic Cr(bcc)+$NbCr_2$ alloy are very similar [20]. Alternating plates of the bcc and Laves phase form a lamellar structure in both systems.

Table 4.3 Annealing treatments of Cr-rich, two-phase alloys.

Alloy	Heat Treatment	Laves phase volume % phase diagram	Laves phase volume % image analyzer	mean intercept spacing (μm)
Ti-80 Cr	as-cast	0%	?	0.5 μm
Ti-87.5 Cr	as-cast	0%	0%	---
Ti-80 Cr	1200°C/1 hr	35%	85%?	1.3 μm
Ti-80 Cr	1200°C/6 hr	35%	35%	2.5 μm
Ti-80 Cr	1000°C/24 hrs	48%	40%	1.8 μm
Ti-87.5 Cr	1000°C/500 hrs	20%	25%	1.2 μm

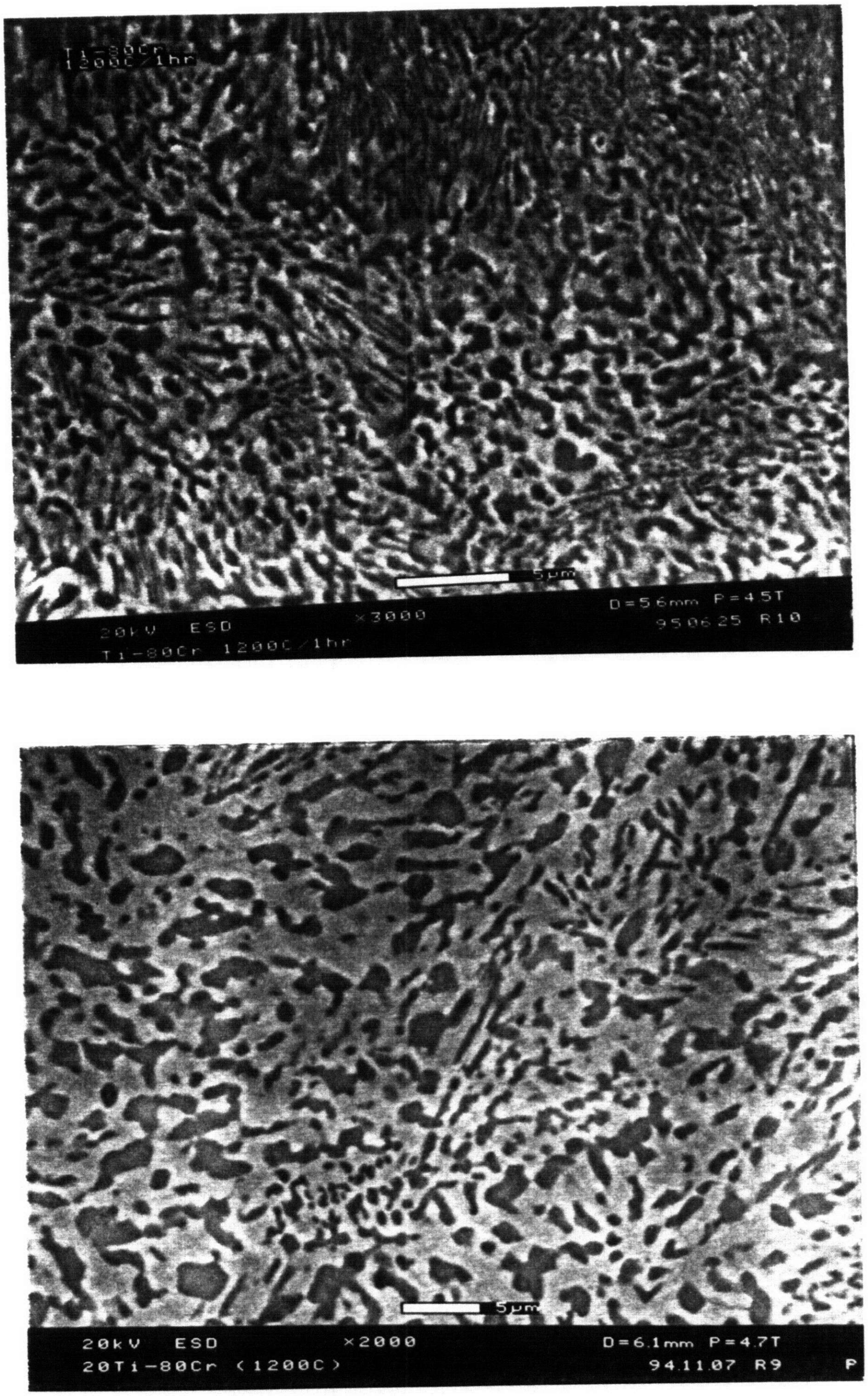

Figure 4.21 SEM of the Ti-80 Cr alloy annealed at 1200°C for **(a)** 1 hour and **(b)** 6 hours.

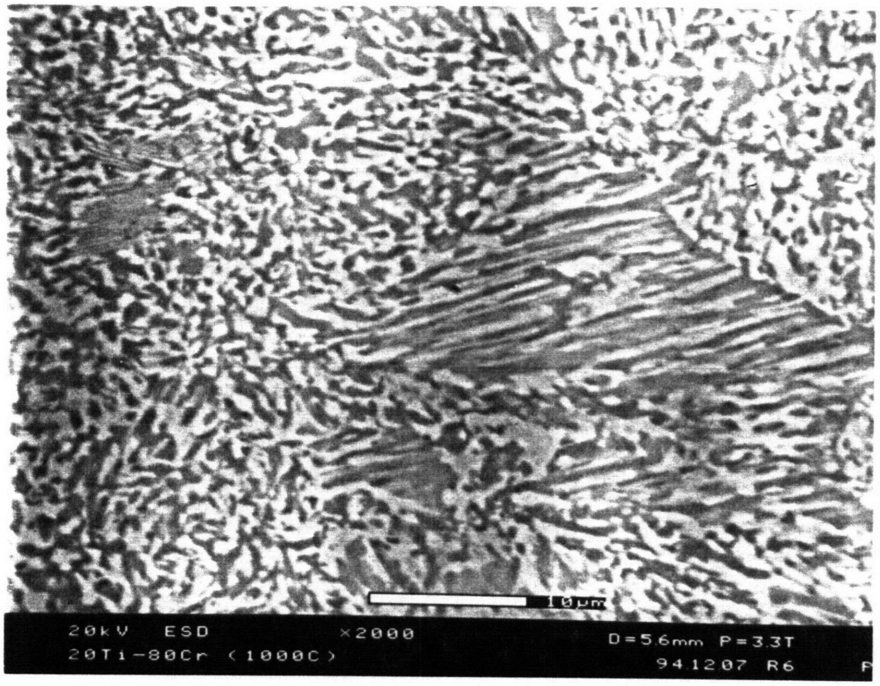

Figure 4.22 SEM of the Ti-80 Cr alloy annealed at 1000°C and 24 hours.

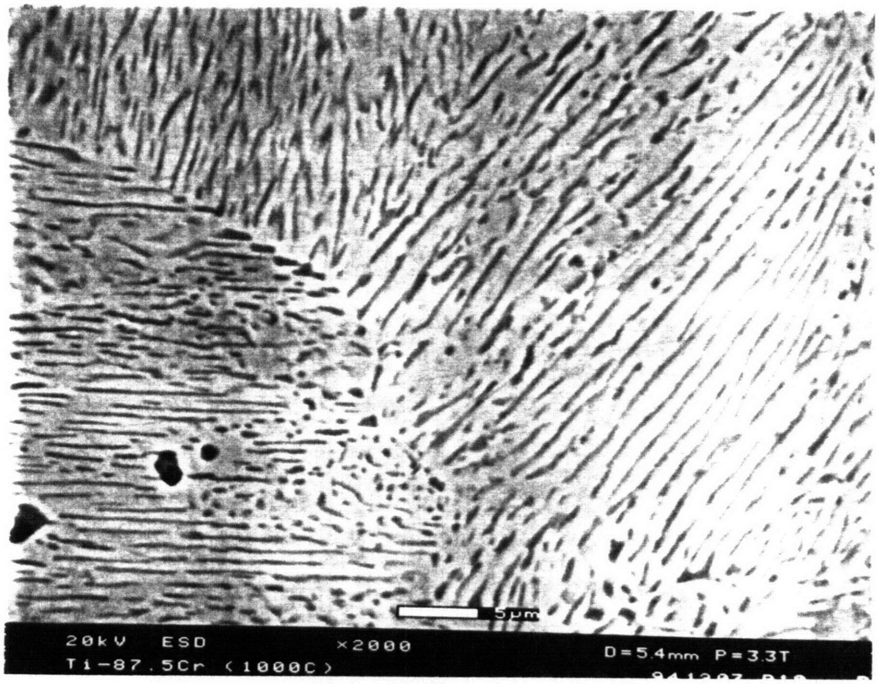

Figure 4.23 SEM of the Ti-87.5 Cr alloy annealed at 1000°C and 500 hours.

Coarsening of the $TiCr_2$ precipitates in the Ti-80 Cr alloy after annealing at 1200°C is shown in Figure 4.21. The $TiCr_2$ phase in the Ti-80 Cr alloy at 1200°C for 6 hours (Figure 4.21(b)) is more disconnected, but sets of distinct precipitates were often in the same orientation, as seen by TEM in Figure 4.24. The faulting in the Laves phase was generally only on one plane, suggesting a hexagonal crystal structure. However, some partial dislocations could also be found (Figure 4.25(a)), indicating some non-basal defects. Liu [25] has identified hexagonal non-basal faults that are bounded by such partials. The electron diffraction pattern indexed as $[11\bar{2}0]_{C14}$ in Figure 4.25(b) shows streaking in the [0001] direction, consistent with the heavy faulting. The streaking also suggests that the Laves phase may be in the midst of a transformation, possibly *C*14 to *C*36, which is the equilibrium structure deduced from the single-phase $TiCr_2$ behavior at 1200°C.

Figure 4.26 demonstrates how the Laves phase in the Ti-80 Cr alloy annealed at 1000°C samples was more interconnected than the alloy annealed at 1200°C. The Ti-87.5 Cr alloy was quite similar, except that the Laves volume fraction was much lower (Figure 4.27). Figure 4.28 shows how the faults could run along the length of the lamella or at an angle to the lamellar structure. The diffraction pattern was again streaked, making crystal structure determination difficult.

Figure 4.24 TEM of the Ti-80 Cr annealed at 1200°C. Some of the distinct $TiCr_2$ precipitates have the same orientation.

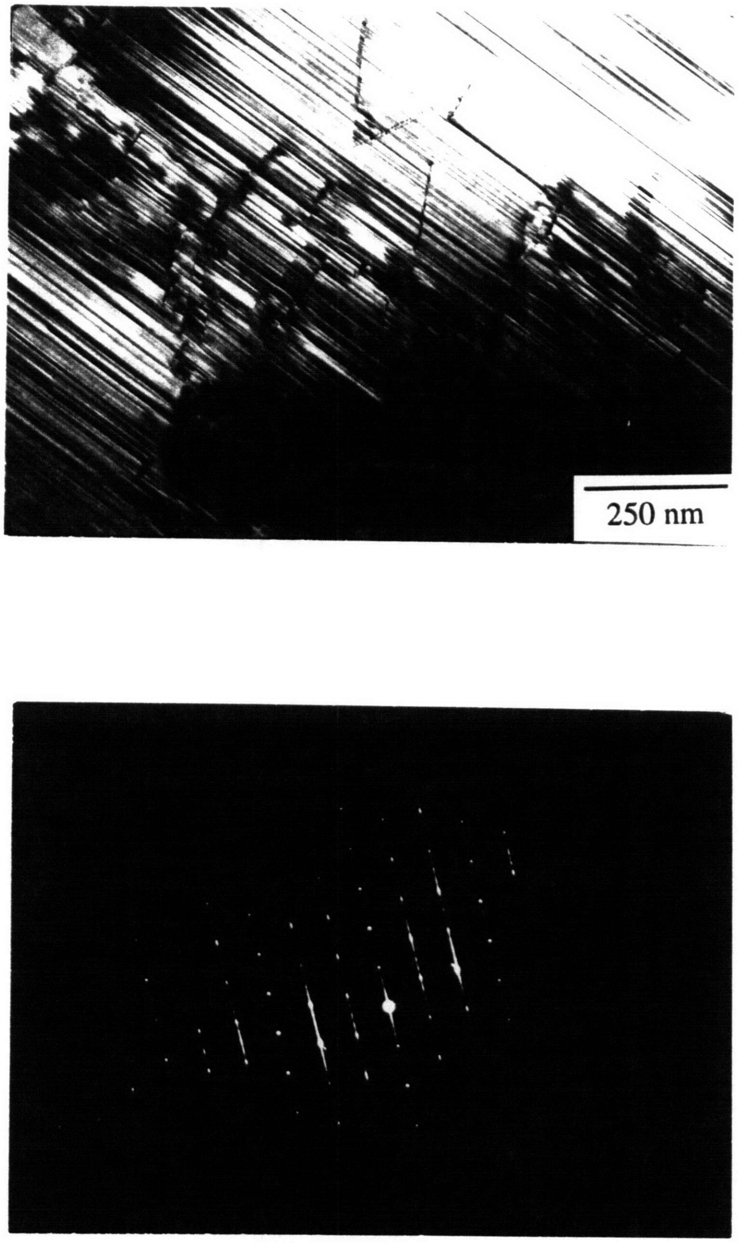

Figure 4.25 **(a)** Heavy faulting on the basal plane with some partial dislocations. **(b)** Streaking in the $[11\bar{2}0]_{C14}$ diffraction pattern.

Figure 4.26 The $TiCr_2$ Laves phase in the Ti-80 Cr alloy annealed at 1000°C is interconnected.

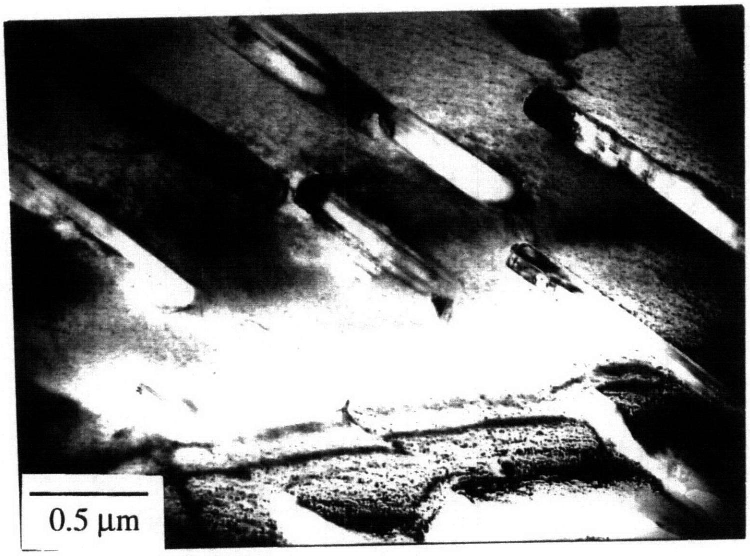

Figure 4.27 TEM of the Ti-87.5 Cr alloy annealed at 1000°C.

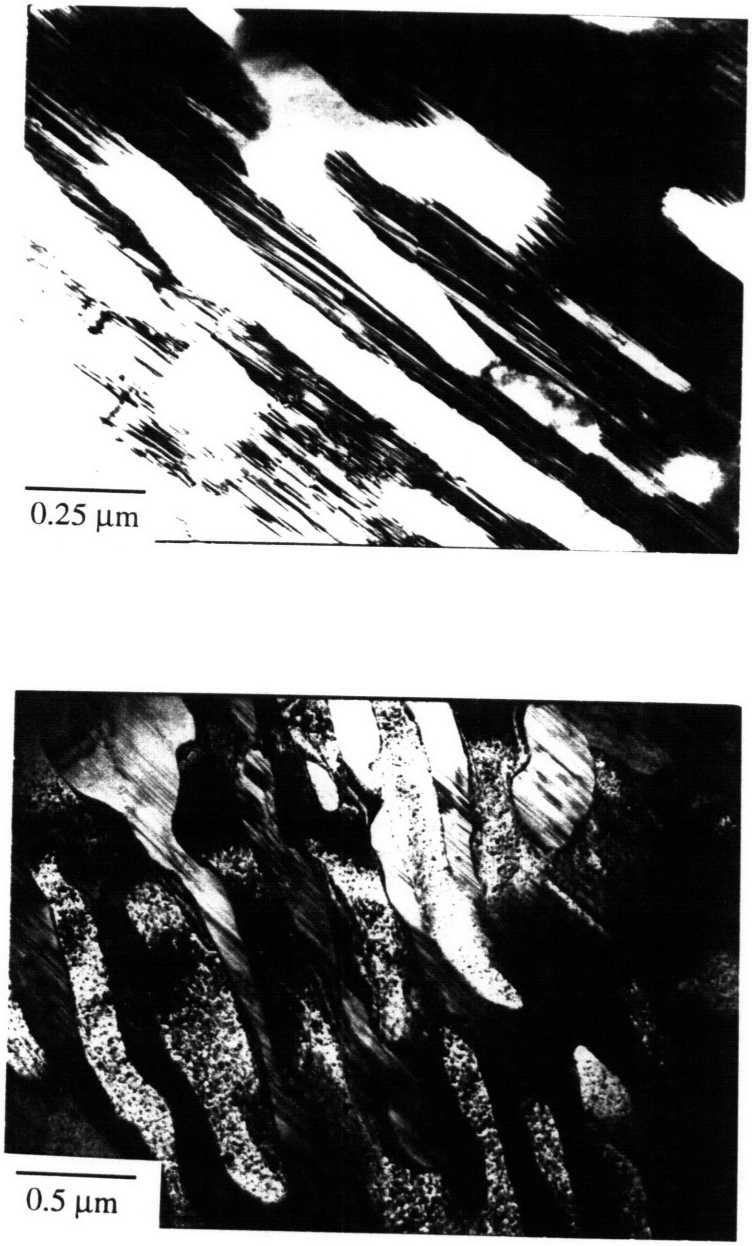

Figure 4.28 TEM of faults **(a)** along and **(b)** at an angle to the lamellar $TiCr_2$ structure.

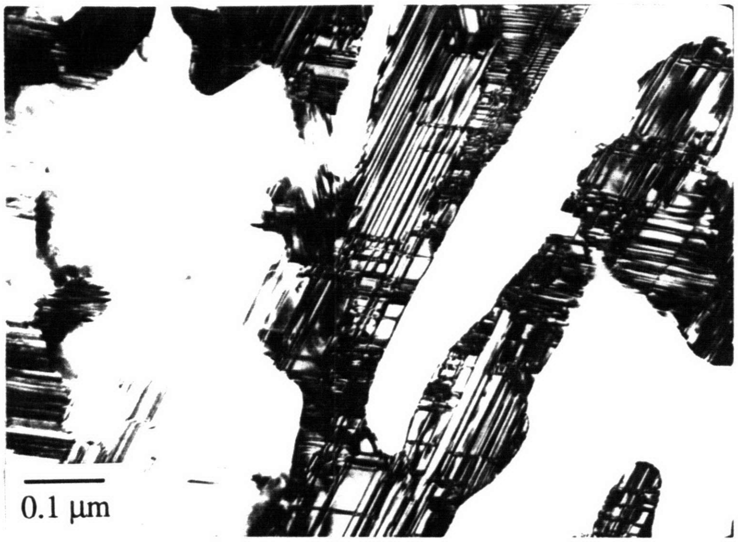

Figure 4.29 Faulting on more than one variant of planes in the Ti-80 Cr alloy annealed at 1000°C.

Occasionally, faulting could be detected in more than one direction (Figure 4.29), hinting at the cubic *C*15 crystal structure at 1000°C. The current phase diagram indicates that on the Cr-rich side of $TiCr_2$, the *C*15 Laves crystal structure is not at equilibrium until 800°C, which is contrary to our results on single-phase $TiCr_2$ in Chapter 2. The *C*36 to *C*15 transformation was found to be very sluggish for Cr-rich compositions, and the *C*15 structure was suggested to be the equilibrium structure at 1000°C. The TEM image of the characteristic *C*15 structure at 1000°C for the Cr-rich alloy supports such an interpretation. The slow diffusion rates in the Cr-rich alloys may be preventing the equilibrium structure from being achieved at these heat treatments.

4.4 ORIENTATION RELATIONSHIPS

4.4.1 Literature Review

The connection between precipitate shape and orientation relationship in a solid has been addressed by several investigators. Dahmen [26] contends that the precipitate grows along the crystallographic invariant line, a direction of zero misfit determined by a transformation strain and lattice rotation from an initial lattice correspondence that follows the phenomenological theory of martensitic transformations [27]. Khachaturyan [28] purports that the habit plane is selected by minimizing an explicit expression for strain energy. A ledge mechanism is advanced by Aaronson [29], where the precipitate shape depends on the anisotropy of boundary mobility. Combinations of these ideas have been used to predict the growth direction and habit planes of lath-shaped precipitates [30-32].

4.4.2 Experimental Procedures

The orientation relationship between the Laves phase and the bcc matrix was determined by TEM. The sample was first tilted to a low index zone axis of the matrix phase. Selected area diffraction (SAD) about the precipitate/matrix interface and SAD of the individual phases were taken. The specimen was then tilted in a known direction in the matrix, via Kikuchi bands, to another zone axis where the requisite electron diffraction patterns were again recorded. The first set of zone axes for each phase was determined and the diffraction patterns were indexed. For the superimposed pattern (containing diffraction spots from both the precipitate and matrix), the orientation relationship could then be quoted as parallel directions and planes from parallel rows of indexed spots in both phases. The second set of diffraction patterns was indexed in a consistent manner according to the tilting, and was used to check for crystallographic equivalence to the previous set of diffraction patterns.

4.4.3 Results

The broad, straight edges of the lath precipitates along particular orientations suggest some degree of coherency between the $C15$ $TiCr_2$ Laves phase and the bcc matrix in the Ti-30 Cr alloy. Different sets of electron diffraction patterns of both phases are displayed and indexed in Figure D.1(a-c) in Appendix D. Because both phases are cubic, indices of parallel planes are also indices of parallel directions. The orientation relationship found can be expressed by parallel close-packed planes and a parallel direction within those planes:

$$(101)_\beta \,||\, (111)_{C15}$$
$$[10\bar{1}]_\beta \,||\, [10\bar{1}]_{C15}$$

Or, the same orientation relationship can be expressed as two sets of parallel planes with the closest d-spacings:

$$(020)_\beta \,||\, (\bar{1}2\bar{1})_{C15}$$
$$(10\bar{1})_\beta \,||\, (10\bar{1})_{C15}$$

The zone axes of the bcc phase and the $C15$ Laves phase reported above are within a few degrees of each other. Two different variants of the Laves habit plane were $(\bar{1}11)$ and $(11\bar{1})$, which were near the $(\bar{1}12)$ and $(21\bar{1})$ planes of the bcc beta phase. Interestingly, Fehrenbach [33] gives the orientation of $C15$ $CuMg_2$ with fcc Cu as :

$$(111)_{fcc} \,||\, (111)_{C15}$$
$$[110]_{fcc} \,||\, [112]_{C15}$$

Transposing the bcc to $C15$ to fcc gives the Nishiyama-Wassermann orientation for bcc-fcc systems.

The above orientation relationship is between the bcc matrix and only one side of the $C15$ lath precipitate, the parent twin. The other side of the lath has the {111}<112> twin relationship to the parent twin, yet does not have other matchings of planes and direction with the bcc phase. In the $V+V_3N$ system, twinning of the precipitate plates has been proposed to result from the restraints of the matrix and to average out the mismatch [34].

The habit plane of the lath precipitates was often parallel to the twin boundary that ran along the length of the lath. Table D.1 in Appendix D lists some of the d-spacings of the beta and Laves phase. The habit planes, $\{111\}_{C15}$ and $\{112\}_\beta$, have only a 2.3% lattice mismatch. Bewlay, et. al [35] have also found $(333)_{C15}$ and $(211)_{Nb}$ to be parallel to the interface plane in the Nb(bcc)+$NbCr_2$ system.

Bywater and Dyson [36] have asserted that precipitate growth will proceed in the direction of small mismatch, which Dahmen terms the "invariant line" [37]. Figure 4.30 shows how the habit planes of the two phases may match up. Given the $(21\bar{1})$ plane of the beta-phase and the $(11\bar{1})$ plane of the Laves phase, two sets of possible growth directions are tested for mismatch by assuming a hard-sphere model and computing the ideal lattice parameter ratio of the bcc and Laves phase. By comparing to the actual lattice constant ratio (a_{C15}/a_{bcc}), one can reason a growth direction due to better fitting. For the parallel $[\bar{1}1\bar{1}]_\beta$ and $[\bar{1}0\bar{1}]_{C15}$ directions:

$$\sqrt{3}/2\, a_{bcc} = \sqrt{2}/2 a_{C15} \tag{4.1}$$

$$a_{C15}/a_{bcc} = 1.22$$

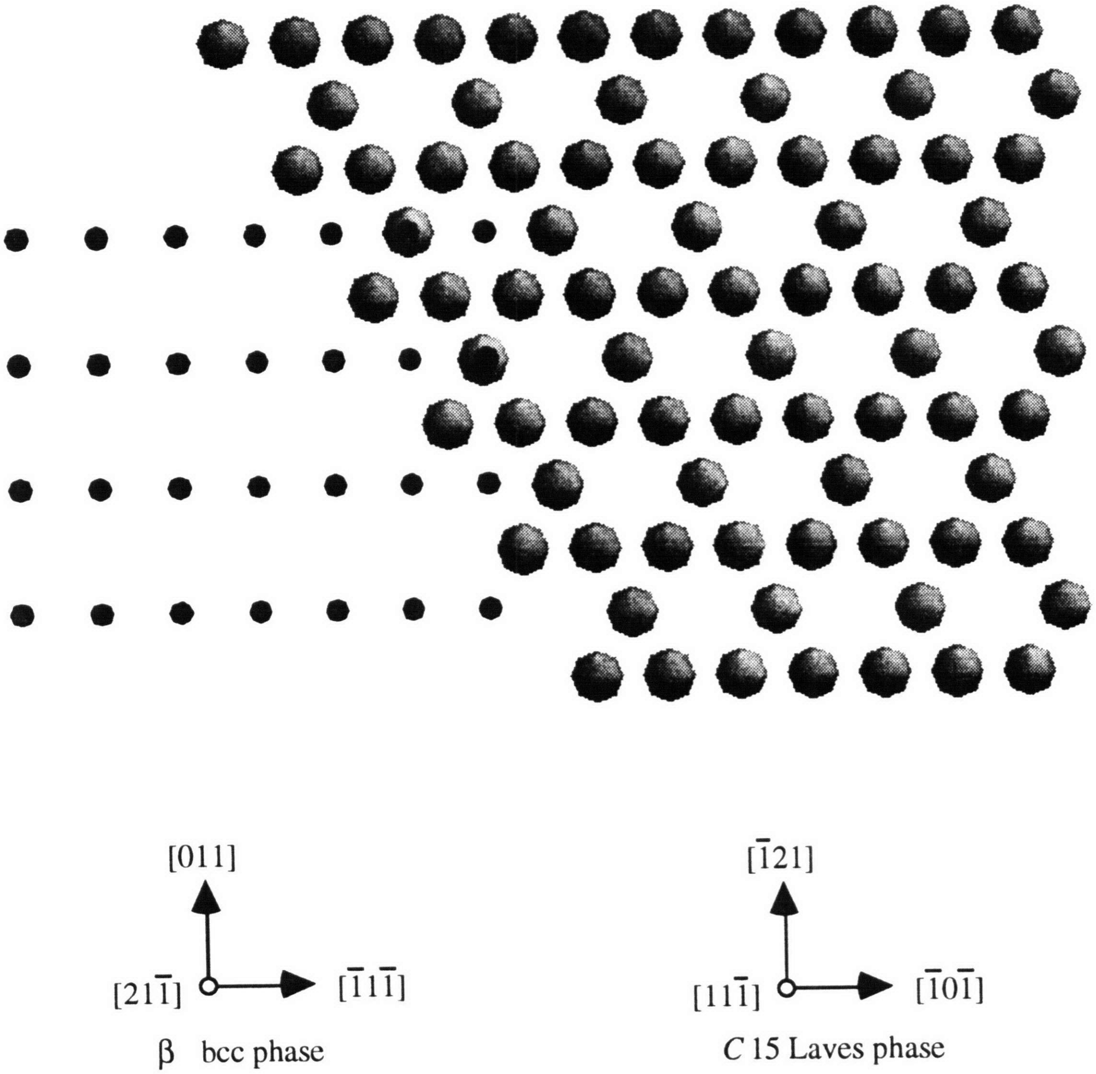

Figure 4.30 The $(21\bar{1})_\beta$ and $(11\bar{1})_{C15}$ habit planes.

and for $[011]_{\beta}$ and $[\bar{1}21]_{C15}$:

$$\sqrt{2}\, a_{bcc} = \sqrt{6}/2\, a_{C15} \tag{4.2}$$

$$a_{C15} / a_{bcc} = 1.15.$$

From the experimentally determined lattice parameters, $a_{C15} / 2a_{bcc} = 1.08$, and thus $[\bar{1}21]_{C15}$ should be the precipitate growth direction. This is the same direction suggested by the twinned dendrite model discussed in section 4.3.3.b. Figure 4.31 is a model of the interface between the habit planes and along the $[\bar{1}21]_{C15}$ direction. The *C*15 Laves phase, $Tb_{0.3}Dy_{0.7}Fe_2$, has been reported to also grow in {111} sheets in the <112> direction, as shown in Figure 4.32 [38].

The use of stereographic projections is helpful in visualizing all the parallel directions at once (Figure D.2 in Appendix D). Variants of one family of planes in one phase may be parallel to planes of completely different families in the other phase, or not matched at all. This illustrates the importance of stating specific planes and directions in a self-consistent manner. Confusion in the literature has resulted from stating crystallographic orientations that are too general [39]. Sinkler et al. [10,40] have found the same orientation relationship in the irradiation-induced dissolution of the $TiCr_2$ Laves compound into a bcc solid solution. Narayanan and Archbold have also reported the same relationship [41], while Kumar and Miracle [2] have found the same orientation relationship in the Cr(bcc)+$HfCr_2$(*C*15) system.

The large equiaxed precipitates in the Ti-40 Cr alloys showed no apparent orientation preference. The large twin bands in different precipitates within the same bcc matrix grain were generally not parallel. However, the $<113>_{\beta} \,||\, <110>_{\text{twinned } C15}$ diffraction pattern was often found. Different variants of this orientation relationship may be exhibited by the Ti-40 Cr alloy. The hexagonal $TiCr_2$ found in the Cr-rich alloys showed the same orientation relationship if close-packed planes and directions of the hexagonal and cubic phases were equated.

The same orientation relationship was found in the several different alloys with a range of beta phase compositions, and thus with a range of beta phase lattice parameters which might affect coherency and preferred orientations. The orientation relationship has been suggested to be dependent on the lattice parameter ratio of the two phases [37]. But as mentioned earlier, the zone axes of the two phases and some of the reported directions were not necessarily exactly parallel, and some subtle changes may occur. For instance, keeping $(101)_{\beta}$ parallel with $(111)_{C15}$ and in the center of the stereographic projections, a

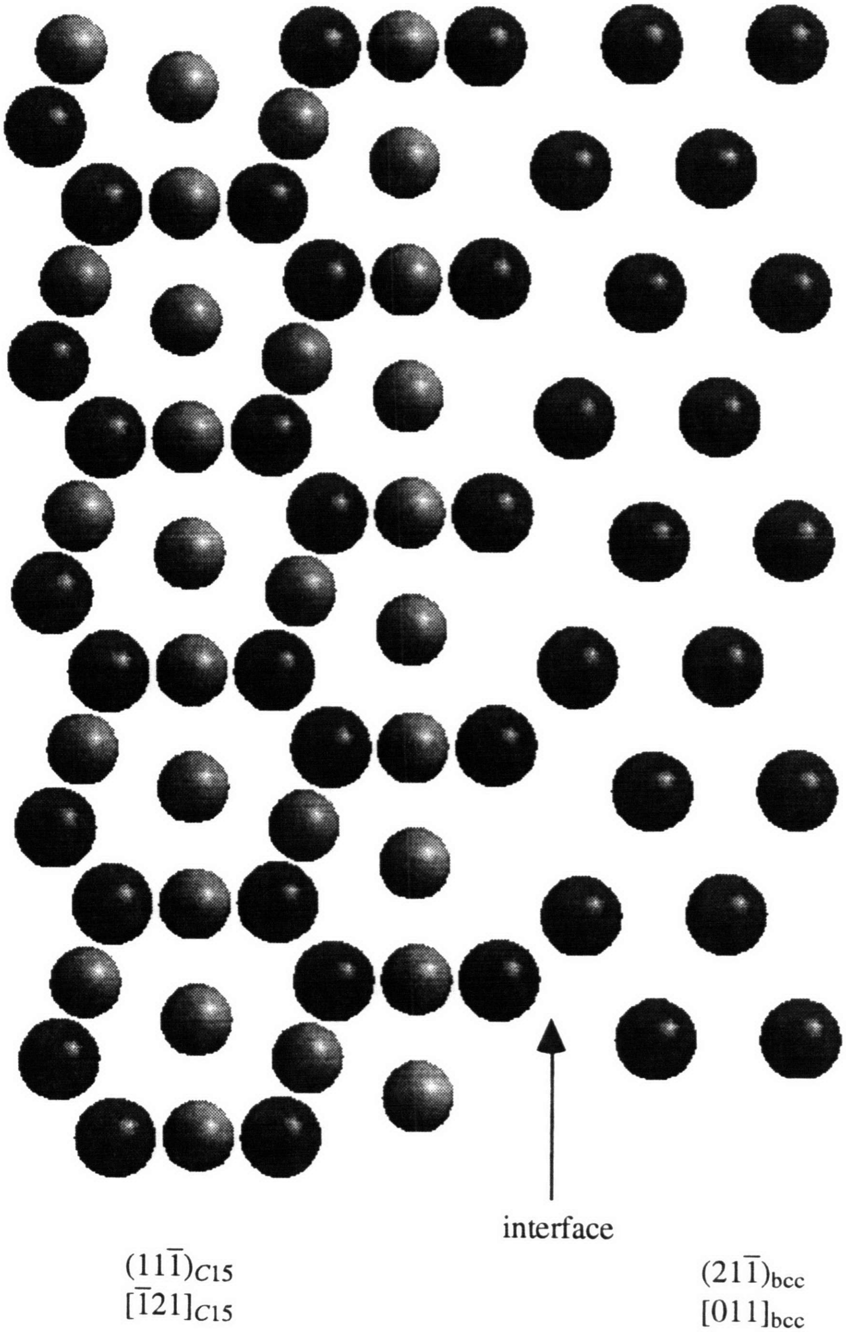

Figure 4.31 Model of the bcc-*C*15 interface along the $[121]_{C15}$ direction.

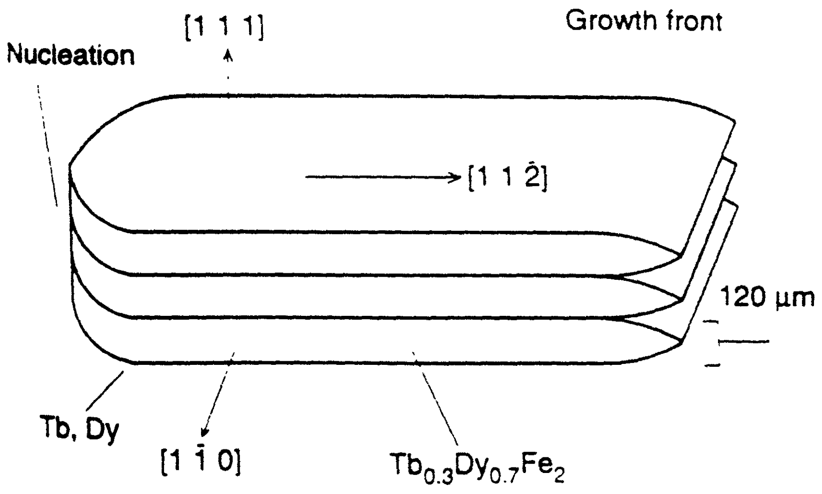

Figure 4.32 Structure of the $Tb_{0.3}Dy_{0.7}Fe_2$ Laves phase. Sheets of {111} planes grow in the <112> direction [38].

slight rotation (4.8°) of one phase relative to the other can bring the $(13\bar{1})_\beta$ in coincidence with $(01\bar{1})_{C15}$ rather than the $(10\bar{1})_\beta$ parallel to $(10\bar{1})_{C15}$. Thus the reported orientation relationship may not always be strictly followed, and some accommodation is possible for changing alloy compositions.

The orientation relationship may also be described by matrix notation, and can be found in Appendix E.

4.5 X-RAY DIFFRACTION ANALYSIS

Figure 4.33 depicts the typical x-ray diffraction scan of the annealed Ti-rich alloys. Peaks from the β-Ti(Cr) bcc phase and the *C*15 $TiCr_2$ Laves phase are present. The relative peak heights or total integral area of the two different phases vary in accordance with the relative volume fractions of the two phases present in the alloy. The Ti-30 Cr alloy has a larger volume fraction of the bcc phase than the Ti-40 Cr alloy at 950°C. In the Cr-rich alloys, there was a lack of strong Laves phase peaks that did not overlap with the β-Cr(Ti) peaks, and the crystal structure determined by x-ray diffraction was inconclusive. The scan in Figure 4.34 shows the Ti-80 Cr alloy at 1000°C, with small Laves peaks at the *C*15 2θ positions.

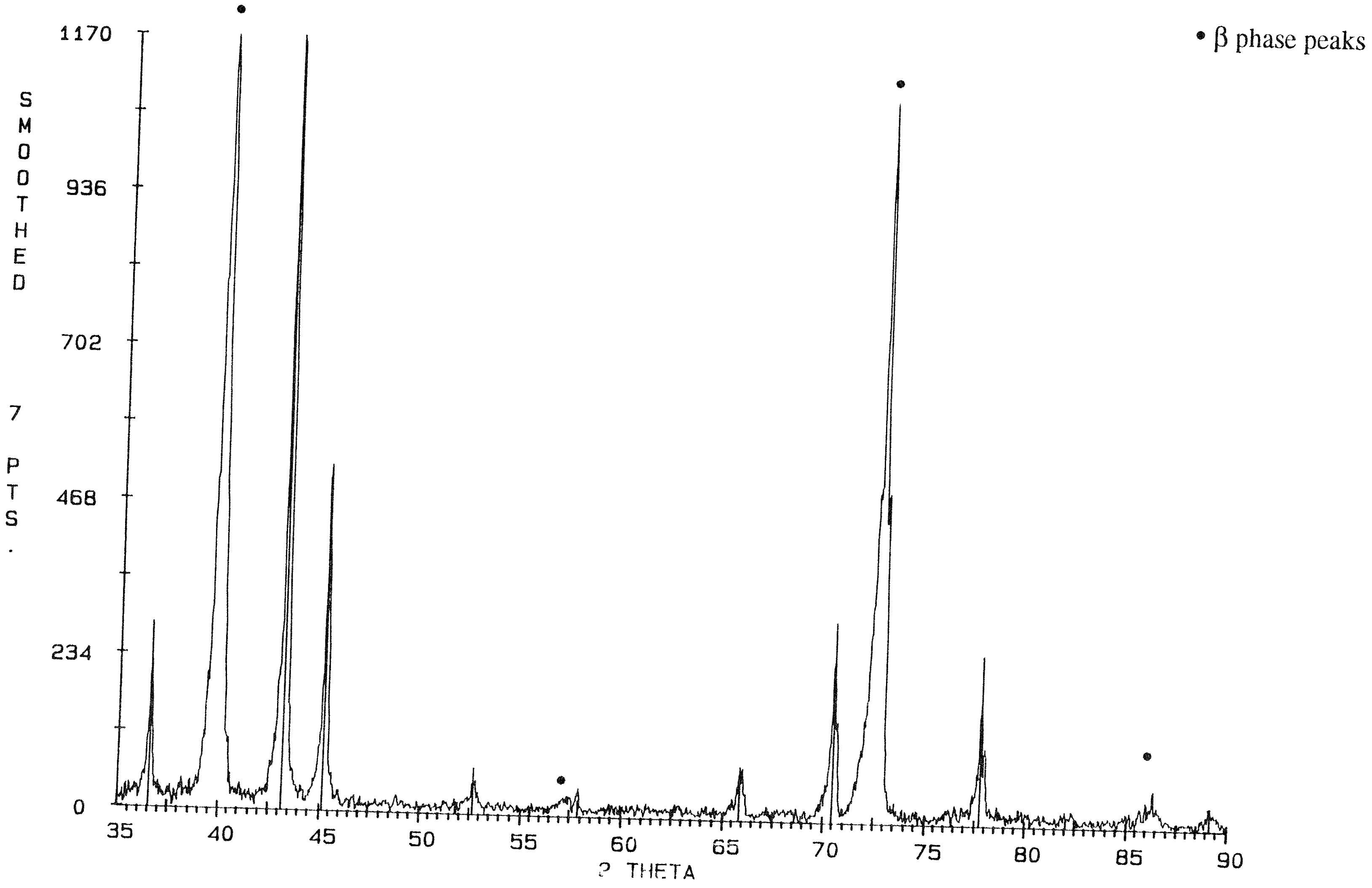

Figure 4.33 (a) X-ray diffraction scan of the Ti-30 Cr alloy annealed at 950°C and 168 hours.

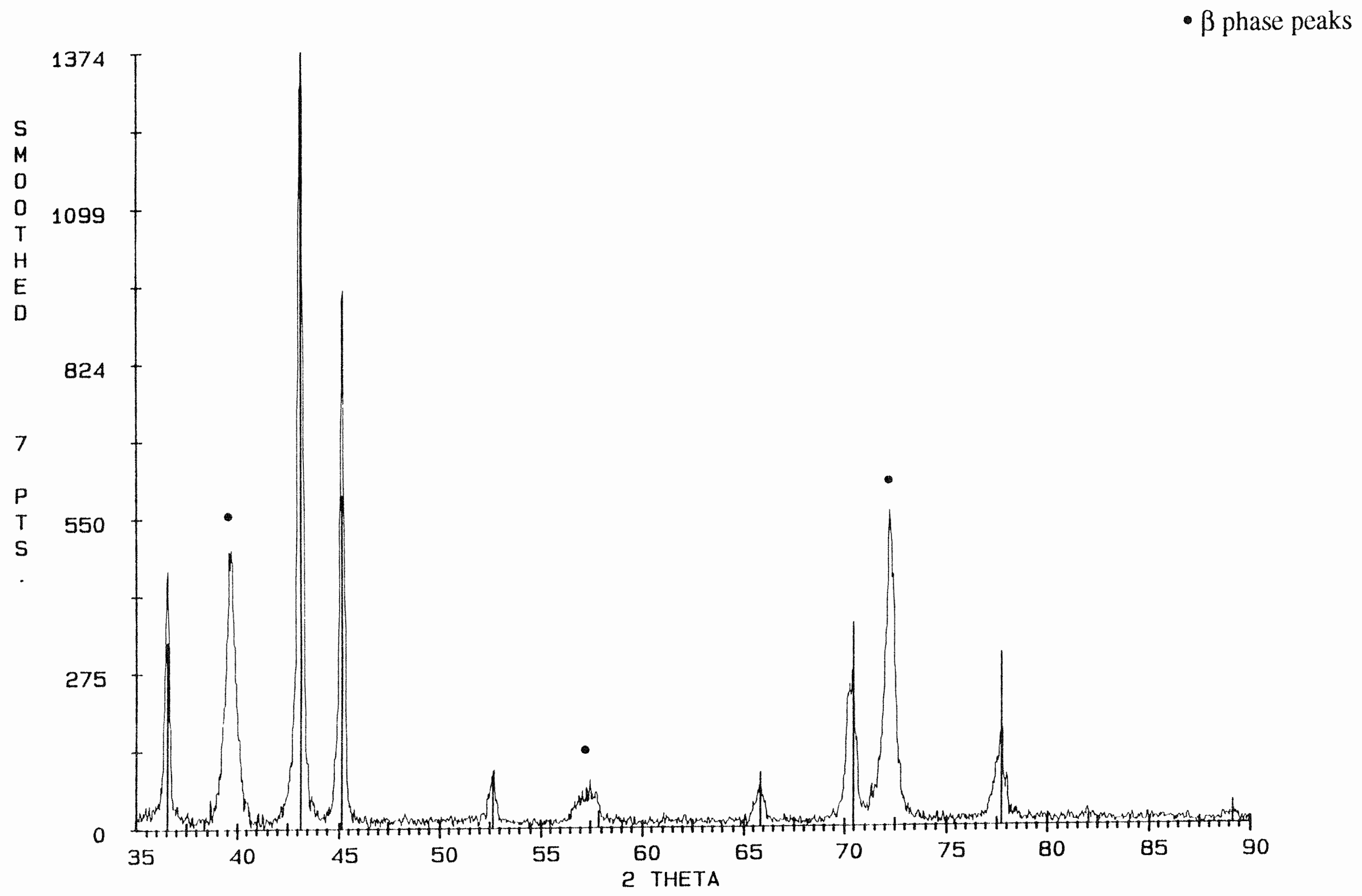

Figure 4.33 (b) X-ray diffraction scan of the Ti-40 Cr alloy annealed at 950°C and 168 hours.

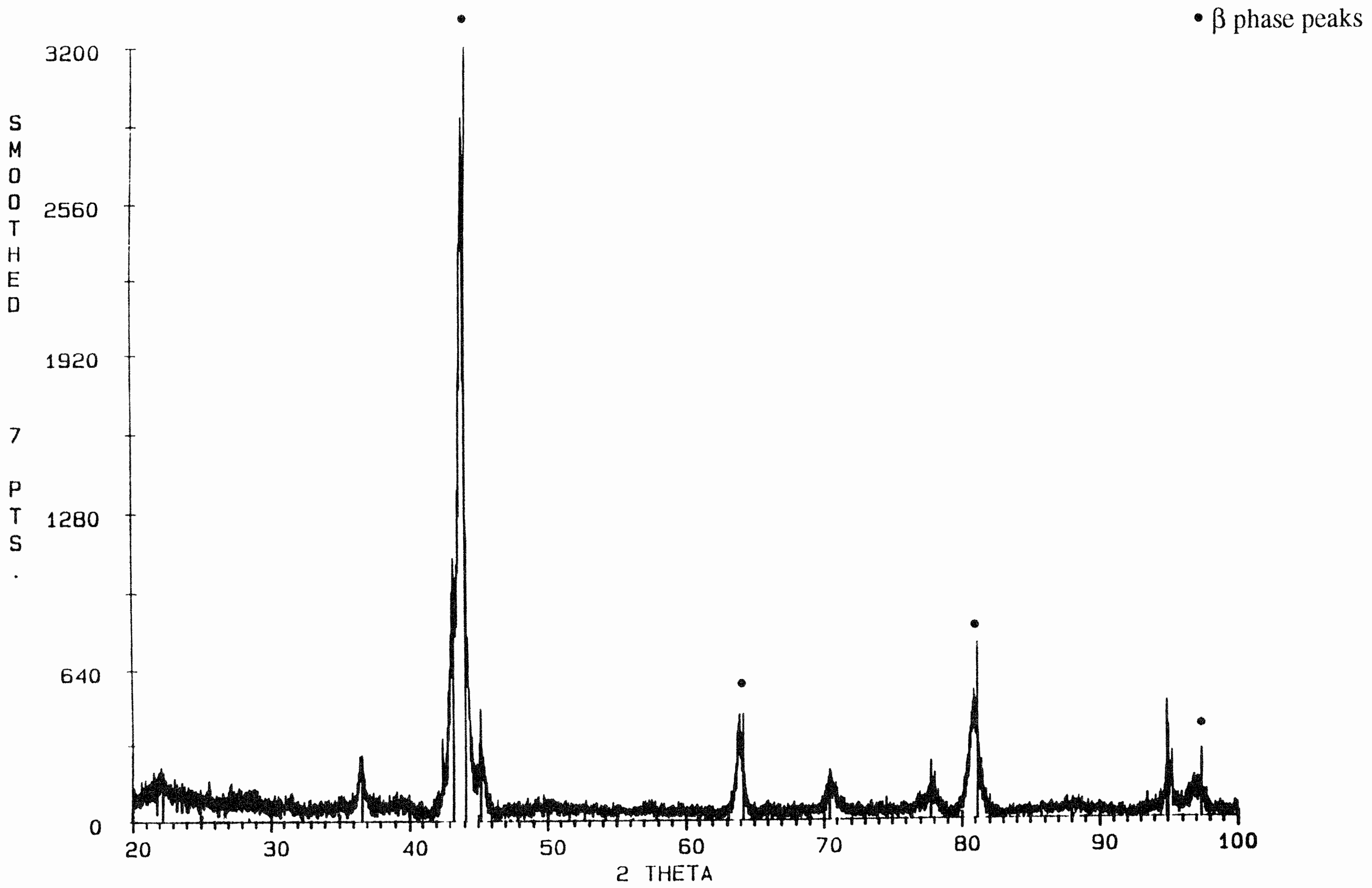

Figure 4.34 X-ray diffraction scan of the Ti-80 Cr alloy annealed at 1000°C.

The lattice constants of the beta phase and the corresponding compositions are found in Tables 4.4 and 4.5. The Ti-rich beta phase compositions determined by electron microprobe analysis match those from the equilibrium phase diagram. The lattice constant values are close to those found in the literature [14,42], as shown in Figure 4.35. Discrepancies may arise from different temperatures and quenching rates of the heat treatments. The lattice parameters also closely follow a linear relationship connecting the lattice parameters of elemental Ti and Cr [43], according to Vegard's Law. The change in lattice parameter with composition of the Ti-Cr beta phase was computed to be da/dc = -0.43 Å.

The only experimental lattice parameter that does not lie on the line following Vegard's Law is that for the Ti-80 Cr alloy. However, this data point comes from the as-cast Ti-80 Cr alloy. As mentioned earlier, parts of this sample showed discontinuous precipitation, and thus the alloy was no longer homogeneously beta phase at the Ti-80 Cr composition. Cellular precipitation of $TiCr_2$ would cause the rejection of Cr into the beta phase. The new beta phase would thus be more Cr-rich and would have a smaller lattice parameter, as the data point indicates.

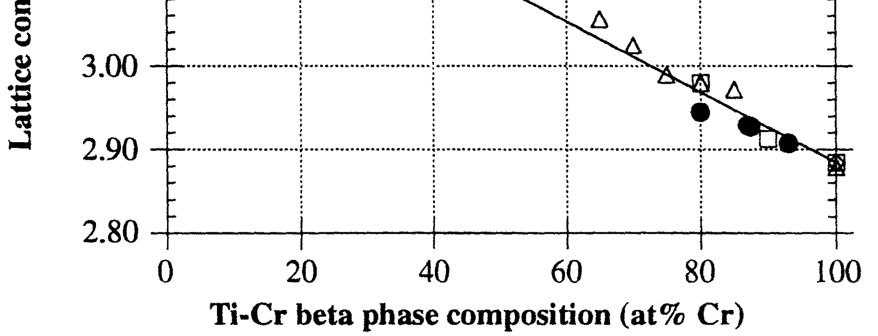

Figure 4.35 The beta-phase lattice constant vs. the Ti-Cr alloy composition.

Table 4.4 The bcc β-Ti(Cr) compositions and lattice constants as a function of temperature.

Temperature	β composition (at%) (phase diagram)	β composition (at%) (microprobe analysis)	lattice constant, **a** (Å) (XRD)
as-cast		Ti-39.40 Cr	3.140
as-cast		Ti-29.15 Cr	3.178
1200°C	Ti-38 Cr	Ti-37.7 Cr	3.135
1000°C	Ti-26 Cr	Ti-26.1 Cr	3.186
950°C	Ti-23.5 Cr	Ti-23.4 Cr	3.202
900°C	Ti-21 Cr		3.212
850°C	Ti-19 Cr		3.230
800°C	Ti-17 Cr		3.236

Table 4.5 The bcc β-Cr(Ti) compositions and lattice constants as a function of temperature.

Temperature	β-phase composition (at%) (phase diagram)	lattice constant, **a** (Å) (x-ray diffraction)
as-cast	Ti-80 Cr	2.9448 ± 0.001
as-cast	Ti-87.5 Cr	2.9273 ± 0.001
1200°C	Ti-87 Cr	2.9288 ± 0.0004
1000°C/48 hrs	Ti-93 Cr?	2.9098 ± 0.0006
1000°C/500 hrs	Ti-93 Cr	2.9078 ± 0.0004

4.6 REFERENCES

1. *Binary Alloy Phase Diagram,* 2nd edition, Ed. T.E. Massalski, ASM International, (1990).
2. K.S. Kumar and D.B. Miracle, Intermetallics, **2**, 257 (1994).
3. E. Ence and H. Margolin, J. Metals, **6**, 346 (1954).
4. R.T. DeHoff and F.N. Rhines, *Quantitative Microscopy*, McGraw-Hill Inc., 1968.
5. M.J. Blackburn and J.C. Williams, Trans. TMS-AIME **239**, 287 (1967).
6. K.S. Kumar and P.M. Hazzledine, *Mater. Res. Soc. Symp. Proc. Vol 364*, 1383 (1994).
7. S.L. Sass, J. Less-Common Metals, **28**, 157 (1972).
8. G.H. Narayanan, T.S. Luhman, T.F. Archbold, R. Taggart and D.H. Polonis, Metallography, **4**, 343 (1971).
9. A. Blatter and M. von Allmen, J. Appl. Phys., **62**, 276 (1987).
10. W. Sinker and D.E. Luzzi, *Mat. Res. Soc. Symp. Proc. Vol 205*, 209 (1992).
11. D. deFontaine, N.E. Paton and J.C. Williams, Acta Metal., **19**, 1154 (1971).
12. W. Sinkler and D.E. Luzzi, J. Alloys and Compounds, **194**, 273 (1993).
13. A.E. Austin and J.R. Doig, J. Metals, **9**, 27 (1957).
14. F.B. Cuff, N.J. Grant and C.F. Floe, J. Metals, **194**, 848, (1952).
15. H.J. Lee and H.I. Aaronson, J. Mat. Sci., **23**, 150 (1988).
16. H.I. Aaronson, W.B. Triplett and G.M. Andes, Trans. Metall. Soc. AIME, **218**, 331 (1960).
17. S.C. Hardy and P.W. Voorhees, Metall. Trans., **19A**, 2713 (1988).
18. R.J. Van Thyne, H.D. Kessler and M. Hansen, Trans. ASM, **44**, 974 (1952).
19. F. Chu, Ph.D. Thesis, U. Penn, (1993).
20. D.J. Thoma and J.H. Perepezko, Mat. Sci. and Eng., **A156**, 97 (1992).
21. A.I. Bennett and R.L. Longini, Phys. Rev., **116**, 53 (1959).
22. D.R. Hamilton and R.G. Seidensticker, J. Appl. Phys., **31**, 1165 (1960).
23. W.A. Tiller, *The Art and Science of Growing Crystals*, ed. J.J. Gilman, John Wiley & Sons, 276 (1963).

24. A. Crosky, P.G. McDougall and J.S. Bowles, Acta Metall., **28**, 1495 (1980).

25. Y. Liu, J.D. Livingston and S.M. Allen, Met. Trans., **26A**, 1441 (1995).

26. U. Dahmen, Metall. Trans., **25A**, 1857 (1994).

27. C.M. Wayman, *Introduction to the Crystallography of Martensitic Transformations*, MacMillan, (1964).

28. A.G. Khachaturyan, *Theory of Structural Transformation in Solid*, John Wiley & Sons, (1983).

29. H.I. Aaronson, C. Liard, and K.R. Kinsman, *Phase Transformations*, ASM, (1970).

30. G. Chen, J.K. Chen, J.K. Lee and W.T. Reynolds, Jr., Metal. Trans., **25A**, 2073 (1994).

31. C.P. Luo and G.C. Weatherly, Acta. Metall., **35**, 1963 (1987).

32. G.C. Weatherly and W.Z. Zhang, Metall. Trans. **25A**, 1865 (1994).

33. J. Fehrenbach, H.W. Kerr and P. Niessen, J. Crystal Growth, **18**, 151 (1973).

34. D.I. Potter, J. Less-Common Metals, **31**, 299 (1973).

35. B.P. Bewlay, J.A. Sutliff, M.R. Jackson and H.A. Lipsitt, Acta Met. et Mat., **42**, 2869 (1994).

36. K.A. Bywater and D.J. Dyson, Metal Science, **9**, 155 (1975).

37. U. Dahmen, Acta Mell., **30**, 63 (1982).

38. R.D. Greenough and M.P. Schulze, Magnetostriction: Materials and Application in *Intermetallic Compounds: Principles and Practice,* ed. J.H. Westbrook and R.L. Fleischer, John Wiley & Sons, p. 389 (1995).

39. H.J. Lee and H.I. Aaronson, Acta Metall., **36**, 1141 (1988).

40. W. Sinkler, to be published.

41. G.H. Narayanan and T.F. Archbold, *Electron Microscopy and Structure of Materials*, Proc. of Fifth International Materials Symp., Berkley, (1971).

42. E. Rudy, Technical Rept. AFML-TR-65-2, (1969), as reported by J.L. Murray, BAPD, **2**, 174 (1981).

43. W.B. Pearson, *A Handbook of Lattice Spacings and Structures of Metals and Alloys*, Pergamon Press, (1958).

Chapter 5

Mechanical properties of two-phase binary alloys

5.1 INTRODUCTION

The use of Laves phases in practical applications will most likely be as a component in two-phase alloys [1]. The brittleness of Laves phases in their monolithic form can be greatly improved with the addition of a second, more ductile phase. There are several other examples of successful ductile phase toughening, such as rubber in glassy amorphous polymers, and the Co+WC system [2].

A "composites" approach to developing Laves phases as useful materials has been adapted by several investigators who have used large volume fractions of a second, more ductile phase in combination with a Laves phase intermetallic. The brittle XCr_2 (X=Hf, Ta, and Zr) Laves phase matrix was toughened by ductile reinforcement of the Cr metallic phase [3]. Even another intermetallic, NiAl, has been shown to absorb some of the crack energy of a two-phase Laves system by the formation of a plastic zone at the crack tip in NiAl+NbNiAl (*C*14) [4]. Also, a two-phase TiCrAl (*C*14)+γ-TiAl showed greater crack resistance in microhardness tests [5].

Directional solidification of Nb-Cr alloys has produced lamellar structures of Nb+$NbCr_2$ and rod or ribbon-like structures of Cr+$NbCr_2$ [6]. $NbCr_2$ has been studied in a Nb-rich [2,7] and a Cr-rich [8] two-phase system. Natural composites of different microstructures were also accomplished in Fe+$NbFe_2$ [9]. Hot working and annealing were used to refine the second-phase morphology in Cr+$HfCr_2$ alloys [10]. Such tailoring of microstructures is essential to designing material systems with optimized properties.

However, the studies of two-phase Laves systems aforementioned, have neglected to address whether the Laves phase itself deformed. Livingston et al. [11] found that HfV_2 could deform by extensive twinning, but questions remained whether other Laves phases could also deform or if HfV_2 was unique due to a lattice instability. (HfV_2 is anomalous, in that both the Young's modulus and shear modulus increase with increasing temperature. Such behavior has been related to a martensitic transformation to orthorhombic symmetry at 120 K and a superconducting transition at 9.4 K.) Liu [12] proceeded to show stress-induced *C*36 to *C*15 phase transformations in $ZrFe_2$ and non-basal slip in $MgNi_2$ [13].

Fleischer and Zabala [14] screened several intermetallics based on specific gravity, hardness, toughness, and elastic moduli for high-temperature applications, and $TiCr_2$ (*C*15) in Ti-Cr-Nb alloys was identified as a promising system that deserved more attention. They also found that the chisel toughness (controlled impact of a chisel to test samples) of Ti-Cr alloys containing $TiCr_2$ improved with an increasing amount of a second phase. Sauthoff [15] has also reported alloys containing $TiCr_2$ to have promising mechanical properties and oxidation resistance at elevated temperatures. To date, the room-temperature mechanical behavior has not been related to the microstructures of Ti-Cr alloys containing $TiCr_2$ in a systematic manner.

Building upon the knowledge of the mechanical properties of single-phase $TiCr_2$ covered in Chapter 3, this chapter investigates the mechanical properties of the $TiCr_2$ Laves phase in two-phase alloys, with both Ti-rich and Cr-rich solid solution phases. Indentation is again used to determine the microhardness and fracture toughness. The mechanical properties are affected by the bcc beta phase properties, beta/Laves phase interfaces, and overall alloy microstructure. Room-temperature compression tests are also performed on the two-phase alloys. Deformation of $TiCr_2$ and the fractography of the alloys are reported.

5.2 EXPERIMENTAL PROCEDURES

Microhardness indentation procedures followed those described in Chapter 3. However, additional indentation testing was performed on the Cr-rich alloys. A larger load was required to produce radial cracking in order to assess the fracture toughness of these alloys. A Vickers indenter (larger than the one used for the microhardness tester) was fitted onto a Rockwell superficial hardness tester to achieve a load of 15 kg. The exact mechanics of the indentation methods are slightly different, but similar hardness values were obtained. The indentation impression diagonals and radial cracks were again measured with SEM.

Cubes of 5 mm were spark-cut from the Ti-rich alloys to be used in the compression tests. The Cr-rich alloys were cut by a diamond saw into cubes of similar size. Compression was performed in air and at room-temperature on an Instron machine. A full load scale of 20,000 lbs. and a crosshead speed of 0.001 in/min was used. A slower crosshead speed of 0.0002 in/min was used for two of the Ti-rich alloys in attempts to achieve more deformability, but proved to be futile. Loading was sometimes stopped before complete fracture in order to prepare TEM samples of the compressed alloys. The large $TiCr_2$ precipitates in the Ti-40 Cr alloy were selected to examine the deformability of the Laves phase by TEM comparisons of deformed and undeformed samples, since the other Laves precipitates were heavily faulted before deformation, precluding easy assessment of deformation-induced microstructural changes. Fractography of some of the compressed samples was performed with SEM.

5.3 INDENTATION

5.3.1 Microhardness

The hardness values of the bcc beta phase are much lower than those of the Laves phase, as expected. The single-phase beta ranged in hardness from about 400 to 550 kg/mm^2, with Cr-rich compositions being harder than Ti-rich compositions. Chapter 3 revealed the $TiCr_2$ Laves phases to have hardness values around 850-900 kg/mm^2. Previous studies on Ti-Cr alloys showed a hardness peak around the Laves phase composition, but none of these studies reported if and how much Laves phase existed [16,17]. McPherson and Fontana [17] also report Cr-rich alloys being more brittle than Ti-rich Ti-Cr alloys, which was also confirmed in the handling and sample preparation of these alloys.

Indentation on the two-phase alloys was performed at a load of 500 g, to ensure that the representative dual-phase microstructure was being sampled, rather than just individual phases. Figures 5.1-5.3 display indentation impressions sampling the entire

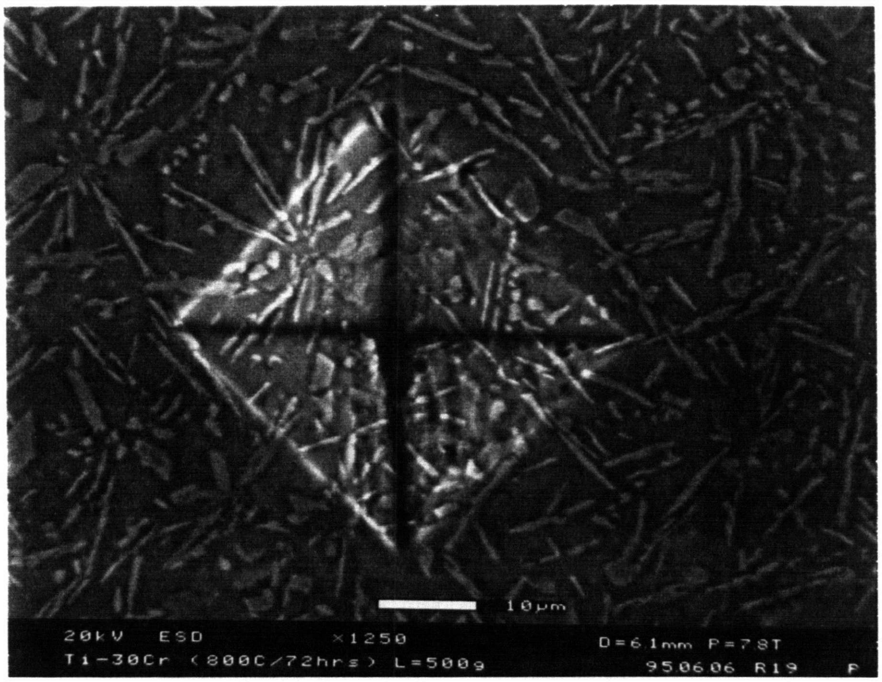

Figure 5.1 Microhardness indentation of the Ti-30 Cr alloy annealed at 800°C. (Load = 500 g)

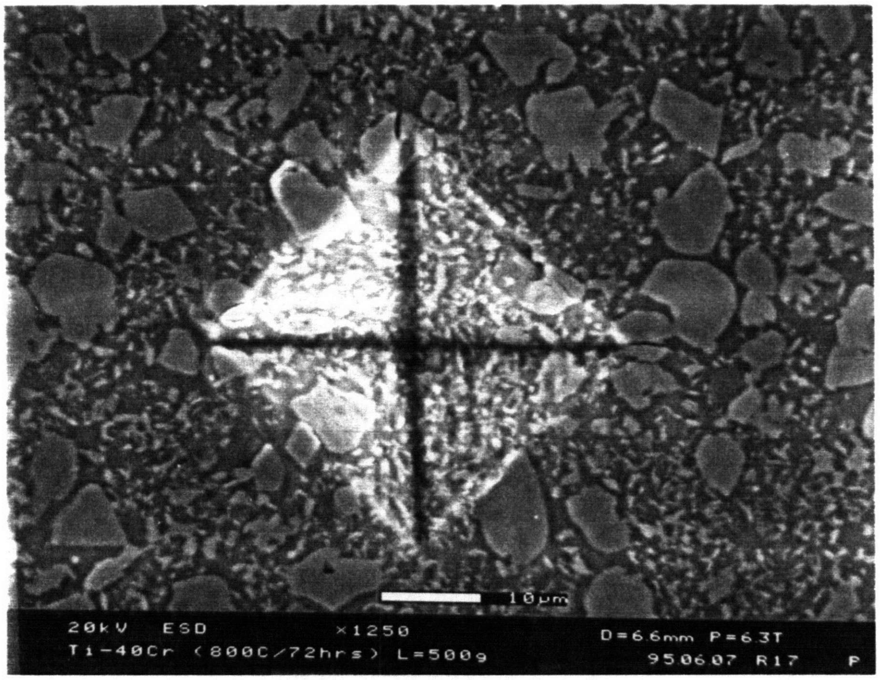

Figure 5.2 Microhardness indentation of the Ti-40 Cr alloy annealed at 800°C. (Load = 500 g)

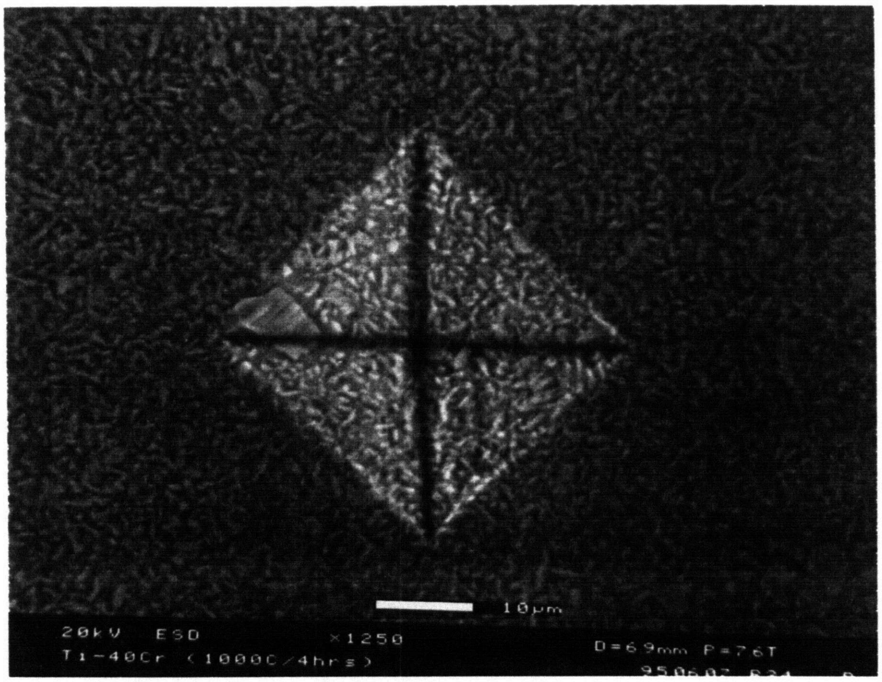

Figure 5.3 Microhardness indentation of the Ti-40 Cr alloy annealed at 1000°C for 4 hours.

two-phase structure in the Ti-rich alloys. Table 5.1 lists the microhardness and microstructure of the Ti-rich alloys. Precipitation of $TiCr_2$ increased the hardness from the single-phase beta microstructure present in the as-cast condition. However, in the Ti-30 Cr alloy, the ageing process increased the hardness only to a value found in the single-phase beta Ti-40 Cr alloy. Thus, the Cr in Ti acts as a comparable solid solution hardener to low volume fractions of Laves phase precipitation. Fleischer [18] has documented that in general, titanium is solution hardened by the combined effect of size and modulus interactions.

The volume fractions of Laves phase in the annealed Ti-30 Cr alloys were quite small, and thus did not have much of a hardening effect. The two-phase structures in the Ti-40 Cr alloy had an almost 100 kg/mm^2 increase in hardness from the as-cast condition. The dense structure of fine precipitates proves to be a potent strengthener. The annealed Ti-40 Cr alloys with fine precipitates all had similar hardness values, despite the different annealing temperatures and Laves phase volume percentages. The larger $TiCr_2$ equiaxed

Table 5.1 Vickers Microhardness of Ti-rich, two-phase alloys (Load = 500g).

Heat Treatment	**Ti-30 Cr** microhardness and microstructure	**Ti-40 Cr** microhardness and microstructure
as-cast	401.6 ± 3.9 single phase beta	436.1 ± 1.9 single phase beta
800°C/72 hours	437.6 ± 5.1 small lath ppts.	515.3 ± 5.4 bimodal ppts.
900°C/24 hours	422.0 ± 5.0 large lath ppts.	
950°C/24 hours		518.5 ± 7.8 fine ppts.
1000°C/4 hours		525.9 ±6.8 fine ppts.
1150°C/1.5 hours		510.2 ± 3.4 fine ppts.

precipitates in the bimodal structure of the Ti-40 Cr alloy at 800°C showed some cracking after indentation. A critical size of the Laves phase precipitate appears to be necessary for cracking.

Recalling the nearly single-phase $TiCr_2$ hardness behavior, the Cr-rich compositions exhibited greater hardness than the Ti-rich compositions. Accordingly, the Cr-rich beta bcc phase has greater hardness values than the Ti-rich beta phase. (Cr has a smaller lattice constant and higher melting temperature than Ti, suggesting that Cr would have a greater modulus and hardness than Ti.) The fineness of the Cr-rich alloy microstructures were well-suited for microhardness indentation. Table 5.2 lists the microhardness values for the Cr-rich alloys.

Table 5.2 Vickers Microhardness of Cr-rich alloys (Load = 500 g).

	Ti-80 Cr alloy		**Ti-87.5 Cr alloy**	
heat treatment	microhardness	Laves vol%	microhardness	Laves vol%
as-cast	875.5 ± 25.5 574.4 ± 15.6	2-phase area single beta area	525.4 ± 12.3	single phase beta
1200°C	697.2 ± 12.3	35%		
1000°C	752.0 ± 18.02	48%	556.5 ± 11.5	20%

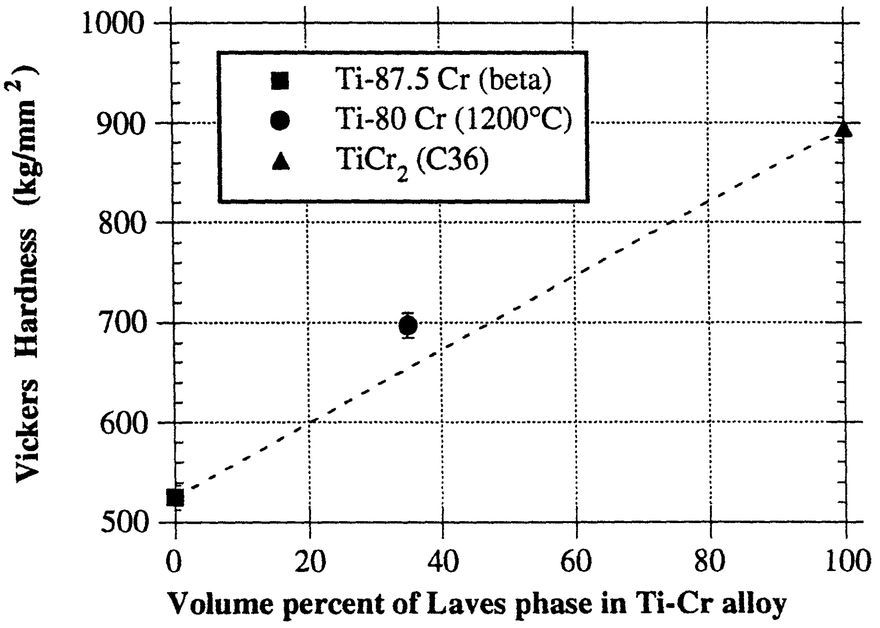

Figure 5.4 Vickers hardness of Cr-rich, two-phase alloys as a function of the volume percent of Laves phase . The dotted line represents the rule of mixtures between the Cr-rich beta phase and single-phase (*C*36) $TiCr_2$.

Figure 5.4 plots the hardness value vs. the Laves phase volume fraction, and takes the *C*36 stoichiometric value for $TiCr_2$. The dotted line represents the rule of mixtures between single-phase beta at Ti-87.5 Cr and single-phase $TiCr_2$. The Ti-80 Cr alloy annealed at 1200°C, with 35 vol% of the Laves phase, had a microhardness value higher than the rule of mixtures would predict. The strengthening effect also comes from the fine, two-phase microstructure. The high microhardness values of 700-750 kg/mm^2 of the annealed Ti-80 Cr alloys are quite appealing, considering that no cracks were formed at a load of 500 g.

5.3.2 Fracture Toughness

The attractiveness of the Cr-rich, two-phase alloys with high hardness and no cracking motivated the attempt to measure the fracture toughness of these alloys. In order to allow comparisons with single-phase $TiCr_2$, indentation with a higher load to produce cracks was employed, rather than using a totally different method, such as bend tests. As described earlier, a large Vickers indenter was attached to a Rockwell superficial hardness tester. Heavy deformation of the beta phase surrounding the indentation impression can be seen clearly in Figure 5.5. Hardness values using the 15 kg load (Table 5.3) were only roughly 20 kg/mm^2, or 3-4%, less than values obtained using a 500 g load, thus indicating that this hardness tester was adequate.

Figures 5.6 (a) and (b) show the indentation of the Ti-80 Cr alloy at 1200°C at the 500 g load and the 15 kg load, respectively. Cracks formed in the Ti-80 Cr alloy with the higher load. The low Laves volume fraction found in the Ti-87.5 Cr alloy would require a higher critical load to initiate cracking. The Ti-rich, two-phase alloys also did not

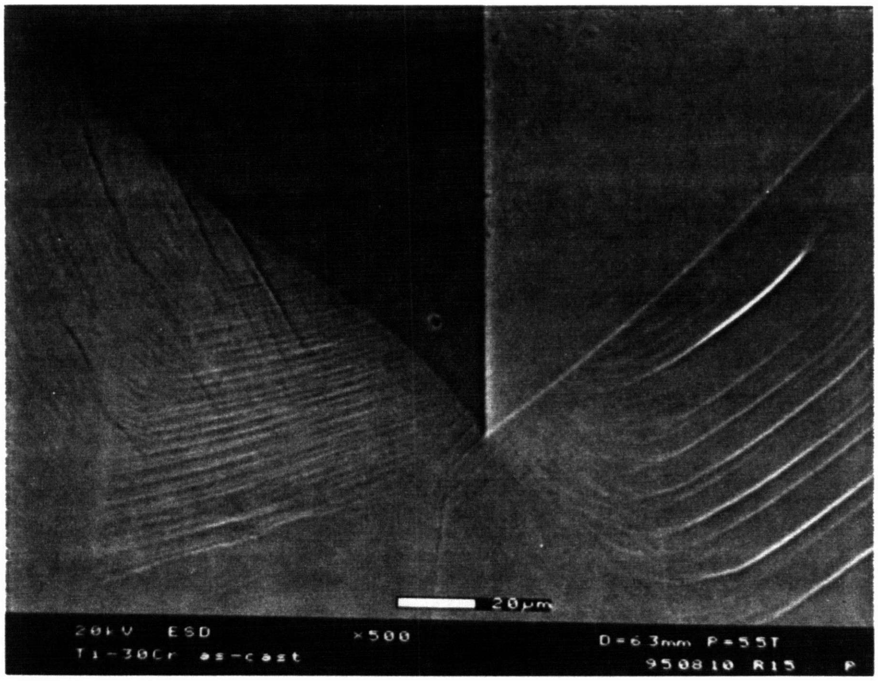

Figure 5.5 Deformation of the Ti-30 Cr bcc beta phase by indentation with a load of 15 kg.

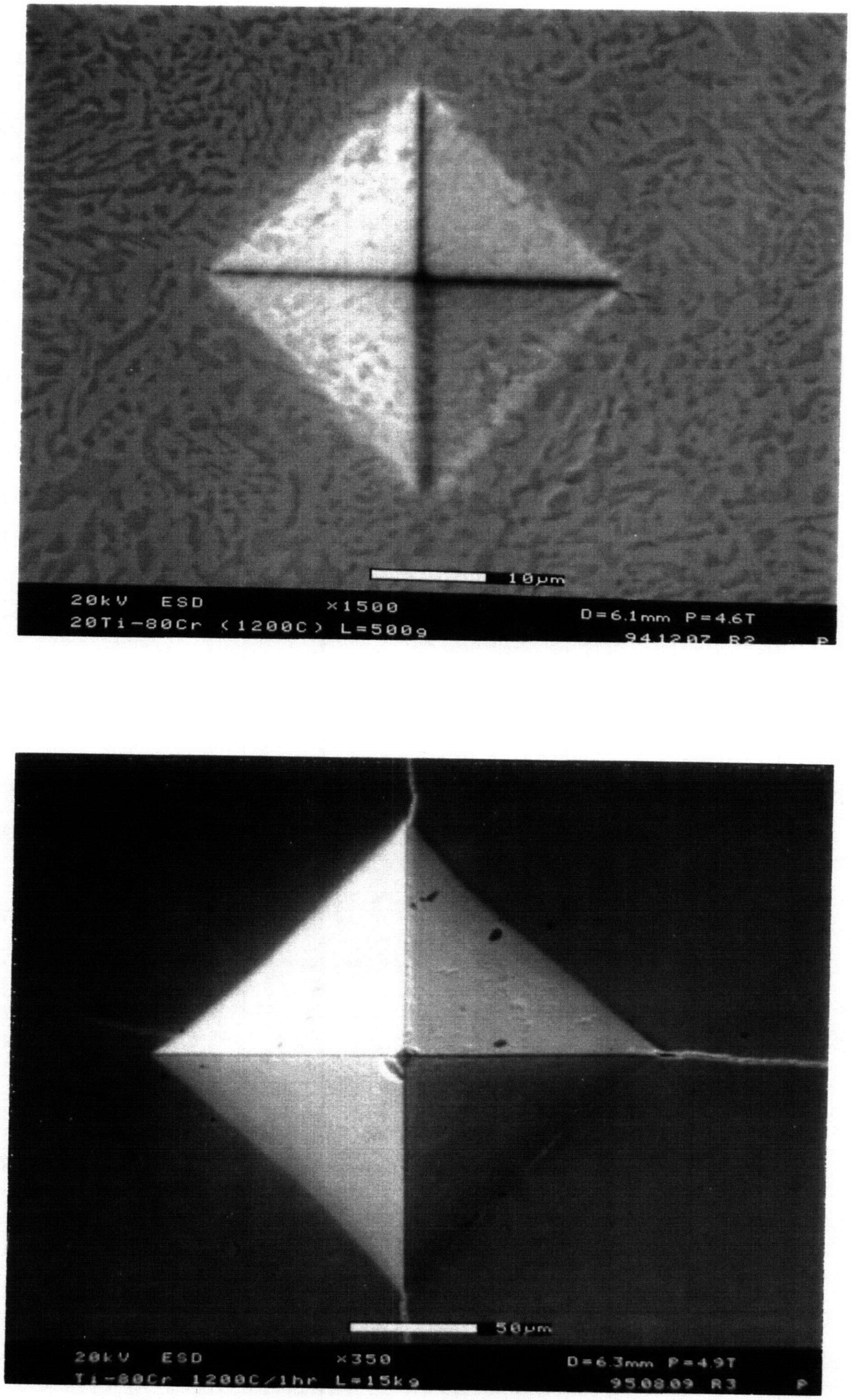

Figure 5.6 The Ti-80 Cr alloy with indentations at loads of **(a)** 500 g and **(b)** 15 kg. Cracks are produced with only high loads.

experience any cracking. For the single-phase $TiCr_2$, loads as small as 10 g could produce cracks. Some investigators have noted the critical load which produces cracks as a significant parameter [19].

The moduli for the $Cr+TiCr_2$ alloys were estimated by the weighted averages of the modulus of the two different phases (Appendix F). Discrepancies exist for the elastic modulus of $TiCr_2$. Fleischer et al. [20] used an ultrasonic technique that measures elastic wave velocities through a rectangular-shaped sample, and have published a value of 184 GPa for $TiCr_2$. Preferred orientation of anisotropic crystals, cracks, and irregular sample shapes can affect the ultrasonic measurements. Thoma [21] used a microindentation mechanical properties microprobe that measures the elastic response during repeated loading and unloading of the indenter before "pop in" or plastic deformation begins. The Thoma value was selected since the test sample is small enough to be free of flaws and since the indentation technique was similar to the testing of the Ti-Cr alloys used here. This value is also slightly higher than the calculated value of $TiCr_2$ based on the same composition in the beta phase using the rule of mixtures of the elastic modulus of elemental Ti and Cr [22]. The intermetallic $TiCr_2$ is a more ordered and close-packed structure than the bcc solid solution, and therefore is expected to have a larger modulus.

Table 5.3 Vickers hardness and fracture toughness of the Cr-rich alloys using a Superficial Rockwell Hardness Tester with a Vickers indenter (Load = 15 kg).

Sample	Vickers hardness (kg/mm^2)	ave. crack length, l (μm)	fracture toughness ($MPa\ m^{1/2}$)
Ti-80 Cr 1200°C/1 hr	719.7 ± 5.4	53.9 ± 15.8	6.6 ± 1.1
Ti-80 Cr 1200°C/6 hrs	671.1 ± 9.1	65.6 ± 24.2	6.0 ± 1.4
Ti-80 Cr 1000°C/48 hrs	732.3 ± 6.7	86.3 ± 9.4	4.9 ± 0.4
Ti-87.5 Cr 1380°C/24 hrs	500.8 ± 9.6		
Ti-87.5 Cr 1000°C/500 hrs	539.9 ± 6.0		

The room-temperature fracture toughness of the Cr-rich β+$TiCr_2$ alloys were measured to be in the range of 5.0-6.5 MPa $m^{1/2}$ (Table 5.3) by indentation techniques. These values are far improved compared with the single-phase $TiCr_2$ alloys, which had toughness values of 0.75-1.5 MPa $m^{1/2}$ (Table 3.3). The Ti-rich β+$TiCr_2$ alloys and Cr-rich alloys with low volume fractions of $TiCr_2$ did not have appreciable cracking with indentation, and thus are expected to have even larger fracture toughness values.

Figure 5.7 shows magnified views of the radial cracks at the corner of the indentation impression in the Ti-80 Cr alloy. The darker phase is the $TiCr_2$ Laves phase. The crack paths were not necessarily straight, sometimes becoming more tortuous near the end of the crack tip. The two different phases obviously affect the crack path, and may disrupt the propagation of the crack. Cracks may be deflected at the matrix/precipitate interface. As mentioned in section 3.4.2, decohesion of the bcc and the Laves phase may occur, expending some of the deformation energy. Ashby et al. [23] have reasoned that the interface must be weak enough to debond in order to maximize the deformation of the ductile phase. Similar arguments have been presented for fiber-reinforced composites.

Soft Cr particles have been found to be effective in preventing crack propagation in the brittle $NbCr_2$ Laves phase [8]. By estimating the size of the plastic zone radius for a sharp crack, Anton and Shah [2] have computed that uniformly distributed ductile particles need to be 6-10 μm in diameter to blunt cracks in Nb+$NbCr_2$. However, the beta phase in the Ti-Cr alloys above is much smaller. Several other materials systems have been shown to be toughened by a second, more ductile phase by interface debonding and crack bridging, branching, deflection, and blunting, as seen in the two-phase Ti-Cr alloys.

Fracture toughness values of other two-phase Laves systems fall within the same range observed in this work for the two-phase $TiCr_2$ alloys. Bewlay et al. [6] report a fracture toughness of 3.1 MPa $m^{1/2}$ for Nb+$NbCr_2$ and 3.6 MPa $m^{1/2}$ for Cr+$NbCr_2$ alloys. Kumar and Miracle [10] achieved a fracture toughness of 7 MPa $m^{1/2}$ with Cr+$HfCr_2$ by notched 3-point bend test. However, this eutectic alloy had a fairly low volume fraction of the *C*14 $HfCr_2$ Laves phase. Cracks were seen along the interface and an extensive plastic zone was found ahead of the crack tip, indicating similar deformation behavior as the two-phase β+$TiCr_2$ alloys. Similarly, Ravichandran et al. [24] report toughness values of 5-7 MPa $m^{1/2}$ for Cr+$HfCr_2$ alloys.

Although comparisons of two-phase Laves systems are difficult because toughness is strongly dependent upon the Laves phase volume fraction, microstructure, and the test method, all the reported toughness measurements were below 10 MPa $m^{1/2}$. Bewlay and Jackson [25] place an upper limit of 10 MPa $m^{1/2}$ on Nb+$NbCr_2$ alloys that are

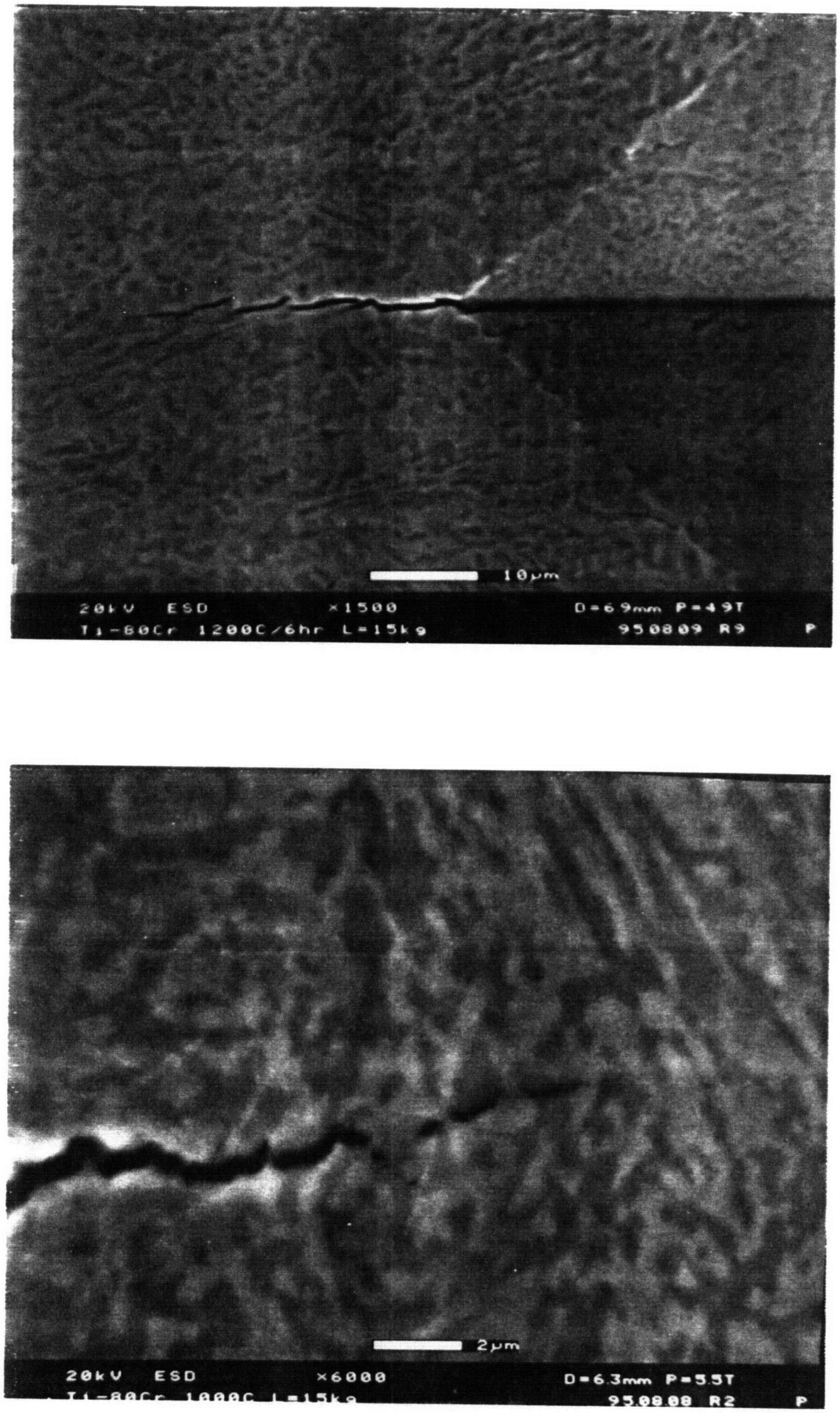

Figure 5.7 SEM images of radial cracks produced in the Ti-80 Cr alloy by indentation at 15 kg at **(a)** 1500X and **(b)** 6000X.

alloyed with Hf and Ti, and in general, such a limit currently holds true for all Laves phase systems reported to date.

Bewlay and Jackson [25,26] compare their alloyed Nb+$NbCr_2$ alloy against a silicide-based composite with a roughly equal 50% Nb-based metallic phase for high-temperature strength and room-temperature toughness. This comparison provides an important indicator of whether Laves phases can seriously compete against other material types for practical applications. The niobium silicide-based composite had a fracture toughness of about 22 MPa $m^{1/2}$ and a strength of about two times the $NbCr_2$ Laves phase alloy. In this case, the silicide composite offers a more attractive balance between room-temperature toughness and high temperature strength than the two-phase Laves alloy. Thus, although the room-temperature toughness of Laves phases may be greatly improved by the incorporation of a second, more ductile phase, the two-phase Laves systems still face other challenges in order to compete with other material systems.

5.4 COMPRESSION TESTS

The main intent of the compression tests was to study the deformation mechanisms in the $TiCr_2$ Laves phase in two-phase alloys. As demonstrated in Chapter 3, single-phase $TiCr_2$ is extremely brittle, and any attempts to compress the single-phase alloys would result in immediate fracture. However, with the $TiCr_2$ precipitates constrained within the more deformable beta bcc phase, chances for room-temperature deformability of the Laves phase are greatly improved. Evidence for deformation by slip, twinning, and/or phase transformations has been documented in the Laves phases, HfV_2 [11], $ZrFe_2$ [12], and $MgNi_2$ [13] in two-phase alloys.

In order to assess whether the $TiCr_2$ Laves phase can also deform at room-temperature, a qualitative TEM comparison of structures in $TiCr_2$ with and without compression is performed. Several other interesting features are revealed by the series of compression tests and are discussed below. Precipitation of the $TiCr_2$ Laves phase strengthens the beta phase, but also decreases the total plastic deformation. Differences in the mechanical response among the different two-phase Ti-Cr alloys are interpreted in terms of the microstructures and properties of the individual phases.

5.4.1 Stress vs. displacement curves and crack behavior

The measured data of the compression tests consisted of the applied load versus the crosshead displacement. A strain gauge was not placed on the samples due to their small size, and thus accurate measurements of the strain are not possible. The measured displacement includes the reduction in height of the test sample, but not in a predictable relationship, and crosshead displacement is tabulated rather than strain. Due to the nonuniform sizes of compression samples, the crosshead displacement was divided by the sample height to give a "normalized displacement".

Results of the room-temperature compression tests are summarized in Table 5.5. The yield stress was determined with a 0.2 percent "normalized displacement" offset. The Ti-80 Cr as-cast sample failed in the elastic regime and no yield stress could be determined. The maximum stress represents the largest stress achieved before a load drop, complete failure, or the point where the compression test was stopped.

Because the behavior of these materials can be severely degraded by pre-existing flaws, such as cracks, the values presented are the "best test" samples out of a group of samples from the same alloy (same composition and heat treatment). Some of the data could be discounted on the basis of pores in the sample or skewness of the compression cube. However, samples of the same alloy generally behaved similarly to one another, and also differently enough from other alloys to form a basis for comparison. Caution must also be used since the reported values do not necessarily represent the full potential of the sample. The sample volume of the compression tests is much larger than the sample volume probed by microindentation. The most serious flaw in the compression cube will dominate the failure response.

Figures 5.8-5.9 display plots of the engineering stress vs. normalized crosshead displacement. The slope was computed from the "elastic" (or linear) region of the plots, and can be used as a relative measure of the Young's modulus. Since the normalized displacement in this "elastic" region is approximately an order of magnitude larger than the elastic strain experienced by most materials, the slope computed from the above plots results in values that are, accordingly, an order of magnitude smaller than the estimated values of the actual Young's modulus. The determination of the slope from these plots gives only relative quantitative values for comparing the moduli of the different Ti-Cr alloys.

The as-cast Ti-40 Cr alloy (bcc phase) had a higher "modulus" than the as-cast Ti-30 Cr alloy, which was also reflected by the microhardness measurements. The qualitative trend between the microhardness and compression behavior is also followed by the

Table 5.4 Room-temperature compression test data for two-phase Ti-Cr alloys.

Sample heat treatment	yield stress (MPa)	maximum stress (MPa)	displacement (cm/cm%)	slope (GPa)	micro-structure
Ti-30 Cr as-cast	1094	3025*	55.9*	11.8	single-phase beta (Ti)
Ti-40 Cr as-cast	1210	1388	8.1	12.3	single-phase beta (Ti)
Ti-80 Cr as-cast	?	770	0.0	11.6	cellular ppt.
Ti-87.5 Cr as-cast	870	1115	6.1	10.9	single-phase beta (Cr)
Ti-30 Cr 950°C/24 hrs	1245	1761*	15.2*	12.9	lath-shaped $TiCr_2$ ppts.
Ti-40 Cr 1000°C/24 hrs	1460	1726	7.6	13.2	equiaxed $TiCr_2$ ppts.
Ti-80 Cr 1200°C/6 hrs	1600	2042	4.6	13.6	eutectic-like
Ti-80 Cr 1000°C/48 hrs	1890	2095	3.1	13.6	eutectic-like
Ti-87.5 Cr 1000°C/500hrs	1170	2008	12.6	12.2	eutectic-like lamellar

* compression test stopped, values not true maximum

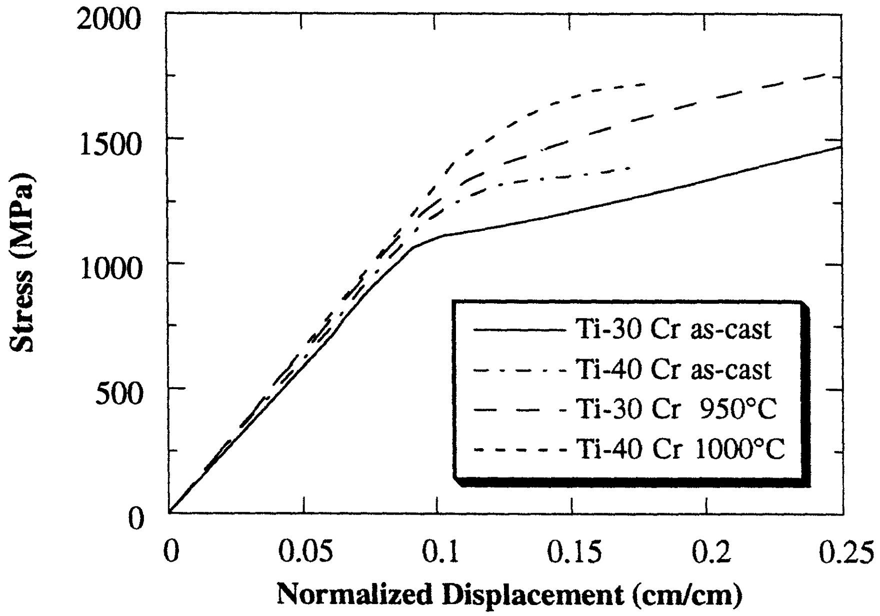

Figure 5.8 Room-temperature compression test stress vs. normalized displacement curves for Ti-rich alloys. Precipitation of the $TiCr_2$ Laves phase strengthens the Ti-Cr alloy.

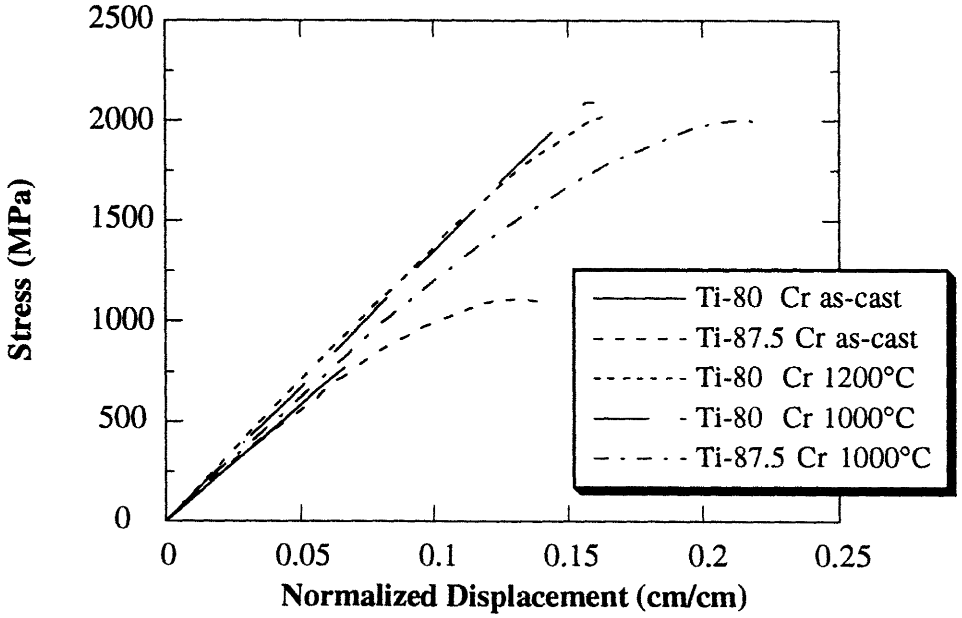

Figure 5.9 Stress vs. normalized displacement curves for Cr-rich alloys from room-temperature compression tests.

Cr-rich, as-cast alloys (Figure 5.10). However, the higher microhardness values of the Cr-rich beta phase did not translate to higher "modulus" relative to the Ti-rich compositions.

Strengthening of the bcc beta phase due to the precipitation of the $TiCr_2$ Laves phase is evident in Figure 5.8. The slope of the stress vs. normalized displacement curve and the yield stress of the annealed Ti-30 Cr alloy with 16 vol% $TiCr_2$ are higher than those of the single-phase beta Ti-30 Cr alloy. All other alloy compositions showed similar strengthening effects from the precipitation of the Laves phase. The annealed Ti-80 Cr alloys showed a much steeper slope and higher yield stress than the annealed Ti-87.5 Cr alloy, most likely due to the greater volume fraction of Laves phase. Takasugi [7] has shown that in Nb+$NbCr_2$ alloys, the flow stress increases with increasing volume fraction of $NbCr_2$. The first evidence of a Laves phase strengthening an alloy was the dispersion of $TaFe_2$ Laves phase in steel [27]. Good high-temperature strength was maintained without low-temperature embrittlement.

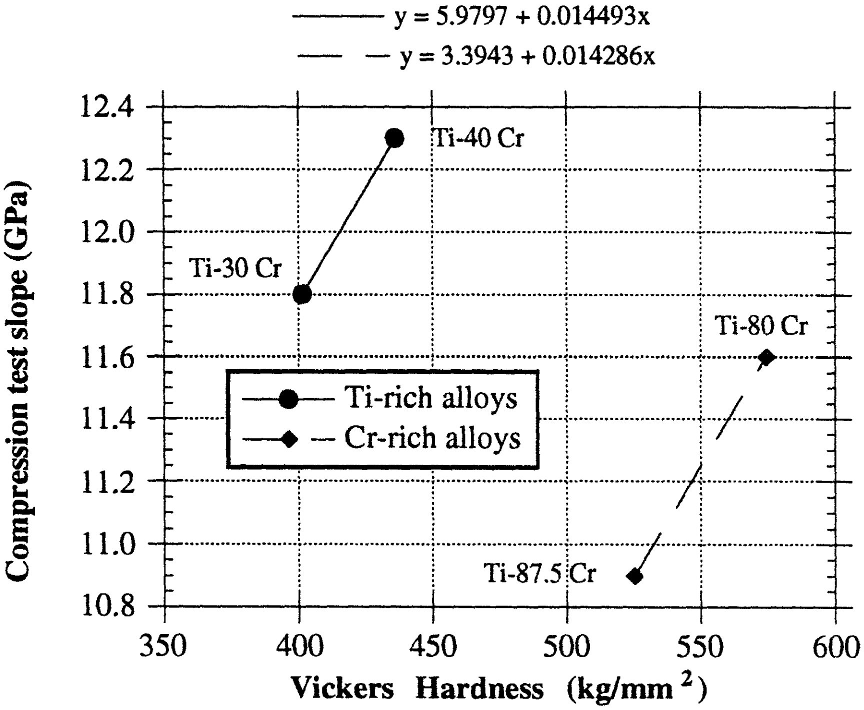

Figure 5.10 Correlation of the hardness and compression test slope in the Ti-Cr solid solution bcc phase.

Substantial deformation was possible with the Ti-rich, two-phase alloys since the discrete $TiCr_2$ particles are surrounded by the continuous and more ductile bcc beta phase. Plastic strains of 8-10% were computed from these alloys by the measurement of sample heights. Optical examination (Figure 5.11) revealed that the Laves phase had cracked many times in the Ti-rich, two-phase alloys. The cracks were roughly parallel to the direction of compression. Figure 5.12 shows that in the Ti-30 Cr alloy, the lath-shaped particles oriented with their lengths normal to the compression axis were cracked several times (reminiscent of the behavior of fiber-reinforced composites), while those parallel to the compression axis were not as likely to be cracked. The titanium-rich solid solution matrix serves to dull the crack as no further crack propagation in the matrix was found by TEM. Debonding of the precipitate/matrix interface was occasionally encountered, and serves as another mechanism to relieve some of the strain energy caused by the deformation. These same mechanisms were found with the indentation studies.

The crack behavior observed in the compression tests of the Cr-rich, two-phase alloys was quite different. Figures 5.13 and 5.14 capture cracks running through the Cr-rich beta phase, and not just confined to the Laves phase. As discussed before, the Cr-rich beta compositions are much more brittle than the Ti-rich beta compositions. The Laves phase in the Cr-rich alloys is also more interconnected and not surrounded by the soft matrix phase as found in the Ti-rich alloys. Thus, the microstructure and the bcc phase brittleness both act to make the Cr-rich, two-phase alloys less deformable. In fact, the Cr-rich alloys often shattered catastrophically and did not withstand much plastic deformation. Kumar and Miracle [10] also report the absence of macroscopic plasticity in Cr+$HfCr_2$ alloys, blaming Cr as an inferior matrix.

The toughness demonstrated in the Cr-rich, two-phase alloys by the indentation studies has most likely been overridden by pre-existing cracks that affect the compression test results. Axial splitting by macroscopic cracks extending in the direction of axial compression occurs in the absence of lateral confining pressure (which occurs in indentation), and thus compression test samples would not be expected to experience as much plastic deformation as achieved in the microhardness tests.

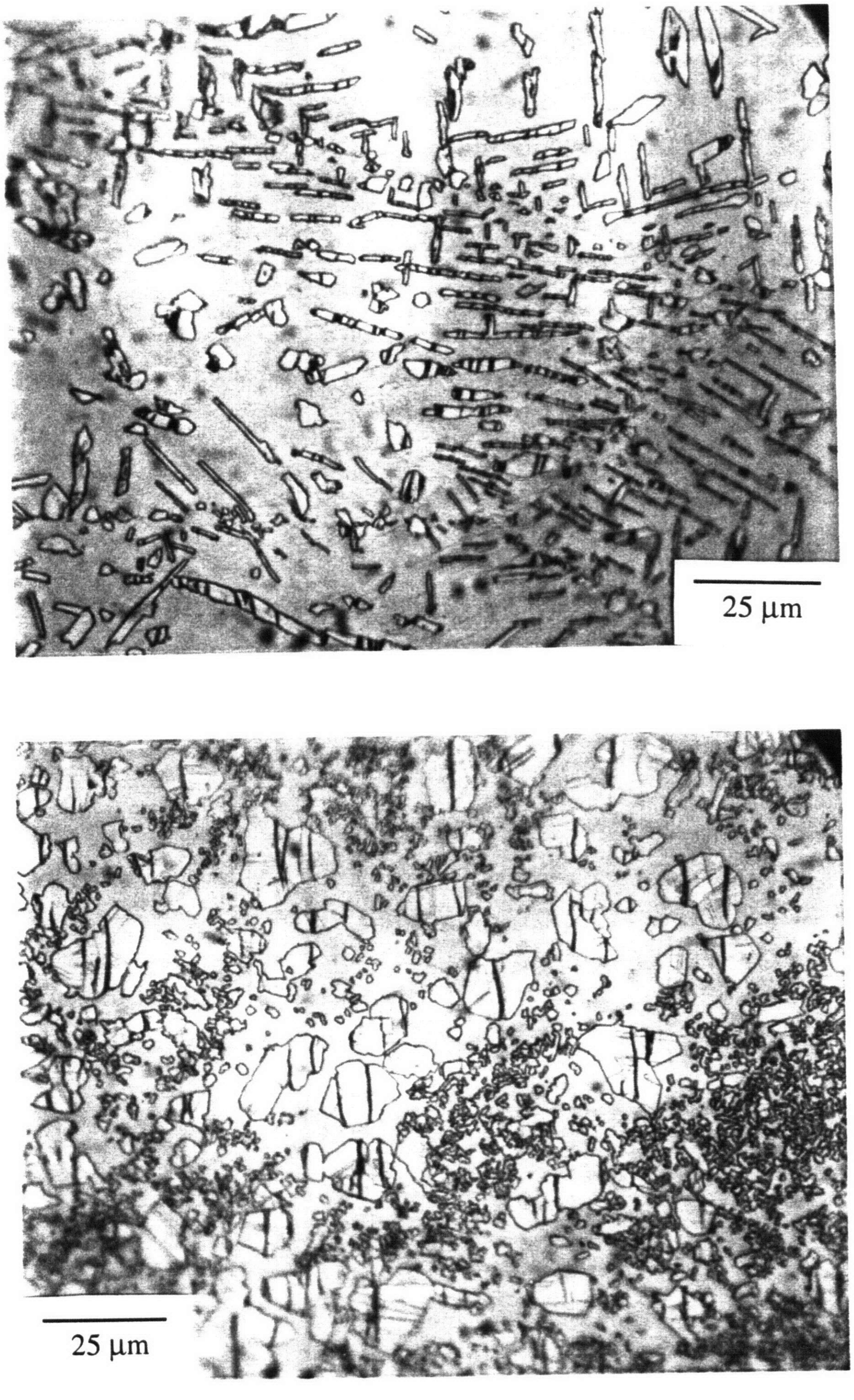

Figure 5.11 Optical micrographs of the compressed Ti-rich, two-phase alloys: **(a)** Ti-30 Cr and **(b)** Ti-40 Cr alloys. Cracks in the $TiCr_2$ Laves phase run parallel to the compression axis.

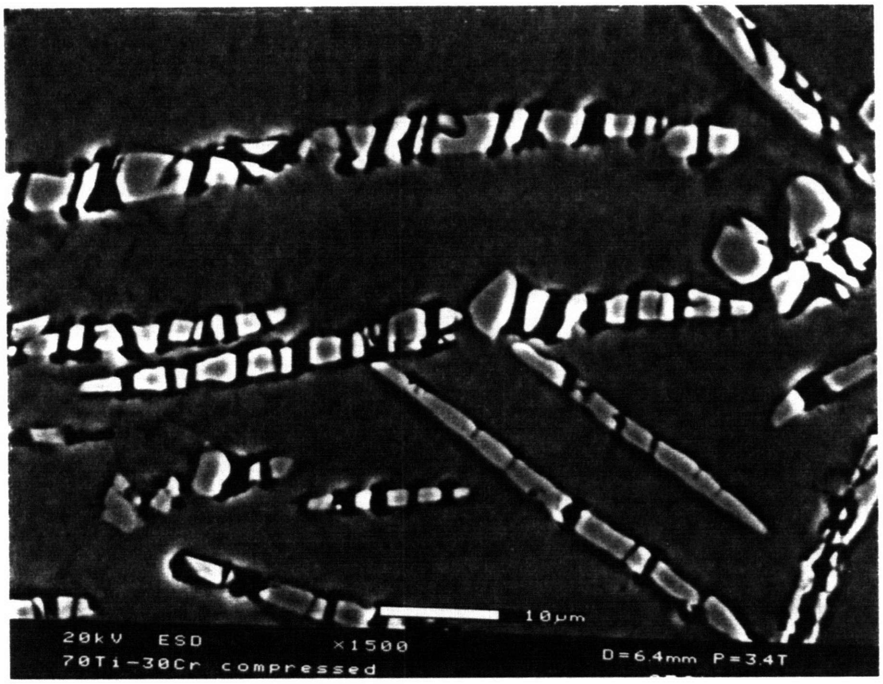

Figure 5.12 SEM of the compressed two-phase Ti-30 Cr alloy, showing multiple cracks confined to the lath-shaped $TiCr_2$.

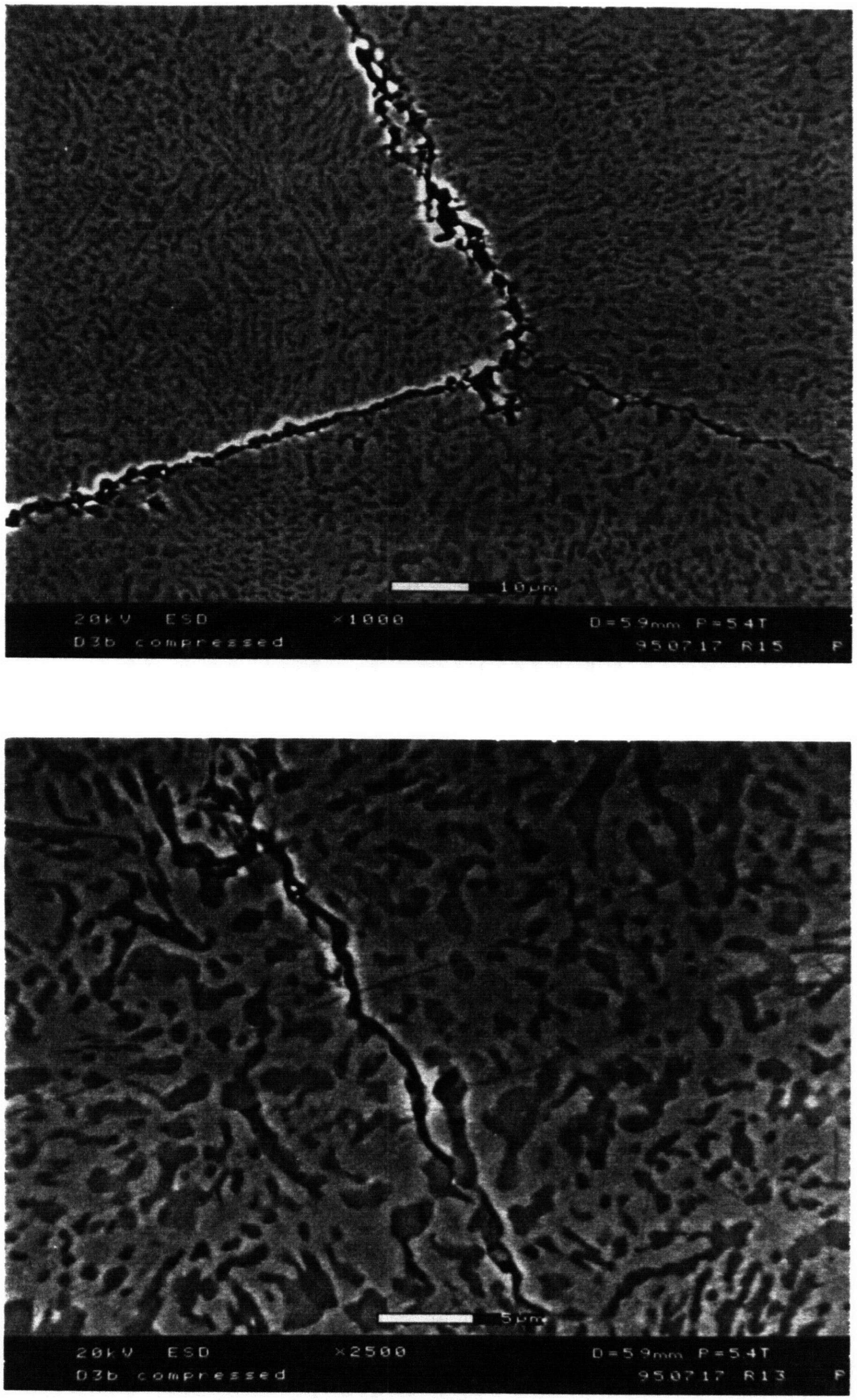

Figure 5.13 SEM of the compressed Ti-80 Cr alloy sample. Cracks run through both the beta and Laves phase shown at **(a)** 1000X and **(b)** 2500X.

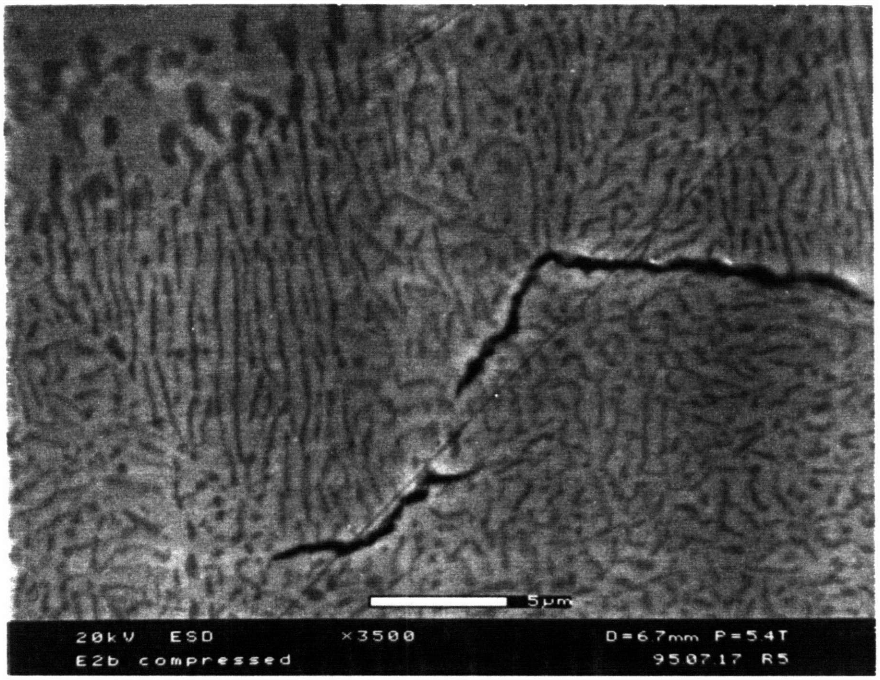

Figure 5.14 SEM of cracks in the Ti-87.5 Cr alloy from room-temperature compression.

5.4.2 Deformation of the Laves phase

Another purpose of the compression tests was to study the possibility of the deformation of the $TiCr_2$ Laves phase itself. Microcracking and plastic flow compete as sources of inelastic response [28]. By putting the Laves phase into a two-phase system, the Laves particles are constrained by the surrounding matrix phase and may be able to deform before failure.

Some deformation of $TiCr_2$ appeared to have occurred, although it was not extensive. No changes in the Laves crystal structure were found, in contrast to the Fe+$ZrFe_2$ system (which experiences a *C*36 to *C*15 transformation) [12], but the $TiCr_2$ in the Ti-rich alloys was already at the equilibrium *C*15 crystal structure.

TEM analysis of the compressed samples of the Ti-rich alloys showed heavy deformation in the matrix and some signs of deformation in the Laves phase. The matrix

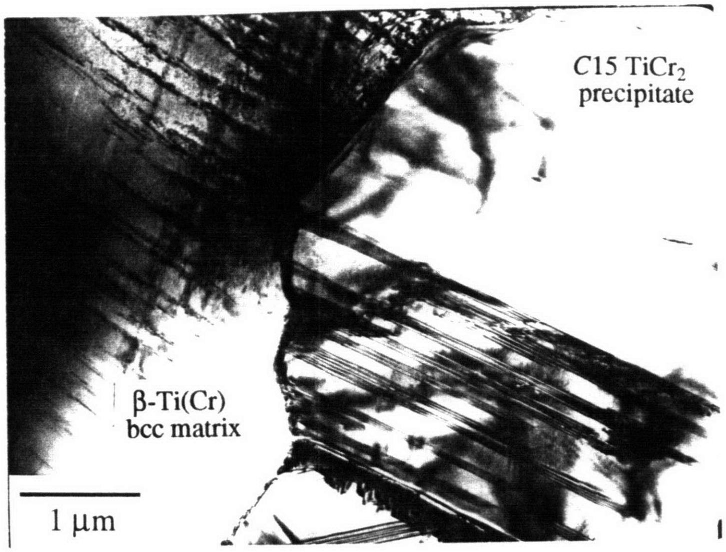

Figure 5.15 TEM of dislocations and slip bands in the bcc matrix, near the $TiCr_2$ Laves phase in the Ti-40 Cr alloy.

contained significant amounts of dislocations concentrated in slip bands, tangles, and networks (Figure 5.15). Because the Laves precipitates were dispersed throughout the alloy, distribution of the compressive stresses becomes quite complex and nonuniform. This may explain the lack of correlation between the dislocation slip bands in the matrix and the faults in the Laves phase. Also, no apparent correlation of the direction of faults and twins among the Laves phase particles could be found.

Although some faulting was present in the undeformed condition of $TiCr_2$, the deformed samples appeared to have more complex faulting and twinning. Figure 5.16 depicts the interaction of different defects. The change in direction or orientation of faults across twin boundaries suggests some type of interaction or sequence of defect formation. Possibly the faults were reoriented with the deformation that produced the twins, or the fault had to change directions when traversing through the twin.

The abundance of twins indicates that twinning may be an important deformation mechanism in Laves phases, as has been found in other studies [11]. The precipitate/matrix interface was often jagged or protruding where there was a twin band. Figure 5.17 shows dislocation pile-ups in the matrix near a twin boundary that suggest that these twins came from the deformation rather than from growth or annealing.

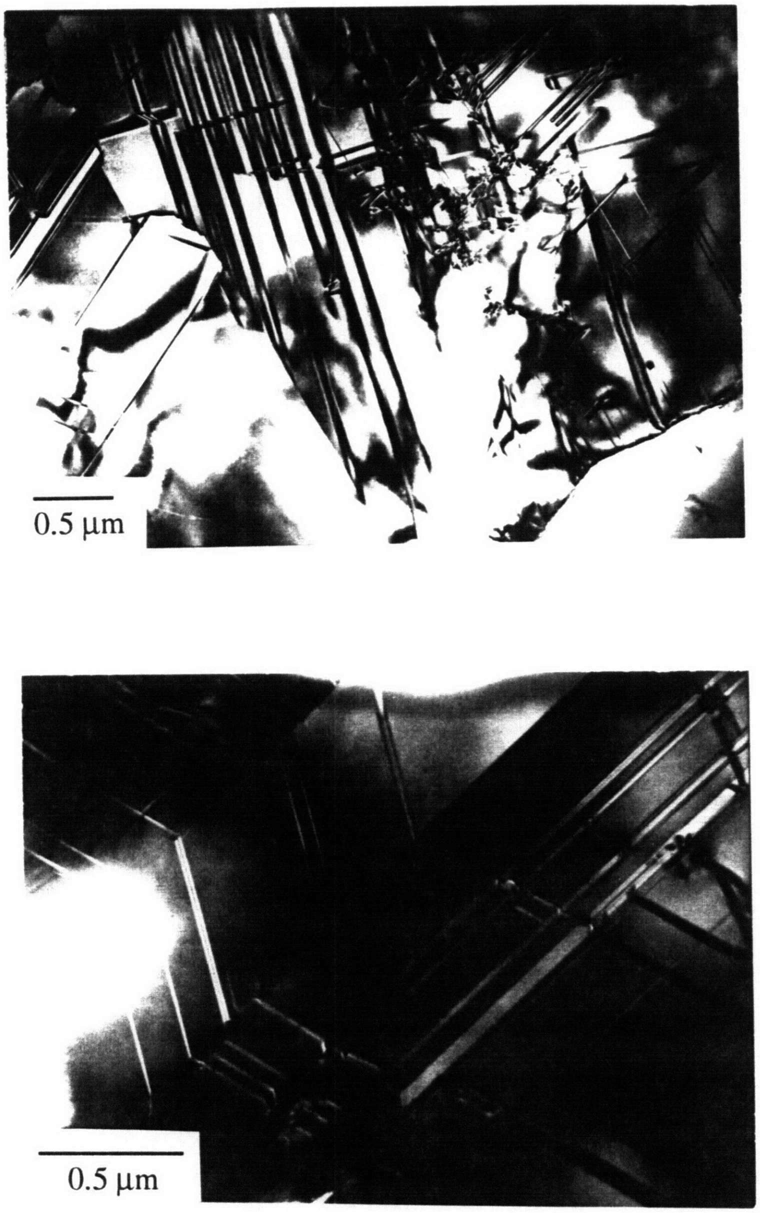

Figure 5.16 TEM images of compressed Laves phases found in the annealed **(a)** Ti-40 Cr alloy and **(b)** Ti-30 Cr alloy. Twins conform to the {111}<112> system.

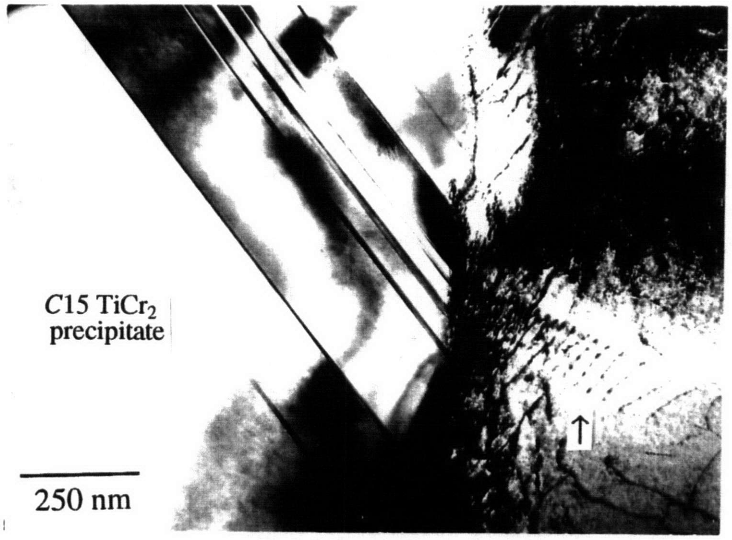

Figure 5.17 Dislocation pile-ups in the bcc matrix, near a twin boundary in the $TiCr_2$ Laves phase.

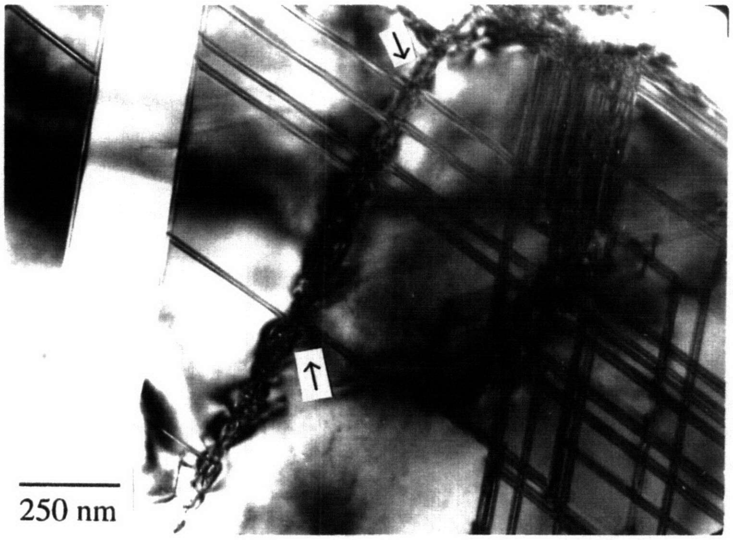

Figure 5.18 Faults displaced about 20 nm across the shear band in the deformed $TiCr_2$.

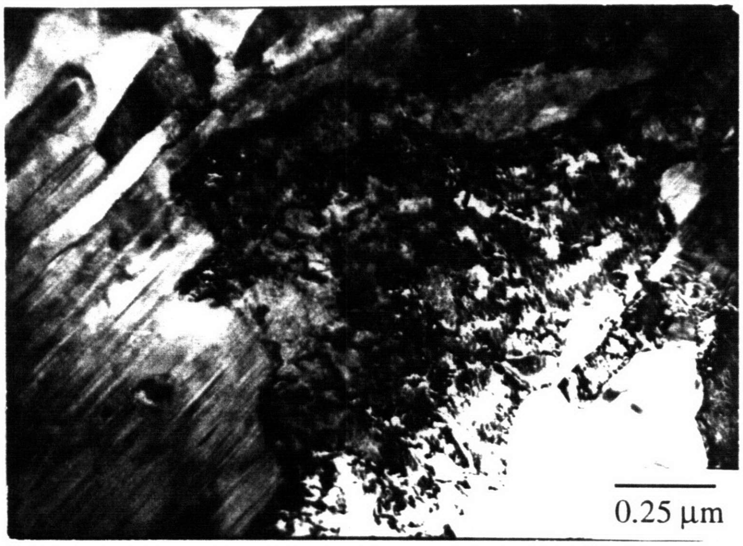

Figure 5.19 TEM of the compressed Ti-80 Cr alloy annealed at 1000°C.

Occasionally one could find areas of concentrated dislocation structure in the Laves phase, as in Figure 5.18. Livingston [11] termed these planar defects as "shear bands", which form subgrain boundaries and mark areas of intense shear. Such defects have been documented in the *C*15 HfV_2 in V-Hf-Nb alloys. Faults were seen to be sheared or displaced across the shear bands.

The Cr-rich alloys, however, contained highly faulted $TiCr_2$ after annealing, and thus comparisons of $TiCr_2$ between undeformed and compressed samples were fruitless. The only significant differences were the dislocations in the matrix phase of the deformed alloys, as seen in Figure 5.19.

5.4.3 Fracture surfaces

SEM images of the fractured surfaces of the compressed Cr-rich, two-phase alloys are shown in Figures 5.20-5.22. Generally, a corner piece or the complete side of a compression sample fell apart during the compression test. A loud pop was heard, and a rapid load drop followed. Several of the Cr-rich alloys shattered into fine bits without warning. The visual appearance of the fracture surfaces was granular and shiny. The brittle-to-ductile transition temperature of $TiCr_2$ has been reported to be around 700°C by hot hardness tests [14], and thus the room-temperature brittleness of the alloys is expected.

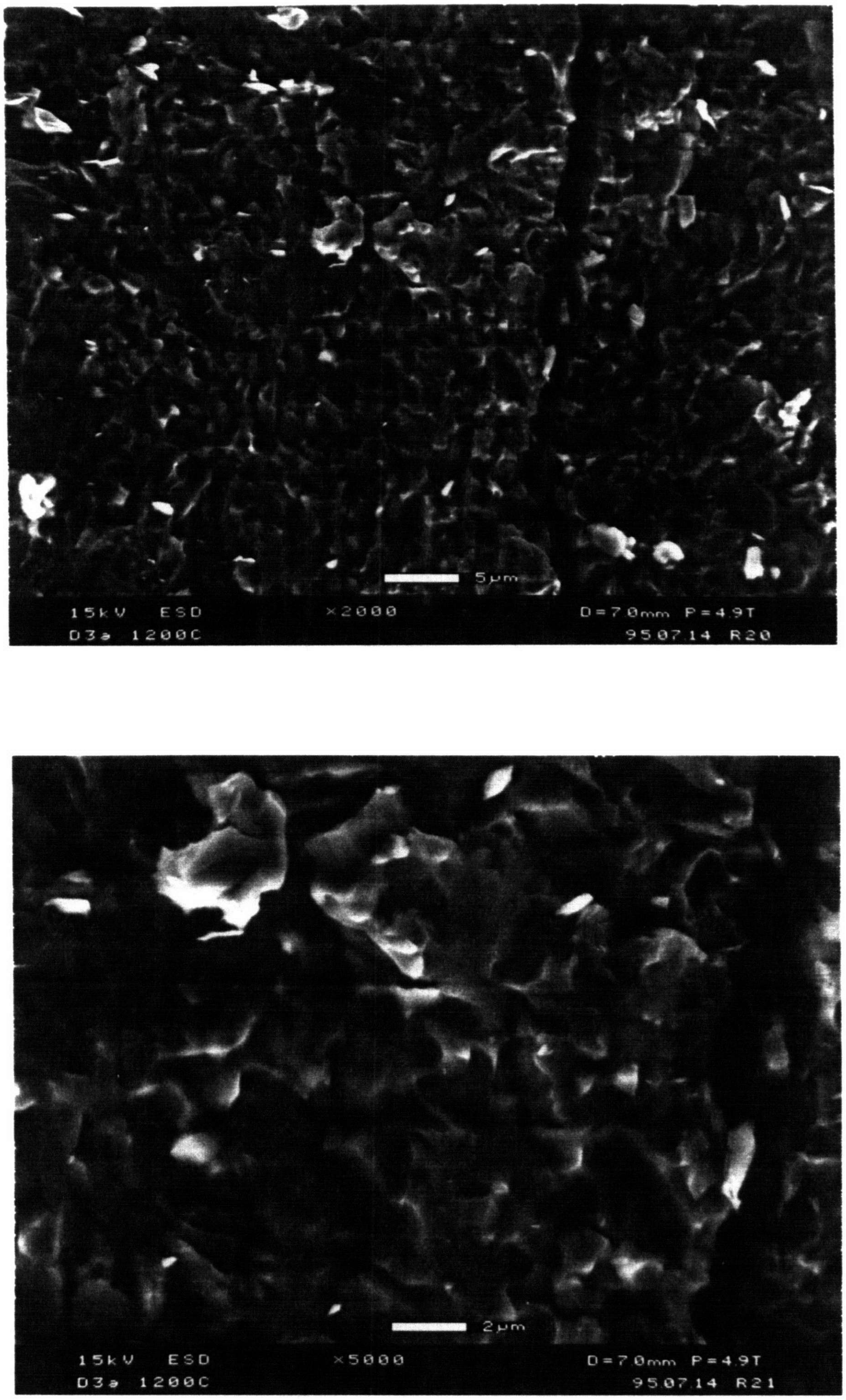

Figure 5.20 SEM images of the fracture surface of the Ti-80 Cr alloy annealed at 1200°C from compression testing at room-temperature at **(a)** 2000X and **(b)** 5000X.

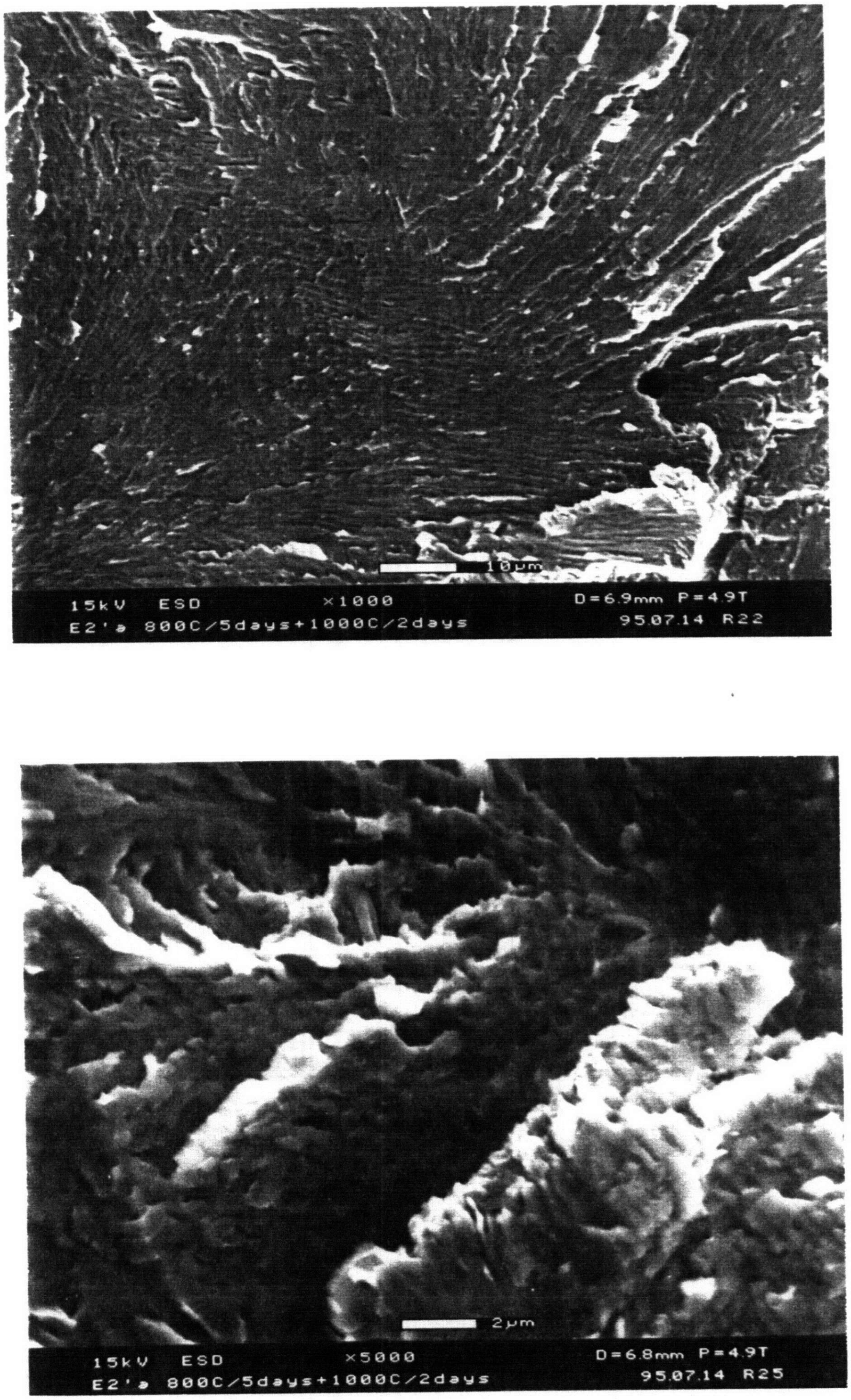

Figure 5.21 SEM images of the transgranular cleavage fracture surface found in the Ti-87.5 Cr alloy annealed at 1000°C at **(a)** 1000X and **(b)** 5000X.

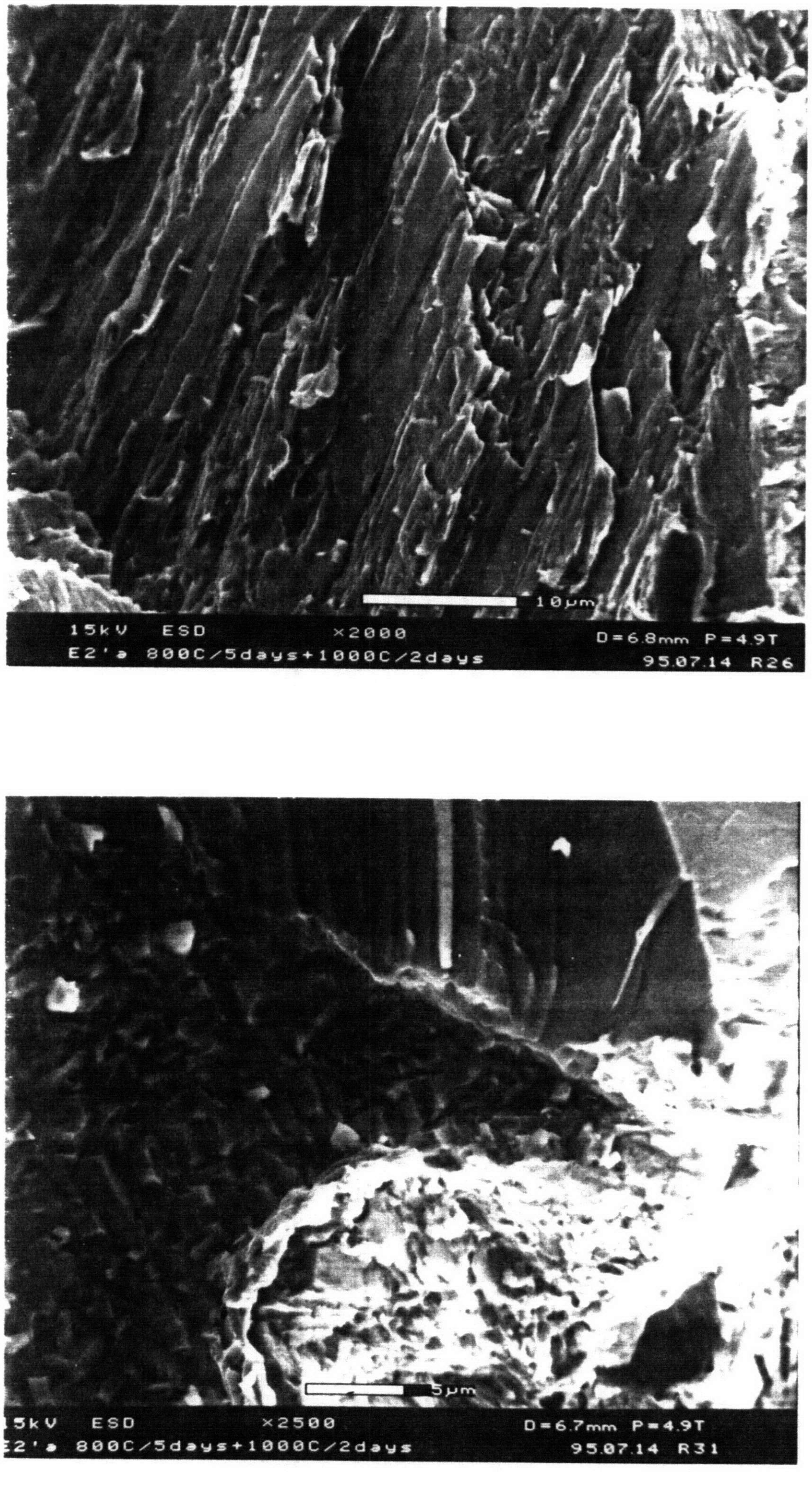

Figure 5.22 SEM of the fracture surface (**a**) parallel and (**b**) transverse to the lamellar structure in the Ti-87.5 Cr alloy.

Figures 5.20 and 5.21 show transgranular cleavage of the fractured Ti-80 Cr alloy annealed at 1200°C and Ti-87.5 Cr alloy annealed at 1000°C, respectively. Cleavage steps can also be seen. Step formation restrains the propagation of brittle cracks by absorbing extra energy [29]. Distinctive of brittle fracture, transgranular cleavage is usually associated with particular crystallographic planes [30]. Microcracks may be formed during the deformation during compression [31] and these, as well as pre-existing cracks, may propagate with higher applied stresses. The Griffith theory of brittle fracture predicts that a crack will propagate when the decrease in elastic strain energy at least equals the energy to create a new crack surface. Thus, although the Cr-rich, two-phase alloys containing $TiCr_2$ are tougher than the single-phase $TiCr_2$ (as demonstrated by indentation), they still experience brittle fracture.

The fracture surfaces also reveal the two-phase microstructure. The lamellar structure in the annealed Ti-87.5 Cr alloy is evident in Figure 5.22 (a). The fracture surface runs parallel along the lamellae, resulting in the faceted appearance. A fracture surface transverse to the lamellae can also be seen in Figure 5.22 (b).

5.5 DISCUSSION OF TWO-PHASE Ti-Cr ALLOYS

The assessment of the mechanical properties of the two-phase Ti-Cr alloys has clearly demonstrated greater deformability in comparison with the single-phase $TiCr_2$ alloys. Overall strengths are compromised but some degree of toughness can be achieved by incorporating the Laves phase in a two-phase system. With the more ductile beta phase as the major, continuous phase, large plastic strains in compression tests are possible. $TiCr_2$ Laves phase precipitates were even seen to deform when contained in the Ti-rich alloys.

In the Ti-rich, two-phase alloys, cracking was confined to the large $TiCr_2$ precipitates after indentation and compression tests. The Ti-rich β solid solution phase effectively blunted the crack propagation. On the other hand, cracks ran through the entire two-phase structure of the Cr-rich, two-phase alloys (although crack deflection and bridging did occur). The Cr-rich β solid solution is stronger but more brittle than the Ti-rich β compositions. The Cr-rich, two-phase alloys had impressive high hardness and fracture toughness values, but also failed in compression without much plasticity and displayed brittle transgranular cleavage fracture. The Cr-rich alloys also had an interconnected $TiCr_2$ phase, which likely contributed to the lower deformability than the Ti-rich alloys.

Thus, the microstructure of the two-phase alloys plays an important part in the overall properties.

The mechanical properties of the two-phase alloys are also dependent on the $TiCr_2$ volume percentage, as both the microhardness values and the stress-displacement curves revealed strengthening of the beta phase with precipitation of the Laves phase. A critical $TiCr_2$ volume percentage also appeared necessary for cracking to occur by indentation.

Various microstructures can be attained by varying alloy compositions and annealing treatments (as described in Chapter 4). The size, shape, distribution, and volume percent of the $TiCr_2$ Laves phase and the properties of the second phase have all been found to affect the mechanical properties of the two-phase system. These same factors will also be important for the development of other two-phase Laves systems. Currently, two-phase Laves systems reach fracture toughness values below about 10 MPa $m^{1/2}$.

5.6 REFERENCES

1. J.D. Livingston, phys. stat. sol. (a), **131**, 415 (1992).
2. D.L. Anton and D.M. Shah, *Mat. Res. Soc. Symp. Proc. Vol 194*, 45 (1990).
3. S. Mazdiyasni and D.B. Miracle, *Mat. Res. Soc. Symp. Proc. Vol 194*, 155 (1990).
4. W. Wunderlich, L. Machon, and G. Sauthoff, Z. Metallk., **83**, 679 (1992).
5. M.P. Brady, J. L. Smialek, and D.L. Humphrey, *Mat. Res. Soc. Symp. Proc. Vol 364*, 1309 (1995).
6. B.P. Bewlay, J.A. Sutliff, M.R. Jackson, and H.A. Lipsett, Acta Met. et Mater., **42**, 2869 (1994).
7. T. Takasugi, S. Hanada, and K. Miyamoto, J. Mater. Res., **8**, 3069 (1993).
8. M. Takeyama and C.T. Liu, Mat. Sci. & Eng., **A132**, 61 (1991).
9. V.M. Azhazha, A.P. Berdnik, A.P. Svinarenko, and A.I. Somov, Flz. metal. metalloved., **41**, 402 (1976).
10. K.S. Kumar and D.B. Miracle, Intermetallics, **2**, 257 (1994).
11. J.D. Livingston and E.L. Hall, J. Mater. Res., **5**, 5 (1990).
12. Y. Liu, J.D. Livingston, and S.M. Allen, Metall. Trans., **23A**, 3303 (1992).

13. Y. Liu, J.D. Livingston, and S.M. Allen, Metall. Trans., **26A**, 1107 (1995).

14. R.L. Fleischer and R.J. Zabala, Metall. Trans., **21A**, 2149 (1990); **21A**, 1951 (1990).

15. G. Sauthoff, Z. Meallk., **80**, 337 (1989); **81**, 855 (1990).

16. F.B. Cuff, N.J. Grant, and C.F. Floe, Trans. AIME, **194**, 848, (1952).

17. D.J. McPherson and M.G. Fontana, Trans. ASM, **43**, 1098 (1951).

18. R.L. Fleischer, Scripta Met., **21**, 1083 (1987).

19. J.P. Nic, S. Zhang, and D.E. Mikkola, Scripta Metall. et Mater., **24**, 1099 (1990).

20. R.L. Fleischer, R.S. Gilmore, and R.J. Zabala, J. Appl. Phys., **64**, 2964 (1988).

21. D.J. Thoma, Ph.D. Thesis, U. of Wisconsin, (1992).

22. R.W. Hertzberg, *Deformation and Fracture Mechanics of Engineering Materials,* Wiley, (1976).

23. M.F. Ashby, F.J. Blunt, and M. Bannister, Acta Metall., **37**, 1847 (1989).

24. K.S. Ravichandran, D.B. Miracle, and M.C. Mendiratta, *Mat. Res. Soc. Symp. Proc. Vol. 350*, 249 (1994).

25. B.P. Bewlay and M.R. Jackson, submitted to the Journal of Material Research.

26. M.R. Jackson, B.P. Bewlay, R.G. Rowe, D.W. Skelly, and H.A. Lipsitt, JOM, **48**, 39 (1996).

27. M.D. Bhandarkar, M.S. Bhat, V.F. Zackay, and E.R. Parker, Metall. Trans., **6A**, 1281 (1975).

28. H. Horii and S. Nemat-Nasser, Phil. Trans. R. Soc. Lond., **A319**, 337 (1986).

29. B. Lawn, *Fracture of Brittle Solids,* 2nd edition, Cambridge University Press, (1993).

30. *Metals Handbook, Volume 12 Fractography*, 9th edition, ASM International, (1987).

31. G.E. Dieter, Mechanical Metallurgy, 3rd edition, McGraw-Hill Book Company, (1996).

Chapter 6

Ternary $TiCr_2$-base Laves phase alloys

6.1 INTRODUCTION

Most Laves phases will accept alloying elements in solution, and in some systems, ternary Laves phases form despite the absence of binary Laves compounds [1]. Alloying of intermetallics can be used for solid-solution strengthening or for introducing elements for high-temperature properties such as oxidation or creep resistance [2]. Much excitement was generated with the improved ductility of the Ni_3Al intermetallic when alloyed with small amounts of B [3]. However, widely-accepted explanations for the phenomenon and the use of alloying to improve the ductility of other intermetallics has been lacking.

There have been scattered reports of increased ductility in Laves phase alloys with the addition of a third element, such as Ni added to $MgCu_2$ [4], Mo to $SmFe_2$ [5], and Ti to $NbCr_2$ [6]. Inoue et al. [7] reported that Nb and Ti additions improved deformability (by rolling at room temperature) of two-phase alloys containing HfV_2-base Laves phases. Livingston and Hall [8] proceeded to show enhanced twinning of the HfV_2-base Laves phase when alloyed with Nb and Ti. They proposed that alloying elements that substitute on both the A and B sublattice sites of AB_2 Laves phases would enhance deformability. Lowering the stacking fault energy by alloying was also suggested to enhance the mechanical twinning (as seen in Cu alloyed with Zn, Al, or Ge [9]). Laves phases near the hexagonal-cubic structure transition point may also experience "transformation toughening" for added deformability and toughness. Questions remained whether HfV_2 was unique due to a lattice instability or if other Laves phases could be made more tough by similar alloying. No published study has purposely alloyed a Laves phase for controlled lattice site substitutions and crystal structure stabilization in attempts to increase the toughness of Laves phases.

The effects of alloying $TiCr_2$ with a third element will be studied systematically in this chapter. Specific alloying elements were chosen to substitute for the Ti atom, the Cr atom, and both atoms simultaneously, in order to investigate the effect of site substitution. The stacking fault energies are also varied, as the alloying element can affect the equilibrium crystal structure due to the electron concentration. After a thorough review of possible alloying elements, four were selected on the basis of atomic radius [10], electronegativity [11], other Laves phases formed, and the available ternary phase diagrams in the literature (Table 6.1).

Fe has a smaller radius than Cr and a continuous $TiCr_2$-$TiFe_2$ solid solution exists, indicating that Fe will substitute for the Cr atom. Likewise, Nb will most likely substitute for Ti due to Nb's slightly larger radius than Ti and the continuous solid solution between $TiCr_2$ and $NbCr_2$. The nominal compositions of the Fe and Nb ternary alloys were chosen for the alloying element to substitute up to about 50% of the appropriate sublattice sites. Neither V nor Mo form a Laves phase with Ti or Cr, and both V and Mo are intermediate in size with Ti and Cr. These two elements were selected as possible candidates to occupy both Ti and Cr sublattices. The nominal alloy compositions of the Ti-V-Cr and Ti-Mo-Cr alloys were designed to test the capacity to accommodate the alloying element preferably on one sublattice over another and to examine the solubility limits of the ternary Laves phases.

Table 6.1 Possible atom sites of alloying elements in ternary $TiCr_2$-base Laves phases based on radius, electronegativity and other Laves phases formed.

element	radius (Å)	electro-negativity	other Laves phases	atom site	ternary Laves
Ti	1.46	1.3			
Nb	1.47	1.35	$NbCr_2$	Ti	$(Ti,Nb)Cr_2$
V	1.35	1.75	---	Ti,Cr?	$(Ti,V)(V,Cr)_2$?
Mo	1.40	1.85	---	Ti,Cr	$(Ti,Mo)(Mo,Cr)_2$
Fe	1.27	1.85	$TiFe_2$	Cr	$Ti(Fe,Cr)_2$
Cr	1.28	1.7			

The ternary alloys are first characterized in terms of microstructures, solubility limits, and crystal structures. The atomic-substitution site of the alloying elements is also identified. Mechanical properties from indentation tests of the ternary $TiCr_2$-base Laves phases are then presented and extend the knowledge base of $TiCr_2$ alloys from the previous chapters. Effects of the alloying elements, alloying concentration, and atomic-site occupancy are investigated. Changes in the stacking fault energy and lattice size of the $TiCr_2$-base Laves phases are also studied in relation to the changes in mechanical properties. The several different possible factors affecting the toughness of $TiCr_2$ are discussed.

6.2 EXPERIMENTAL PROCEDURES

The same experimental procedures of the binary Ti-Cr alloys were repeated for the $TiCr_2$-base Laves phase ternaries. The ternary alloys were arc-cast at Ames Laboratory, where the alloying element and Ti were first melted together before the highly-volatile Cr was added. The oxygen and nitrogen contents of the ternaries were in the same ranges as the binary alloys except for the Fe alloys, which contained slightly more oxygen than the other alloys (200-250 ppm).

Annealing treatments and metallographic procedures followed those described in Chapter 2. Electron microprobe analysis on V-containing alloys was slightly more difficult due to the overlap of Ti and Cr energy dispersion peaks. (Since Ti, V, and Cr are consecutive in the periodic table, the L-line of Ti interferes with the K-line of V, and then the L-line of V coincides with the K-line of Cr.) Compositions of the V alloys were adjusted according to the known relative peak areas of the K and L-lines of each element. X-ray diffraction on powder samples with a Si standard was used to determine the crystal structures and lattice constants.

Mechanical properties were again assessed by indentation to measure the hardness and fracture toughness of the ternary Laves phases. A weighted average was computed for the elastic modulus needed in the equation for fracture toughness (Chapter 3) for the ternary Ti-Nb-Cr and Ti-Fe-Cr Laves phases. A value of 235 GPa for $TiCr_2$ and 260 GPa for $NbCr_2$ were taken from Thoma's indentation work [6], and a weighted average of 180 GPa was estimated for $TiFe_2$. No adjustments to the elastic modulus were made for the Ti-V-Cr and Ti-Mo-Cr alloys since the amounts of V and Mo were relatively small and therefore should not change the modulus significantly.

6.3 CHARACTERIZATION

6.3.1 Microstructures

The as-cast Ti-Nb-Cr, Ti-V-Cr and Ti-Mo-Cr alloys were dendritic (Figures 6.1-6.3) and were thus subjected to a homogenization treatment at 1395°C for 24 hours. However, no single-phase beta field existed for the Ti-Nb-Cr alloys and the dendritic structure persisted for the Nb-rich alloys.

The as-cast Ti-Fe-Cr alloys were not dendritic and were heat treated at 1300°C for 15 hours. The Fe alloys were almost entirely single-phase, with small amounts of a second phase along the grain boundaries, as seen in Figure 6.4. The microstructures of the Fe alloys were featureless, except for numerous cracks. The as-cast and annealed alloys were very brittle, and cracks persisted throughout polishing steps. Quenching effects and the high oxygen content may have contributed to the apparent high brittleness of the Fe alloys. Compositions of the Fe alloys are found in Table 6.2.

The microstructure of the as-cast Ti-15 Nb-Cr alloy in Figure 6.1(b) shows a more rod-like morphology of the dendrites than the other Nb alloys. Thoma [6] also noted such a morphological trend with Nb-rich, Ti-Nb-Cr alloys. Separate annealing treatments at 1300°C and 1200°C for 6 hours each were performed on the Nb alloys. The dendritic structures were not fully dissolved, but fairly uniform regions were produced in the low Nb-content alloys (Figure 6.5). Compositions of the Ti-Nb-Cr Laves phases annealed at 1300°C are listed in Table 6.3. The compositions for the 15 Nb alloy are averaged from the center and edge of the dendrite. The back-scattered electron images from EMPA of the 15 Nb alloy in Figure 6.6 show varying contrast, and thus varying compositions within the Laves phase. (The small black areas are beta particles rather than voids.) Small amounts of a Cr-rich second phase were present in all the alloys. The Nb alloys also contained numerous faults, as seen in Figure 6.7. Faulting in Ti-Nb-Cr Laves phases have been documented by others [6] and has been suggested to be caused by a $C14 \rightarrow C15$ transformation.

The microstructures of the V and Mo alloys revealed limited solubility of the alloying elements in $TiCr_2$, as several of the annealed alloys contained two phases. The microstructures are described in Tables 6.4 and 6.5. (The different alloy compositions are given names in the Tables for easier identification.) Annealing treatments at 1300°C for 6 hours, 1200°C for 45 hours, and 1000°C for 48 hours were performed on most of the V

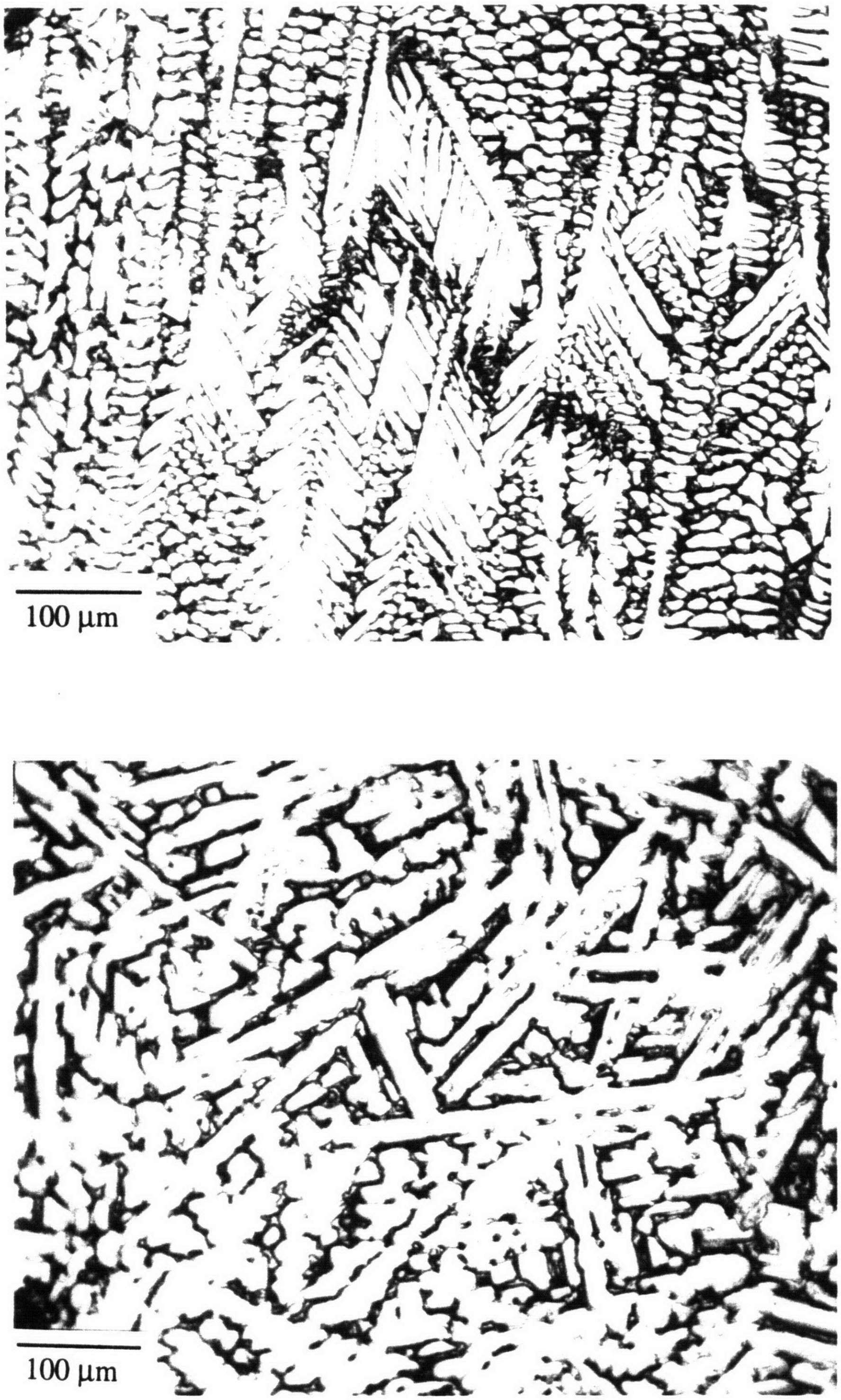

Figure 6.1 Optical micrograph of the **(a)** Ti-10 Nb-Cr and **(b)** Ti-15 Nb-Cr dendritic as-cast alloys.

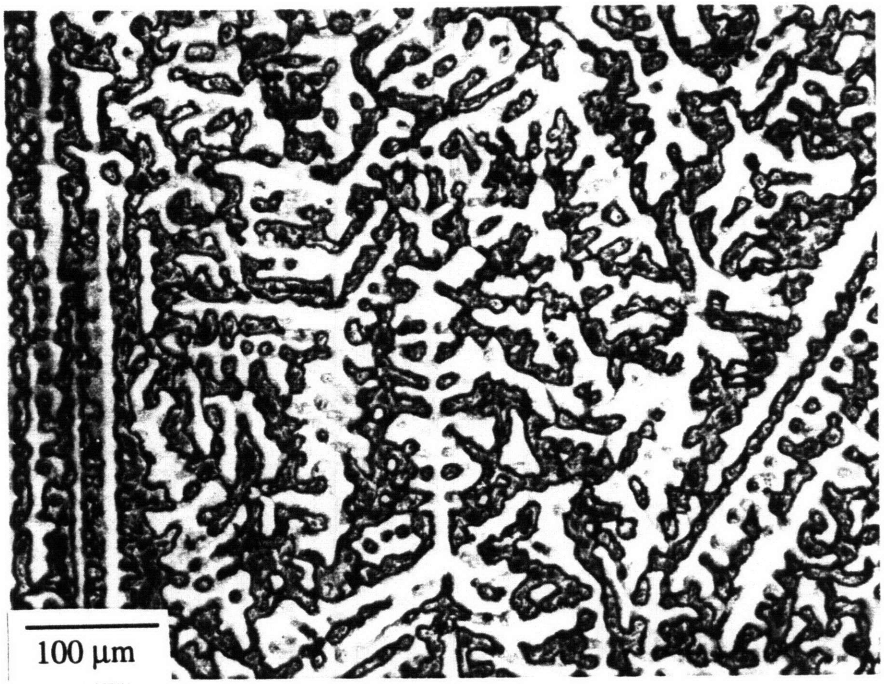

Figure 6.2 Optical micrograph of the as-cast Ti-V-Cr alloy.

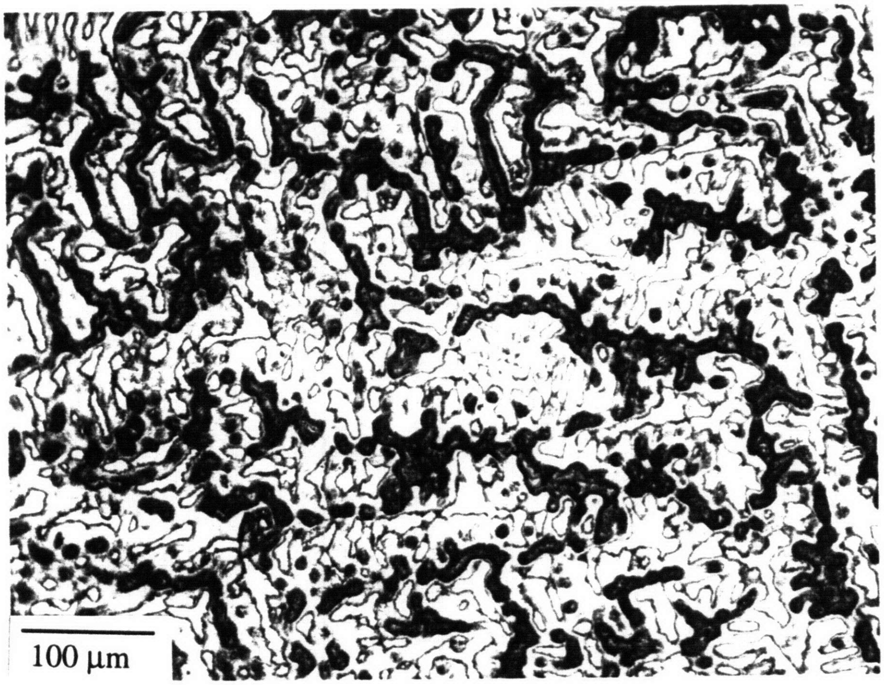

Figure 6.3 Optical micrograph of the as-cast Ti-Mo-Cr alloy.

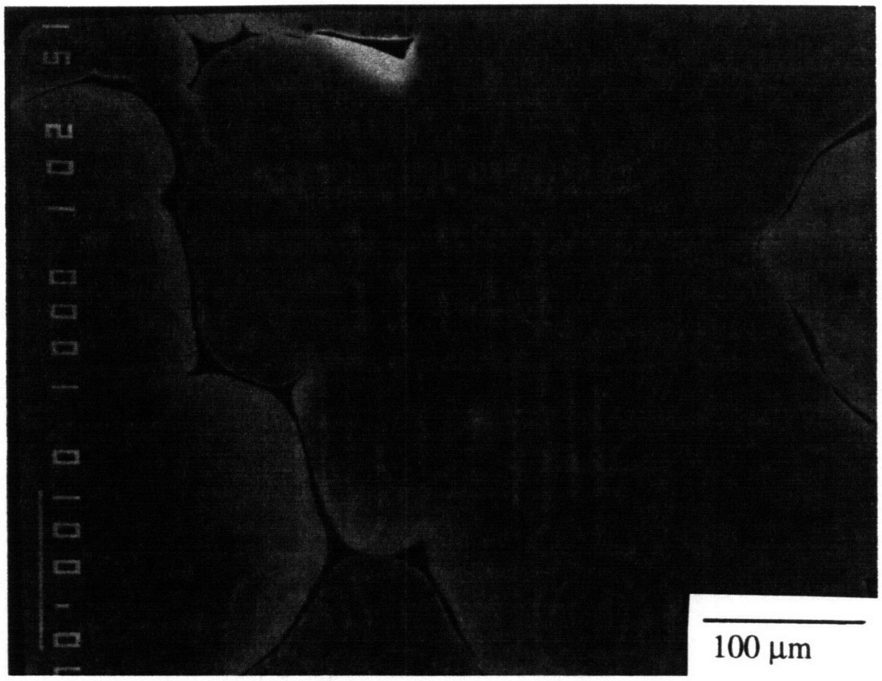

Figure 6.4 The nearly single-phase Ti-10 Fe-Cr alloy.

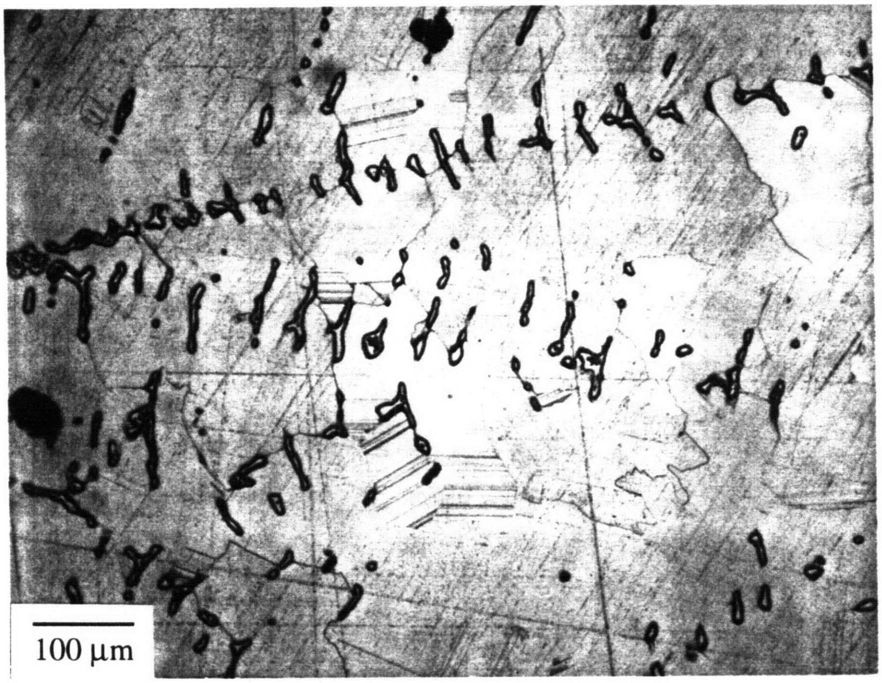

Figure 6.5 The Ti-5 Nb-Cr alloy annealed at 1300°C.

Table 6.2 Compositions of Ti-Fe-Cr Laves phase alloys by electron microprobe analysis (EMPA).

target alloy composition (at%)	ICP-AES composition (at%)	Ti (at%)	Fe (at%)	Cr (at%)	(Fe+Cr)/Ti	second phase?
33Ti-10Fe-57Cr	34.0Ti-9.9Fe-56.1Cr	34.95 ± 0.15	10.32 ± 0.06	54.73 ± 0.13	1.86	none
33Ti-20Fe-47Cr	32.6Ti-19.2Fe-48.2Cr	33.67 ± 0.16	19.95 ± 0.09	46.37 ± 0.21	1.97	Ti-rich
33Ti-30Fe-37Cr	32.4Ti-29.3Fe-38.3Cr	33.47 ± 0.15	29.91 ± 0.16	36.62 ± 0.16	1.99	Ti-rich

Table 6.3 Compositions of ternary Ti-Nb-Cr Laves phase alloys by electron microprobe analysis (EMPA).

target alloy composition (at%)	Ti (at%)	Nb (at%)	Cr (at%)	Cr/(Ti+Nb)	second phase?
28Ti-05Nb-67Cr	28.59 ± 0.09	5.40 ± 0.19	66.01 ± 0.19	1.94	Cr-rich
23Ti-10Nb-67Cr	23.65 ± 0.51	10.24 ± 0.57	66.11 ± 0.14	1.95	Cr-rich
18Ti-15Nb-67Cr	(ave.) 17.45 ± 1.49	16.46 ± 1.69	66.09 ± 0.22	1.95	Cr-rich
(A) center of dendrite	(A) 16.08 ± 0.26	18.01 ± 0.33	65.91 ± 0.12	1.93	
(B) edge of dendrite	(B) 18.81 ± 0.37	14.91 ± 0.37	66.28 ± 0.09	1.97	

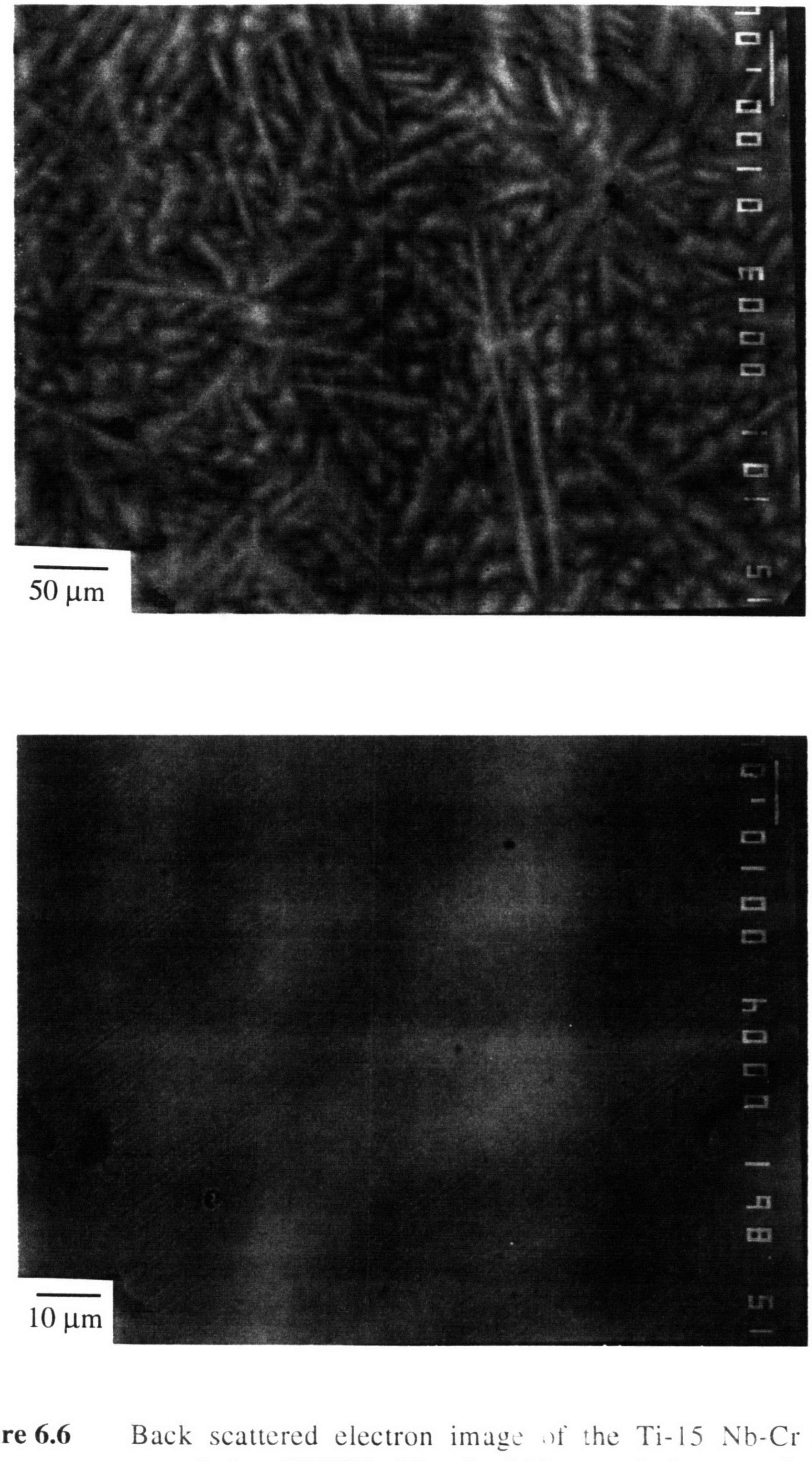

Figure 6.6 Back scattered electron image of the Ti-15 Nb-Cr alloy annealed at 1300°C. The dendritic morphology persists and chemical inhomogeneities exists in areas of varying contrast.

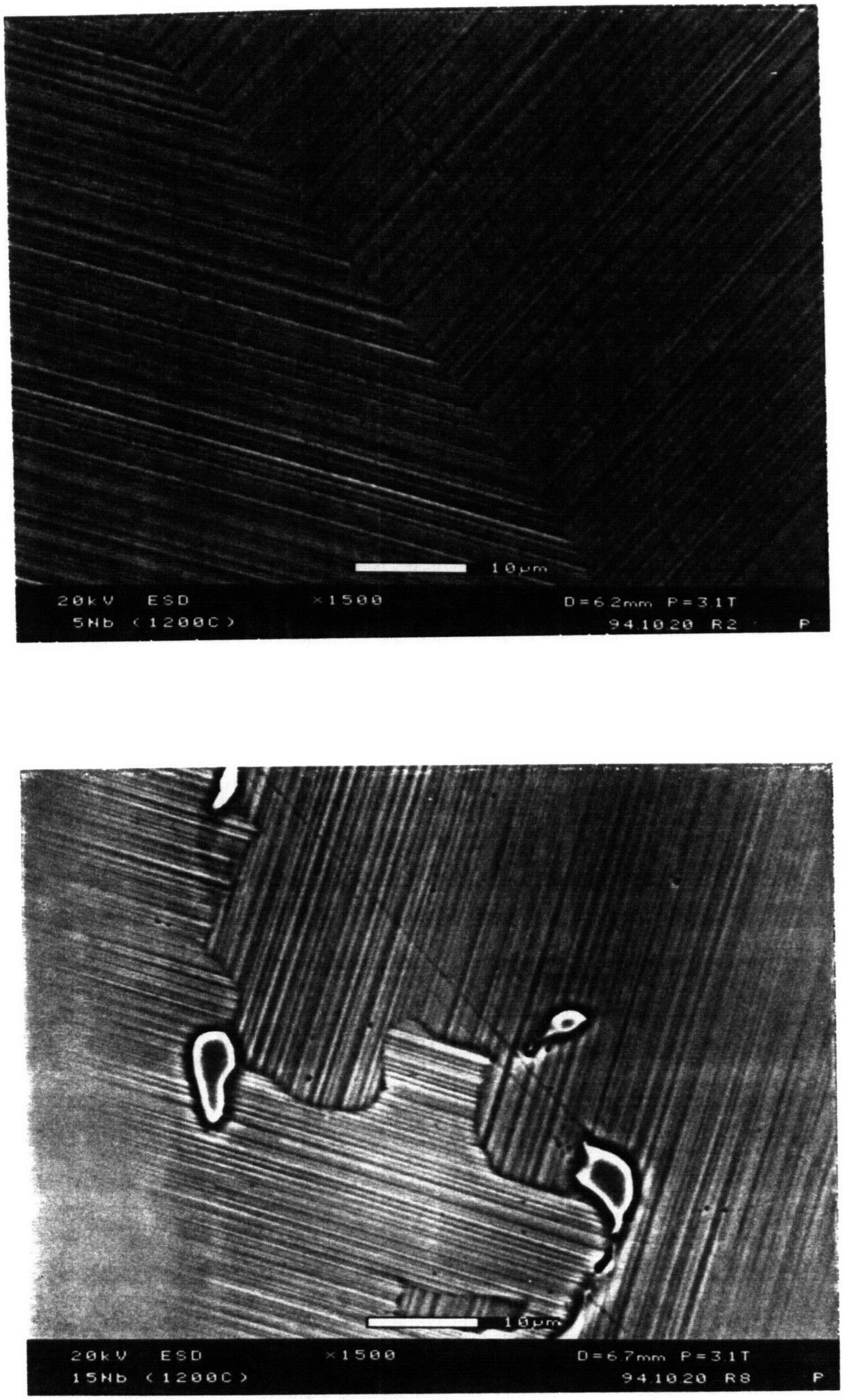

Figure 6.7 Numerous faults in the **(a)** Ti-5 Nb-Cr alloy and **(b)** Ti-15 Nb-Cr alloy, both annealed at 1200°C.

Table 6.4 Microstructures, crystal structures, compositions, and lattice constants of Ti-V-Cr alloys.

alloy (target composition)	Temp	microstructure	crystal structure	Laves phase composition (at%)	Laves Cr/Ti	Laves lattice constant (Å)	beta phase composition (at%)	beta lattice constant (Å)
4V2	1300°C	coarse 2-phase large Laves ppt.	*C*14 + β	34.7Ti-2.3V-63.0Cr	1.82	a=4.9281±0.0003 c=7.9580±0.0005	30.7Ti-6.1V-63.2Cr	a=2.957
31.8Ti-4.5V-63.7Cr	1200°C	two-phase fine beta ppts.	*C*15/(*C*36)+β	33.9Ti-3.7V-62.4Cr	1.84	a=6.947±0.001	20.1Ti-12.1V-67.8Cr	a=2.957
	1000°C	two-phase fine beta ppts.	*C*15 + β	32.7Ti-4.4V-62.9Cr	1.93	a=6.942±0.002	---	a=2.93
7V1	1300°C	single-phase	*C*15	33.5Ti-7.0V-59.4Cr	1.77	a=6.948±0.001	28.5Ti-13V-58.5Cr	a=3.000
32Ti-7V-61Cr	1200°C	coarse 2-phase long beta ppts.	*C*15/(*C*36)+β	33.9Ti-5.0V-61.1Cr	1.80	a=6.956±0.001		
	1000°C	single-phase	*C*15 + (β)	32.8Ti-7.1V-60.1Cr	1.83	a=6.947±0.001		
7V2	1300°C	single-phase	β				33.0Ti-7.8V-59.2Cr	
30.8Ti-7.5V-61.7Cr	1200°C	coarse 2-phase long beta ppts.	*C*15/(*C*36)+β	34.0Ti-4.8V-61.3Cr	1.80	a=6.957±0.001	29.2Ti-13.1V-57.7Cr	a=3.003
7V3	1300°C	single-phase	β				29.9Ti-7.0V-63.1Cr	
29Ti-7V-64Cr	1200°C	coarse 2-phase long beta ppts.	*C*15/(*C*36)+β	33.6Ti-4.1V-62.3Cr	1.85	a=6.951±0.002	23.5Ti-12.4V-64.1Cr	a=2.97

Table 6.5 Microstructures, crystal structures, compositions, and lattice constants of Ti-Mo-Cr alloys.

alloy (target composition)	Temp	microstructure	crystal structure	Laves phase composition (at%)	Laves Cr/Ti	Laves lattice constant (Å)	beta phase composition (at%)	beta lattice constant (Å)
4M1	1300°C	coarse 2-phase large Laves ppt.	*C*14 + β	34.0Ti-2.1Mo-63.9Cr	1.88	a=4.9265±0.0002 c=7.9751±0.0004	35.2Ti-5.9Mo-59.0Cr	a=3.031
34Ti-4Mo-62Cr	1200°C	small dispersed beta ppts.	*C*15/(*C*36)+β	33.5Ti-3.4Mo-63.1Cr	1.88	a=6.955±0.001	---	a=3.088
	1000°C	small dispersed beta ppts.	*C*15 + (β)	34.2Ti-3.5Mo-62.3Cr	1.82	a=6.951±0.002	---	a=2.930
4M2	1300°C	coarse 2-phase beta ppts.	*C*14 + β	33.4Ti-2.3Mo-64.3Cr	1.92	a=4.9224±0.0003 c=7.9751±0.0005	31.4Ti-5.8Mo-62.9Cr	a=3.015
32Ti-4Mo-64Cr	1200°C	single phase	*C*15/(*C*36)	32.7Ti-3.4Mo-63.9Cr	1.95	a=6.948±0.0009		
	1000°C	single phase	*C*15	33.0Ti-3.4Mo-63.6Cr	1.93	a=6.948±0.001		
4M3	1300°C	2-phase, dispersed Laves	*C*14 + β	33.2Ti-2.1Mo-64.7Cr	1.95	a=4.9210±0.0003 c=7.9721±0.0005	29.5Ti-5.0Mo-64.7Cr	a=3.005
30Ti-4Mo-66Cr	1200°C	fine 2-phase long beta ppts.	*C*15/(*C*36)+β	31.3Ti-3.8Mo-64.9Cr	2.07	a=6.936±0.001	22.8Ti-6.4Mo-70.9Cr	a=2.975
	1000°C	single phase	*C*15	30.5Ti-4.0Mo-65.5Cr	2.15	a=6.925±0.002		

and Mo alloys. At an annealing temperature of 1300°C, some of the alloys displayed a coarse two-phase microstructure (Figures 6.8-6.9). Compression test results of these coarse two-phase, $TiCr_2$-base ternary alloys are reported in Appendix G.

The orientation relationship of the large *C*14 Laves phase precipitates in the Ti-V-Cr alloy annealed at 1300°C was determined by TEM (Figure 6.10) and found to be:

$$(0001)_{C14} \parallel (101)_{\beta}$$

$$[2\bar{1}10]_{C14} \parallel [10\bar{1}]_{\beta}$$

$$[0\bar{1}\bar{1}0]_{C14} \parallel [020]_{\beta}$$

By equating close-packed planes and directions of the hexagonal and cubic Laves structures, the above orientation relationship is equivalent to that found in the binary Ti-Cr alloys containing *C*15 $TiCr_2$ described in Chapter 4.

Figures 6.11 and 6.12 show that by 1000°C, the beta phase volume was reduced to small particles, reminiscent of the Ti-68 Cr and Ti-69 Cr binary alloys. Laves phase

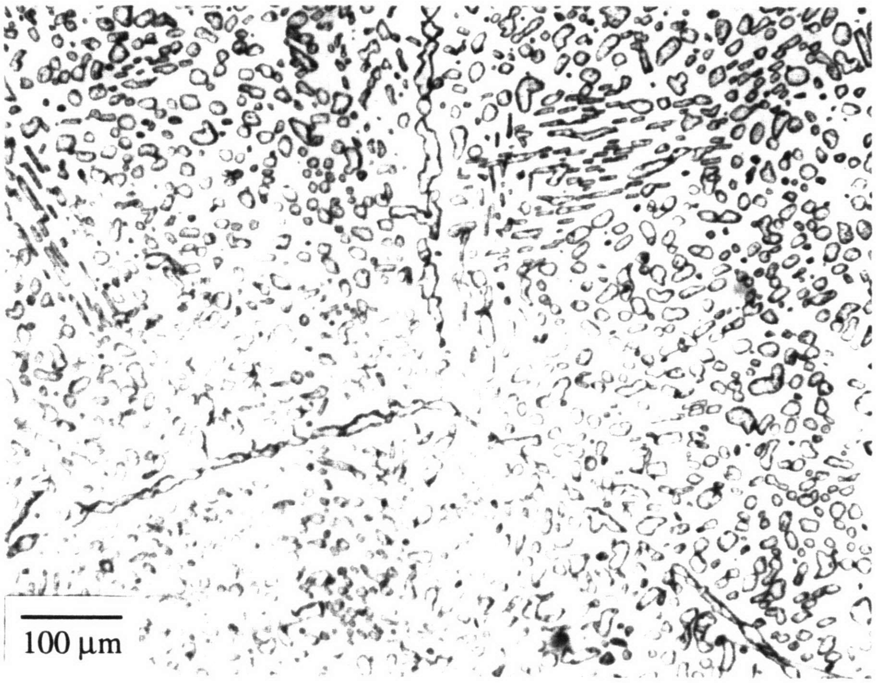

Figure 6.8 Coarse two-phase microstructure of Ti-4 Mo-Cr (4M3) alloy annealed at 1300°C. The discrete dark precipitates are the Laves phase.

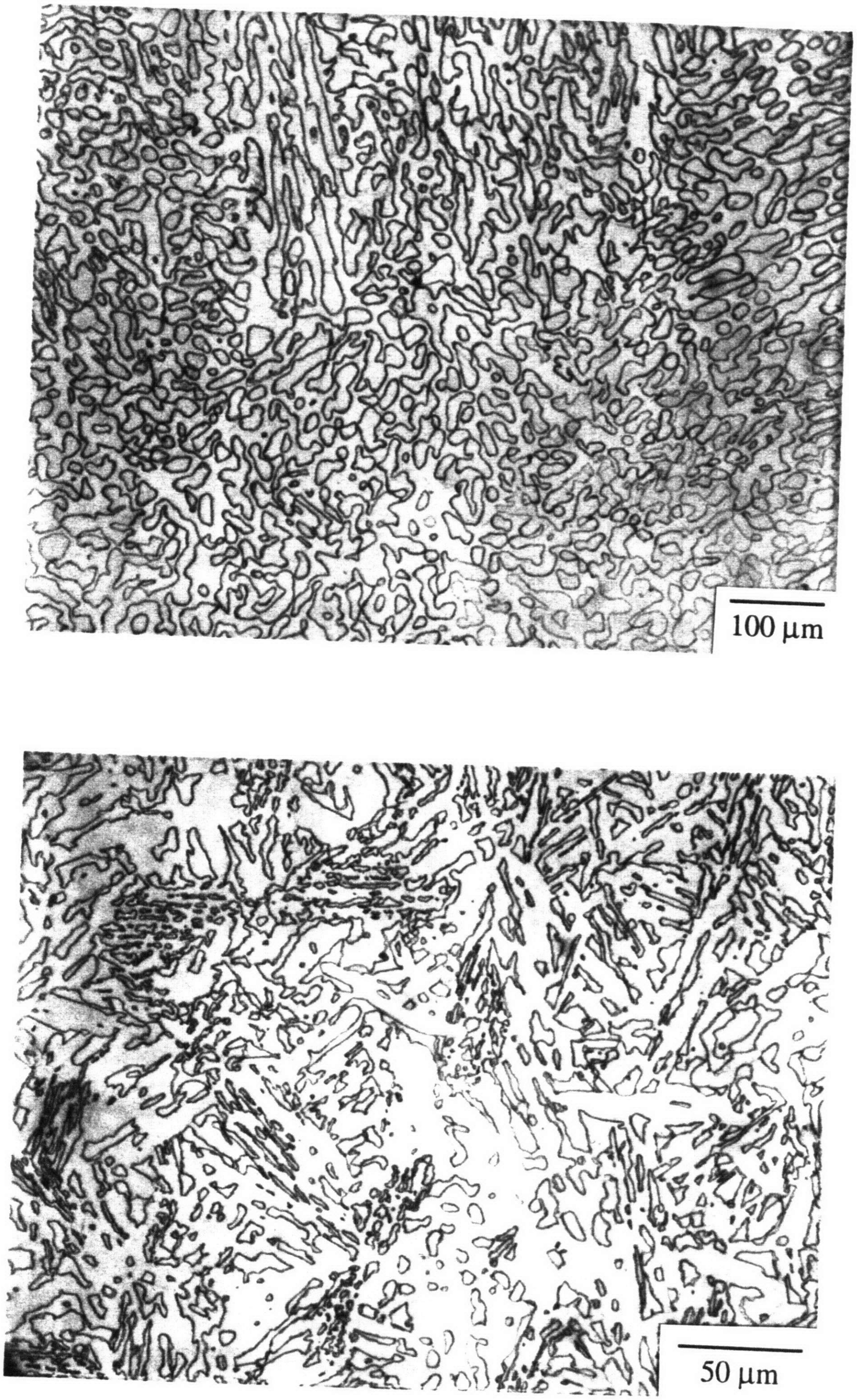

Figure 6.9 Coarse two-phase microstructures of the **(a)** Ti-4 V-Cr (4V2) alloy annealed at 1300°C, and **(b)** Ti-7 V-Cr (7V1) alloy annealed at 1200°C.

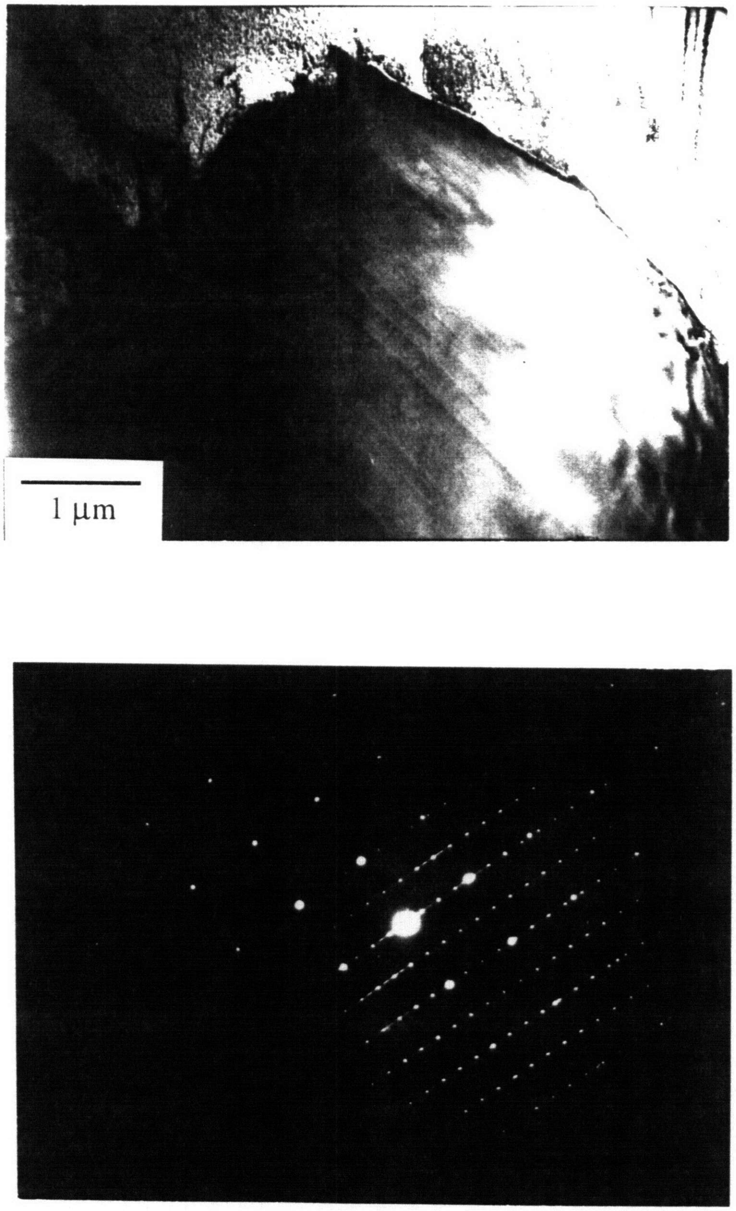

Figure 6.10 (**a**) TEM image of Laves phase precipitate in the Ti-4 V-Cr alloy annealed at 1300°C (1500X) and (**b**) the selected area diffraction pattern of the *C*14 Laves phase and beta phase.

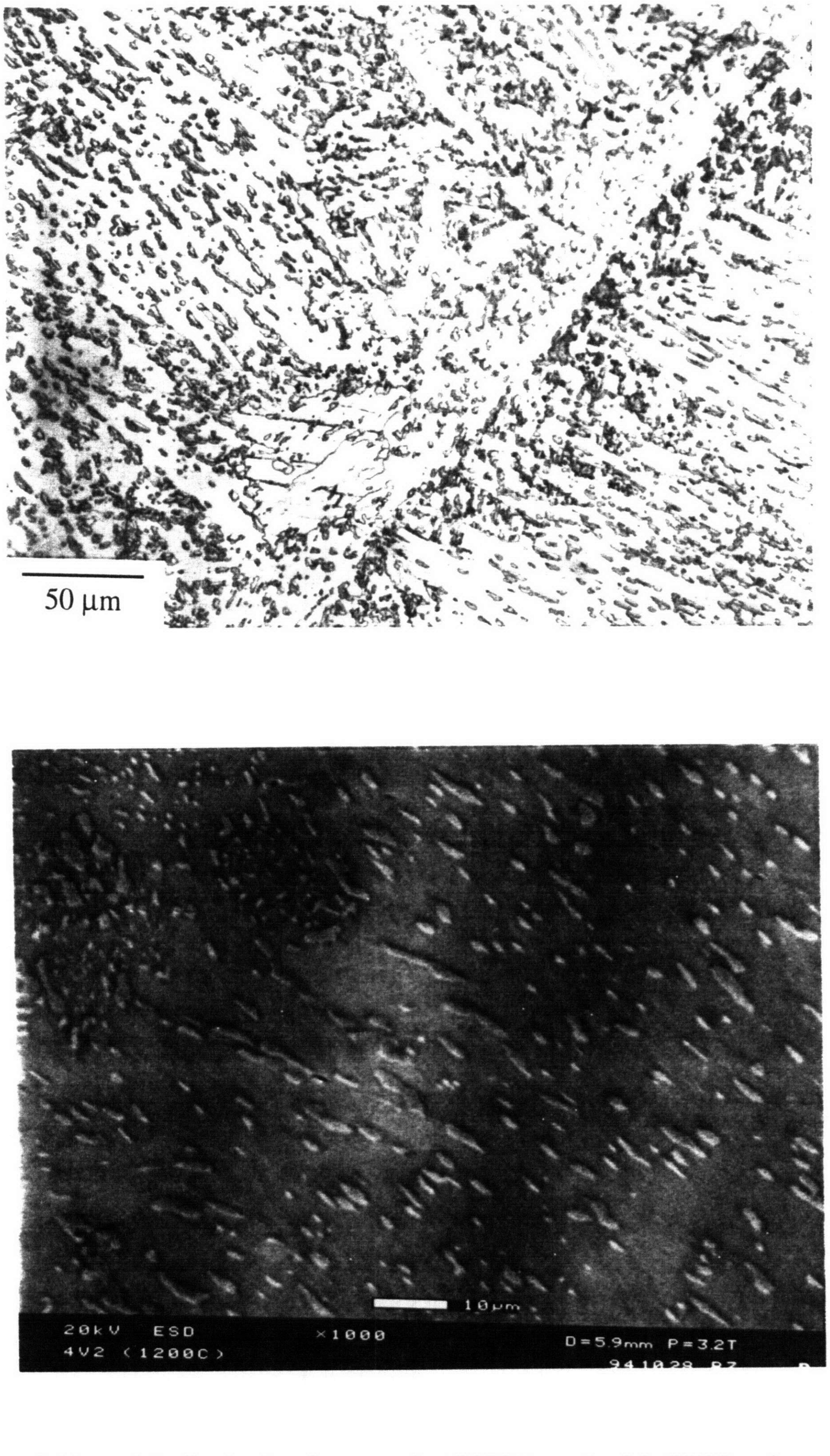

Figure 6.11 (**a**) Optical micrograph (330X) and (**b**) SEM micrograph (1000X) of the Ti-4 V-Cr (4V2) alloy annealed at 1200°C. The small minor phase is the beta phase.

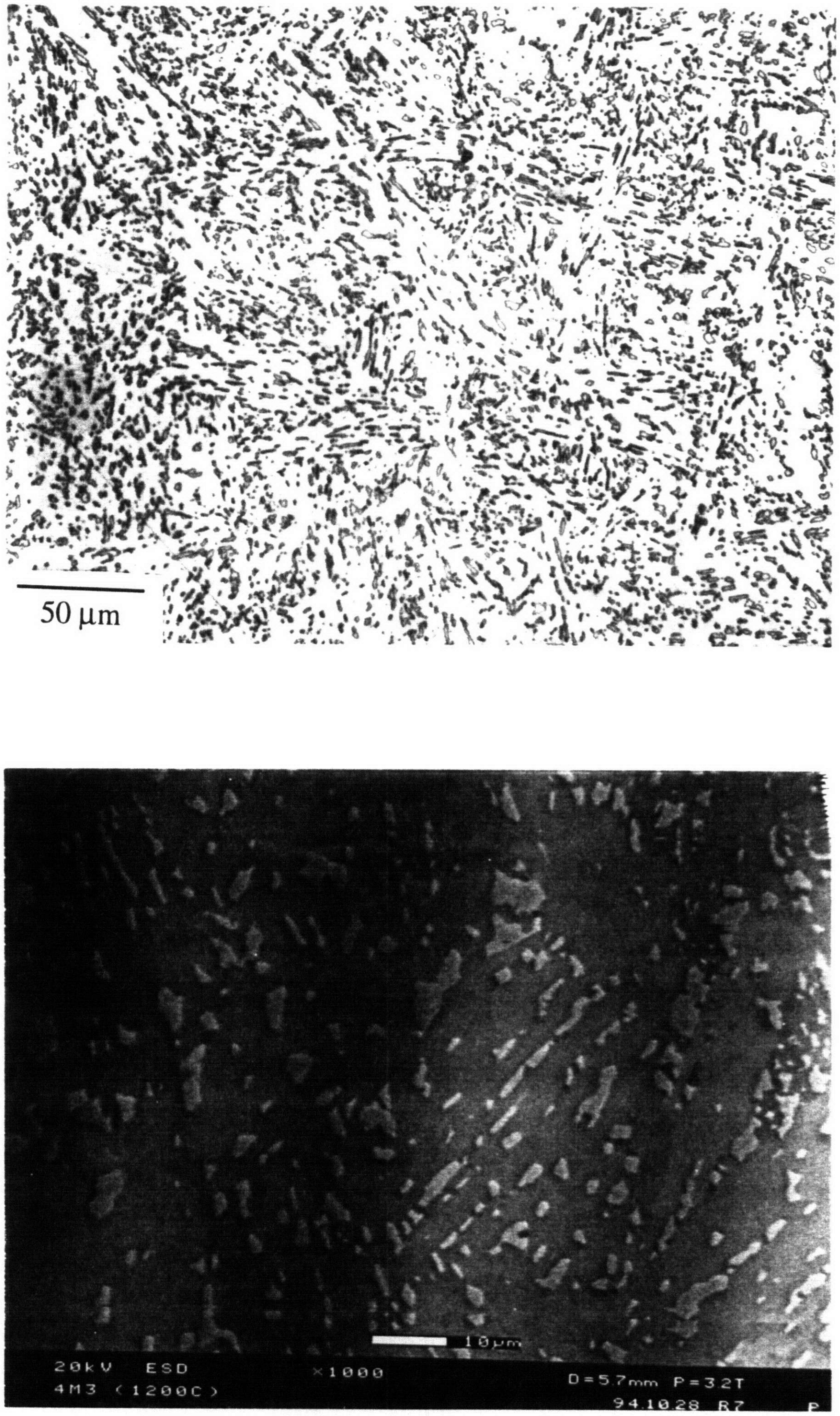

Figure 6.12 (**a**) Optical micrograph (330X) and (**b**) SEM micrograph (1000X) of the Ti-4 Mo-Cr (4M3) alloy annealed at 1200°C. The small minor phase is the beta phase.

compositions from EMPA listed in Tables 6.4 and 6.5 demonstrate that generally the solubilities of V and Mo in $TiCr_2$ increased as the annealing temperature decreased. The solubilities of V and Mo found in these studies are less than expected from previous results reported in the literature [12-14]. As mentioned in Chapter 2, the atomic radius ratio of the Laves phase elements, r_A/r_B, tends to be close to the ideal value when large Laves phase solubility limits are found [15]. Since r_{Ti}/r_{Cr} is far less than the ideal value, the small solubility of $TiCr_2$ for V and Mo is not surprising.

6.3.2 X-Ray Diffraction

6.3.2.a *crystal structures*

The crystal structures of the Fe alloys were *C*14, as to be expected since $TiFe_2$ is *C*14 and Fe is a *C*14-stabilizer of $TiCr_2$ due to the increase in electron concentration [16,17]. The addition of Fe to $NbCr_2$ was found to promote the *C*14→*C*36 transformation over the equilibrium *C*14→*C*15 transformation [18]. On the other hand, Nb is a *C*15-stabilizer [19] and the 5 Nb alloy at 1300°C had a mix of *C*15 and *C*36, while the alloys with greater Nb-content were *C*15 (Table 6.6). At an annealing temperature of 1200°C, all the Nb alloys were *C*15. The binary $TiCr_2$ alloys were *C*14 at 1300°C and *C*36 at 1200°C.

Crystal structures of the Ti-V-Cr and Ti-Mo-Cr alloys are reported in Tables 6.4 and 6.5. The structures were dependent upon the annealing temperature and alloy composition. Both V and Mo are considered to be *C*15 and beta phase stabilizers [12-14,20], which the experimental results confirmed. The equilibrium structure of the binary

Table 6.6 Crystal structure and lattice constants of ternary $(Ti,Nb)Cr_2$ Laves phases by x-ray diffraction.

alloy composition (at%)	crystal structure (1300°C)	crystal structure (1200°C)	*C*15 lattice constant (Å)
Ti-66 Cr	*C*14	*C*36	6.9387 ± 0.0004
28Ti-05Nb-67Cr	*C*15/*C*36	*C*15	6.9388 ± 0.0003
23Ti-10Nb-67Cr	*C*15	*C*15	6.9455 ± 0.0002
18Ti-15Nb-67Cr	*C*15	*C*15	6.9536 ± 0.0003

$TiCr_2$ alloys was determined to be *C*36 at 1200°C, but at that temperature, the *C*15 structure appears in the V and Mo alloys. At 1300°C, the 4V2 sample had a *C*14 structure, while the greater V-content sample, 7V1, was *C*15. The other alloys with about 7 at% V, but greater Cr-content, were single-phase beta at 1300°C. However, the introduction of the beta phase and the *C*36 structure in the 1200°C annealing treatment of the 7V1 sample is not understood.

6.3.2.b *lattice constants*

The lattice constants for the Ti-Fe-Cr Laves phases are listed in Table 6.7 and plotted as a function of Fe-content in Figure 6.13. The error bar for each experimental lattice constant is within the marker point. The $TiCr_2$ data point is taken from the Ti-rich *C*14 $TiCr_2$ Laves composition. The **c**-lattice constant for the 10 at% Fe alloy is higher than that for binary $TiCr_2$, but decreases with further increase in Fe-content. This result is not understood. Other published values [16,17] show a decrease in the lattice constants with Fe-content. However, the overall volume of the Ti-Fe-Cr alloys from the experimental data decreases with the increase of Fe-content.

The lattice constants for the *C*15 structure in the Ti-Nb-Cr Laves phases annealed at 1200°C are reported in Table 6.6 and plotted in Figure 6.14. A Cr-rich *C*15 $TiCr_2$ lattice constant is used for 0% Nb and again, the error bars associated with the experimental lattice constant are about the size of the markers in the plot. The lattice constant of $TiCr_2$ does not immediately change with the addition of Nb. The lattice constant vs. Nb-content behavior is also nonlinear. Data from Thoma's [6] lattice constants along the pseudobinary of $TiCr_2$-$NbCr_2$ indicates a positive curvature from a straight line between the lattice constants of $TiCr_2$ and $NbCr_2$.

Table 6.7 Lattice constants of *C*14 ternary $Ti(Fe,Cr)_2$ Laves phases by x-ray diffraction.

alloy composition (at%)	*C*14 lattice constant, **a** (Å)	*C*14 lattice constant, **c** (Å)	c/a	volume (Å^3)	**a'** (Å)
Ti-67 Cr (1300°C)	4.9184 ± 0.0002	7.9596 ± 0.0003	1.618	166.8	6.9348
33Ti-10Fe-57Cr	4.8848 ± 0.0004	7.9978 ± 0.0007	1.637	165.27	6.914
33Ti-20Fe-47Cr	4.8574 ± 0.0004	7.9696 ± 0.0007	1.641	162.85	6.880
33Ti-30Fe-37Cr	4.8414 ± 0.0003	7.9349 ± 0.0005	1.639	161.07	6.855

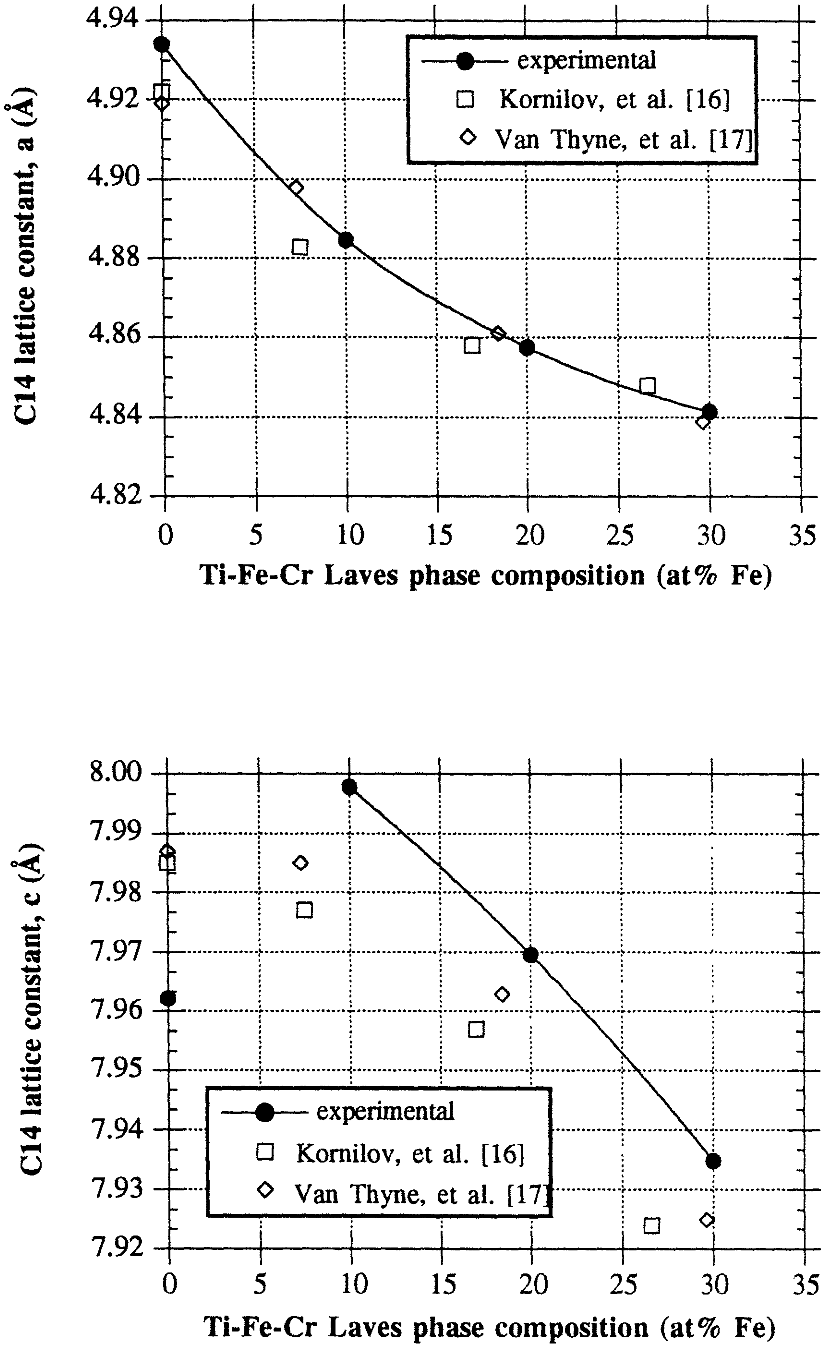

Figure 6.13 The $C14$ lattice constants, **a** and **c**, of the $Ti(Fe,Cr)_2$ Laves phases as a function of the composition.

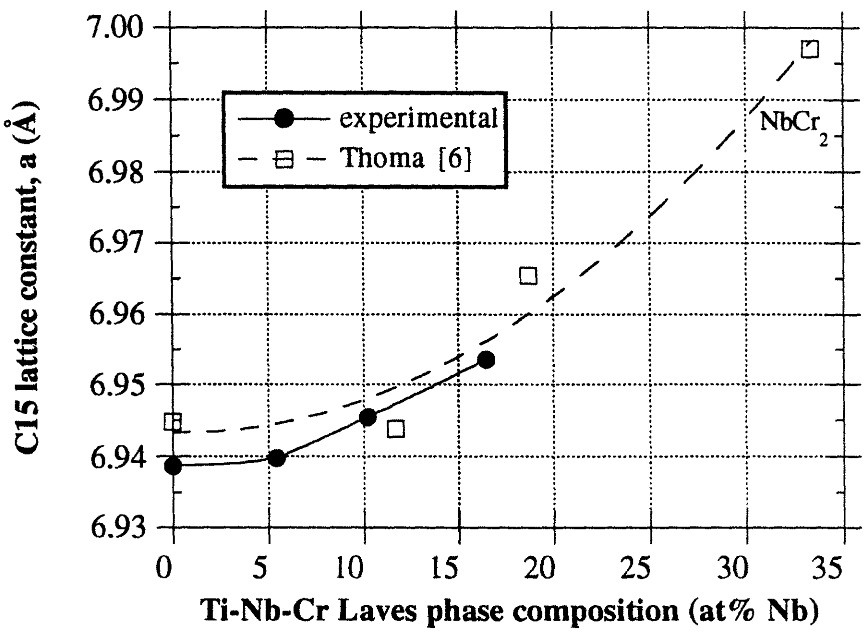

Figure 6.14 The $C15$ lattice constant of the (Ti,Nb)Cr_2 Laves phase as a function of composition.

The lattice constants of the Ti-V-Cr and Ti-Mo-Cr Laves phases are listed in Tables 6.4 and 6.5. A combination of the Laves phase lattice constants and compositions are used to help determine the sublattice sites in which the V and Mo alloying elements reside in the following section.

6.4 DISCUSSION OF ALLOYING ELEMENT ATOMIC-SITE OCCUPANCY

The results presented above were used to establish or confirm the sublattice site occupancies of the alloying elements. The alloying element, Fe resides on the Cr-sublattice. Since a continuous solid solution exists between $TiCr_2$ and $TiFe_2$ [16,17], single phase Ti-Fe-Cr Laves phases were possible. Additions of Fe to $TiCr_2$ were found to decrease the *C*14 **a** lattice constant (and the **c** lattice constant after 10 at% Fe). Fe has a smaller atomic radius than Cr, and the electronegativity difference between Fe and Cr is smaller than the difference between Fe and Ti. The Ti-Fe-Cr Laves phase composition determined by EMPA also confirms that the Fe atoms replace the Cr atoms to form $Ti(Fe,Cr)_2$ ternary Laves phases.

Similarly, Nb atoms replace the Ti atoms along the continuum of $TiCr_2$ to $NbCr_2$ [19,21]. As the Nb concentration increases, the *C*14 to *C*15 transition temperature increases and the lattice constant increases, as reported in the literature [6,19]. EMPA-determined compositions of the Ti-Nb-Cr alloys consistently showed 66 at% Cr, indicating $(Ti,Nb)Cr_2$ ternary Laves phases.

V and Mo were selected to replace both the Ti and Cr atoms. Since the solubility of V and Mo were quite small and the binary $TiCr_2$ Laves phase is not a strict line compound, the analysis for the lattice site replacement of V and Mo in $TiCr_2$ was more difficult. A plot of *C*15 lattice constant vs. "alloy addition" to $TiCr_2$ (Figure 6.15) did not

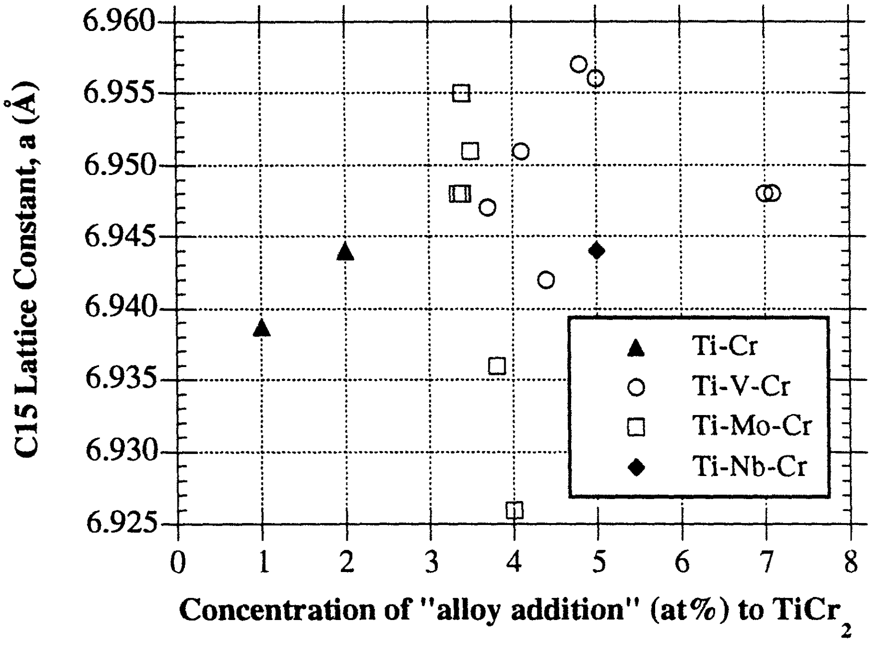

Figure 6.15 Concentration of "alloy addition" to $TiCr_2$ vs. the *C*15 lattice constant.

reveal any systematic trend. (Alloy addition is set in quotes because non-stoichiometric $TiCr_2$ data points are included, and excess Ti atoms and/or vacancies are treated as "alloy additions" to $TiCr_2$.) However, a plot of the Cr/Ti composition ratio vs. alloying element concentration (Figure 6.16) indicates which sublattice the alloying element resides. The lines on the plot are computed from the replacement of Cr atoms in $Ti_{36}Cr_{64}$ and replacement of Ti atoms in $Ti_{33}Cr_{67}$. All the ternary Laves phase compositions fall within the computed lines on the plot. The Fe data point is seen to be close to the $Ti(X,Cr)_2$ line, and the Nb data point lies near the $(Ti,X)Cr_2$ line. A plot of the lattice constant vs. the Cr/Ti composition ratio (Figure 6.17) also helps in the determination of lattice site occupancy of V and Mo. If the alloying element replaces the Cr atoms, the Cr/Ti composition ratio decreases, and since the alloying element is larger than Cr (and smaller than Ti), the ternary Laves phase lattice constant should increase. The opposite trends would occur with the replacement of Ti atoms. Such behavior was observed in the experiments, as seen in Figure 6.17.

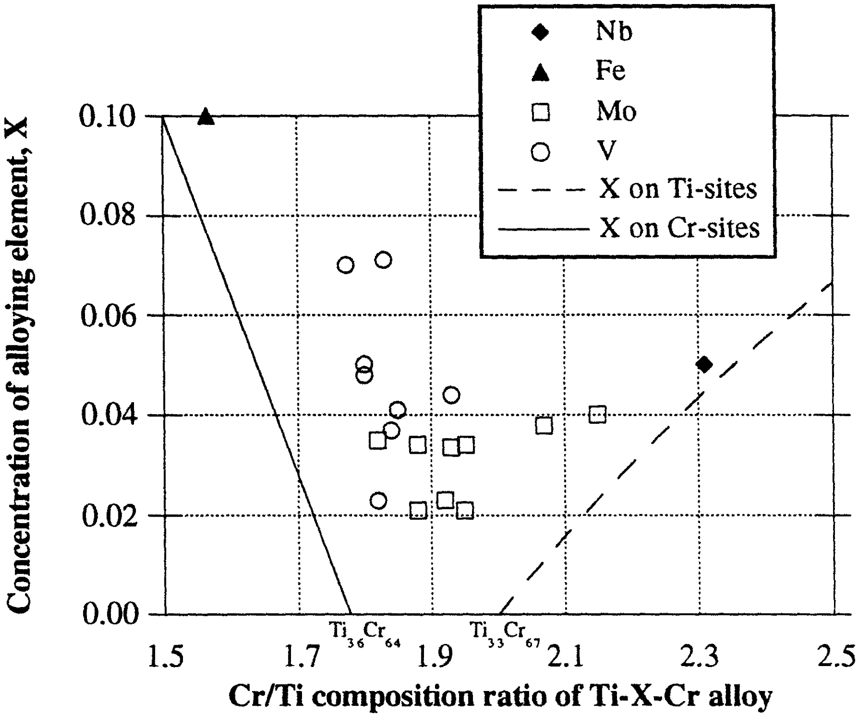

Figure 6.16 The Cr/Ti composition ratio vs. the concentration of alloying element. The placement of a data point on the plot indicates the atomic-site occupancy (Ti or Cr sublattice).

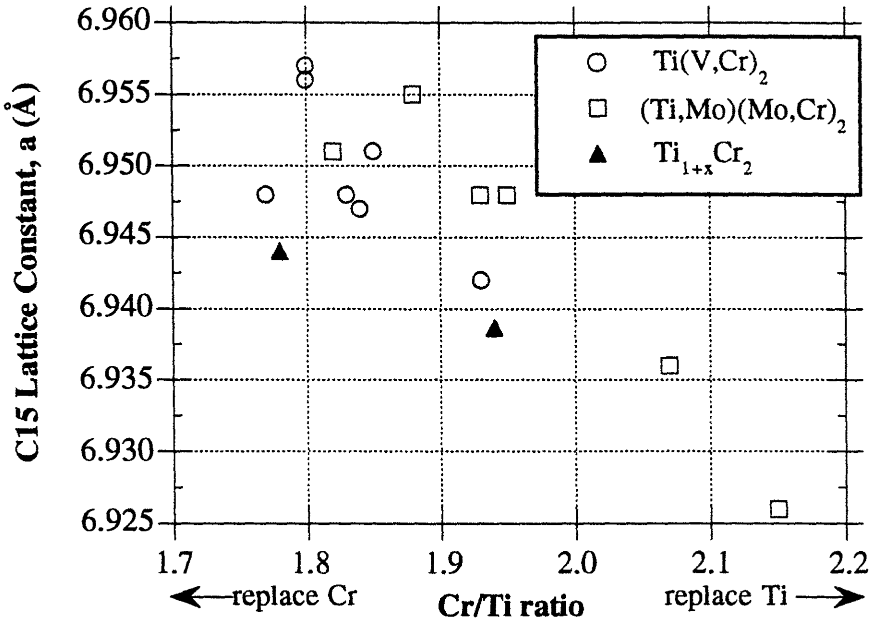

Figure 6.17 The Cr/Ti composition ratio vs. the *C*15 lattice constant. The lattice constant tends to increase when V or Mo substitutes on the Cr-sublattice, and decrease when substituting on the Ti-sublattice.

The Mo alloys span the Cr/Ti composition ratio range, and display lattice constants larger and smaller than $TiCr_2$. Thus, Mo can replace both the Ti and Cr atoms in $TiCr_2$. The initial alloy composition forces the Mo atoms onto either the Ti sublattice or Cr sublattice. However, V alloys are consistently seen to have Cr/Ti composition ratios less than 2.0 and have lattice constants larger than the binary $TiCr_2$. Thus, most of the V atoms must occupy the Cr sites.

6.5 MECHANICAL PROPERTIES

As inferred in the previous chapters, the mechanical properties of Laves phases are heavily influenced by the crystal structure, defect structures, and presence of other phases. The alloying additions add to the complexity of factors, such as alloying element size, electronegativity, and atom-site occupancy. In addition, constitutional defects (such as vacancies) may be present in the ternary phases. Fleischer [22] notes several different possible defects that may form from ternary substitutions and that superimposing their combined effects are difficult to predict. However, he concludes that primary strengthening comes from the familiar elastic forces between point defects and moving dislocations due to size and modulus interactions.

The following section attempts to interpret general trends of alloying additions to $TiCr_2$ in order to suggest ways of improving the room temperature toughness of Laves phases. Vickers hardness and fracture toughness by microindentation are presented for the single-phase (or nearly so) ternary Laves phase.

6.5.1 Indentation Results

Figures 6.18-6.20 show representative indentations of the ternary Laves phases. The hardness and fracture toughness of the Fe alloys are presented in Table 6.8. The $Ti(Fe,Cr)_2$ ternary alloys all show a decrease in hardness value and a large decrease in fracture toughness compared to the binary *C*14 $TiCr_2$.

Table 6.8 Vickers hardness, fracture toughness, and brittleness of $Ti(Fe,Cr)_2$ ternary Laves phases by indentation at a 500 g load.

alloy composition (at%)	Vickers hardness (kg/mm^2)	Fracture toughness (MPa $m^{1/2}$)	Brittleness ($\mu m^{-1/2}$)
Ti-67 Cr (*C*14)	845.4 ± 13.1	0.75 ± 0.17	11.3 ± 2.6
33Ti-10Fe-57Cr	829.9 ± 6.6	0.41 ± 0.09	20.2 ± 4.4
33Ti-20Fe-47Cr	827.3 ± 14.0	0.40 ± 0.08	20.7 ± 4.1
33Ti-30Fe-37Cr	840.3 ± 11.6	0.66 ± 0.16	12.7 ± 3.1
$TiFe_2$	850.1 ± 29.4	0.52 ± 0.06	16.3 ± 1.9

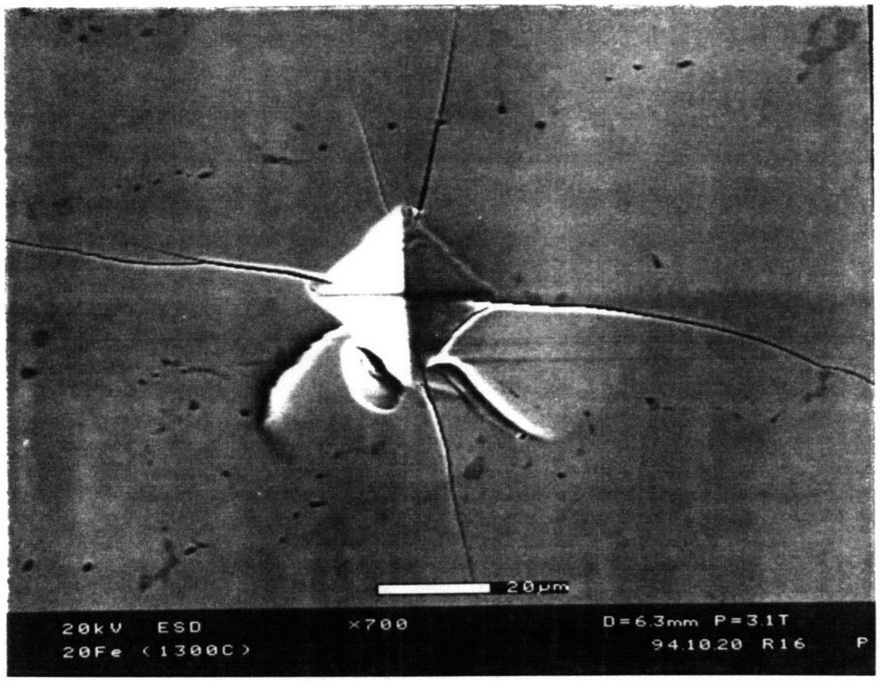

Figure 6.18 Indentation of the Ti(20 Fe,Cr)$_2$ ternary Laves phase annealed at 1300°C.

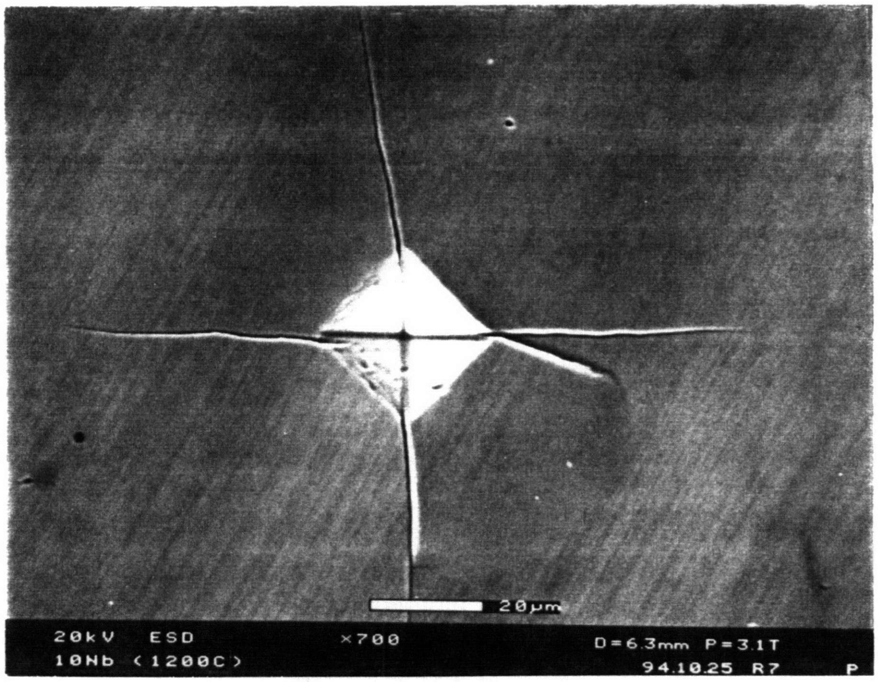

Figure 6.19 Indentation of the (Ti,10 Nb)Cr$_2$ ternary Laves phase annealed at 1200°C.

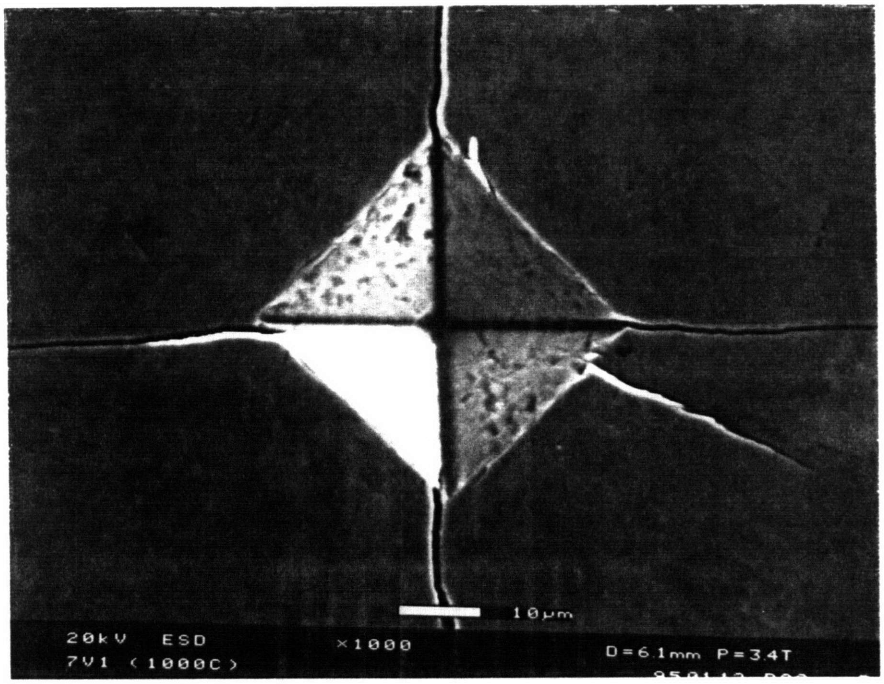

Figure 6.20 Indentation of the single-phase Ti-7 V-Cr (7V1) alloy annealed at 1000°C.

Table 6.9 lists the indentation results of the (Ti,Nb)Cr_2 alloys. The 5 Nb alloy shows comparable hardness to the binary $TiCr_2$ alloys, and with increasing Nb-content, the hardness increases. Shakhova and Budberg [23] have demonstrated that Nb increases the bond forces in $TiCr_2$, and an increase in hardness should result. The fracture toughness of the Nb alloys gradually decreases with Nb-content. The increase in hardness and decrease in fracture toughness with Nb-content is not so surprising since the binary $NbCr_2$ Laves phase has a higher hardness and lower toughness than $TiCr_2$ [6,24]. Thoma [6] claimed that Ti added to $NbCr_2$ increases the ductility, yet from this study, Nb added to $TiCr_2$ worsens the fracture toughness. Ti was also thought by Thoma to have replaced both the Nb and Cr atoms since the Ti radius is between the radii of Nb and Cr. However by virtue of the pseudobinary join between $TiCr_2$ and $NbCr_2$ and other arguments presented earlier, Ti and Nb are interchangeable and the added Ti in Thoma's study most likely went onto the Nb-sublattice. The resulting alloying effects may be more of the

Table 6.9 Vickers hardness, fracture toughness, and brittleness of (Ti,Nb)Cr_2 ternary Laves phases annealed at 1200°C by indentation at a 500 g load.

alloy composition (at%)	Vickers hardness (kg/mm^2)	Fracture toughness (MPa $m^{1/2}$)	Brittleness ($\mu m^{-1/2}$)
Ti-67 Cr (*C*36)	894.4 ± 11.7	0.91 ± 0.14	9.8 ± 1.5
28Ti-05Nb-67Cr	871.1 ± 23.0	0.82 ± 0.16	10.6 ± 2.1
23Ti-10Nb-67Cr	912.2 ± 12.2	0.74 ± 0.09	12.3 ± 1.5
18Ti-15Nb-67Cr	914.2 ± 19.4	0.69 ± 0.03	13.3 ± 0.6

averaging of properties along the material systems continuum ($TiCr_2$-$NbCr_2$), rather than any marked effect of the alloying element site occupancy.

Table 6.10 lists the hardness and fracture toughness values of the single-phase and the fine two-phase Ti-V-Cr and Ti-Mo-Cr alloys (Figures 6.21-6.22). The single-phase Ti(V,Cr)$_2$ and (Ti,Mo)(Mo,Cr)$_2$ alloys have slightly higher hardness values than the binary $TiCr_2$ alloys. The fine two-phase microstructures of the ternary alloys give a slightly lower hardness value, due to the incorporation of the softer beta phase. Alloys with a *C*15/*C*36 structure also showed a lower hardness than those with the *C*15 structure. These trends were also found with the binary Ti-Cr alloys near stoichiometry (Chapter 3). Generally, the V and Mo alloys had higher toughness than the binary $TiCr_2$ alloys. Although some ternaries display a 25% increase in toughness, the improvements were not as substantial as those seen in the binary two-phase structures in Chapter 5. The alloying element site occupancy of Mo also did not appear to have a large effect.

The Vickers hardness of the single-phase ternary Laves compounds are plotted in Figure 6.23 as a function of the concentration of “alloying element”. The fracture toughness is plotted in Figure 6.24. The off-stoichiometric $TiCr_2$ binary Laves phases of each crystal structure are included in the plots. Overall, the effects of the ternary alloying elements are not substantial.

Table 6.10 Vickers hardness, fracture toughness, and brittleness of single-phase (or nearly so) Ti-V-Cr and Ti-Mo-Cr ternary Laves phase alloys.

alloy composition and heat treatment	Laves phase structure	Vickers hardness (kg/mm^2)	Fracture toughness (MPa m$^{1/2}$)	Brittleness (µm$^{-1/2}$)
7V1 1300°C single-phase	*C*15	907.9 ± 17.8	1.33 ± 0.30	6.8 ± 1.5
7V1 1000°C single-phase	*C*15	896.7 ± 11.6	1.28 ± 0.09	7.0 ± 0.5
4M2 1200°C single-phase	*C*15/*C*36	888.4 ± 15.6	1.01 ± 0.10	8.8 ± 0.9
4M2 1000°C single-phase	*C*15	907.8 ± 7.3	1.25 ± 0.30	7.2 ± 1.7
4M3 1000°C single-phase	*C*15	911.4 ± 18.7	1.04 ± 0.23	8.8 ± 1.9
4V2 1200°C fine beta ppts.	*C*15/*C*36	856.9 ± 19.4	1.28 ± 0.23	6.7 ± 1.2
4V2 1000°C fine beta ppts.	*C*15	880.3 ± 30.9	1.20 ± 0.16	7.3 ± 1.0
4M1 1200°C fine beta ppts.	*C*15/*C*36	867.8 ± 13.1	1.30 ± 0.20	6.7 ± 1.0
4M1 1000°C fine beta ppts.	*C*15	879.9 ± 25.2	1.14 ± 0.25	7.7 ± 1.7
4M3 1200°C fine beta ppts.	*C*15/*C*36	866.9 ± 44.1	1.13 ± 0.18	7.7 ± 1.2

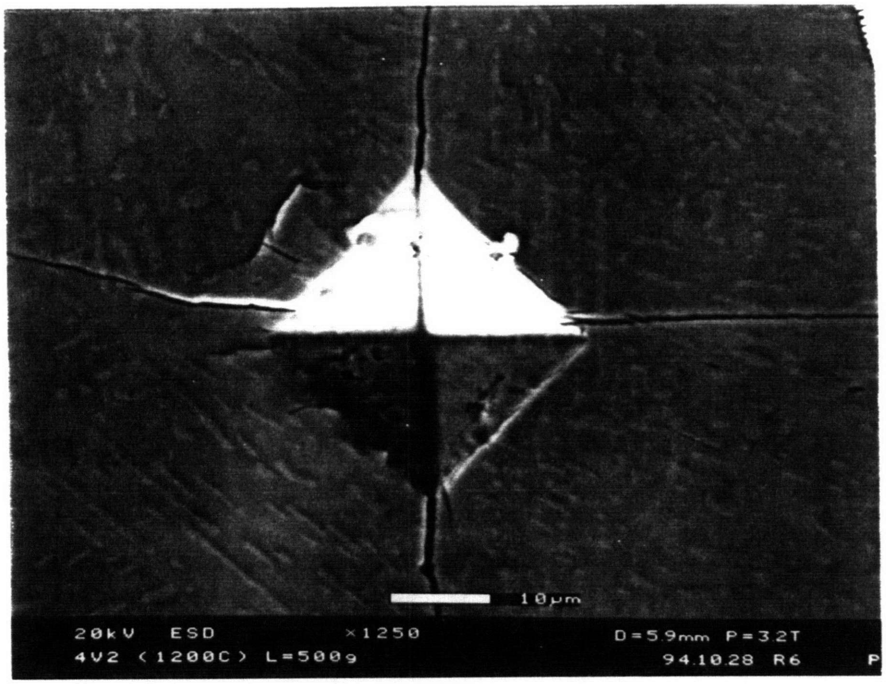

Figure 6.21 Indentation of the fine two-phase Ti-4 V-Cr (4V2) alloy annealed at 1200°C.

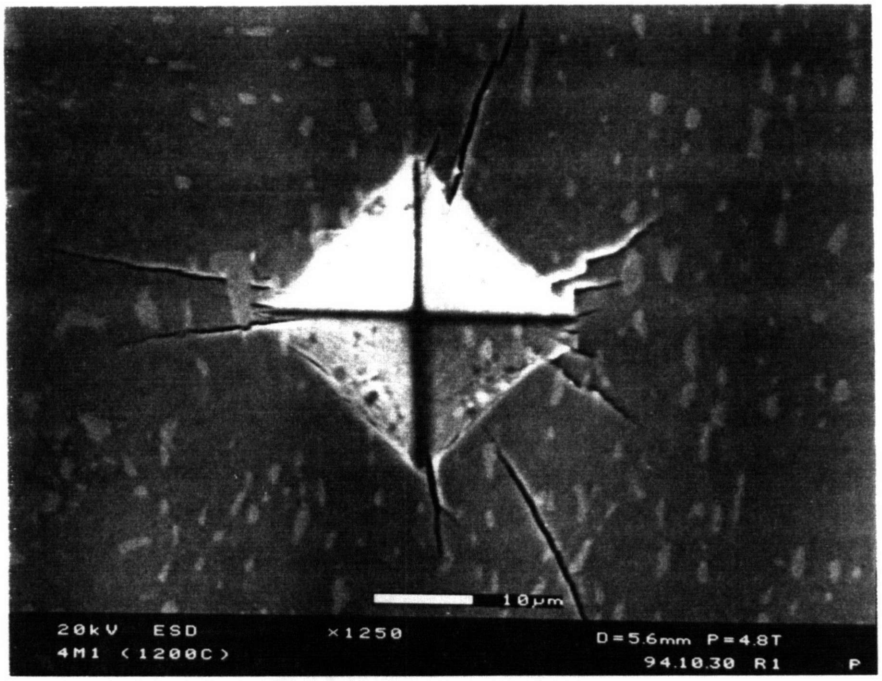

Figure 6.22 Indentation of the fine two-phase Ti-4 Mo-Cr (4M1) alloy annealed at 1200°C.

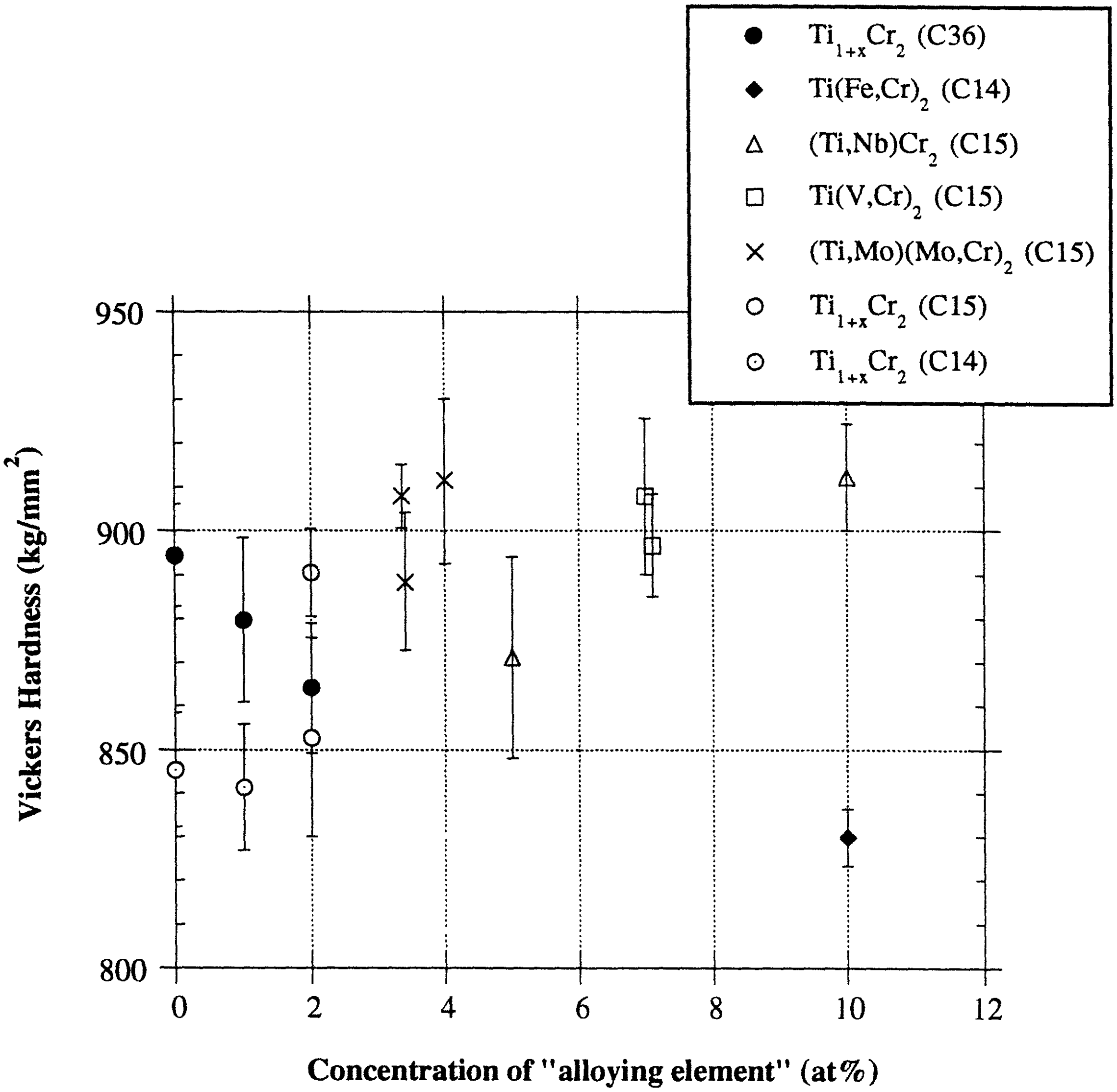

Figure 6.23 Concentration of "alloying element" to $TiCr_2$ Laves phase (of the single-phase alloys) vs. the Vickers hardness (at a load of 500 g).

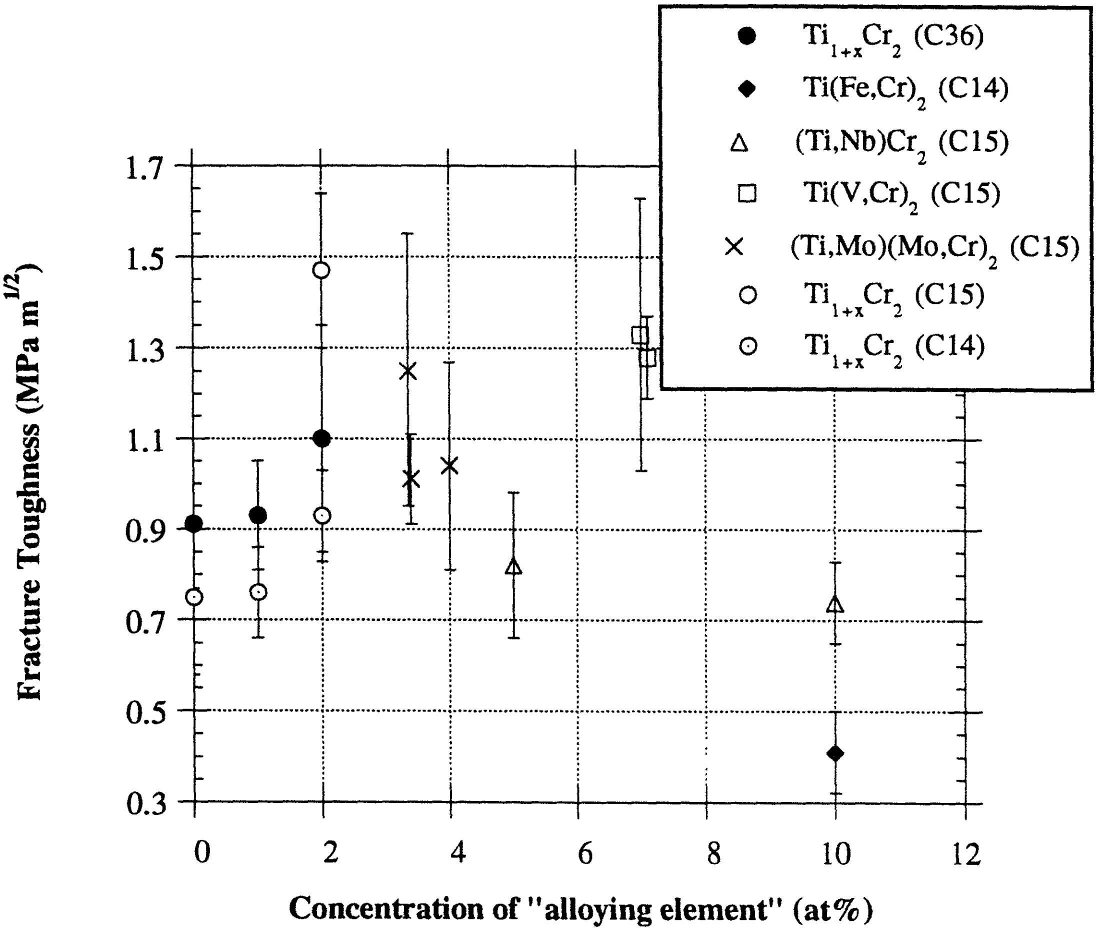

Figure 6.24 Concentration of "alloying element" to $TiCr_2$ Laves phase (of the single-phase alloys) vs. the fracture toughness.

6.5.2 Discussion

Some of the changes in hardness and fracture toughness can be correlated with changes in the lattice constants (and indirectly with alloying element site occupation). As described earlier, Laves phases (AB_2) are often referred to as "size-factor" compounds that have a close-packed structure with an ideal radius ratio of the A atom to the B atom of 1.225. In a rigid-sphere model, this radius ratio enables spheres of the same size to be in contact with each other, while spheres of different sizes do not have any contact. Laves phases actually exist with a range of radius ratios, from 1.05 to 1.68. Atoms are thought to expand or contract accordingly to reach the ideal ratio, which may introduce A-B contacts, as well as internal strain [25]. The $TiCr_2$ Laves phase has a radius ratio of 1.14, which falls well below the ideal value. Following Pearson's dimensional analyses [26], the first interatomic contacts to be made are by the Cr atoms, and therefore the unit cell is controlled by the Cr-Cr contacts. The Cr-sublattice undergoes compression in order to achieve the optimum packing dictated by geometrical considerations.

Large changes in the unit cell dimensions, i.e. the lattice constant, can therefore be affected by substitution on the Cr-sublattice. Excess Ti on Cr-sites has already been seen to increase the lattice constant in the binary alloys in Chapter 2. Fe has been determined to reside on the Cr-sublattice. Fe is slightly smaller than Cr and the unit cell has been seen to decrease with Fe-content. Possibly, the effect of Fe contracting the unit cell puts the B-sublattice under further compression and causes the Laves phase to become more brittle. Several other Laves phases have been documented to display a decrease in hardness with the addition of another element. Blazina et al. [27,28] have studied a series of Laves phases (ZrW_2, HfW_2, $HfMo_2$, and $ZrMo_2$) in which the lattice constant decreases and hardness value decreases as the alloying element concentration increases (and is contrary to solid solution hardening theories).

Nb is slightly larger than Ti, and at 5 at% Nb the lattice constant remains unchanged within experimental error, and only at larger concentrations of Nb does the lattice constant increase (Figure 6.14). Thus replacing the A atoms in a lattice controlled by the B-B contacts has a smaller effect than replacing the B atoms. The hardening effect seen in the 10 Nb alloy and not the 5 Nb alloy parallels the changes in the lattice constant for the $(Ti,Nb)Cr_2$ alloys. Solid-solution hardening in intermetallics has been attributed to lattice strains from alloying, although other factors may play a role as well [29].

Thus the role of atom-site occupation may have significance in that the lattice size can be affected. Selection of the appropriate alloying element on particular sublattices can either increase or decrease the unit cell. Nb added to HfV_2 was suggested to improve the deformability because Nb "opened up" the lattice for easier atomic movements in the synchroshear deformation [30]. However, the general rule of selecting an alloying element that resides on both sublattices of a Laves phase to improve ductility is not emphatically upheld for all other Laves phases. The desirable effects seen in HfV_2 may be more complicated, and not generally applicable to other systems.

A greater influence of the alloying elements on the mechanical properties of $TiCr_2$ turns out to be the ability to stabilize certain crystal structures. Alloying elements can increase or decrease the electron concentration of Laves phases, and thereby affect stacking fault energies and the phase (crystal structure) stability. Nb, V, and Mo all extended the equilibrium $C15$ region of $TiCr_2$, and the $C15$ structure has consistently shown the highest hardness and toughness values. The large number of slip systems associated with cubic structures may inherently offer greater deformability and toughness than the hexagonal Laves crystal structures. The VCo_3 intermetallic with a low-symmetry hexagonal structure has been alloyed with Fe to transform into the higher symmetry cubic $L1_2$ structure for improved ductility [3]. Similarly, $TiAl_3$ alloyed with Mn and Cr to form the $L1_2$ structure has been shown to have improved crack resistance [31]. In addition, the cubic $C15$ Laves phase can also deform by twinning, as seen in the $TiCr_2$ precipitates in Ti-rich, two-phase Ti-Cr alloys (Chapter 5).

Solubility limits were also affected by the alloying elements V and Mo, as many of the alloys had a two-phase microstructure. Again, the presence of a second, more ductile phase can greatly improve the fracture toughness without sacrificing much of the strength of an alloy. Thus, the appropriate alloying element may improve the toughness of the Laves phase itself, and may also induce the precipitation of a second phase that could further improve the toughness of the whole alloy system.

From these studies on $TiCr_2$-base Laves ternaries, alloying did not produce remarkable improvements in the fracture toughness. Evidence for the $C36$ to $C15$ transformation toughening mechanism due to low stacking fault energies (as seen in $ZrFe_2$) were not seen with the $TiCr_2$-base Laves phases. Alloying element occupancy did not show any overwhelming effect on the properties. However, the studies did indicate that alloying elements may be used to stabilize the cubic $C15$ structure or to affect the single-phase solubility limits in order to improve the toughness of Laves phases.

The main conclusions of these studies on the binary and ternary $TiCr_2$ alloys will be summarized in the next and final chapter.

6.6 REFERENCES

1. J.D. Livingston, phys. stat. sol. (a), **131**, 415 (1992).

2. D.M. Shah and D.L. Anton, *Mat. Res. Soc. Symp. Proc. Vol. 213*, 63 (1991).

3. E.P George and C.T. Liu, *Mat. Res Soc. Symp. Proc. Vol. 186*, 309 (1991).

4. P.J. Fehrenbach, H.W. Kerr, and P. Niessen, J. Crystal Growth, **18**, 151 (1973).

5. Z.B. Liu and L.C. Tai, J. Appl. Phys., **52**, 2064 (1981).

6. D.J. Thoma, Ph.D. Thesis, U. of Wisconsin, (1992).

7. K. Inoue and K. Tachikawa, IEEE Trans. Magnetics, **13**, 840 (1977); **15**, 635 (1979).

8. J.D. Livingston and E.L. Hall, J. Mater. Res., **5**, 5 (1990).

9. J.A. Venables, *Deformation Twinning*, ed. R.E. Reed-Hill, J.P. Hirth, and H.C. Rogers, Gordon and Breach, p.77 (1964).

10. W.B. Pearson, *Crystal chemistry and physics of metals and alloys*, (1972).

11. A.R. Edwards, Metall. Trans., **3**, 1365 (1972).

12. N.N. Samsonova and P.B. Budberg, Izvestiya Akademi Nauk SSSR, Neorgan. Mat. **1** 1558, (1965); **3**, 817 (1967).

13. N.N. Samsonova, P.B. Budberg, I.I. Kornilov, and V.A. Sanov, Izestiya Akademi Nauk SSSR, Neogran. Mat., **2**, 1882 (1966); **2**, 1878 (1966).

14. N.N. Samsonova and P.B. Budberg, Poroshkovaya Metallurgiya, **8**, 49 (1966).

15 D.J. Thoma and J.H. Perepezko, submitted to Journal of Alloys and Compounds.

16. I.I. Kornilov and N.G. Boriskina, Zhur. Neorg. Khim., **9**, 702 (1964).

17. R.J. Van Thyne, H.D. Kessler, and M. Hansen, Trans. AIME, **197**, 1209 (1953).

18. M. Grujicic, S. Tangrila, O.B. Calvin, and C.R. Hubbard, Mat. Sci. and Eng., **160**, 37 (1993).

19. I.I. Kornilov, K.I. Shakhova, P.B. Budberg, and N.A. Nedumov, Doklady Akademi Nauk SSSR, **149**, 1340 (1963).

20. P.A. Farrar and H. Margolin, Trans. ASM, **60**, 57 (1967).

21. P.B. Budberg and S.P. Alisova, Poroshkovaya Metallurgiya, **10**, 65 (1966).

22. R.L. Fleischer, *Structural Intermetallics*, ed. R. Darolia, J.J. Lewandowski, C.T. Liu, P.L. Martin, D.B. Miracle, and M.V. Nathal, TMS, p.691 (1993).

23. K.I. Shakhova and P.B. Budberg, *Physical Metallurgy of Titanium*, (NASA translation), 223 (1964).

24. K.I. Shakhova and P.B. Budberg, Izvest. Akad. Nauk SSSR Metally, **2**, 128 (1965).

25. R.L. Berry and G.V. Raynor, Acta Cryst., **6**, 178 (1953).

26. W.B. Pearson, Acta Cryst., **B37**, 1174 (1981).

27. Z. Blazina and Z. Ban, J. Less-Common Metals, **90**, 223 (1983).

28. R. Trojko, Z. Blazina, and Z. Ban, J. Less-Common Metals, **92**, 67 (1983); **97**, 91 (1984).

29. R.L. Fleischer, Scripta Metall. et Mater., **27**, 799 (1992).

30. F. Chu and D.P. Pope, *Mat. Res. Soc. Symp. Proc. Vol. 288*, (1992); Mat. Sci. Eng., **A170**, 39 (1993).

31. S. Zhang, J.P. Nic, and D.E. Mikola, Scripta Metall. et Mater., **24**, 57 (1990); **24**, 1099 (1990).

32. *Metals Handbook Ninth Edition, Vol. 12 Fractography*, ASM International, (1987).

Chapter 7

Summary, conclusions and suggested future work

7.1 SUMMARY

The motivating force behind this thesis was to understand the compositional influences on the mechanical properties of $TiCr_2$ Laves phase alloys. The limiting feature that keeps this class of intermetallics from realizing their full potential as high-temperature structural materials is their room-temperature brittleness. Various postulated toughening mechanisms, such as alloying on specific atomic sites, changing the stacking fault energy (or crystal structure stability), and stress-induced phase transformations were systematically tested on $TiCr_2$. The most significant factors influencing the toughness and deformability of the $TiCr_2$ alloys were determined, and these results offer directions and indicate the probability of success to toughen other Laves phase intermetallics. Several other significant findings on $TiCr_2$, as a single-phase entity and as part of a two-phase system, were also determined.

A comprehensive survey of the mechanical properties (by Vickers indentation and room-temperature compression tests) of several different $TiCr_2$-base alloys revealed dependencies on the alloy composition and annealing treatment. Quantitative measurements allowed for the comparison of different effects. Studies of single-phase $TiCr_2$ served as the baseline for comparisons of properties with single-phase, ternary $TiCr_2$-base Laves compounds and two-phase, binary alloys containing $TiCr_2$. Thus, the potential for alloying to improve the toughness, and the microstructural possibilities of two-phase Ti-Cr alloys were explored.

Finer details of the current Ti-Cr phase diagram and of the $TiCr_2$ compound were also elucidated. The single-phase $TiCr_2$ Laves field was identified as only a few atomic percent wide, extending towards Ti-rich compositions. The defect mechanism accompanying the off-stoichiometric, Ti-rich $TiCr_2$ compositions was determined to be a combination of anti-site substitutions and Cr-site vacancies (established by microprobe-determined compositions, crystal structure transformation rates, lattice constants, and density measurements). These defects, in turn, are associated with the improved fracture toughness displayed by the off-stoichiometric $TiCr_2$ compositions. Vickers indentation measurements showed a decrease in hardness and increase in fracture toughness values with departure from the stoichiometric $TiCr_2$ composition. These results lend credence to the postulate that vacancies play an important role in the movement of Shockley partial dislocations involved in the synchroshear deformation process. The vacancies (i.e., the removal of atoms) allow for easier atomic shifting within the close-packed Laves structure, which results in greater deformability. However, these improvements in the toughness with off-stoichiometric $TiCr_2$ compositions are quite small, and other factors can have a stronger influence on the toughness.

The Laves phase crystal structure was also determined to be a significant factor affecting the mechanical properties of $TiCr_2$. The *C*15 structure in the binary and ternary $TiCr_2$-base Laves phases consistently displayed the highest hardness and fracture toughness values. Alloys with a *C*36/*C*15 structure showed no evidence of phase (crystal structure) transformation toughening, as exhibited by the $ZrFe_2$ Laves phase system. The greater deformability seen in the cubic *C*15 alloys over the hexagonal alloys can be attributed to the greater number of slip systems and the ability to twin as an additional deformation mechanism. These conclusions demonstrate the importance of identifying both the composition and crystal structure of the Laves phase intermetallic when reporting mechanical properties.

The last part of this thesis concentrated on the effects of alloying additions to $TiCr_2$. Previous reports have suggested that the improved ductility seen in alloyed Laves phases results from the alloying elements occupying both sublattice sites and/or the lowering of stacking fault energies. However, no studies existed in the literature where the effects of alloying element site occupancy or crystal structure stabilization were studied directly. Alloying elements and ternary Laves compositions were selected to allow the alloying element to reside on a specific sublattice (e.g., the Ti-sublattice, the Cr-sublattice, or both sublattices). Confirmation of atomic site occupancy was made by microprobe analysis and lattice constant measurements. Control of the Laves phase crystal structure through alloying additions and annealing treatments (by changing the electron concentrations and stacking fault energies) was also established. Alloying $TiCr_2$ did not result in greatly improved toughness, and the sublattice-site occupancy proved to have little effect. These findings, although discouraging, are significant in the sense that alloying strategies to toughen other Laves phase intermetallics may be quite limited, and that the alloying success found in the HfV_2 Laves phase system may be unique. Nonetheless, the study of ternary $TiCr_2$-base alloys revealed that alloying elements may be best selected to stabilize the cubic *C*15 structure or to affect the single-phase solubility limit (and precipitate a second phase) in efforts to increase the toughness of Laves phase alloys.

Overall, this work on $TiCr_2$-base alloys confirms the general thought that Laves phases are much too brittle at ambient temperatures to be used in their monolithic form, and if Laves phases are to ever find a practical application for structural purposes, they will most likely be in a two-phase system. The largest influence on the toughness of $TiCr_2$ was the presence of a second, more ductile phase. Even small amounts of the beta bcc phase with the $TiCr_2$-base compounds resulted in marked improvements in the fracture toughness. In the two-phase alloys with large volume fractions of the Ti-rich beta phase, $TiCr_2$ precipitates were seen to deform under room-temperature compression. The Cr-rich, two-phase alloys displayed fracture toughness values about five to seven times larger than the single-phase alloys. The Ti-rich, two-phase alloys did not experience any indentation cracking and are expected to have an even larger fracture toughness, although the strength may be compromised. Improvements in the fracture toughness of the two-phase alloys can be attributed to crack deflection, crack bridging, and beta phase/$TiCr_2$ interface debonding. The deformability and toughness of $TiCr_2$ alloys greatly improve with a two-phase structure and this result points to the future direction of the development of Laves phases as structural materials.

Through the proper choice of alloy composition and annealing treatments, microstructural design and control is possible with two-phase alloys containing $TiCr_2$. Different microstructures of several two-phase Ti-Cr alloys with $TiCr_2$ were characterized in this thesis. The Ti-rich, two-phase alloys displayed discrete lath or equiaxed $TiCr_2$ precipitates, while the Cr-rich, two-phase alloys resembled fine eutectoid-like microstructures. High strengths could also be retained in the two-phase alloys, and engineering requirements will dictate the optimum alloy composition and microstructure.

This thesis has extended the knowledge of Laves phases by collectively examining and assessing the potential of several proposed toughening mechanisms in a systematic manner that has not been accomplished before. Although the research work concentrated on the $TiCr_2$ Laves phase, the basic findings extend to the many other Laves phase intermetallics. Understanding the extent to which different factors affect mechanical properties and the accompanying explanations for such effects will aid in the future research and development of other Laves phases.

In the never-ending quest to develop new materials, engineers are faced with a myriad of possibilities in material systems and materials processing. Only by understanding the influences on the properties can one be well-equipped to design materials for the desired application. This thesis has investigated the compositional influences on the microstructures, phase stability, and mechanical properties of $TiCr_2$ Laves phase alloys and has contributed to the efforts of toughening Laves phase intermetallics that is essential for their realization as high-temperature structural materials.

7.2 CONCLUSIONS

single-phase $TiCr_2$*:*

1. A narrow single-phase $TiCr_2$ Laves phase field exists towards Ti-rich compositions. Off-stoichiometry was found to be accommodated by both anti-site substitutions (Ti on Cr-sites) and vacancy formation.

2. $TiCr_2$ displays polytypism, exhibiting the *C*14, *C*36, and *C*15 crystal structures at different annealing temperatures. The *C*36 to *C*15 transformation rate was found to be sluggish, and compositionally dependent (due to the presence of vacancies).

3. Cracks introduced by Vickers indentation on $TiCr_2$ alloys were Palmqvist or shallow radial cracks in character, but followed the half-penny crack model: $P/c^{3/2}=k$ (where P = load, c = crack length, and k = constant related to the fracture toughness).

4. Microindentation on alloys near the $TiCr_2$ composition revealed that the maximum hardness and minimum fracture toughness values occurred at the stoichiometric composition. Vacancies in the off-stoichiometric $TiCr_2$ compositions may aid the movement of dislocations involved in the synchroshear deformation mechanism, thus improving deformability.

5. The $TiCr_2$ *C*15 structure had the highest hardness and toughness values among the different Laves crystal structures. Small amounts of the beta bcc phase improved the crack resistance by crack deflection, crack bridging, and beta/$TiCr_2$ interface debonding.

two-phase binary alloys with $TiCr_2$*:*

6. Two-phase alloys of β-(Ti,Cr)+$TiCr_2$ exhibited a variety of microstructures, depending on the initial alloy composition and annealing treatment. Ti-rich alloys contained equiaxed or lath-shaped $TiCr_2$ precipitates, while the Cr-rich alloys had a eutectoid-like microstructure. The orientation relationship between the β-bcc phase and *C*15 $TiCr_2$ Laves phase was found to be a 35.3° rotation about a common $[10\bar{1}]$ axis.

7. Twinning was often seen in the *C*15 $TiCr_2$, and suggested a means of growth for the Laves phase, as well as a mode of deformation.

8. The fine microstructure of the Cr-rich, two-phase alloys showed much greater crack resistance from indentation over the single-phase $TiCr_2$, while still exhibiting high hardness values. However, these alloys also failed quickly under room-temperature compression, without significant plasticity.

9. Two-phase Laves systems (including $TiCr_2$) have much greater toughness over single-phase Laves compounds, but to date, have fracture toughness values only up to about 10 MPa $m^{1/2}$.

10. Compression tests of the Ti-rich, two-phase alloys showed some signs that the $TiCr_2$ Laves phase deforms at room-temperature by complex faulting, twinning, and the formation of "shear bands". However, extensive room-temperature deformation did not occur, nor did any stress-induced transformations.

ternary $TiCr_2$*-base Laves phases:*

11. Alloying on specific atomic sites of $TiCr_2$ was accomplished, yet did not have a significant effect on the mechanical properties (as had been proposed with the HfV_2 Laves phase). Changes in the lattice constant could be correlated with the alloying element site occupancy and, to some extent, with changes in the microhardness.

12. Alloying was also used to affect the stacking fault energies and crystal structure stabilities. Ternary $TiCr_2$-base Laves phases near the *C*36/*C*15 structure transition composition (and therefore possessing low stacking fault energies) did not show increased toughness. However, alloying $TiCr_2$ to stabilize the *C*15 structure or to affect the single-phase solubility limit (i.e., to precipitate the bcc beta phase) demonstrated greater toughness without sacrificing hardness levels.

7.3 SUGGESTED FUTURE WORK

Although the research contained in this thesis has provided new insights to the understanding of the mechanical properties of Laves phases, several issues still remain. Revisitation of the HfV_2 system might be worthwhile to understand why this particular Laves phase experiences greater deformation upon alloying, while $TiCr_2$ does not. The exciting results of the HfV_2-based Laves phase may indeed prove to be unique.

The $TiCr_2$ Laves phase was shown to have a small solubility range, but several other Laves phase compounds have a larger range and can accommodate off-stoichiometry on both sides of the strict AB_2 composition. Studies of the compositional dependencies of the mechanical properties of other Laves phases would help to generalize the findings from this thesis. Large solubility ranges usually indicate the ready acceptance of alloying additions and offer inviting opportunities to manipulate the Laves phase compositions for desired properties.

Theoretical studies to model and predict the intrinsic defects of binary Laves phases and of those that may be formed upon alloying would be helpful. Models could also be developed to predict and understand the alloying effects on solubility limits and crystal structure stabilization. Dynamic models simulating the atomic motions involved in the synchroshear mechanism would be very useful. Effects of vacancies, obstacles (e.g., other atoms), and packing efficiency could then be added to the simulated synchroshear process. This would assist the understanding of the interaction of defects (from nonstoichiometry, alloying, or deformation) with dislocations. The compositional trends found in this thesis provide experimental work for comparisons with modeling efforts.

The use of Laves phase intermetallics as high-temperature structural materials is still an unfulfilled idea, although the knowledge of this class of intermetallics has been greatly expanded in the past few years. Based on this work and work of other investigators, the direction of research for Laves phases as practical structural materials involves the development of two-phase systems. Future designs may evolve from a "composites approach" and the mechanics of two-phase systems will require some attention (such as the crack interaction and interface debonding between phases).

Microstructural effects also become very important, and novel processing techniques for producing fine-scale microstructures should be pursued. (For example, a two-phase system of very small, dispersed $TiCr_2$ precipitates within a Ti-rich beta bcc solid solution matrix should result in very high strengths, yet still retaining ductility from the continuous beta phase.) Some examples of alternative processing techniques are powder metallurgy, mechanical alloying, hot working, drop-casting, hot extrusion, and directional solidification.

Since the properties of two-phase alloys depend on the properties of the individual phases, alloying to improve the toughness of the Laves phase would still be a worthwhile endeavor. Alloying may be employed for other purposes also, such as oxidation resistance and solid-solution strengthening.

Laves phases have been shown to possess some attractive properties, but have yet to outshine other material types for structural purposes at this time. However, research and development on Laves phases is still relatively new. The study of Laves phases is fascinating from a basic scientific perspective due to the electronic and geometrical nature of these compounds. Advances in the understanding of these materials will put the Laves phases at a more competitive status as they realize their full potential as structural materials.

Appendix A: TEM of $TiCr_2$ Laves Structures

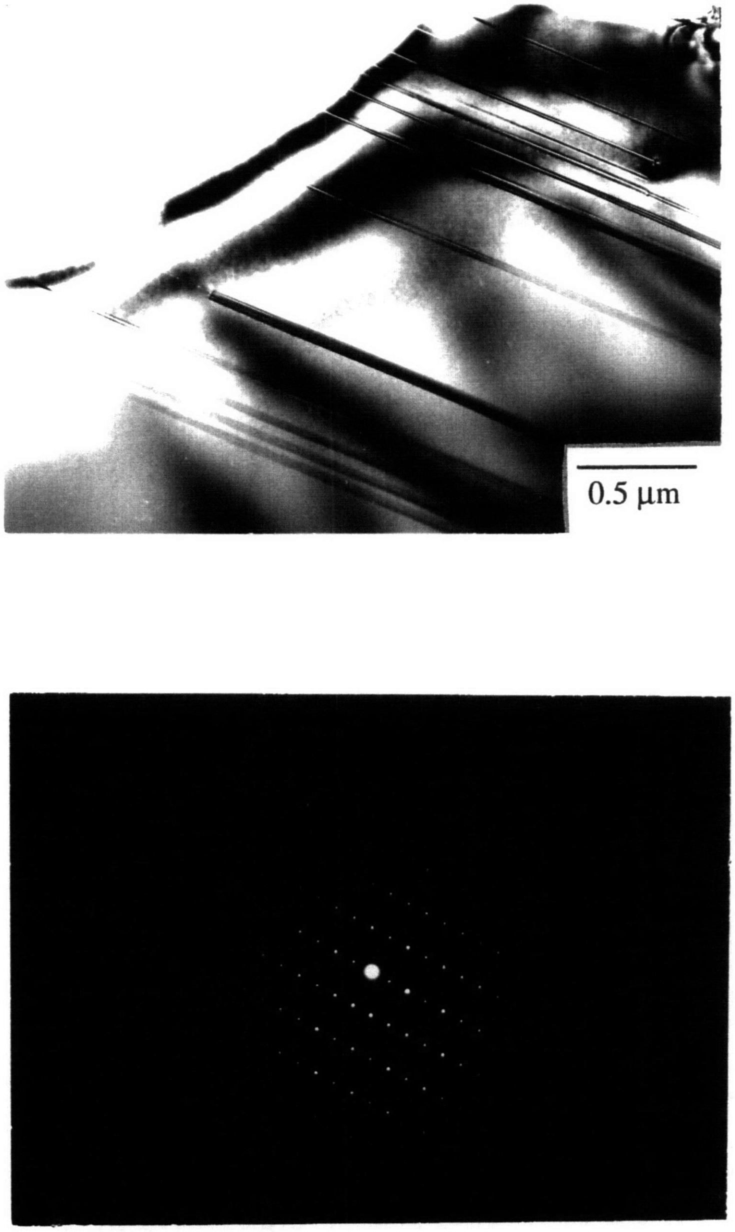

Figure A.1 **(a)** TEM image and **(b)** the $[1\bar{2}10]$ electron diffraction pattern of *C*14 $TiCr_2$ in a Ti-60 Cr alloy annealed at 1300°C.

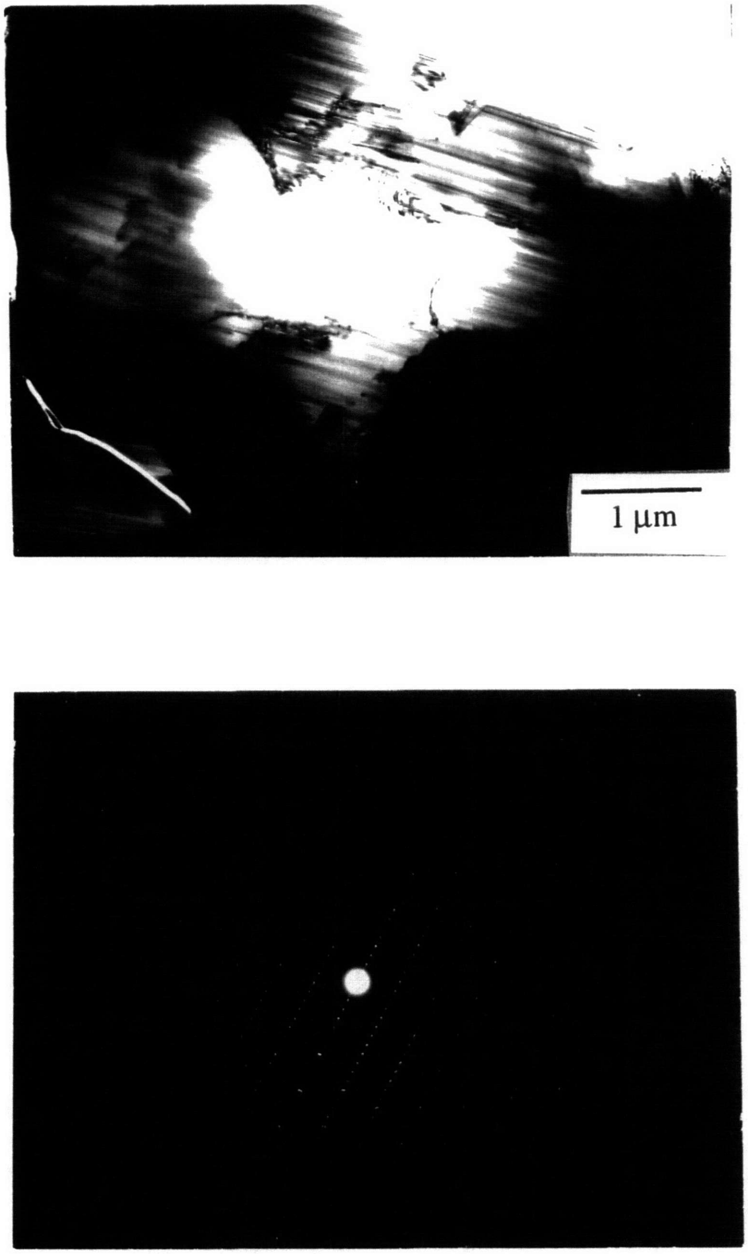

Figure A.2 **(a)** TEM image and **(b)** the $[1\bar{2}10]$ electron diffraction pattern of *C*36 $TiCr_2$ in a Ti-60 Cr alloy annealed at 1230°C.

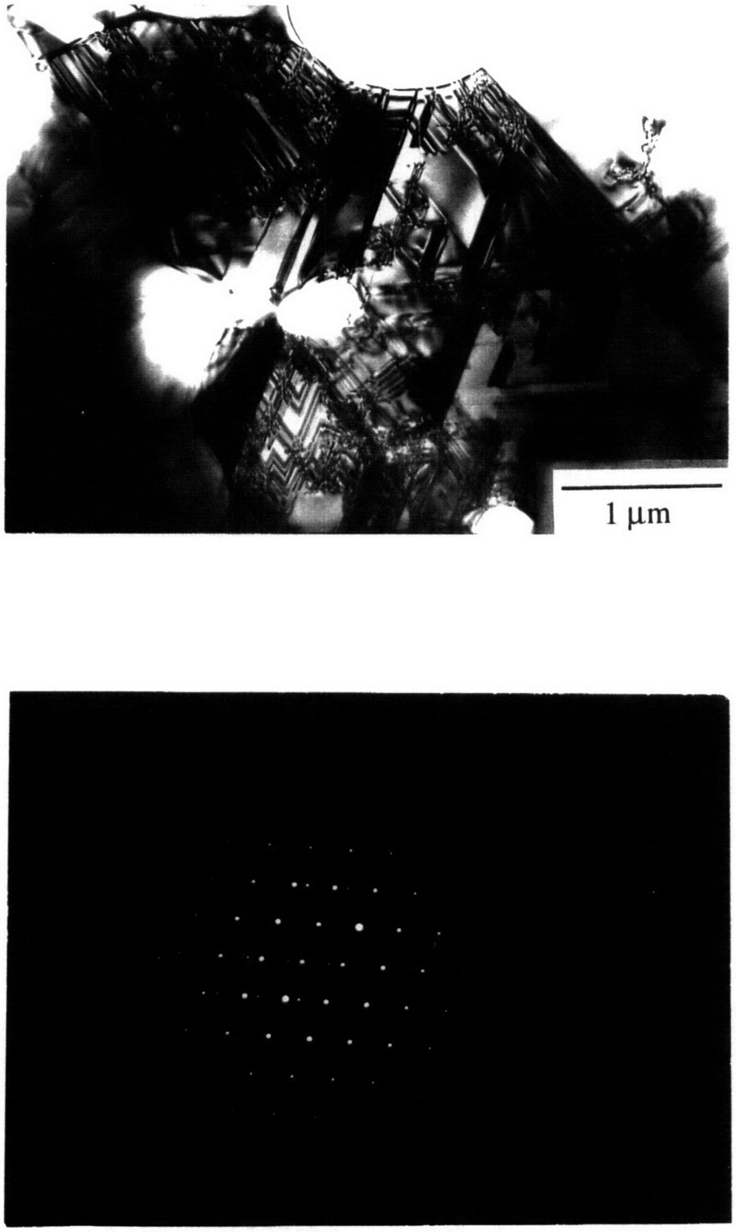

Figure A.3 **(a)** TEM image and **(b)** the [110] electron diffraction pattern of *C*15 TiCr$_2$ in a Ti-60 Cr alloy annealed at 1000°C. Notice twinning on the {111}<112> system.

Appendix B: Calculated X-Ray Diffraction Data

Table B.1 Calculated peak position (2θ) and relative intensities for X-ray diffraction of *C*14, *C*36, and *C*15 TiCr$_2$.

hkl			calculated angle (2θ)			calculated relative intensity		
*C*14	*C*36	*C*15	*C*14	*C*36	*C*15	*C*14	*C*36	*C*15
100	100		20.823	20.823		14.24	3.38	
	101			21.564			10.93	
002	004	111	22.314	22.314	22.168	5.73	5.47	11.42
101	102		23.657	23.657		3.76	3.06	
	103			26.802			0.02	
102	104		30.705	30.705		0.45	0.12	
	105			35.146			5.75	
110	110	220	36.481	36.481	36.594	24.61	24.41	24.34
103	106		39.986	39.986		62.36	46.04	
200	200		42.375	42.375		9.71	2.36	
	201			42.772			16.93	
112	114	311	43.182	43.182	43.200	100.00	100.00	100.00
201	202		43.943	43.943		91.41	67.81	
	107			45.141			17.62	
004	008	222	45.534	45.534	45.225	21.32	21.55	43.83
	203			45.843			24.21	
202	204		48.405	48.405		23.23	5.78	
104	108		50.568	50.568		13.23	3.17	
	205			51.556			7.19	
		400			52.716			6.21
203	206		55.231	55.231		5.98	4.46	
	109			56.248			1.49	
210	210		57.125	57.125		1.43	0.34	
	211			57.444			1.21	
211	212	331	58.393	58.393	57.869	0.55	0.45	2.04
	207			59.374			0.24	
	213			59.955			0.01	
212	214		62.100	62.100		0.07	0.02	
105	10(10)		62.181	62.181		0.87	0.66	
204	208		63.946	63.946		0.63	0.17	
	215			64.799			1.58	
300	300	422	65.658	65.658	65.880	3.67	3.64	7.24
213	216		68.018	68.018		21.83	16.14	
	10(11)			68.383			1.74	
	209			68.920			2.48	
302	304	511,333	70.288	70.288	70.443	19.66	19.66	26.05
006	00(12)		70.969	70.969		3.22	3.11	
	217			71.731			7.38	
205	20(10)		74.291	74.291		25.00	18.82	
106	10(12)		74.884	74.884		1.90	0.46	
214	218		75.920	75.920		6.56	1.57	

Table B.1 (continued)

hkl			calculated angle (2θ)			calculated relative intensity		
*C*14	*C*36	*C*15	*C*14	*C*36	*C*15	*C*14	*C*36	*C*15
220	220	440	77.512	77.512	77.787	22.77	22.60	22.50
	20(11)			80.069			8.72	
	219			80.577			0.88	
	311			81.591			0.39	
	10(13)			81.734			0.11	
222	224	531	81.874	81.874	82.090	0.65	0.62	1.27
311	312		82.403	82.403		0.13	0.13	
116	11(12)		82.522	82.522		0.60	0.66	
312	314		85.639	85.639		0.08	0.01	
215	21(10)		85.710	85.710		0.63	0.48	
206	20(12)		86.283	86.283		10.05	2.45	
	315			88.056			0.65	
107	10(14)	620	89.003	89.003	89.173	1.93	1.55	3.00
313	316		91.006	91.006		9.25	7.05	
	21(11)			91.345			1.58	
400	400		92.580	92.580		0.83	0.22	
	401			92.849			1.53	
	20(13)			92.991			3.61	
401	402	533	93.655	93.655	93.411	8.76	6.47	9.16
	317			94.497			3.62	
224	228	622	94.777	94.777	94.826	13.34	13.49	13.41
	403			94.999			2.56	
	10(15)			96.795			2.34	
402	404		96.886	96.886		2.87	0.69	
216	21(12)		97.534	97.534		2.12	0.52	
314	318		98.546	98.546		3.90	0.88	
	405			99.324			1.02	
207	20(14)	444	100.284	100.284	100.526	3.20	2.25	1.26
008	00(16)		101.425	101.425		0.63	0.62	
403	406		102.328	102.328		1.01	0.78	
	319			103.189			0.55	
320	320		103.943	103.943		0.35	0.07	
	321			104.220			0.25	
	21(13)			104.366			0.15	
321	322	551	105.051	105.051	104.869	0.08	0.07	0.80
306	30(12)		105.174	105.174		0.38	0.42	
108	10(16)		105.271	105.271		4.36	1.08	
	407			105.923			0.05	
322	324		108.412	108.412		0.07	0.01	
315	31(10)		108.486	108.486		0.54	0.39	
404	408		110.154	110.154		0.18	0.05	
	325			110.975			0.53	
410	410		111.814	111.814		2.43	2.41	
217	21(14)	642	111.992	111.992	112.322	3.11	2.50	4.85

Table B.1 (continued)

hkl			calculated angle (2θ)			calculated relative intensity		
*C*14	*C*36	*C*15	*C*14	*C*36	*C*15	*C*14	*C*36	*C*15
118	11(16)		113.205	113.205		2.43	2.42	
323	326		114.170	114.170		7.73	5.83	
	31(11)			114.542			1.32	
	10(17)			114.698			2.12	
	409			115.094			0.96	
412	414	731,553	116.517	116.517	116.983	16.21	16.24	24.46
226	22(12)		117.238	117.238		8.26	8.00	
208	20(16)		117.344	117.344		0.14	0.03	
	327			118.053			3.34	
	21(15)			120.677			4.51	
405	40(10)		120.865	120.865		12.83	9.56	
316	31(12)		121.534	121.534		1.90	0.49	
324	328		122.717	122.717		4.02	0.91	
109	10(18)	800	125.565	125.565	125.234	1.83	1.24	6.94
	40(11)			127.684			6.08	
	329			128.319			0.62	
500	500		129.260	129.260		0.11	0.04	
	501			129.608			0.13	
	31(13)			129.792			0.17	
501	502	733	130.660	130.660	130.605	0.08	0.05	0.45
218	21(16)		130.941	130.941		10.31	2.56	
325	32(10)		135.151	135.151		0.78	0.55	
406	40(12)		135.967	135.967		9.70	2.40	
	505			138.577			0.35	
	10(19)			139.007			0.13	
330	330		139.771	139.771		1.79	1.77	
317	31(14)		140.028	140.028		4.29	3.60	
209	20(18)	660,822	141.039	141.039	140.718	4.24	3.37	5.48
308	30(16)		141.804	141.804		3.76	3.73	
503	506		143.257	143.257		6.51	4.80	
	32(11)			143.827			2.10	
	21(17)			144.068			6.73	
420	420		145.974	145.974		2.53	0.62	
	421			146.457			4.56	
	40(13)			146.714			5.34	
332	334		146.967	146.967		13.95	13.97	
421	422	555,751	147.942	147.942	147.990	27.27	20.25	33.66
	507			149.561			2.98	
	423			150.564			8.79	
00(10)	00(20)	662	150.692	150.692	150.761	2.58	2.67	23.18
	31(15)			154.433			9.72	
422	424		154.644	154.644		11.40	2.84	

Appendix C: X-Ray Diffraction Scans

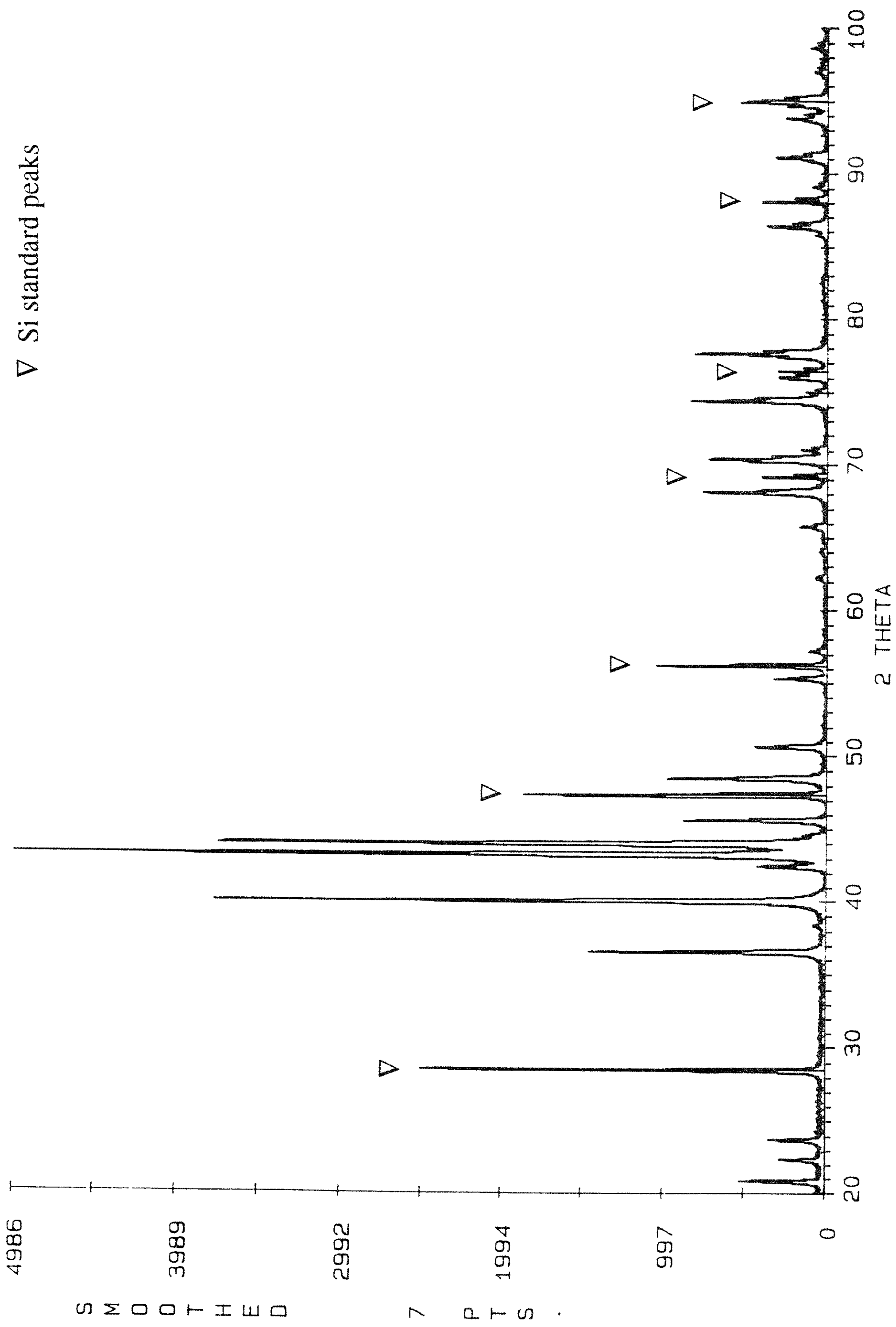

Figure C.1 (a) The 2θ vs. intensity x-ray diffraction scan for the C14 Ti-67 Cr at 1300°C. (2θ = 20-100°)

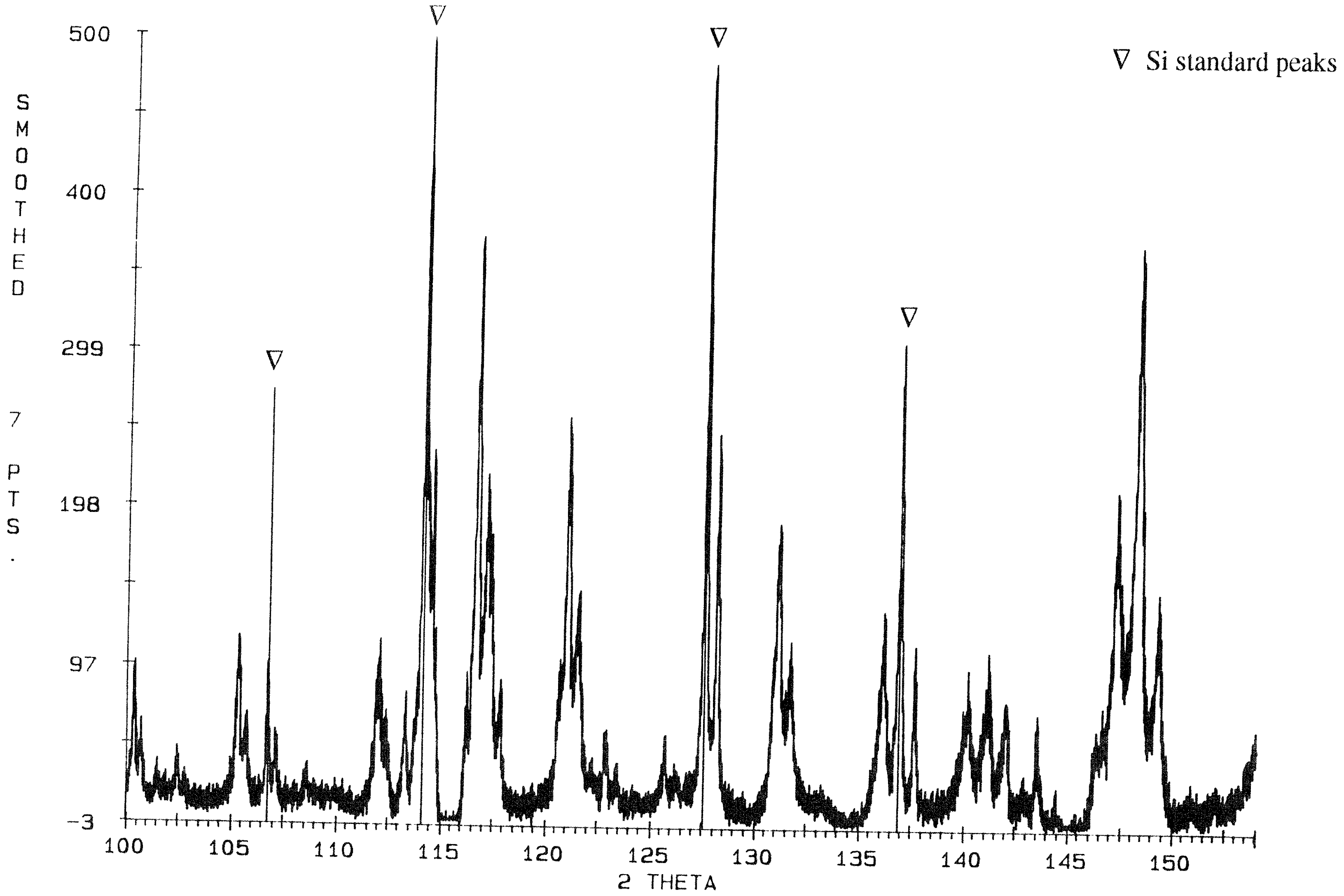

Figure C.1 (b) The 2θ vs. intensity x-ray diffraction scan for the C14 Ti-67 Cr at 1300°C. (2θ = 100-154°)

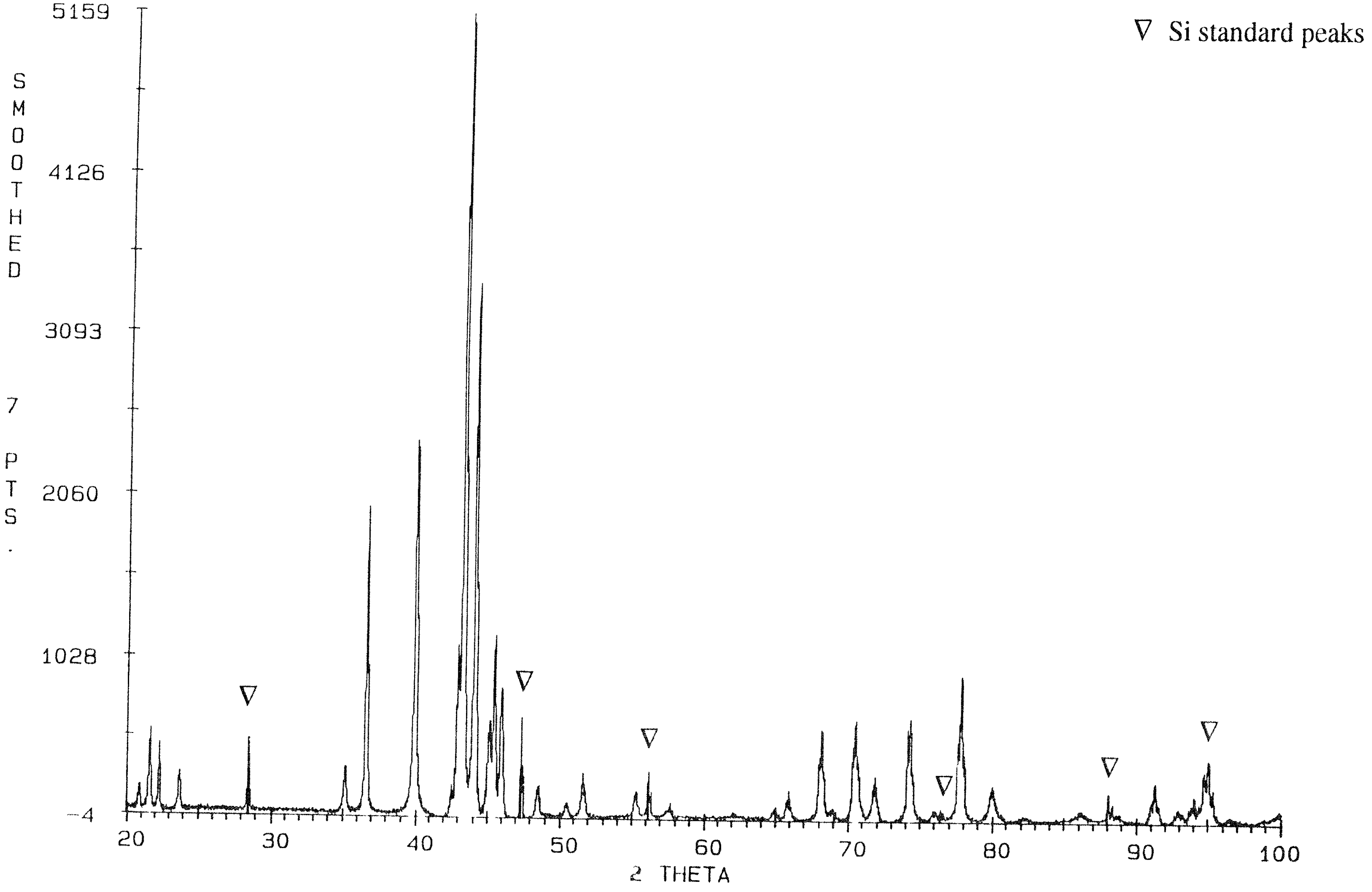

Figure C.2 (a) The 2θ vs. intensity x-ray diffraction scan for the *C*36 Ti-67 Cr at 1200°C. (2θ = 20-100°)

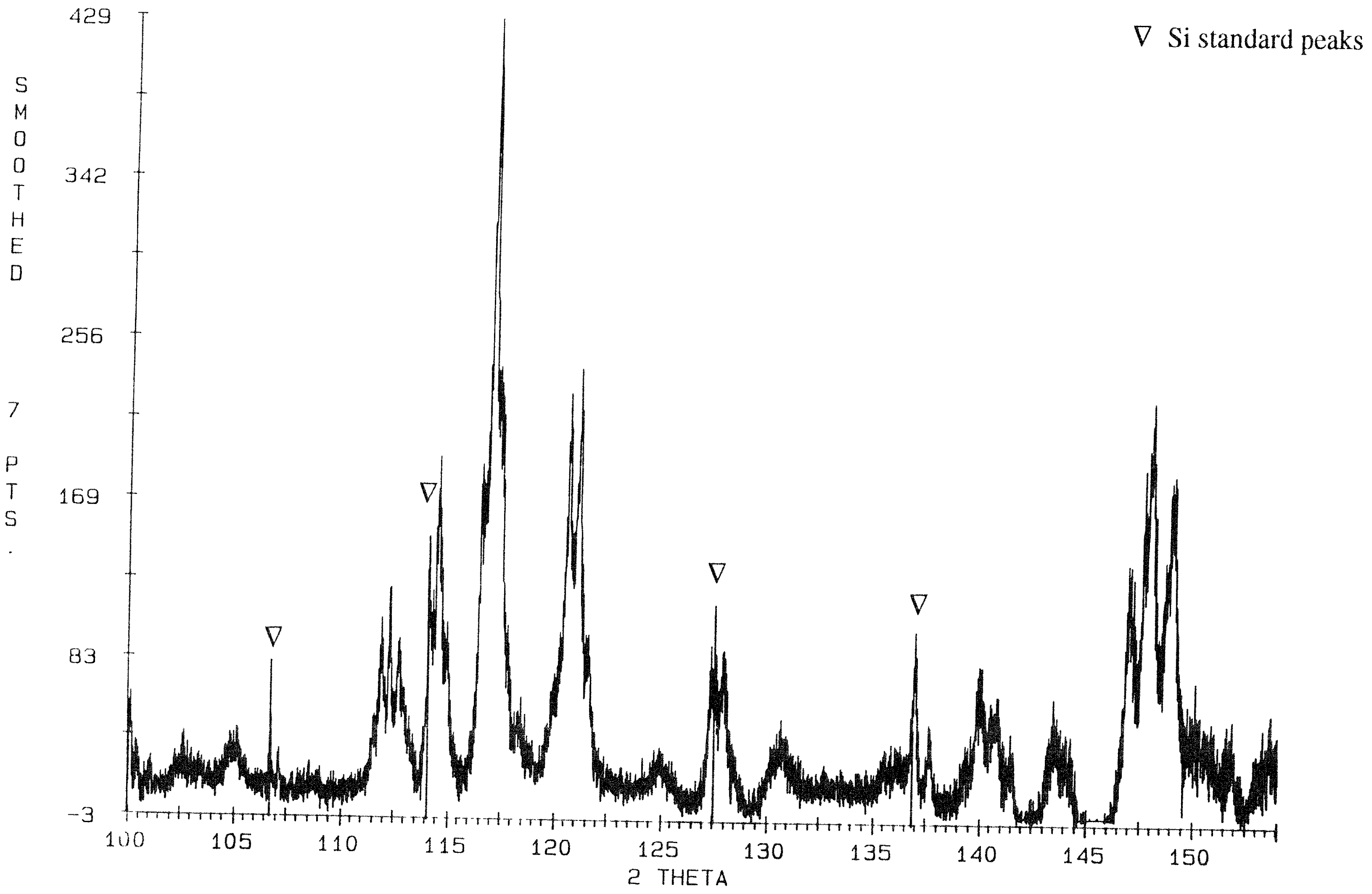

Figure C.2 (b) The 2θ vs. intensity x-ray diffraction scan for the *C*36 Ti-67 Cr at 1200°C. (2θ = 100-154°)

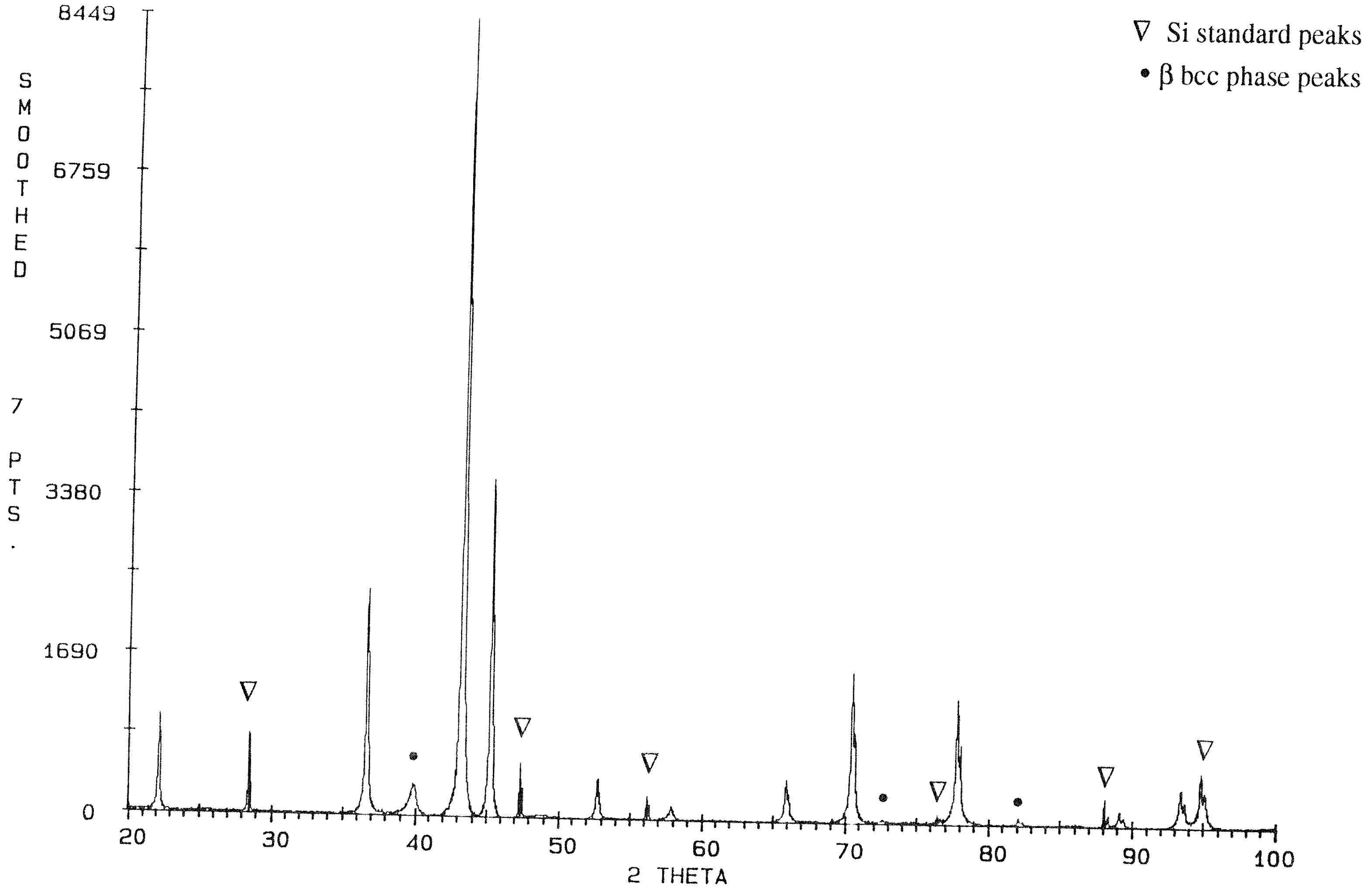

Figure C.3 (a) The 2θ vs. intensity x-ray diffraction scan for the *C*15 Ti-62 Cr at 1000°C with β-Ti(Cr) and *C*15 $TiCr_2$. (2θ = 20-100°)

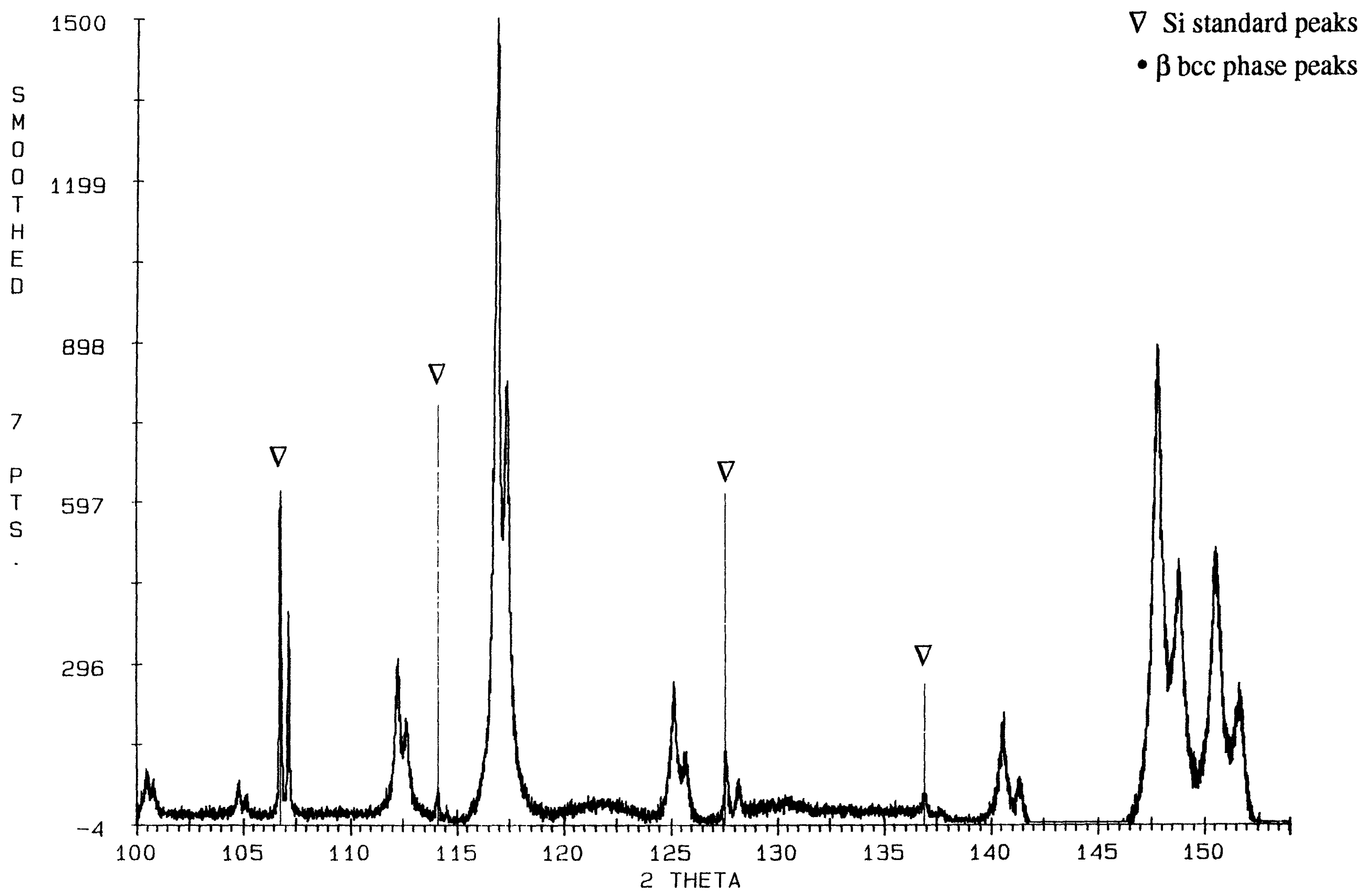

Figure C.3 (b) The 2θ vs. intensity x-ray diffraction scan for the *C*15 Ti-62 Cr at 1000°C with β-Ti(Cr) and *C*15 $TiCr_2$. (2θ = 100-154°)

Appendix D: Orientation Relationships

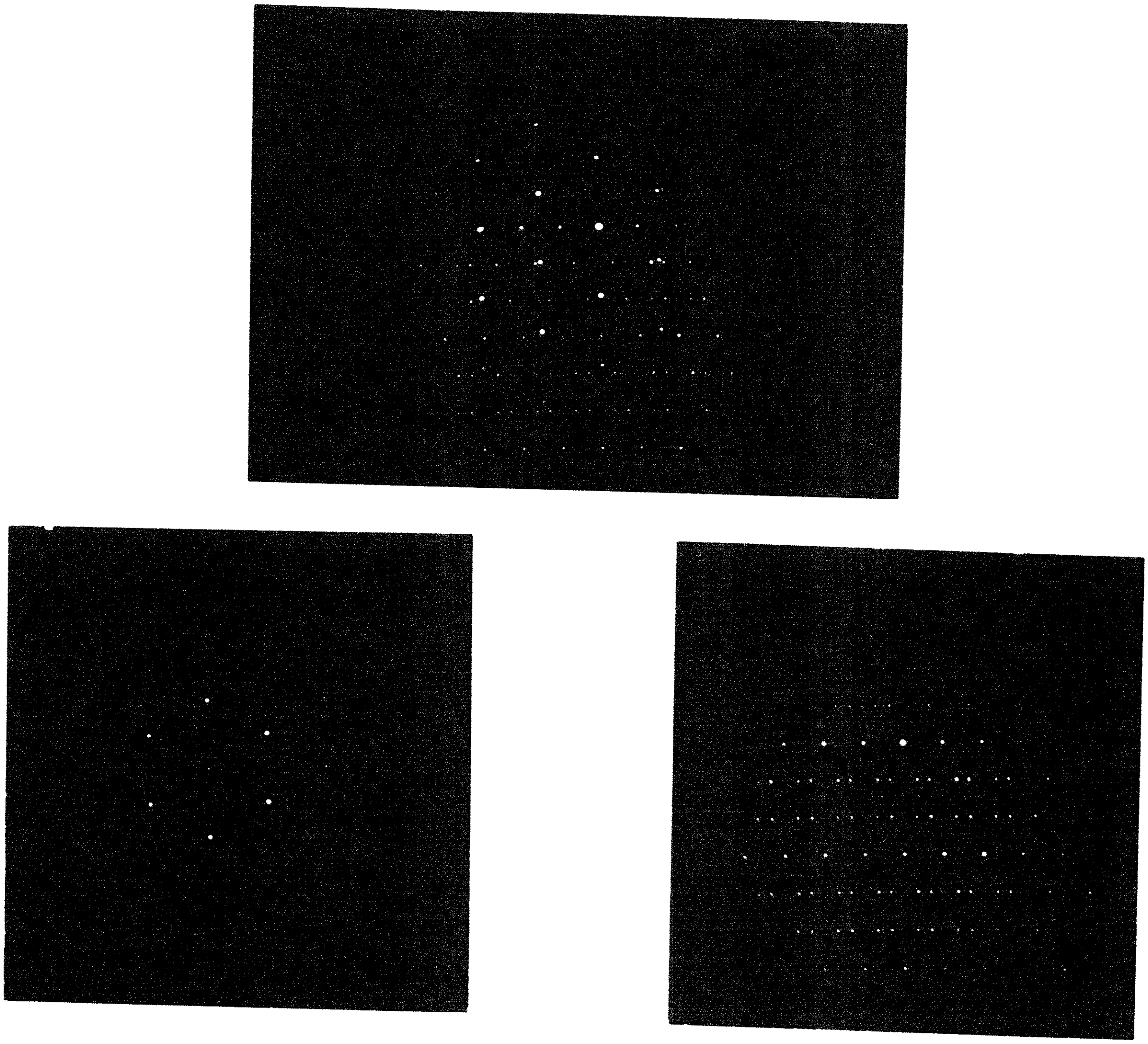

$[1\bar{1}1]_\beta \,||\, [101]_{C15}$

$(10\bar{1})_\beta \,||\, (10\bar{1})_{C15}$

$\sim(21\bar{1})_\beta \,||\, \sim(11\bar{1})_{C15}$

$\sim(\bar{1}12)_\beta \,||\, \sim(\bar{1}11)_{C15}$

$(121)_\beta \,||\, (020)_{C15}$

Figure D.1 (a) Orientation relationships from electron diffraction patterns at low-indexed zone axes of the bcc beta-phase and $C15$ $TiCr_2$ Laves phase.

$\sim[\bar{1}11]_{\beta} \,||\, \sim[\bar{2}11]_{C15}$
$(101)_{\beta} \,||\, (111)_{C15}$
$(110)_{\beta} \,||\, (13\bar{1})_{C15}$

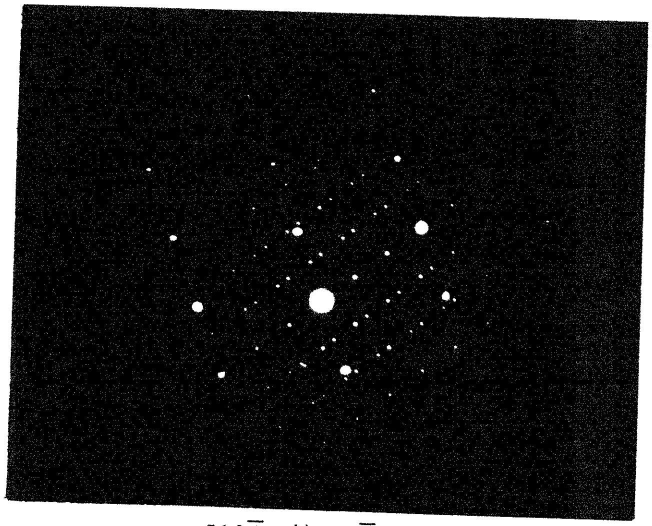

$[13\bar{1}]_{\beta} \,||\, [01\bar{1}]_{C15}$
$(101)_{\beta} \,||\, (111)_{C15}$
$\sim(\bar{1}12)_{\beta} \,||\, \sim(\bar{1}11)_{C15}$

Figure D.1 (b) & (c) Orientation relationships from electron diffraction patterns at low-indexed zone axes of the bcc beta-phase and $C15$ $TiCr_2$ Laves phase.

Table D.1. Interplanar distances of bcc β-Ti(Cr) and $TiCr_2$.

bcc β-Ti(Cr) (a=3.20Å)

(hkl)	*d* (Å)
100	3.200
110	2.263
111	1.848
200	1.600
210	1.431
211	**1.306**
220	1.131
221/300	1.067
310	1.012
311	0.965
222	0.924

***C*15-TiCr$_2$** (a=6.94Å)

(hkl)	*d* (Å)
100	6.940
110	4.907
111	4.007
200	3.470
210	3.104
211	2.833
220	2.454
221/330	2.313
310	2.195
311	2.092
222	2.003
320	1.925
321	1.855
400	1.735
410/322	1.683
411	1.636
331	1.592
420	1.552
422	1.417
511/**333**	**1.336**
440	1.227
531	1.173
620	1.097
533	1.058
622	1.046
444	1.002
550	0.981
711/551	0.972
642	0.927

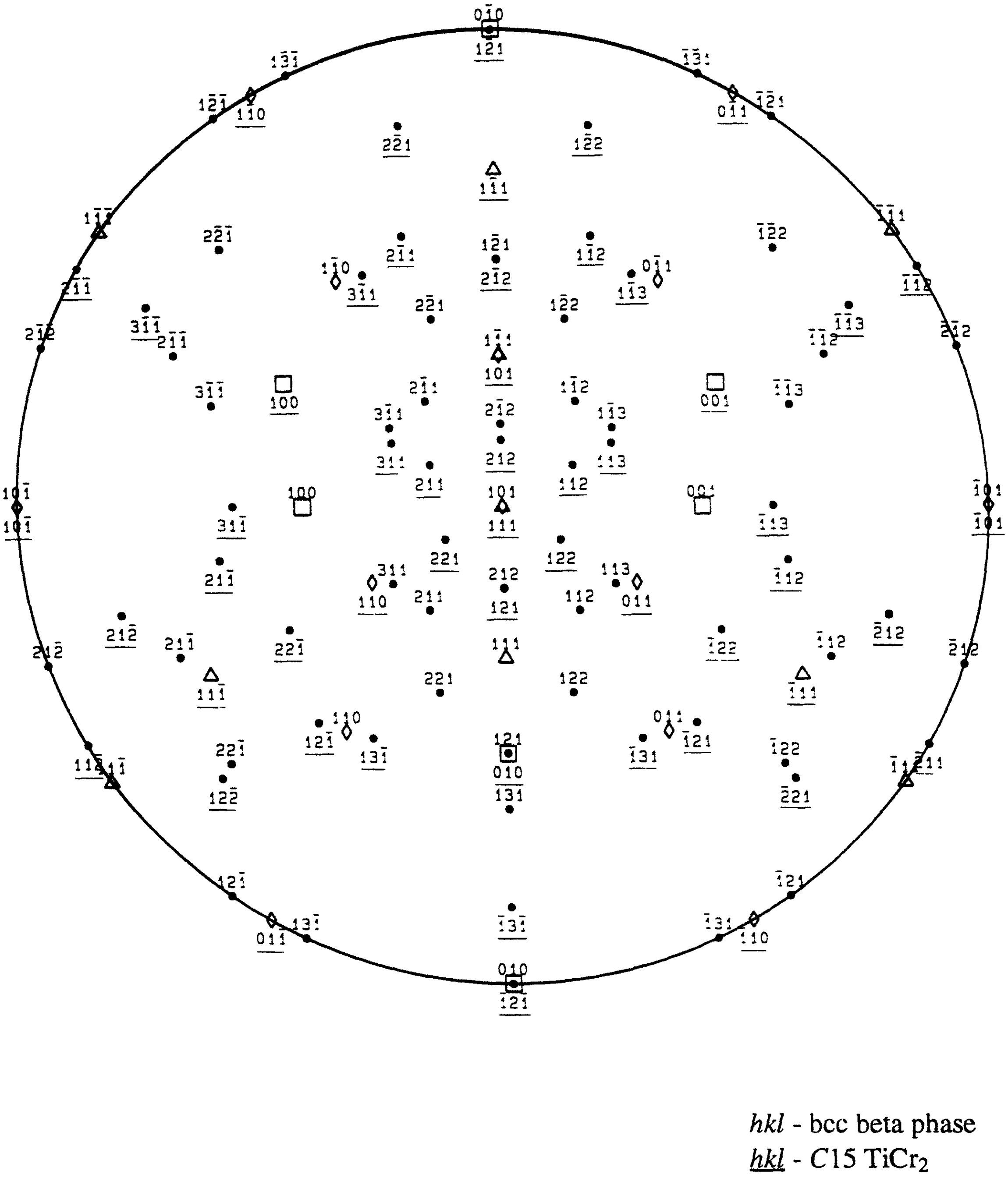

Figure D.2 Stereographic projection of the orientation relationship between the bcc beta-phase and *C*15 TiCr$_2$ Laves phase.

Appendix E: Orientation Relationship Matrix Notation

The orientation relationship between two phases can also be described using matrix algebra. This representation corresponds to a rotation, ϕ, about a common direction which brings the axes of one lattice into coincidence with the axes of the other lattice. For this reason, a common direction of $[10\bar{1}]$ was assigned to the diffraction patterns, and relieved the ambiguity of randomly assigning any variant as the zone axis of the precipitate phase once the bcc-matrix zone axis was assigned.

The lattice of one phase may be transformed to that of the other phase through a mathematical matrix, according to the following equation:

$$a_i' = S_{ij} a_j \tag{E.1}$$

where a_j represents any vector in the original lattice (say β), a_i' is the corresponding parallel vector in the transformed lattice ($C15$-TiCr$_2$), and S_{ij} is a 9x9 matrix of transformation. Repeated indices on the same side of the equation are summed. Using the 3 sets of parallel planes found by TEM, the transformation matrix was determined analytically by solving nine simultaneous equations for the nine unknowns to be:

$$S_{ij} = \begin{bmatrix} \frac{2+\sqrt{6}}{2\sqrt{6}} & \frac{-1}{\sqrt{6}} & \frac{2-\sqrt{6}}{2\sqrt{6}} \\ \frac{1}{\sqrt{6}} & \frac{2}{\sqrt{6}} & \frac{1}{\sqrt{6}} \\ \frac{2-\sqrt{6}}{2\sqrt{6}} & \frac{-1}{\sqrt{6}} & \frac{2+\sqrt{6}}{2\sqrt{6}} \end{bmatrix} \tag{E.2}$$

This matrix represents a 35.3° rotation about the $[10\bar{1}]$ direction.

The same transformation matrix could also be found by rotating one lattice into another through a reference coordinate system, A_j (i.e. cube axes),

$$A = \begin{bmatrix} 1 & 0 & 0 \\ 0 & 1 & 0 \\ 0 & 0 & 1 \end{bmatrix}$$

There are three mutually orthogonal parallel directions found experimentally in the bcc and $TiCr_2$ phases, and each direction can be represented by a matrix column as in:

$$B = \begin{bmatrix} 0 & 1 & -1 \\ 2 & 0 & 0 \\ 0 & -1 & -1 \end{bmatrix}$$

$$C = \begin{bmatrix} -1 & 1 & -1 \\ 2 & 0 & -1 \\ -1 & -1 & -1 \end{bmatrix}$$

These directions can be rotated into the cube axes of the reference coordinate system by :

$$B_i = M_{ij} A_j \tag{E.3}$$

where B_i are the three orthogonal vectors found in the bcc phase. M_{ij} can easily be computed as the direction cosines between the vectors in the old and new lattice.

$$M_{ij} = \begin{bmatrix} 0 & \frac{1}{\sqrt{2}} & -\frac{1}{\sqrt{2}} \\ 1 & 0 & 0 \\ 0 & -\frac{1}{\sqrt{2}} & -\frac{1}{\sqrt{2}} \end{bmatrix} \tag{E.4}$$

Similarly, the three orthogonal vectors in the Laves phase (C_i) that were found parallel to the bcc phase are rotated into the same reference coordinate system by the matrix, N_{ij}:

$$C_i = N_{ij} Aj. \tag{E.5}$$

$$N_{ij} = \begin{bmatrix} -\frac{1}{\sqrt{6}} & \frac{1}{\sqrt{2}} & -\frac{1}{\sqrt{3}} \\ \frac{2}{\sqrt{6}} & 0 & -\frac{1}{\sqrt{3}} \\ -\frac{1}{\sqrt{6}} & -\frac{1}{\sqrt{2}} & -\frac{1}{\sqrt{3}} \end{bmatrix} \tag{E.6}$$

By simple matrix manipulation, vectors in the bcc phase can be rotated into the corresponding parallel vectors in the Laves phase by the equation:

$$C_i = N_{ik} M_{jk}^{-1} B_j \tag{E.7}$$

$$N_{ik} M_{jk}^{-1} = S_{ij} \,. \tag{E.8}$$

Effectively, the bcc lattice is rotated to the reference coordinate system and then rotated into the Laves phase lattice.

Appendix F: Elastic Moduli

Table F.1 Elastic moduli of $TiCr_2$, solid solutions, and two-phase alloys.

material	elastic modulus (GPa)	technique, reference
Ti	115.7	Hertzberg [5.22]
Cr	279.1	Hertzberg [5.22]
$TiCr_2$	184	ultrasonic, Fleischer [5.20]
$TiCr_2$	**235**	indentation, Thoma [5.21]
$TiCr_2$	224.6	rule of mixtures
Ti-87 Cr (1200°C)	257.9	rule of mixtures
Ti-93 Cr (1000°C)	267.7	rule of mixtures
Ti-80 Cr (1200°C) Cr + $TiCr_2$	249.9	weighted averages of beta and Laves phase
Ti-80 Cr (1000°C) Cr + $TiCr_2$	252.0	weighted averages of beta and Laves phase

References in Chapter 5

Appendix G: Compression Tests of two-phase, ternary $TiCr_2$-base Laves alloys

The 4V2 and 4M3 alloys at 1300°C both displayed a coarse two-phase microstructure with large discrete ternary Laves phase precipitates. Table G.1 lists the compression test results with the binary Ti-40 Cr alloy (which had a similar microstructure of equiaxed Laves precipitates), and Figure G.1 plots the stress vs. "normalized displacement" of these alloys. The ternary alloys have a much larger "stiffness" than the binary alloys, due to solid solution strengthening in both the Laves phase and the beta phase, as well as larger volume percentages of the Laves phase. The ternary alloys, however, showed little plastic deformation and experienced abrupt failures. (TEM examination of the compressed samples was not performed since few deformation-induced structures would be expected.)

Figure G.2 shows a polished section of the compressed Mo sample. The discrete dark phase is the ternary Laves phase. A large crack runs throughout the sample, with large gaps at the Laves phase. The cracks are not confined to the individual Laves precipitates, as found in the binary Ti-Cr alloys (Chapter 5). The cracks run through both the Laves phase and the beta phase, rather than debonding the precipitate/matrix interface. The beta phase no longer acts as a binder or arrests the cracks as the Laves phase deforms. Thus, very little plasticity was seen in the ternary alloys. Despite the brittle behavior of these two samples, in no way do they imply that all two-phase ternary alloys would behave in the same manner.

Table G.1 Compression tests data for two-phase binary and ternary (Ti-V-Cr and Ti-Mo-Cr) alloys.

alloy	yield stress (MPa)	max stress (MPa)	displacement (cm/cm%)	slope (GPa)
Ti-40 Cr 1000°C/24 hrs	1406	1726	7.6	13.2
4V2 1300°C/6 hrs (31.8Ti-4.5V-63.7Cr)	1099	1258	1.1	17.0
4M3 1300°C/6 hrs (30Ti-4Mo-66Cr)	1240	1290	0.6	14.2

The fracture surface of the V sample is shown in Figure G.3. The two-phase microstructure is clearly evident, as the two phases display different fracture morphologies. The discrete Laves precipitates show flat, glass-like fracture surfaces, while the beta phase displays brittle transgranular fracture with many facets. The different cleavage facets at slightly different heights constitute river patterns in the beta phase [32].

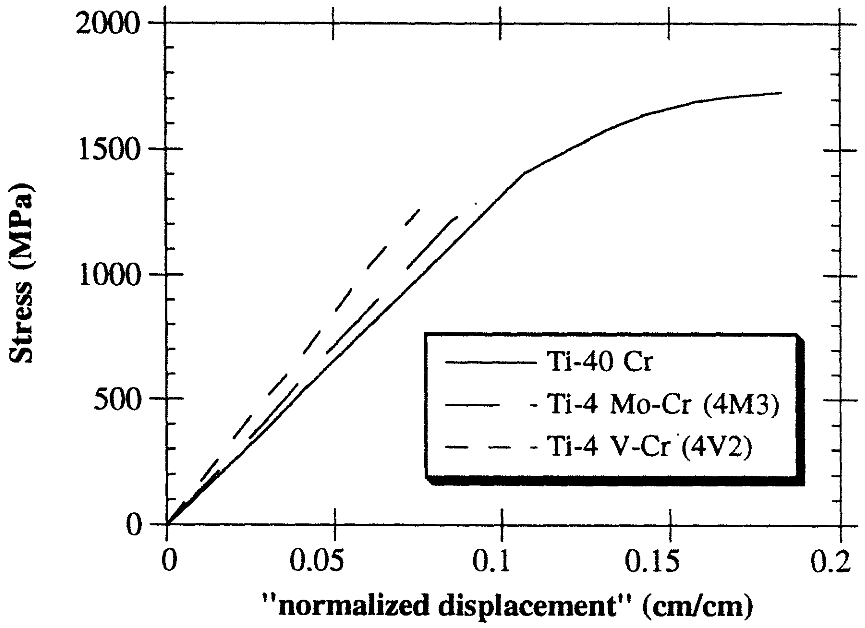

Figure G.1 Stress vs. "normalized displacement" from room-temperature compression tests of the coarse two-phase Ti-V-Cr and Ti-Mo-Cr alloys compared to the binary Ti-40 Cr alloy with large equiaxed Laves precipitates.

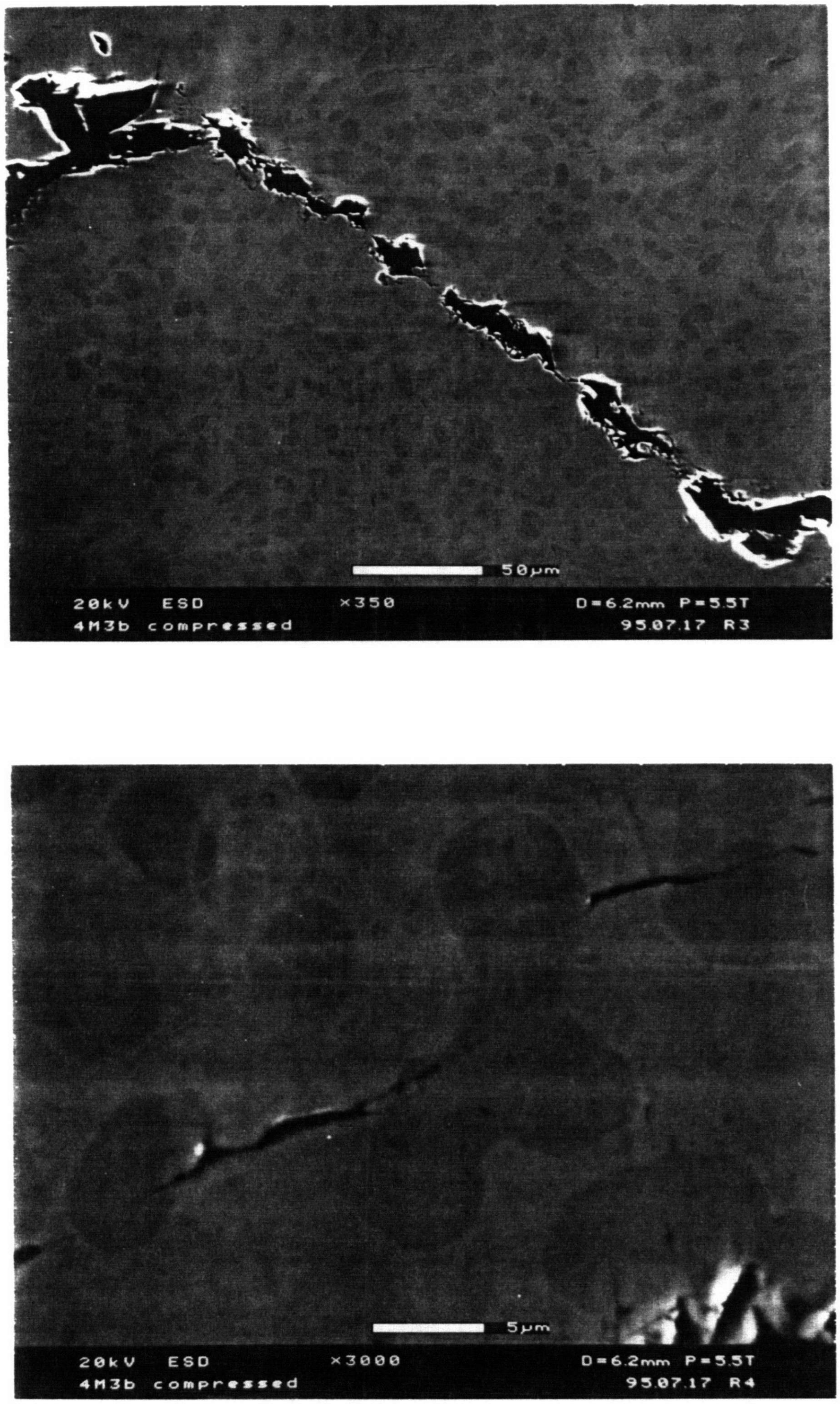

Figure G.2 SEM at **(a)** 350X and **(b)** 3000X of a polished section of the compressed Ti-4Mo-Cr (4M3) alloy. The crack runs through the entire two-phase microstructure.

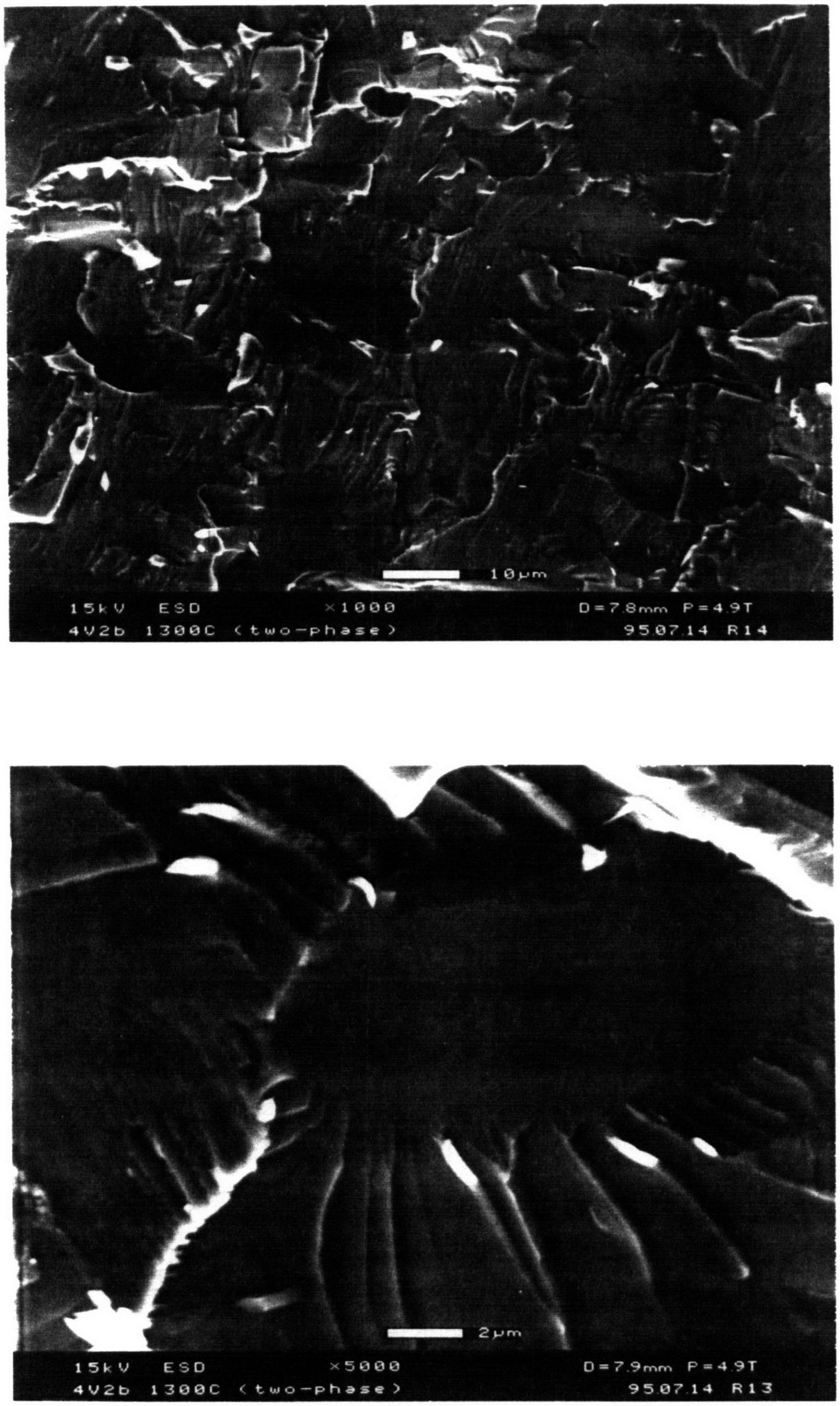

Figure G.3 SEM of brittle transgranular fracture surface at **(a)** 1000X and **(b)** 5000X of the compressed Ti-4 V-Cr alloy. The beta phase shows many cleavage facets and river patterns.